

Inaugural Dissertation
for
obtaining the doctoral degree
of the
Combined Faculty of Mathematics, Engineering and Natural Sciences
of the
Ruprecht-Karls-University
Heidelberg

Presented by
M.Sc. Isabel Marina Kemmer geb. Martin
born in: Bad Dürkheim, Germany
Oral examination: 31.05.2022

Exploring Mechanical Signaling at Cellular Force Transduction Hubs using Molecular Simulations

Referees: Prof. Dr. Frauke Gräter
Prof. Dr. Rebecca Wade

Abstract

Cells are subjected to mechanical forces and must sense and adequately react to them in order to develop and survive – a process known as mechanotransduction. This conversion of mechanical into biochemical signals is clustered at mechanotransduction hubs, i.e. protein complexes specialized for this purpose. Two examples of such hubs are on the one hand focal adhesions at the plasma membrane, which mediate signaling of the cellular inside with the outside matrix, and on the other hand the kinetochores, which control the proper segregation of chromosomes during cell division. In this work, I primarily used molecular dynamics simulations to investigate one protein from each of these two mechanotransduction hubs to further decipher their mechanisms for transducing mechanical signals.

For the crucial focal adhesion component Integrin-linked Kinase (ILK) I elucidated a non-conventional function of ATP-binding to the pseudokinase ILK. ATP promotes the structural stability of ILK and allosterically influences the interaction between ILK and its binding partner parvin, which leads to enhanced mechanoresistance of the ILK:parvin complex. Cell-level experiments from collaborators demonstrated that these features result in focal adhesion stabilization and proper traction force buildup, which manifests itself in efficient cell migration. Combined, these results suggest that ILK, stabilized and altered by the presence of ATP, might be capable to function as an active mechanotransducer.

The partially disordered inner centromere protein (INCENP), on the other hand, is a passive participant in mechanotransduction at kinetochores. I detected that its disordered region transitions from globular to coil states in response to phosphorylation, which considerably tunes its length and may influence its phase separation properties. These features would allow INCENP to act as length-variable tether to regulate the activity of the chromosome segregation kinase Aurora B by controlling Aurora B's access to targets in response to kinetochore tension.

My work thus sheds light on two widely different mechanisms by which non-enzymatic scaffold proteins are involved in mechanotransduction. In this way, we are expanding our palette of the manifold principles of mechanical signaling and thereby coming closer to grasping the complexity of cells.

Zusammenfassung

Zellen sind mechanischen Kräften ausgesetzt und müssen diese, um sich zu entwickeln und zu überleben, wahrnehmen und angemessen darauf reagieren – die sogenannte Mechanotransduktion. Diese Umwandlung von mechanischen zu biochemischen Signalen findet an Mechanotransduktionszentren statt, d.h. in Proteinkomplexen, die für diesen Zweck spezialisiert sind. Zwei Beispiele solcher Zentren sind zum einen die fokalen Adhäsionen an der Zellmembran, welche die Signalübertragung zwischen dem Zellinneren und der äußeren Matrix vermitteln, und zum anderen die Kinetochore, die im Zuge der Zellteilung die korrekte Trennung der Chromosomen sicherstellen. Unter Verwendung von in erster Linie molekulardynamischen Simulationen habe ich in dieser Arbeit jeweils ein Protein dieser beiden Mechanotransduktionszentren untersucht, um ihre Mechanismen zur Übertragung mechanischer Signale weiter zu entschlüsseln.

Für die Integrin-linked Kinase (ILK), eine wichtige Komponente fokaler Adhäsionen, habe ich eine unkonventionelle Funktion der ATP-Bindung an die Pseudokinase ILK aufgeklärt. ATP unterstützt die strukturelle Stabilität von ILK und beeinflusst allosterisch die Interaktion zwischen ILK und seinem Bindungspartner Parvin. Dies führt zu einer erhöhten mechanischen Widerstandsfähigkeit des ILK:Parvin-Komplexes. Experimente von Kollaborationspartner*innen auf Zellebene zeigten, dass diese Eigenschaften eine Stabilisierung fokaler Adhäsionen und eine ordnungsgemäße Erzeugung von Zugkräften bewirken, was sich in effizienter Zellmigration äußert. Diese kombinierten Ergebnisse deuten darauf hin, dass ILK, stabilisiert und verändert durch die Anwesenheit von ATP, in der Lage sein könnte als aktiver Mechanotransduktor zu fungieren.

Das zum Teil ungeordnete innere Zentromerprotein (INCENP) hingegen ist ein passiver Teilnehmer der Mechanotransduktion an Kinetochoren. Ich habe nachgewiesen, dass der ungeordnete Bereich von INCENP in Abhängigkeit von Phosphorylierungen von kompakten, kugelähnlichen Zuständen zu gestreckten Zuständen übergeht, was seine Länge erheblich verändert und seine Phasentrennungseigenschaften beeinflussen kann. Diese Merkmale würden es INCENP erlauben, die Aktivität der Kinase Aurora B zu regulieren, indem es als längenveränderlicher Anker agiert, um so den Zugriff von Aurora B zu seinen Substraten im Zusammenspiel mit der Kinetochorspannung zu kontrollieren.

Meine Arbeit beleuchtet somit zwei sehr unterschiedliche Mechanismen, durch die nicht-enzymatische Gerüstproteine an der Mechanotransduktion beteiligt sind. Dadurch erweitern wir die Palette der vielfältigen Prinzipien von mechanischer Signalübertragung und kommen so dem Verständnis der Komplexität der Zelle näher.

Acknowledgements

Zuallererst möchte ich diese Arbeit meinen Eltern widmen, um ihnen dafür zu danken, dass sie mich immer uneingeschränkt unterstützt und mir alles ermöglicht haben, was in ihrer Macht stand. Es ist nicht zuletzt ihren unermüdlichen Erklärungen und passenden Beispielen zu verdanken, dass ich ein naturwissenschaftliches Interesse entwickelt habe, um jetzt an diesem Punkt zu sein und diese Arbeit verfasst zu haben. Auch gäbe es diese Arbeit nicht ohne meinen Mann, der mich seit Beginn des Studiums begleitet, bedingungslos hinter mir steht und mich immer wieder ermutigt hat, wieder aufzustehen; von ganzem Herzen: Danke.

Within the scientific context, there are of course many people who have supported, encouraged and assisted me during the past four years and to whom I would like to express my gratitude. Obviously, I will not be able to acknowledge all the people who have influenced this work, but I would like to mention a number of them in particular. First and foremost, I would like to sincerely thank Frauke Gräter for the opportunity to work in her group on this interesting topic, for her valuable advice and guidance that led me through my project when I got stuck. I am also grateful to her for having confidence in my abilities, although I sometimes doubted myself. In addition, I would like to express my gratitude to the members of my thesis advisory committee, Rebecca Wade and Alba Diz-Muñoz, for their constructive discussions and suggestions, which were of great value to the progress of this project.

For the ILK project in particular, I would also like to acknowledge the great collaboration with Sara Wickström and Michele Nava from the University of Helsinki, who greatly complemented the project and thus shaped it to the form it has now; without them the story would have been only partially complete.

Regarding the INCENP project, I want to thank Camilo from the MBM group for setting up the coarse-grained model and the months he spend to analyze the data with me, as well as for always coming up with new ideas for the project.

This already brings me to the point of mentioning all the current and former MBM group members I have met, and who deserve special recognition for their collective wisdom and discussions that have moved my projects forward. Particularly, I would like to mention Svenja and Jannik, who provided me with direct feedback on the written version of the thesis. Also, I would like to highlight Jannik's insightful discussions and tips about statistics. Furthermore, I would like to thank former MBM members Christopher and

Csaba for mentoring me and introducing me to the world of molecular simulations. Additionally, I want to thank the great IT support at HITS and all system administrators of the MBM group who helped me with one or the other technical problem. Speaking of technical support, I acknowledge the state of Baden-Württemberg through bwHPC, where I was able to use the infrastructure of the bwForCluster.

I also want to sincerely thank the HITS communications team, especially Angela, for their help in making my research accessible to a wider audience and encouraging me to think about the really important aspects of my work. On top of that, I want to extend my thanks to all HITSters who make the institute what it is and warmly welcomed me.

Without all of you, this work would not have the final form you are about to read.

Acronyms

AA all-atom

AFM atomic force microscopy

AMBER Assisted Model Building with Energy Refinement

ATP Adenosine triphosphate

CG coarse-grain

CH calponin-homology

COM center of mass

CPC Chromosomal Passenger Complex

DNA Deoxyribonucleic acid

ECM extracellular matrix

FA focal adhesion

FAK focal adhesion kinase

FDA force distribution analysis

FERM 4.1-ezrin-radixin-moesin

GROMACS GRoningen MACHine for Chemical Simulations

HADDOCK High Ambiguity Driven Protein-Protein Docking

HITS Heidelberg Institute for Theoretical Studies

IDP intrinsically disordered protein

IDR intrinsically disordered region

ILK Integrin-linked kinase

INCENP inner centromere protein

IPP Integrin-linked Kinase, parvin, PINCH

JMB Journal of Molecular Biology

KT kinetochore

LINC linker of nucleoskeleton and cytoskeleton

LINCS linear constraint solver

LLPS liquid-liquid phase separation

MD molecular dynamics

MT microtubule

NMR nuclear magnetic resonance

np non-phosphorylated

NTC non-trivial contacts

P-level phosphorylation level

PAA polyacrylamide

PBC periodic boundary condition

PC principle component

PCA principle component analysis

PDB protein data bank

PH pleckstrin homology

PINCH particularly interesting new cysteine-histidine rich protein

PIP2 Phosphatidylinositol-4,5-bisphosphat

PME Particle Mesh Ewald

PNAS Proceedings of the National Academy of Sciences of the United States of America

REMD replica exchange molecular dynamics

RMSD root mean square deviation

RMSF root mean square fluctuation

SAC spindle-assembly checkpoint

SAH single α -helix

SASA solvent accessible surface area

SAXS small-angle X-ray scattering

SKAP small kinetochore-associated protein

TFM traction force microscopy

VMD visual molecular dynamics

Contents

Acronyms	xi
1 Introduction	1
1.1 Mechanical force in biology	1
1.2 Converting force into biochemical signals	2
1.3 Cellular mechanotransduction hubs	3
1.4 Overview of this thesis	4
2 Theory of Simulations and Experiments	7
2.1 Molecular dynamics simulations	7
2.1.1 Force fields	8
2.1.2 Integrating the equations of motion	10
2.1.3 Advanced procedures of MD simulations	11
2.1.4 Coarse-grained modeling	14
2.2 Biasing MD simulations	15
2.2.1 Replica-exchange MD	15
2.2.2 Force-probe molecular dynamics	16
2.3 Analysis of MD trajectories	17
2.3.1 Root mean square deviation and fluctuation	17
2.3.2 Radius of gyration	17
2.3.3 Principle component analysis	18
2.3.4 Force distribution analysis	18
2.4 Molecular docking	20
2.5 Traction force microscopy	21
3 Case Study I: Integrin-linked Kinase at Focal Adhesions	23
3.1 Background: Focal adhesions – the main hub for cell-matrix interaction .	23
3.1.1 The extracellular matrix	23
3.1.2 Focal adhesions	24
3.1.3 The ILK/PINCH/parvin complex	26
3.1.4 Integrin-linked kinase as a pseudokinase	28
3.1.5 Aim of this project	30

3.2	Methods	32
3.2.1	Simulation details	32
3.2.2	Experimental methods	36
3.3	ATP stabilizes ILK and focal adhesions	39
3.4	ATP allosterically influences parvin-binding saltbridges	42
3.5	Saltbridge-coordinating residues stabilize α -parvin binding and focal adhesions	47
3.6	ATP increases the mechanical stability of the ILK:parvin complex	49
3.6.1	Force through the ankyrin-actin axis	50
3.6.2	Force through the kindlin-actin axis	51
3.7	ATP- and α -parvin-binding defective ILK impairs traction force generation and cell migration	55
3.8	Discussion	57
3.8.1	ILK stability and its binding partners	57
3.8.2	ATP-induced allostery	58
3.8.3	ILK under mechanical stress	60
3.8.4	Focal adhesion dynamics	61
3.8.5	Outlook on ILK as a pseudokinase	62
4	Case Study II: INCENP at the Kinetochores	65
4.1	Background: Keeping genomic integrity	65
4.1.1	Cell division	65
4.1.2	Kinetochores-microtubule attachments	66
4.1.3	INCENP: Scaffolding the chromosomal passenger complex	67
4.1.4	Mechanism of Aurora B action	68
4.1.5	Intrinsically disordered proteins	69
4.1.6	Aim of this project	70
4.2	Simulation details	72
4.2.1	All-atom simulations	72
4.2.2	Coarse-grained simulations	74
4.2.3	Analysis of simulations and predictions	76
4.3	Charge distribution of INCENP IDR is altered by phosphorylation	80
4.4	Conformational ensemble of 75-residue fragments	82
4.5	Establishment of a coarse-grain framework for INCENP	86
4.6	Phosphorylation-induced conformational dynamics of whole INCENP IDR	87
4.7	Cohesion of INCENP IDR condensates	93
4.8	Discussion	95
4.8.1	Multiscale MD simulation approach	95
4.8.2	Influence of phosphorylation on INCENP	96

4.8.3	Participation of the INCENP IDR in the dog-leash model	98
4.8.4	Liquid-liquid phase separation	100
4.8.5	Outlook on INCENP function	101
5	Concluding Remarks and Future Perspectives	103
5.1	Signal integration at mechanotransduction hubs	103
5.2	The different roles of scaffold proteins	105
5.3	Life in the shadow of classic enzymes	105
5.4	Future perspectives of molecular simulations	107
	Bibliography	109
A	Appendix for chapter 3: Integrin-linked kinase	133
B	Appendix for chapter 4: INCENP	143

Introduction

” *The same few dozen organic molecules are used over and over again in biology for the widest variety of functions.*

— Carl Sagan

All structures, from rocks to humans, require physical forces to hold themselves together. Only due to mechanical forces nature was able to build and operate the most complex biological structures we know of – arguably the human body. Nevertheless, most of the enormous success in explaining biological phenomena is still only attributed to the explanatory power of the omnipresent reaction-diffusion model of biochemistry. However, this chemical mindset is not always sufficient to explain biological processes. Consequently, over the last years mechanical forces have emerged more and more as one missing factor of biological signal transduction and thus as a universal concept of biological language across all kingdoms of life.

1.1 Mechanical force in biology

The effects of forces in the biological context are perhaps most evident on larger scale processes like physical exercise, breathing and blood flow, among others. But underlying all those processes lies the potential of forces to regulate biological processes on the microscopic scale. Recently this was highlighted by the awarding of the Nobel price in physiology/medicine to David Julius and Ardem Patapoutian in October 2021 for their discoveries of receptors for temperature and touch – ion channels that mediate thermal and mechanical signal transduction¹. Beyond to such specialized sensory cells, nearly every cell is subjected to mechanical force and as a result they can adjust their shape, migration, differentiation and proliferation. Stem cells for example differentiate into their fated specialized cells in response to the geometry and stiffness of the substrate on which they grow (L. R. Smith et al., 2018). Likewise, the function of many other

¹The Nobel Prize in Physiology or Medicine 2021. NobelPrize.org. Nobel Prize Outreach AB 2022. Tue. 8 Mar 2022. <<https://www.nobelprize.org/prizes/medicine/2021/summary/>>

cells highly depends on the connection of the cell to the so-called extracellular matrix (ECM) to which they adhere. Therefore, it is not surprising that many diseases arise from defects in proper conversion of mechanical into biological signals, such as deafness, heart muscle disease, asthma, cancer and many more (Jaalouk and Lammerding, 2009; Ingber, 2003).

The ability of cells to sense mechanical signals from their environment is defined as mechanosensing. The detected physical cues are then transformed into an adequate, context-specific biological response in a process called mechanotransduction. Therein, a protein or protein complex that triggers biochemical signaling in response to a mechanical stimulus is defined as a mechanotransducer.

1.2 Converting force into biochemical signals

To understand the big picture of cellular mechanotransduction we require knowledge of the mechanical properties of proteins and other biomolecules. To fulfill mechanoresponsive functions, proteins need to be embedded in molecular networks that are physically coupled to force-bearing cellular structures like for example the contractile cytoskeleton. Therefore, the crucial question in mechanotransduction concerns the different ways in which proteins and their corresponding biological signaling networks are designed on the nanoscale to respond specifically to mechanical forces. Of particular interest here are the integration principles of such events into mechanoresponsive pathways.

The equilibrium structures and functions of proteins are extensively studied. Insight into protein dynamics and the resulting relation between mechanical force and altered protein conformations has further emerged in the last years. The nature and degree of responses to mechanical stimuli on proteins is greatly variable. Those include, but are not limited to, formation or disruption of protein-protein interaction (Y. Chen et al., 2015), introduction or removal of post-translational modifications (Qin et al., 2015; Hashimoto et al., 2019), exposition of molecular recognition sites (Butera et al., 2018) and protein unfolding (Jagannathan and Marqusee, 2013). For the latter, the mechanical stability of a protein to unfolding is regulated by the positions of its secondary structure motifs and the interaction between them. How these motifs are oriented relative to the external force vector ultimately determines the protein unfolding pattern, including the order in which force-bearing interactions rupture (Vogel, 2006; Carrion-Vazquez et al., 2003).

While single-molecule rupture experiments like atomic force microscopy (AFM) (Nandi and Ainarapu, 2021) or optical tweezers (Bustamante et al., 2020) can determine the overall effect of force on proteins, the investigation of such mechanical effects on the

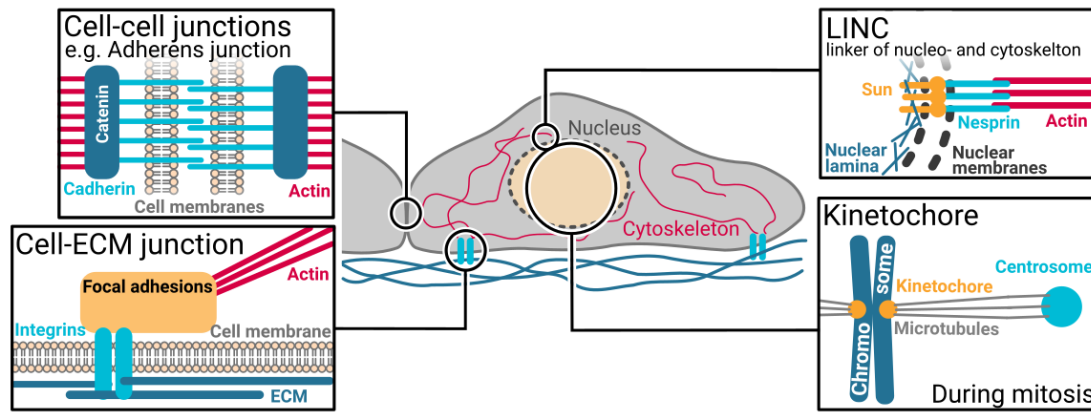


Fig. 1.1.: Sites of cellular force transduction. So called mechanotransduction hubs exist both at the cell membrane for mechanical communication between cellular outside and inside (for example focal adhesions and adherens junctions) and also within the cell for intracellular force signaling (for example the kinetochores and the linker of nucleoskeleton and cytoskeleton (LINC)).

atomic level requires sophisticated computational methods such as force-probe molecular dynamics simulations (Grubmüller, 2005), which are described in detail in chapter 2. Both computational and biophysical methods are best combined for cross-validation and full determination of the biological process.

1.3 Cellular mechanotransduction hubs

The combined effort in the field of mechanosensing achieved the identification of various subcellular structures that mediate cellular force transduction, so called mechanotransduction hubs. Such large and specialized protein complexes exist both at the plasma membrane managing the force signaling between the cellular outside and inside, and equally at compartments inside the cell, including intracellular membranes mediating intracellular force transduction (Figure 1.1). For example, cells probe the mechanical stiffness of their environment at focal adhesions (FAs), contacts between the cell and the ECM. FAs are membrane-attached signaling platforms at the interface between intra- and extracellular tension (Burrige, 2017). The intracellular forces are generated by the actin-myosin cytoskeleton machinery, whereas mechanical signals from the extracellular space depend on the density, topography and stiffness of the ECM. Further, cells are able to regulate the mechanical coupling between neighboring cells by cell-cell junctions (Angulo-Urarte et al., 2020).

Regarding intracellular force transduction, the nucleus and its transcriptional programs are mechanically coupled to the cytoskeleton through the linker of nucleoskeleton and

cytoskeleton (LINC) (Lityagina and Dobрева, 2021). Furthermore, in the process of cell division, kinetochores mechanically control faithful chromosome separation. Kinetochores are large protein complexes that assemble on the centromeric region of the chromosomes during mitosis (Cheeseman, 2014). They mediate the attachment of the mitotic spindle microtubules to the chromosomes to ultimately separate the two chromatids and pull them to the opposite cell poles. Only correct chromosomal bi-orientation lead to faultless division of the genomic material. The build-up of molecular tension due to microtubule binding and pulling is used to detect such correct bi-orientation. However, the precise molecular mechanisms governing force transduction at those different intracellular structures are still largely poorly understood.

1.4 Overview of this thesis

This thesis aims to contribute to the understanding of signaling mechanisms employed by cells to transduce mechanical forces inside force transduction hubs by means of molecular simulations. These mechanisms on the molecular level can only fully be grasped by molecular simulations as those provide the necessary resolution. In contrast, experimental methods can determine the larger scale effects of such molecular alterations. This thesis covers the investigation of a protein involved in outside-in signaling and one protein implicated in intracellular force transduction. A detailed biological overview of the two studied force transduction hubs, namely FAs and the kinetochore, and of the specific proteins under investigation, that is ILK and INCENP, are addressed further in the background sections of the corresponding chapters.

Case Study I: ILK at Focal Adhesions The first results chapter (chapter 3) concerns the function of the pseudokinase ILK, a crucial component of FAs. The investigations elucidate the non-canonical effect of the small molecule ATP, normally critical for kinase catalysis, on the signaling of a non-catalytic mechanotransducer. The molecular simulations are combined with cellular and biochemical experiments, including traction force microscopy, performed by Michele Nava and Sara Wickström (Helsinki University, Finland) to cross-validate and complement the simulation results providing a view of ILK across two different orders of magnitude.

Case Study II: INCENP at the Kinetochore The second results chapter (chapter 4) sheds light onto a more passive participant in the big picture of mechanotransduction at kinetochores, the inner centromere protein (INCENP). It is co-responsible for correct

chromosome segregation by scaffolding and thereby regulating the kinase Aurora B which removes incorrectly attached microtubules. Based on a current hypothesis, the detection of correct kinetochore tension is achieved through the distance-restricted access of Aurora B to substrate proteins. Molecular simulations at different resolutions allowed to explore the role of INCENP within this mechanism by examining the conformational ensemble of INCENP's intrinsically disordered region as a function of its phosphorylation state as well as exploring its phase separation capacity.

Theory of Simulations and Experiments

This chapter describes the general theories behind the methods used in this thesis. For the molecular simulations, these include molecular dynamics simulations (section 2.1), its biasing and analysis techniques (section 2.2, section 2.3) as well as molecular docking (section 2.4). Additionally, traction force microscopy experiments are outlined in section 2.5. Details on the specific parameters used for the different biological systems can be found in the methods section of the respective results chapters.

2.1 Molecular dynamics simulations

Comprehension of protein dynamics is essential to our understanding of the underlying mechanisms of biological processes. Molecular dynamics (MD) simulations, that follow the structure and properties of molecules as they evolve in time, are one technique to decipher protein dynamics at atomic resolution (Hollingsworth and Dror, 2018; González, 2011; Karplus and Kuriyan, 2005). In MD simulations, the motions of molecules can be described on timescales from bond-vibrations occurring within femtoseconds to large-scale conformational transitions within microseconds and beyond.

Figure 2.1 shows a simplified workflow of a typical MD simulation. In short, the initial starting structures, namely the atomic coordinates in 3-dimensional space, are usually obtained from experimental techniques such as X-ray crystallography (Shi, 2014) or nuclear magnetic resonance (NMR) (Marion, 2013). The atoms are assigned initial velocities and their positions are then propagated in time by integration of Newton's equations of motion. To do so, an accurate description of the forces between atoms is needed. Ideally, forces would be derived from first principles, i.e. by solving the electronic structure and subsequently calculating the resulting forces on each atom with quantum mechanical calculations (Kohanoff, 2006). However such computationally expensive treatment is only feasible for a few tens to hundreds of atoms, while typical protein systems can encompass up to millions of atoms. Therefore, in MD simulations the atoms are represented as spheres interacting with spring-like potentials, which are described in so called 'force fields'.

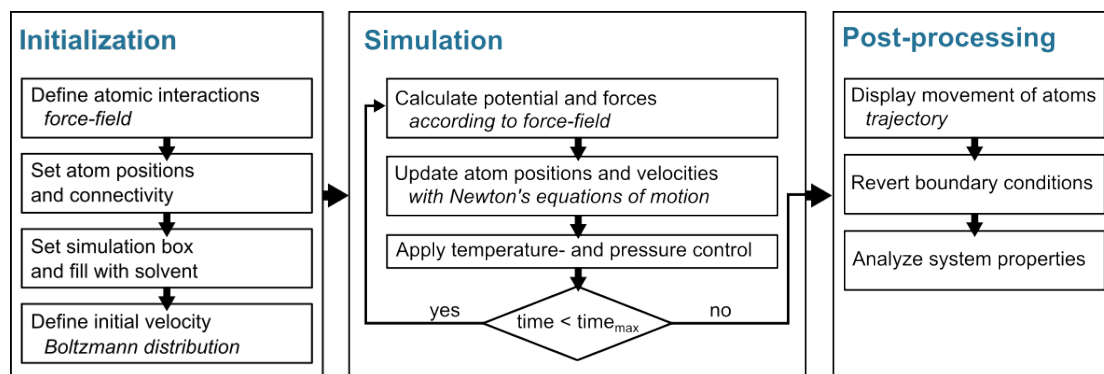


Fig. 2.1.: Typical workflow of MD simulations. First, the positions of atoms and interactions between them are defined. Taking into account their interatomic forces, which are described by force fields, the atom positions are propagated in time by integration of Newton's equations of motion for a small timestep. The integration is repeated until the desired trajectory length is reached. The dynamic properties are calculated and visualized in the post-processing step.

2.1.1 Force fields

A force field mathematically describes the dependence of the system's energy on its atomic coordinates. It contains an empirical set of functions and their respective parameters defining the interatomic potential energy ($V(r_1, r_2, \dots, r_N)$) as a function of the atom positions (r_1, r_2, \dots, r_N). This potential energy function consists of the sum of the individual bonded and non-bonded interactions (Figure 2.2). The bonded terms define the interactions between covalently bound atoms (i.e. bonds, angles, dihedrals). The intra- and intermolecular interactions between atoms that are not linked by covalent bonds are termed the non-bonded interactions and comprise electrostatics and van der Waals interactions. Thus the potential energy function is defined as

$$V = V_{\text{bond}} + V_{\text{angle}} + V_{\text{dihedral}} + V_{\text{LJ}} + V_{\text{coulomb}}. \quad (2.1)$$

Therein, the bond energy resulting from the covalent interaction of atoms i and j is defined as

$$V_{\text{bond}} = \sum_{\text{bonds}} \frac{1}{2} k_i^{\text{bond}} (r_{ij} - r_0)^2 \quad (2.2)$$

where r_{ij} is the actual bond length between two atoms, r_0 is the equilibrium bond length and k_i^{bond} is the harmonic force constant.

The energy of angle bending relative to the equilibrium bond angle θ_0 can be described as

$$V_{\text{angle}} = \sum_{\text{angles}} \frac{1}{2} k_i^{\text{angle}} (\theta_i - \theta_0)^2 \quad (2.3)$$

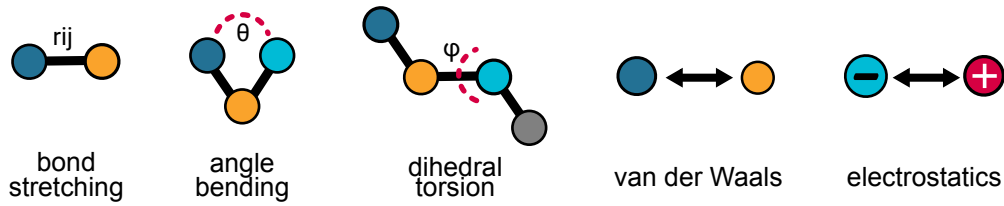


Fig. 2.2.: Atomic interactions in force fields. In a classical force field the energy contributions from bonded interactions including bond stretching, angle bending and dihedral torsions are combined with the non-bonded interactions comprising van der Waals interactions and electrostatics.

where θ_i is the actual bond angle between three atoms and k_i^{angle} is the harmonic force constant.

In a system of four atoms, the energy due to deviation from the equilibrium dihedral angles ϕ is calculated according to:

$$V_{\text{dihedral}} = \sum_{\text{dihedrals}} \frac{1}{2} k_i^{\phi} (1 + \cos(n\phi - \gamma)) \quad (2.4)$$

where k_i^{ϕ} is the height of the torsional energy barrier, n is the multiplicity of the potential function and γ is the phase shift angle.

The non-bonded van der Waals interactions are described by a Lennard-Jones potential where the interaction energy between the atoms i and j at distance r_{ij} is defined as

$$V_{\text{LJ}} = 4\epsilon_{ij} \left[\left(\frac{\sigma_{ij}}{r_{ij}} \right)^{12} - \left(\frac{\sigma_{ij}}{r_{ij}} \right)^6 \right] \quad (2.5)$$

in which ϵ_{ij} and σ_{ij} are the depth and the width of the 6-12 Lennard-Jones potential. ϵ is commonly referred to as the dispersion energy and σ describes the particle size and thereby marks the distance at which the particle-particle potential energy is zero.

The non-bonded electrostatic interactions are described by Coulomb's law where the electric potential between a pair of atoms with charges q_i and q_j at distance r_{ij} is defined as

$$V_{\text{coulomb}} = \frac{q_i q_j}{4\pi\epsilon_0 r_{ij}} \quad (2.6)$$

with ϵ_0 being the dielectric constant.

The accuracy of MD simulations is directly related to the quality of the force field parameters, which are calibrated by quantum mechanical calculations and experiments of small model molecules. Further, the ability of force fields to reproduce physical properties is ensured by comparison to experimental methods like for example small

angle X-ray scattering (Boldon et al., 2015; Latham and B. Zhang, 2019). Consequently each force field is optimized for the specific class of molecules that they are developed for, i.e. proteins for the AMBER force field used here.

2.1.2 Integrating the equations of motion

Once the potential energy of the system (V) is known, the forces acting on each atom (F_i) depending on the atomic coordinates (r_i) are calculated as:

$$F_i = -\frac{\delta V}{\delta r_i} \quad (2.7)$$

Subsequently, the motions of the nuclei are described classically – as opposed to an extremely computationally expensive quantum mechanical treatment – by Newton’s equations of motions:

$$F_i = m_i a_i = m_i \frac{d^2 r_i}{dt^2} \quad (2.8)$$

where F_i is the total force acting on atom i and m_i , a_i , and r_i are its mass, acceleration and position, respectively. Newton’s equations of motion are numerically integrated, as they cannot be solved analytically, using the Verlet algorithm (Verlet, 1967) which is based on the Taylor expansions for velocity and position or the leap-frog algorithm, which is mathematically equivalent to Verlet, but updates the positions and velocities asynchronously.

This integration, performed for each atom separately, is executed over a small, finite time increment, a timestep, to calculate the atomic positions at the next timestep. By subsequently repeating these steps, the temporal evolution of the system, a trajectory, is generated. Therein, the timestep (Δt) must be small in comparison to the fastest motions in the system to accurately represent those high-frequency vibrations. Bond vibrations involving hydrogens that occur within a few femtoseconds would impose a timestep of 1 fs (González, 2011). However, these have only a negligible effect on the protein’s time evolution. Therefore, we can constrain the bond lengths and bond angles between heavy atoms and hydrogens. This allows the timestep to be increased to 2 fs, effectively doubling the time that can be simulated in one timestep and halving the computational effort for a given trajectory length. To this end, many algorithms for H-bond constraining were developed and are currently used in standard MD simulations, like the LINCS algorithm employed in this thesis (Hess, 2008).

2.1.3 Advanced procedures of MD simulations

Calculation of long-range interactions

The evaluation of non-bonded interactions is the limiting factor for the computational efficiency of each integration step in MD simulations. Therefore, the calculation of the non-bonded interactions is commonly restricted to atoms within a set cutoff which greatly enhances the computational efficiency. Such cutoff-based approaches work well for the Lennard-Jones potential that decays rapidly with distance. However, the Coulomb potential does not decay fast enough to allow for safe truncation with a simple cutoff. Thus, the contribution of the long-range electrostatic interactions is typically approximated using the Particle Mesh Ewald (PME) scheme that possesses more favorable scaling properties (Darden et al., 1993; Essmann et al., 1995). In short, using PME the coulomb potential beyond the cutoff is calculated in the reciprocal space via a Fourier transform. The charge density is evaluated on a discrete mesh using interpolation, where each grid point contains a charge based on the atoms in its immediate neighborhood. The convolution of each mesh point with every other, denoting the interaction between mesh points, can be performed by taking the Fourier transform of the original density mesh. The back-transformation applies the resulting forces to each atom based on its position within the mesh. This way, a high accuracy in the evaluation of the long-range interactions can be maintained while drastically increasing computational speed.

Water models

The natural environment of proteins is usually the aqueous cytoplasm. In simulations, proteins are consequently solvated by the addition of water molecules supplemented with sodium and chloride ions in physiological concentration. The computational treatment of this solvent is the biggest factor that determines the system size, i.e. the number of atoms, both proteins and solvent, to be simulated. Thus, the system size ultimately dictates the accessible timescale. Several water models have been developed to represent water in simulations. A water molecule in a three-site model, like the commonly used TIP3P water model (Jorgensen et al., 1983), contains three interaction points corresponding to the three participating atoms. Here, each site is assigned a point charge. Additionally, Lennard-Jones parameters are given to the site corresponding to the oxygen. Further, the model uses a rigid geometry to match that of actual water. Such three-point water models usually provide enough accuracy of the water properties while at the same time maintaining a reasonable computational effort.

However, the use of more elaborate water models can be beneficial for specific applications. With the above described water model, the conformational ensembles of disordered proteins (subsection 4.1.5) are structurally too compact in comparison to experiments. One way of counteracting this is the use of an optimized water model for disordered proteins, TIP4P-D (Piana et al., 2015). This four-site model contains four interaction points by adding a dummy atom near the oxygen. Additionally, it corrects for the underestimation of water dispersion interactions thereby improving the electrostatic distribution around the water molecule. Simulated with the TIP4P-D water model, disordered proteins are typically substantially more expanded and therefore in better agreement with experiments. However, such a four-point water model significantly increases the computational cost by the introduction of a fourth particle in each solvent molecule.

The particle number can be drastically reduced by treating the solvent implicitly. Here, the explicit solvent molecules are replaced by a continuous medium describing electrostatic interactions of the solvent with a solute molecule. The solute, in most biological cases a protein, is encapsulated in a tiled cavity which is embedded in a homogeneously polarizable continuum describing the solvent. The solvent's dielectric constant (ϵ) determines the degree of its polarizability. The implicit solvent interacts with the charges on the cavity surface, that are defined by the enclosed protein which in turn changes the polarization of the protein. In this thesis, implicit solvent was used in combination with the coarse-grained model described in subsection 2.1.4.

Adjusting temperature and pressure

The integration of Newton's equations of motions keeps the number of particles (N), the volume of the simulation box (V) and the total energy of the system (E) constant. Thus, a trajectory in the microcanonical (NVE) ensemble is generated, where an ensemble describes the probability distribution of a system's states. However, due to numerical integration errors and the approximations used to evaluate the non-bonded interactions, the total energy of the system is not completely conserved. Further, to ensure comparability with experiments, MD simulations are often performed at constant temperature or/and pressure. Thus, the newtonian MD scheme is modified by thermostat or/and barostat algorithms to sample conformations from an NVT (canonical) and NPT ensemble, respectively.

The macroscopic temperature of a system is directly related to its average internal kinetic energy according to the equipartition theorem. Therefore, a constant temperature can be maintained by adjusting the atom velocities. In the commonly used Berendsen thermostat

(Berendsen et al., 1984), the temperature of the system is adjusted by a weak coupling of the system to a heat bath with reference temperature T_{bath} according to

$$\frac{dT}{dt} = \frac{T_{\text{bath}} - T}{\tau_t} \quad (2.9)$$

with the coupling constant τ_t determining the strength of the coupling. The different parts constituting the simulation system, here protein atoms and solvent atoms, are coupled to separate heat baths.

However, the ensemble generated by the Berendsen thermostat is not a true canonical ensemble. Occasionally, energy is transferred from high frequency to low frequency degrees of freedom (Harvey et al., 1998). These artifacts are summarized by the term "flying ice cube effect". Building upon Berendsen, the stochastic velocity rescaling thermostat employs the same scaling using τ_t but the stochastic term ensures a proper canonical ensemble (Bussi et al., 2007). This thermostat was used for the MD simulations presented in this thesis.

Similarly to the thermostats, the pressure is kept constant by a barostat. The adjustment of pressure relies on the virial theorem that relates the average kinetic and potential energy. The pressure is controlled by scaling the volume of the unit cell. In this thesis, the Parrinello-Rhman barostat was used which additionally allows for changes in the shape of the simulation cell (Parrinello and Rahman, 1981).

Periodic boundary conditions

In MD simulations with explicit solvent, most particles represent solvent molecules. Thus, the dimensions of the simulation box critically determine the system size. However, a finite box size poses the question of how to treat the system boundaries while subjecting the protein to the same forces as in a bulk solvent. The use of periodic boundary conditions (PBCs) is a standard way to treat the system boundaries without the introduction of large artifacts. Here, the unit box is virtually and infinitely replicated in all directions giving the appearance of a limitless system. An atom that moves beyond its box appears to re-enter the box on the opposite boundary, keeping the number of atoms in the actual box constant. With this technique it is still crucial to use a sufficiently large box size to avoid artificial long-range interactions between the protein and its mirror image. Usually, this is ensured by selecting a distance to the boarder of at least 1.5 nm.

2.1.4 Coarse-grained modeling

The reachable timescales of MD simulations are limited by the system size. To study processes on longer timescales and/or larger systems, for example phase transition events, one technique of reducing the computational effort is coarse-graining. Here, several single atoms are condensed into one coarse-grain (CG) bead according to specific mapping operators. The properties of the CG bead should represent the properties of all the summarized atoms. In general, all CG approaches aim to significantly increase the simulatable timescale while at the same time accurately reproducing the all-atom behaviors. Therefore, one should reduce only those degrees of freedom that are considered negligible for the specific problem under study.

Within the CG framework employed in this thesis a peptide is modeled as a chain of CG beads, where each bead represents one aminoacid (Dignon, W. Zheng, Kim, et al., 2018; Mammen Regy et al., 2021). The chemical properties of each aminoacid are incorporated by the hydrophathy scale model (Kapcha and Rossky, 2014) providing sequence specificity. To obtain the hydrophobicity (λ) at the residue level, λ at the atomic scale is summed up and scaled from 0 to 1. This simple spectrum captures the anticipated hydrophobic character for those residues. The bonded interactions are modeled by harmonic springs connecting the beads. Additionally, beads that are separated by at least two bonds interact by non-bonded short-range (V_{SR}) and electrostatic interactions (V_E). The short-range pairwise potentials also account for the protein-solvent interactions. The attractiveness of these interactions are scaled by the average hydrophobicity of the two interacting aminoacids ($\lambda_{ij} = (\lambda_i + \lambda_j)/2$) within the Ashbaugh-Hatch functional form (Ashbaugh and Hatch, 2008). This Lennard-Jones like functional form has previously been applied to study disordered proteins (Miller et al., 2016). Here, the non-bonded interactions of two beads that are separated by a distance r_{ij} are described by:

$$\begin{aligned} V_{SR}(i, j) &= V_{LJ} + (1 - \lambda_{ij})\epsilon, \quad \text{if } r_{ij} < r_0 \\ &= \lambda_{ij}V_{LJ}, \quad \text{otherwise.} \end{aligned} \tag{2.10}$$

where $r_0 = 2^{1/6}\sigma_{ij}$ i.e. the distance at which the Lennard-Jones potential takes a minimum value. V_{LJ} is the Lennard-Jones potential (Equation 2.5) where in this case $\sigma_{ij} = (\sigma_i + \sigma_j)/2$ with σ_i and σ_j being the size of each aminoacid obtained to match the van der Waals volume of an aminoacid to a sphere.

The electrostatic interactions are modeled using a coulombic term with Debye-Hückel electrostatic screening (Debye and Hückel, 1923) defined by:

$$E_{ij}(r) = \frac{q_i q_j}{4\pi\epsilon_0\epsilon_r r} e^{-\frac{r}{\kappa}} \quad (2.11)$$

where q is the net charge of each bead, ϵ_0 is the vacuum permittivity, ϵ_r is the dielectric constant of the solvent, here water, and κ is the Debye-Hückel screening length, that relates to the ionic strength of the solvent. The solvent implicitity is further taken into account by a random force and a viscous force, representing the effect of collisions with the solvent and the solvent's viscous aspect, respectively, within the employed stochastic dynamics.

2.2 Biasing MD simulations

2.2.1 Replica-exchange MD

MD simulations are limited by the accessible timescale that with today's computational power and system sizes can rarely exceed the lower microsecond range. Additionally, the conformational landscape usually contains many states characterized by a local minimum of the energy. The system can only overcome the barriers between the energy wells if the barrier height is smaller than a few $k_B T$, where k_B is the Boltzmann constant. Therefore, the system might not overcome higher energy barriers resulting in a trajectory that does not sample all physiologically reachable configurations. To solve this problem, several advanced MD simulation methods are nowadays used to enhance the conformational sampling, one of which is replica exchange molecular dynamics (REMD) (Sugita and Okamoto, 1999).

In REMD simulations, replicas of the system at different temperatures are simulated with conventional MD. After a defined amount of MD steps, pairwise exchange between the replicas is attempted where the exchange probability is calculated using a Metropolis criterion. In this way, a system trapped in an energy minimum at a low temperature can escape it by overcoming the energy barrier at a higher temperature. A prerequisite for successful exchange between the replicas is sufficient overlap between the two potential energy distributions. Satisfactory acceptance ratios (of 10 % to 50 %) are ensured by small temperature differences between the replicas and a low number of degrees of freedom of the system. The latter is often achieved by limiting the system size to a few thousand atoms, which in many cases requires the use of implicit solvents.

2.2.2 Force-probe molecular dynamics

Mechanical force impacts many biological processes and can be investigated in simulations through the application of a well-defined external force using force-probe MD simulations (Grubmüller, 2005). In addition, force-probe MD can also help to simulate otherwise very slow processes within the accessible timescales of MD by pulling the system along a certain reaction coordinate.

The force can be applied to a single atom or a group of atoms, a so called pull group. In the latter case, the force is distributed in a mass-weighted fashion to the center of masses (COMs) of the atoms involved. The external force is added directly to the atomic force at each simulation step by subjecting the pulled atoms to harmonic spring potentials:

$$V_{\text{spring},i}(t) = k_0[z_i(t) - z_{\text{spring},i}(t)]^2 \quad (2.12)$$

where k_0 is the force constant of the spring, $z_i(t)$ the position of the COM of the pulled atoms, and $z_{\text{spring},i}$ is the position of the spring. The force can either pull one atom or pull group in a specific direction or move two pull groups in opposite directions. In the latter case, the force is applied along the vector connecting the two pull groups. Generally, the distance between the pull group and a reference point regulates the magnitude of applied force. In constant velocity pulling, as used in this thesis, the reference point travels at a constant speed along the pulling direction. Here, mechanical stress is administered by moving the spring or multiple springs in the direction of pulling with a constant velocity v according to:

$$z_{\text{spring},i}(t) = z_i(0) \pm \Delta z(t) \quad (2.13)$$

where $\Delta z(t) = vt$ is the spring dislocation.

The pulling speeds for protein simulations in explicit solvent have decreased over the years and can now reach well below 1 m s^{-1} even extending to 0.001 m s^{-1} (Rico et al., 2019; Goktas et al., 2018). Therefore, the velocities reachable in MD simulations approach or even partially overlap with the simultaneously increased velocities of single-molecule pulling experiments such as AFM or optical tweezers (Franz et al., 2020). Yet in this thesis, the results of force-probe MD are compared and related to higher scale cellular processes triggered by force that are far beyond the currently achievable time and length scales of simulations or single molecule experiments.

2.3 Analysis of MD trajectories

2.3.1 Root mean square deviation and fluctuation

The root mean square deviation (RMSD) is a numerical measure of the difference between two structures, where a small RMSD indicates a high degree of similarity. In a protein system, the RMSD at each time step is commonly calculated for the C α atoms with respect to the starting structure after rigid superposition. The RMSD between the current coordinates ($r_i(t)$) and the reference coordinates ($r_i(t_{\text{ref}})$) for a set of N points is calculated by:

$$\text{RMSD}(t, t_{\text{ref}}) = \left[\frac{1}{M} \sum_{i=1}^N m_i \|r_i(t) - r_i(t_{\text{ref}})\|^2 \right]^{\frac{1}{2}} \quad (2.14)$$

where $M = \sum_{i=1}^N m_i$ and m_i is the mass of atom i .

In contrast, the root mean square fluctuation (RMSF) gives an estimate of the flexibility of a specific atom or residue. For proteins, the RMSF is typically calculated for the C α atoms of each residue, giving insight into the flexible regions of a protein. It measures the variance of the fluctuation around the mean atom position:

$$\text{RMSF}_i = \left[\frac{1}{T} \sum_{t_i=1}^T \|r_i(t_i) - r_i^{\text{ref}}\|^2 \right]^{\frac{1}{2}} \quad (2.15)$$

where r_i^{ref} is the reference position of particle i i.e. the position of i averaged over time T .

Thus, the difference between RMSD and RMSF is that the RMSD averages the fluctuations over the atoms leading to a time trajectory, whereas the fluctuations in the RMSF are averaged over time giving estimates for each atom or residue.

2.3.2 Radius of gyration

As a rough measure for the compactness of a protein, the radius of gyration (R_g) can be calculated. The R_g is the root mean square distance from each atom to the protein's COM according to:

$$R_g = \left(\frac{\sum_i \|r_i\|^2 m_i}{\sum_i m_i} \right)^{\frac{1}{2}} \quad (2.16)$$

where m_i is the mass of atom i and r_i the position of atom i with respect to the center of mass of the molecule.

The distribution of the R_g is especially useful to represent the large conformational ensemble of an intrinsically disordered protein (see subsection 4.1.5 and subsection 4.2.3). Thus, their compactness represented by R_g can be compared to other sequences of similar lengths.

2.3.3 Principle component analysis

The extraction of correlated and significant motions from high-dimensional MD data is one challenge in the analysis of MD simulations. Principle component analysis (PCA) simplifies the complexity of MD data by identifying coordinate transformations that describe lower-dimensional, major movements (Sittel et al., 2014). These so called principle components (PCs) are geometrically orthogonal, which means that the motions described by two PCs are uncorrelated.

At the heart of PCA, the atomic fluctuations are expressed in terms of their covariance. The diagonalization of this positional covariance matrix gives a set of orthogonal eigenvectors. These eigenvectors describe the direction of the extracted collective protein motions. The eigenvalues corresponding to each eigenvector describe the magnitude of the movement along that eigenvector. Therefore, eigenvalues represent the energetic contribution of each principle component to the global protein motion. Eigenvectors are naturally arranged in decreasing order meaning that the first principle component explains the majority of the system's covariance. Most of the variance in the original data is usually described by only a few principle components. Hence, the motions along those PCs dominate the dynamics and contain the most important structural fluctuations of the system.

Projection of the MD trajectory onto the subspace spanned by a specific eigenvector is achieved by forming the dot product of atomic displacements with that eigenvector at each timestep. This projection allows to visualize the motion of the protein captured by that principle component.

2.3.4 Force distribution analysis

Force distribution analysis (FDA) is an analysis technique for MD simulations that can detect the internal distribution of atomic-level stresses in equilibrium states or as a response to mechanical or allosteric cues (Stacklies et al., 2011; Costescu and Gräter,

2013). FDA can visualize the propagation of these internal forces through the protein core and side chains. Thereby, it is able to identify low-amplitude fluctuations of stresses with potential significance for protein function.

During a conventional MD step the forces acting on one atom are calculated by the sum of pairwise forces between that atom and any other interacting atoms. In contrast, FDA recovers the individual pairwise forces between atom i and a specific atom j . Thus, these pairwise forces can be non-zero even in equilibrium simulations and can consider all interaction types (bonded, nonbonded) separately or summed up. Further, the pairwise forces describe the atomic interactions independent of the actual positions and are therefore a more sensitive measure for alterations in internal strain.

The examination of pairwise forces on single atoms might not be conclusive for detecting allosteric events and moreover is computationally expensive. Instead, calculating the residue-based pairwise forces provides a mapping of the disturbed parts to the primary and secondary structure of a protein. For such residue-wise analysis, the pairwise force between residues u and v that acts on the COMs of the two residues is calculated:

$$F_{u,v} = \sum_{i \in u, j \in v} F_{ij} \quad (2.17)$$

where i is an atom of residue u and j is an atom of residue v , with u and v being different.

The effect of any perturbation, mechanical or allosteric, can be extracted by comparing the pairwise forces to an undisturbed reference. In this work, FDA is used to study the differences between a protein in its apo and holo state. Therefore, the non-bound state is used as a reference to identify the effect of the ligand. To visualize such perturbations, pairwise forces are mapped onto the protein structure, generating a network representation. Here, the pairwise forces are represented as edges connecting the residues. These edges are weighted by the magnitude of $\Delta F_{u,v}$. For force differences larger than a given threshold, a set of paths (i.e. connected edges) is generated. The path lengths depend on the defined minimal number of connected edges.

To identify perturbed single atoms or residues, in contrast to residue pairs, a mapping of the pairwise space to the atom space can be employed. Here, the punctual stress is the sum of the absolute values of scalar pairwise forces acting on each atom or residue i :

$$S_i = \sum_j |F_{ji}| \quad (2.18)$$

2.4 Molecular docking

Interaction with other proteins or ligands often is a prerequisite for protein function. Those interactions are mainly controlled by a complex array of intermolecular contacts involving the ligand's binding pocket as well as the outside of the pocket. Additionally, the binding pocket is usually quite flexible and can undergo structural changes upon a binding event. Taken together, the determination of protein-protein or protein-ligand complexes can be quite challenging. While many experimental methods, like yeast two-hybrid screening, Förster resonance energy transfer, X-ray crystallization or NMR, are available to investigate such complexes at different resolutions, the full picture in atomic detail and/or dynamic information is often missing.

Computational predictions of protein-protein or protein-ligand complexes are one solution to this dilemma. Generally, such docking algorithms generate a large number of diverse conformations and use empirical scoring functions to rank the predicted complexes according to their likelihood to be correct. Although in some cases, molecular docking can generate complexes virtually identical to experimental structures, an approximately correct model is rarely the top-scoring one (Radom et al., 2018; Kozakov et al., 2008). Reasons for this are the intrinsic flexibility of proteins, the ruggedness of the free-energy landscape and approximations used in the scoring functions. Therefore, the main challenge in molecular docking is still the discrimination of near-native structures from decoys.

One way to improve the quality of the docking ensemble is to drive the docking process by biochemical and/or biophysical data on the complex formation. Employed in this thesis, the molecular docking software HADDOCK (High Ambiguity Driven Protein-Protein Docking) (Dominguez et al., 2003; van Zundert et al., 2016) uses so called ambiguous interaction restraints (AIRs), i.e. residues that are involved in the intermolecular interaction. These AIRs are derived from any experimental information like for example mutagenesis data or chemical shift perturbation data from NMR experiments. HADDOCK distinguishes between "passive" and "active" binding residues. Active residues were shown to be directly involved in complex binding and are solvent exposed. The passive residues are surface neighbors of the active residues and show a solvent accessibility of over 50%. HADDOCK employs a three-step docking protocol where as a first step the orientations of the ligand are randomized and a rigid-body energy minimization is performed. In a second step, a semirigid simulated annealing is executed in torsion angle space. Here, movement of amino acids at the interface is allowed to optimize the interface packing. Thirdly, the docking is refined with explicit solvent in Cartesian space. The docking itself is followed by a cluster analysis where the structures are clustered

according to their pairwise backbone RMSD at the interface. The clusters are ranked according to their average buried surface area and interaction energies, that is the sum of electrostatic, van der Waals and AIR energy terms.

2.5 Traction force microscopy

Adherent cells exert active force, so called traction force, to probe the mechanical properties of the underlying surface. In experiments, traction forces are not measured directly but can be quantified by traction force microscopy (TFM) (for recent reviews see Hur et al., 2020; Lekka et al., 2021). This perturbation-free method produces a spatial image of the positions and magnitudes of the exerted stresses. The traction forces are reconstructed from the deformations that a cell applies to the surface (Roca-Cusachs et al., 2017). Hence, cells are seeded onto an optically transparent gel that mimics the ECM, usually a polyacrylamide hydrogel. The stiffness of these gels can be tuned over a large range – from single pascal to hundreds of kPa – to match the physiologically relevant mechanics of the ECM under study. Embedded in the gel are fluorescent microbeads, that get displaced by the exerted force of the spreading and/or migrating cell. The cell surface and the bead displacement is recorded by confocal fluorescence microscopy. Typically, the first image consists of the beads surrounding an isolated cell, the reference configuration, and the second image contains the displaced beads after cell detachment. Subsequently, a displacement field is calculated by comparing the position of the beads. As a last, but computationally elaborate step, the traction forces are calculated from the displacement field by making use of a mechanical model of the elastic substrate. The traction force experiments described in this thesis were performed and analyzed by Dr. Michele Nava (Helsinki University, Finland) according to the protocol described by Dembo and Y. I. Wang, 1999.

Case Study I: Integrin-linked Kinase at Focal Adhesions

This chapter introduces focal adhesions and pseudokinases and describes the results from MD simulations of the pseudokinase ILK both in equilibrium condition and under mechanical load to explore its mechanosensitivity. Those simulations are complemented by biochemical and cellular experiments provided by Dr. Michele Nava and Prof. Dr. Sara Wickström ("Stem cells and tissue architecture" group, University of Helsinki, Finland) to assess the implications of the simulation results on the cellular scale. Interpretation of the results in the light of the simulations was a joint effort. The combined results were published in PNAS in March 2022 (I. M. Martin, Nava, et al., 2022).

3.1 Background: Focal adhesions – the main hub for cell-matrix interaction

3.1.1 The extracellular matrix

Cells are capable of sensing and responding to a broad range of signals of biochemical and mechanical nature from their surrounding microenvironment. As one such external component, the extracellular matrix (ECM) serves as a physical scaffold for tissues. Generally, the ECM is composed of proteoglycans and fibrous proteins like collagens, elastins, fibronectins and laminins (Frantz et al., 2010). Collagen, the most abundant protein of mammals (Di Lullo et al., 2002) provides structural support to resident cells. Proteoglycans fill the extracellular space in the form of a hydrogel to be able to withstand compressive forces. The ECM is produced and actively remodeled by cells and thus its detailed composition and topology is unique for each tissue. Further, the ECM guides tissue homeostasis and development by regulating a broad range of cellular processes including cell growth and differentiation, adhesion as well as cell migration (Hynes, 2002; Legate, Wickström, et al., 2009).

This bidirectional cell-ECM signaling is mediated by the direct contact between the cell membrane and the ECM through members of the integrin family of cellular surface

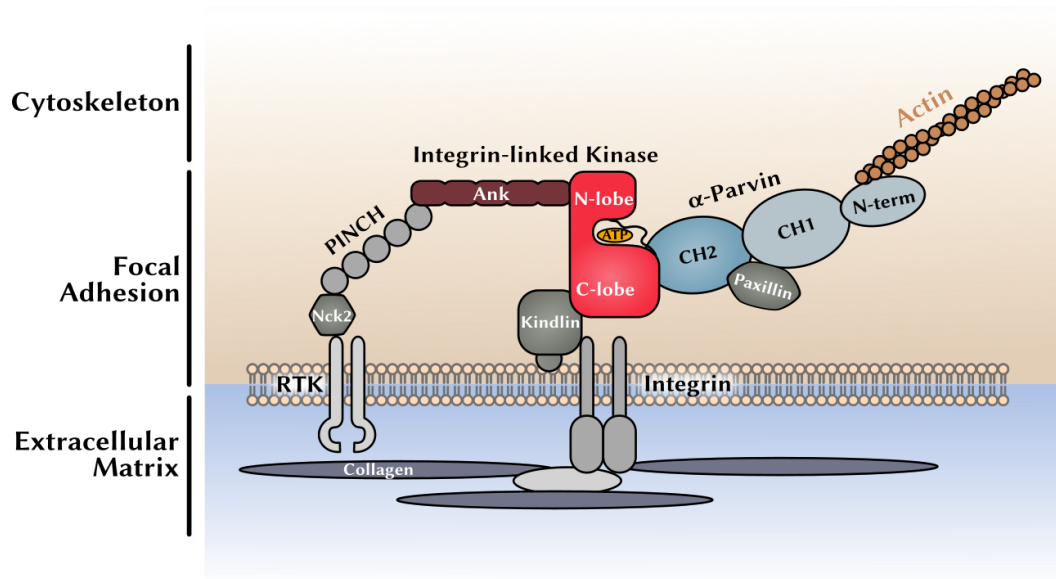


Fig. 3.1.: ILK-containing focal adhesions. FAs are the major mechanical and biochemical signal integration platform between the extracellular matrix and the intracellular cytoskeleton. From the over 100 constituents, selected proteins are shown which are important for Integrin-linked kinase (ILK)-containing FAs like parvin, paxillin and kindlin-2. (RTK: Receptor tyrosine kinase).

receptors. Binding of integrins to the ECM leads to recruitment of filamentous (F-) actin. Thus, mechanotransduction and force generation through the actomyosin cytoskeleton is mediated by integrin-based cell-matrix adhesions.

3.1.2 Focal adhesions

Mechanotransduction through integrins depends on establishing and maintaining large complexes that link the ECM to the actomyosin cytoskeleton, so called focal adhesions (FAs) (Schiller et al., 2011; Burridge, 2017). Upon contacting a stiff substrate the cell develops small, dot-shaped nascent adhesions. Those mature into proper FAs by a hierarchical, force-dependent process (Oakes et al., 2012). FAs are the major signal integration platform of cell adhesions that mediate the precise spatio-temporal coordination of integrin-based signalling (Geiger and Yamada, 2011; Hoffman et al., 2011). Consisting of over 100 different proteins, FAs are of dimensions on the order of a micrometer, and have a lifetime of minutes to hours. They are structured into the integrin-containing transmembrane layer and the intracellular layers which consists of actin-binding and -regulatory proteins, since integrins themselves lack enzymatic activity (Kanchanawong et al., 2010). An additional level of complexity in integrin signaling

is conveyed by different molecular compositions of FAs. This chapter focuses on the ILK-containing focal adhesions (Figure 3.1, subsection 3.1.3).

FA kinetics and associated mechanotransduction are proposed to be regulated by force-dependent, conformational changes of the constituent proteins. Forces transmitted over a period sufficient to alter protein conformation are able to regulate cellular processes, whereas forces high enough to induce protein dissociation will terminate the force transmission (Vogel, 2006). Thus, the magnitude and duration of force application are critical factors affecting the balance of conformational change and bond breakage, especially for FAs under high traction stresses (Hoffman et al., 2011; Kechagia et al., 2019). Previously identified examples of force-regulated FA proteins include focal adhesion kinase (FAK) and talin. Their mechanosensing roles have been shown to depend on parameters such as loading rate and direction of force, which influence the competition between force-induced unfolding and rupture from binding partners (Zhou et al., 2015; Tapia-Rojo et al., 2020; Goult et al., 2018; Mofrad et al., 2004; Rahikainen et al., 2019; Bauer et al., 2019).

FA dynamics and actomyosin contractility are modulated by mechanical cues such as ECM rigidity, tension and shear (Martino et al., 2018). Plating cells on stiff substrates or exposing them to large, rapidly applied forces results in FAs that exchange adaptor molecules at a slower rate which leads to longer FA lifetimes (Elosegui-Artola et al., 2018). This dynamic nature of the cytoskeleton-ECM connection and its relationship to cell movement is collectively termed the molecular clutch model. The precise coordination of FA stability and their actomyosin linkage is thus a prerequisite for effective traction force generation during mechanotransduction as well as during cell migration (Hoffman et al., 2011; Kechagia et al., 2019).

Cell migration Cell migration is defined as the directed movement of cells following mechanical and chemical signals (Figure 3.2). It is essential in biological processes like tissue development, wound healing and immune response but also for cancer metastasis (Ridley et al., 2003; Friedl and Gilmour, 2009; Treppe et al., 2012). Tight regulation of cellular adhesion assembly and disassembly is necessary for successful cell migration (D. J. Webb et al., 2002). Through actin polymerization at the leading edge, the cell extends protrusions in the direction of desired movement. These finger-like protrusions contain thick, contractile actin-bundles called stress fibers, that contact FAs and are especially prominent under high-force conditions (Tojkander et al., 2012; Livne and Geiger, 2016). Where the cell contacts the substrate, nascent adhesions form which rapidly link to the actin network. They can either be turned over or can mature into FAs in a force-dependent manner (Oakes et al., 2012). According to the molecular clutch

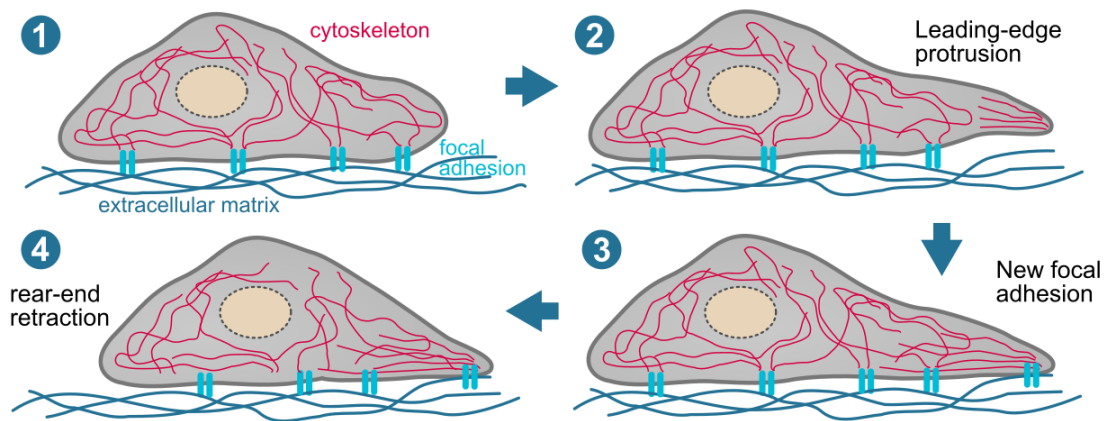


Fig. 3.2.: Mechanism of cell migration. (1) A cell is adhering to the matrix. Direction of intended movement to the right. (2) Polymerization of actin filaments occurs at the leading edge which develops protrusions. (3) Membrane protrusions contact the matrix. New adhesions are produced and rapidly linked to the actin network. (4) Retrograde actin flow and contractile forces generate a net forward movement of the cell body. Adhesions at the cell rear are disassembled.

model, FAs tethered to the ECM impede the retrograde flow of actin, i.e. opposite the direction of cell movement, resulting in the generation of traction stresses. At the rear end of the cell, FAs are disassembled in a less well understood process. This leads to retraction of the cells trailing edge and, in combination with cytoskeletal contractions, to a net forward movement of the cell body. The traction forces exerted by the cell to the substrate can be visualized and quantified by traction force microscopy (TFM) (section 2.5).

3.1.3 The ILK/PINCH/parvin complex

Integrin-linked kinase (ILK), one of the few essential and evolutionary conserved FA components, regulates the stability and dynamics of FAs downstream of $\beta 1$ integrins (Chuanyue Wu, 2004; Legate, Montañez, et al., 2006). ILK consists of two distinct domains (Figure 3.1, Figure 3.3): its N-terminal ankyrin-repeat domain is associated with PINCH (particularly interesting new cysteine-histidine rich protein) (Chiswell et al., 2008) and its C-terminal atypical kinase domain binds to the CH2 (calponin-homology) domain of α -parvin (K. Fukuda, Gupta, et al., 2009). Thus, ILK is the central component of the tripartite IPP-complex (ILK/PINCH/Parvin-complex) (Wickström et al., 2010), that is currently thought to serve as a signal processing platform by recruiting a variety of proteins (Figure 3.3 B).

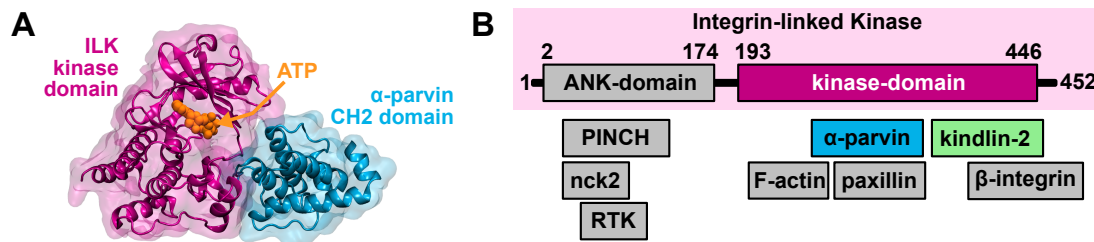


Fig. 3.3.: Integrin-linked Kinase (A) ILK:parvin complex rendered from PDB-code: 3KMW (K. Fukuda, Gupta, et al., 2009). ILK contains a kinase-like domain and binds ATP in the nucleotide cleft in an unusual binding mode. (B) Schematic overview of ILK and its associated proteins.

For example, PINCH influences receptor tyrosine kinases via interaction with nck2 (Velyvis et al., 2003) and α -parvin directly interacts with paxillin (Nikolopoulos and Turner, 2001; Lorenz et al., 2008; X. Wang et al., 2008). Additionally, both PINCH and parvin contain WASP-homology domains that bind F-actin (Vaynberg et al., 2018; Yang et al., 2021) connecting the IPP to the cytoskeleton and promoting actin bundling. Apart from the N-terminal WASP-homology domain, α -parvin contains two C-terminal CH-domains, the second of which is the one interacting with ILK. In addition to the ubiquitously expressed α -parvin, two more parvin isoforms exist, namely β -parvin expressed primarily in heart and skeletal muscle and γ -parvin in the hematopoietic system (Nikolopoulos and Turner, 2001; Olski et al., 2001; Tu et al., 2001; Yamaji et al., 2001; Chu et al., 2006; Sepulveda and C. Wu, 2006).

As a cell-matrix signal transduction platform, the IPP is also connected to the ECM. Upon its discovery, ILK was believed to directly associate with β -integrin tails (G. E. Hannigan, Leung-Hagesteijn, et al., 1996), though more recent studies show that ILK rather indirectly contacts integrins by binding to kindlin-2 (Montanez et al., 2008; Huet-Calderwood et al., 2014; Kadry et al., 2018). Kindlin-2 itself directly contacts β -integrins (Calderwood et al., 2013; Harburger et al., 2009; H. Li et al., 2017; Qadota et al., 2012; Jahed et al., 2019) and binds to a conserved patch in the C-terminus of ILK (Kadry et al., 2018). The non-typical FERM (4.1-ezrin-radixin-moesin) domain of kindlin-2 is interrupted in the F2 subdomain by a PH-domain (pleckstrin homology domain). This PH-domain mediates the interaction of kindlin-2 with the membrane lipid PIP2 (Jianmin Liu et al., 2011; Y. Liu et al., 2012; Yamamoto et al., 2016; Palmere et al., 2021), anchoring the IPP at the cytoplasmic face of the plasma membrane at sites of FAs.

On the cellular level, ILK deficiency leads to aberrant cytoskeletal remodeling and also compromises FA formation, cell migration and ECM remodeling (Friedrich et al., 2004; T. Fukuda et al., 2003; Sakai et al., 2003; Stanchi et al., 2009; Wickström et al., 2010).

The importance of the IPP on the organismal level is evident by deletion studies where ILK depletion results in failure in epiblast polarization and severe defects in F-actin organization leading to embryonic lethality (Sakai et al., 2003). Moreover, tissue-specific deletion of ILK is associated with heart diseases (Gregory E. Hannigan et al., 2007), cancer progression (C.-C. Zheng et al., 2019) and might also play a role in ageing (Olmos et al., 2017).

3.1.4 Integrin-linked kinase as a pseudokinase

Given the importance of the IPP as a whole and its component ILK in detail for the integrin-actin connection, it is unfortunate that the specific function of ILK is still widely unknown. Contrary to what its name suggests, the catalytic activity of Integrin-linked kinase has been heavily debated about (G. Hannigan et al., 2005; Legate, Montañez, et al., 2006; K. Fukuda, Gupta, et al., 2009; K. Fukuda, Knight, et al., 2011; Maydan et al., 2010; Wickström et al., 2010; G. E. Hannigan, McDonald, et al., 2011). Now, ILK is widely regarded as a pseudokinase.

Catalytic kinases Protein kinases play a pivotal role in regulating cellular processes and maintaining homeostasis. They catalyze the transfer of phosphate groups from phosphate-donors, most commonly ATP (Adenosine triphosphate), to specific substrates. This shared enzymatic function entails the conservation of the bilobed kinase fold in which the core catalytic elements show only little variation. The conserved core of catalytically competent kinases thus exhibits three functions: (1) to bind ATP, which is mediated by a glycine-rich loop and a lysine residue of the VAIK motif within the N-lobe; (2) coordination of two Mg^{2+} by an aspartate in the DFG-motif of the activation loop, that also orients ATP and (3) to finally catalyze the phosphoryl transfer, carried out by an aspartate, acting as the catalytic base, from the HRD-loop of the C-lobe (Kemp and Pearson, 1990; Hanks et al., 1988; Manning et al., 2002; Nolen et al., 2004; Möbitz, 2015). Despite their preserved kinase fold and associated catalytic residues, members of the kinase family are remarkably diverse in their ability to recognize unique substrates.

Pseudokinases Interestingly, approximately 10 % of the over 500 known human kinases are predicted to be inactive because their sequence lacks one or more of those critical, conserved residues (Boudeau et al., 2006; Manning et al., 2002; Zehiraj and van Aalten, 2010). These members of the kinase family are termed pseudokinases classifying them as the catalytically defective counterparts of conventional kinases. Due to the large percentage of pseudokinases in the kinome, they are suggested to have remarkably

diverse noncatalytic functions (Jacobsen and Murphy, 2017; Mace and Murphy, 2021). The study of pseudokinases have led to the realization that pseudoenzymes in general, despite their catalytic inactivity, perform important biological functions (Ribeiro et al., 2019). This shift from thinking about pseudokinases as dead evolutionary remnants to active participants in biological pathways was also governed by a large body of work deciphering their precise functions. They act for example as allosteric modulators, scaffolds for signaling complexes, competitive inhibitors or protein-based switches (Mace and Murphy, 2021). The common theme for these functions is that they evolutionary repurpose the versatile kinase fold as a protein-protein interaction platform. Thus, pseudokinases provide an opportunity to understand the potential for nonenzymatic functions inherent in the kinase fold that also might be performed by their active counterparts.

The ILK pseudokinase controversy

Since the initial discovery of ILK (G. E. Hannigan, Leung-Hagesteijn, et al., 1996) its kinase activity has been doubted despite its high degree of sequence similarity to Ser/Thr kinases. Although ILK lacks crucial conserved motifs of conventional kinases, one can not prematurely exclude the possibility of a catalytically active ILK as it may have a non-conventional active site where key residues are spatially compensated for by alternative residues.

Initially, ILK was shown to be able to phosphorylate $\beta 1$ integrin by in vitro kinase assays (G. E. Hannigan, Leung-Hagesteijn, et al., 1996) and potential ILK targets were identified (Persad et al., 2001; Legate, Montañez, et al., 2006). Although several mutations have been described to eliminate the kinase activity (S343A, R211A, K220M) or to result in a constitutionally active kinase (S343D) (Persad et al., 2001; Filipenko et al., 2005), those mutations were also shown to disrupt the interaction of ILK with essential binding partners (Attwell et al., 2003; Yamaji et al., 2001; Lange et al., 2009). Further, kinase-dead mutants were able to rescue ILK deficiency in invertebrates (Zervas et al., 2001; Mackinnon et al., 2002) and did not alter the phosphorylation pattern in mice (Sakai et al., 2003; Lange et al., 2009).

Only upon determination of the molecular structure of ILK did its pseudokinase nature fully become apparent (K. Fukuda, Gupta, et al., 2009; K. Fukuda, Knight, et al., 2011). ILK contains a kinase fold with a characteristic bilobal structure and, surprisingly, was able to bind ATP, although previous sequence-based analysis suggested that ATP might not be bound by ILKs dramatically altered ATP-binding loop (Scheeff et al., 2009). While there was a well defined ATP-molecule in the nucleotide-binding cleft, demonstrating

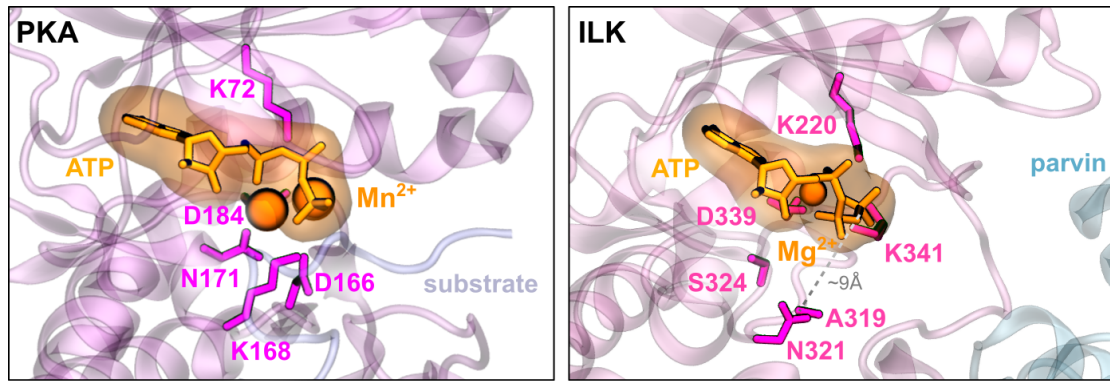


Fig. 3.4.: ILK as a pseudokinase. (left) Conventional ATP-binding to kinases exemplified by Protein Kinase A (PDB-code: 1ATP). (right) Abnormal ATP-binding to ILK. ATP coordinates only one Mg^{2+} or Mn^{2+} and its γ -phosphate is rotated, interacts with K341 from the degraded DFG-loop (D339, V340, K341) and is $\sim 9 \text{ \AA}$ away from the degraded catalytic loop (A319, N321).

that ILK is not able to hydrolyze ATP, it is bound in an unusual binding mode (K. Fukuda, Gupta, et al., 2009): ATP is far away from the putative activation loop and its γ -phosphate is coordinated by K341 of the ILK activation loop and is thus rotated compared to conventional kinases (Figure 3.4). Further and different from functional kinases, the degraded DFG-loop is locked in the active, 'flipped in' conformation and the activation loop is well-ordered (K. Fukuda, Gupta, et al., 2009). Additionally, parvin binds to the putative substrate entry site within the kinase domain and disruption of ILK:parvin binding reduces the localization of ILK to FAs (K. Fukuda, Gupta, et al., 2009).

Previous studies of ILK possessing kinase activity as well as claims of ILK as a functional kinase depending on Mn^{2+} as a cofactor instead of Mg^{2+} (Maydan et al., 2010) were convincingly disproved by a comprehensive structural, biochemical and thermodynamic study (K. Fukuda, Knight, et al., 2011). It revealed that the observed ILK kinase activity was most likely an artifact of active kinases retained in the purified ILK to a small extent. Taken together, overwhelming evidence supports the notion of ILK as a pseudokinase that is incapable of catalysis while interestingly still being able to bind ATP.

3.1.5 Aim of this project

Since the pseudokinase ILK still has the ability to stably bind ATP, it can be speculated that ATP has acquired a new role beyond acting as a phosphate donor. Elucidating the function of ATP might provide a new mechanism of pseudokinase signal transduction. However, the molecular mechanism by which ATP impacts ILK function within FAs remains fairly

unclear. First hints towards a molecular function of ATP apart from biochemical catalysis came from studies with an ATP-binding deficient ILK (L207W) that impairs actin bundling in stress fibers (Vaynberg et al., 2018).

ILK stability is required for its interaction with parvin and ILK turnover is regulated by the E3 ligase CHIP–Hsp 90 axis (Radovanac et al., 2013). Disruption of proper ILK turnover leads to its detachment from FAs, which is accompanied by reduction of cellular force generation and migration (Radovanac et al., 2013). Additionally and as described above, intrinsic and extrinsic forces lead to dynamic assembly and disassembly of adhesions during processes like cell migration. Force-induced disruption of ILK is thus one imaginable mechanism to influence FA signal transduction by promoting disassembly of force-bearing adhesions. However, how ILK responds to mechanical forces is not yet investigated.

In this chapter, I examine the role of retained ATP-binding to the pseudokinase ILK and probe the mechanosensitivity of ILK and its molecular relevance for FA signal processing. I therefore employ extensive MD simulations in equilibrium conditions and under mechanical load. These are complemented by and coupled to biochemical and cellular experiments performed by Dr. Michele Nava in the group of Prof. Dr. Sara Wickström (University of Helsinki).

3.2 Methods

The methodological details, both in simulation and experimental, used in the ILK project are described below. I carried out all simulations and analysis while the experiments were performed and analyzed by Dr. Michele Nava (University of Helsinki). For both the simulations and the experiments, the statistical analysis was performed using Python and Graphpad Prism. Statistical significance was determined by the specific tests indicated for each figure. No datapoints were excluded from the analysis.

3.2.1 Simulation details

This section describes the specific simulation conditions and analysis parameters. The underlying principles of the simulation and analysis methods are described in chapter 2.

Equilibrium MD simulations

The atomic coordinates used as starting configurations for the MD simulations stem from crystal structures of the human ILK(WT) kinase domain in complex with the CH2-domain of α -parvin either including ATP (PDB-code 3KMW, (K. Fukuda, Gupta, et al., 2009)) or without ATP (3KMU, (K. Fukuda, Gupta, et al., 2009)). The point mutations from arginine to alanine for the ILK(R225A/R349A) mutant were introduced to the holo and apo structures using PyMOL (Schrödinger, LLC, 2015). For simulations without parvin, the parvin coordinates from the previously mentioned crystal structures were deleted. Simulations with the ILK(L207W) mutation were carried out using the crystal structure solved by Vaynberg et al., 2018 (PDB-code 6MIB).

MD simulations were performed with the molecular simulation suite GROMACS 2018.1 (Abraham et al., 2015) alongside the Amber99sb*-ILDNP force-field (Best and Hummer, 2009; Aliev et al., 2014) and ATP-parameters (Meagher et al., 2003). The starting coordinates derived from the crystal structures were placed in the center of a dodecahedron box with (at least) 3 nm between the periodic images and solvated with water molecules represented by the TIP3-water model (Jorgensen et al., 1983). A system with overall zero charge and physiological salt concentration of 100 mM was achieved by replacing solvent molecules with sodium and chloride ions. The simulation protocol included an energy minimization using the steepest descent method, followed by 500 ps in the NVT and 500 ps in the NPT ensemble with harmonic constraints on all protein atoms with a force constant of $1000 \text{ kJ mol}^{-1} \text{ nm}^{-1}$ to equilibrate water and ions. During the production runs in the NPT ensemble no constraint was applied to protein heavy atoms.

Here, only bonds between hydrogens and protein heavy atoms were constrained using the LINCS algorithm (Hess, 2008) imposing a timestep of 2 fs. The temperature was kept constant at $T = 300$ K using the velocity rescaling thermostat (Bussi et al., 2007) with a coupling time of 0.1 ps. All protein atoms including ATP atoms were coupled to a separate heat bath as compared to all water atoms and ions. The pressure was kept constant at 1 bar using the isotropic Parrinello-Rhman barostat (Parrinello and Rahman, 1981) with a coupling time of 2 ps and a compressibility of $4.5 \times 10^{-5} \text{ bar}^{-1}$. Using the Verlet scheme, the neighbors list was updated every 10 fs. All non-bonded interactions were cut off at 1.0 nm. Long-range electrostatic interactions were treated using PME (Darden et al., 1993) with a grid spacing of 0.16 nm with cubic interpolation.

Each system was simulated for 20 individual production runs, each with new random velocities and own equilibration phases. Each run was 500 ns long, and the first 20 ns were neglected as equilibration period, as inspected from the protein backbone RMSD, totaling to a total simulation time used for the analysis of $9.6 \mu\text{s}$ per condition.

Molecular docking

A molecular modeling and guided molecular docking approach was employed to determine a patch of residues within ILK that is most likely in contact with kindlin-2.

The only nearly complete crystal structure of a kindlin-2 (PDB: 5XPY, H. Li et al., 2017) is from *Mus musculus* (mouse) and is missing a loop within the F1 domain, which is far apart from the ILK binding site and can thus be regarded negligible for ILK binding. More importantly, the kindlin-2 main body structure does not include the PH-domain and instead has an artificial connection between the two halves of the F2 domain (see Figure 3.14). The ILK-binding helix (PDB: 2MSU, K. Fukuda, Bledzka, et al., 2014) is however only partially included within the sequence of the near-complete structure as it is located at the edge of the PH-domain. Also, the two available structures of the free PH-domain (4F7H and 2LKO; Jianmin Liu et al., 2011; Y. Liu et al., 2012) do not have direct sequence contact to the near-complete structure. Therefore, I structurally aligned these partial kindlin-2 structures, including the one for the N-terminus (2LGX; Perera et al., 2011) with the main body of kindlin-2 (PDB: 5XPY) using UCSF-Chimera (Pettersen et al., 2004). The basis for this structural alignment was a sequence alignment of the partial mouse structures with the human kindlin-2 generated with T-coffee (Di Tommaso et al., 2011).

As stated above, the available structures of the free PH-domain do not overlap in sequence with the structure of the main kindlin-2 body. Thus, I placed them near the artificial connection within the F2 domain in such a way that the residues that follow in the

sequence have a minimal distance to each other, generating six rotations of the PH-domain (Figure A.5). Homology modeling using MODELLER (B. Webb and Sali, 2016) based on the positions of the placed fragments generated final full models of the human kindlin-2. For each of the six conformations, four models were generated. Eleven models in which the F1-loop was not threaded through the protein were subjected to short, 20 ns to 30 ns MD simulations. The most populated structure from each trajectory, as determined by cluster analysis, was selected for guided molecular docking with HADDOCK2.2 (van Zundert et al., 2016). The most populated structure from a 100 ns MD simulation of holo ILK (PDB: 3KMW) provided the structure of ILK for the docking. The experimentally validated residues of ILK that are in direct contact with kindlin-2 (K423, I427; Kadry et al., 2018) were chosen as the active residues. Residues within kindlin-2 that directly interact with ILK (L353, E354, L357, E358; K. Fukuda, Bledzka, et al., 2014) were also set as active residues. For both proteins, passive residues were automatically defined around the active residues. Six successful docking protocols, generating over 160 highest scoring docking poses, were used for further analysis.

Determination of pulling sites

From the above described ILK:kindlin-2 docking poses, I determined a cluster of residues on ILK that is most physiological for mechanical perturbation. All residues of ILK that contact kindlin-2 within a cutoff of 0.35 nm were determined. Those residues occurring in most of the docking poses (P419, H420, K423, I427, K435, M441, K448), within a cutoff of at least 90 docking poses, were set as the patch of residues for force-probe MD.

For parvin, a similar approach was adopted to determine the cluster of residues to be pulled. Those residues of the parvin CH2-domain interacting with the paxillin LD1 domain within the same threshold of 0.35 nm were determined from parvin:paxillin crystal structures (PDB-codes: 4EDN (Lorenz et al., 2008) and 2K2R (X. Wang et al., 2008)). The resulting residues (A249, T252, V264, T267, R369) were set as the pulling patch on parvin.

Force-probe MD simulations

The effects of mechanical perturbation on the system were determined in simulations using force-probe MD. The end-conformations of 10 equilibrium simulations (subsubsection 3.2.1) were used as starting structures and thus placed in the center of a rectangular

box with dimensions of $30 \text{ \AA} \times 15 \text{ \AA} \times 15 \text{ \AA}$. They were rotated such that the vector connecting the pulling patches is in line with the x-axis of the box. Upon solvating the system, an energy minimization was followed by short simulations in the NVT and NPT ensemble as described above. In the production runs, the residue patches as identified above were subjected to harmonic spring potentials with a force constant of $50 \text{ kJ mol}^{-1} \text{ nm}^{-2}$ moving in opposite direction with constant velocities of 1 m s^{-1} , 0.1 m s^{-1} and 0.01 m s^{-1} . For each velocity and condition, 10 force-probe simulations were performed and stopped upon dissociation of ILK:parvin (paragraph 3.2.1).

MD analysis and visualization

GROMACS tools and Python 3 were used for the computational post-processing of MD simulations. If not stated otherwise, the first 20 ns of each equilibrium simulation were excluded from the analysis as equilibration period. I used VMD (visual molecular dynamics; Humphrey et al., 1996) for visualization of protein structures and Inkscape for the generation of the final figures.

RMSD/RMSF The RMSD and RMSF calculations were carried out on the backbone atoms and calculated in relation to the first frame of the production run.

PCA To identify the major correlated structural motions, I performed PCA with GROMACS utilities covar and ana eig on the C- α atoms of the cumulative trajectories. Here, the translational and rotational motions were removed by superimposing the structures onto the invariant core along the trajectory. The trajectories were projected onto the eigenvectors of the apo state to display the protein movement along this mode of motion. The top two eigenvectors were considered to construct the two-dimensional histogram.

FDA Force distribution analysis implemented into GROMACS (Costescu and Gräter, 2013) was used to determine the changes in internal force between the holo and apo states. All interaction types between protein atom pairs (bonded, nonbonded) were considered. The pairwise forces between two residues were calculated from the pairwise forces on the atom-level according to Equation 2.17. The pairwise forces per condition were computed for each individual equilibrium trajectory and averaged over the trajectory. To determine the effect of ATP on ILK, the time-averaged pairwise forces of the apo state were subtracted from those of the holo state. The internal force differences were visualized by a network of at least 3 connected edges. Here, each edge represents a statistically significant force difference (Mann-Whitney test, $p < 0.05$) above a given

threshold as indicated in the corresponding figure. Note that the sign and magnitude of the changes in force do not necessarily represent a strengthening or weakening of the interaction but are indicative of change in internal force upon lack of ATP. To identify perturbed single residues, I calculated the punctual stress using FDA according to Equation 2.18.

Saltbridge occupancy The number of frames out of the whole trajectory with a residue-residue distance below 0.35 nm was defined as the residue contact probability, i.e. salt-bridge occupancy in cases of saltbridge forming residues.

Interface area The interface area between ILK and parvin was calculated using the solvent accessible surface area (SASA) (Eisenhaber et al., 1995) of both proteins alone and the complex according to

$$\text{interface area} = \frac{1}{2}(\text{SASA}_{\text{ILK}} + \text{SASA}_{\text{parvin}} - \text{SASA}_{\text{complex}}) \quad (3.1)$$

A complex dissociation event is defined to occur at the extension at which the interface area drops below 0.6 nm² for the first time.

3.2.2 Experimental methods

This section briefly describes the experimental protocols used by Dr. Michele Nava to obtain the results discussed below. An extended description of the experimental protocols can be found in our joint publication (I. M. Martin, Nava, et al., 2022).

Plasmid constructs, transfection, and cell culture ILK mutants were generated by site-directed mutagenesis using the Quik Change II Mutagenesis Kit (Agilent) in mouse ILK cDNA cloned into pEGFP-N1 (Clontech). Plasmids have been deposited in the Addgene database (accession numbers: 176896 (mILK-EGFP), 176897 (mILK-R255A-EGFP), 176898 (mILK-R349AEGFP), 176899 (mILK-R225A/R349A-EGFP), and 176900 (mILK-L207W-EGFP)). ILK^{-/-} mouse fibroblasts were obtained (Radovanac et al., 2013) and transiently transfected with Lipofectamine 3000 for 24 h.

Immunoprecipitation GFP immunoprecipitation was performed using Miltenyi Biotec MultiMACS GFP Isolation Kit (MylteniBiotec 130-091-125). After elution of the immunocomplexes in Laemmli sample buffer, they were analyzed with western blotting. Quantification of western blots were performed from four independent experiments using densitometry in ImageJ (Schindelin et al., 2012).

Substrate engineering and traction force microscopy Polyacrylamide gels were cast with fibronectin being chemically crosslinked on gels using Sulfo-SANPAH (Pierce) and their stiffness was measured (Pelham and Y. I. Wang, 1997). Traction force microscopy was performed as previously described (Dembo and Y. I. Wang, 1999), using a spinning disc microscope to image the cells before and after detachment by addition of 10X trypsin to obtain images of bead displacement. Calculation of traction forces was performed as described (Tseng et al., 2011) using particle imaging velocimetry and Fourier transform traction cytometry with Fiji (Schindelin et al., 2012) analyzing at least 30 cells per condition.

Live imaging for migration assay and cell tracking Micropatterned adhesive surfaces (crossbow-shaped micropatterns) were generated using the PRIMO optical module (Alveole, France) with a uniform coating of 10 $\mu\text{g}/\text{ml}$ fibronectin, to which cells adhered for 16 h. Live cell imaging was performed with a Zeiss Axiovert inverted microscope coupled to a CSUX1 spinning-disc device (Yokogawa), a 488 nm laser and sCMOS camera (Hamamatsu). FA dynamics were imaged for 30 min (1 frame/30 s) and cell migration over 12 h (1 frame/30 min). FA dynamics were monitored by the Focal Adhesion Server Analysis (Berginski and Gomez, 2013), with the FA count per cell being normalized to the cell area obtained by manual cell edge tracing. Migration was analyzed by manual cell tracking performed with the Fiji plugin Trackmate (Tinevez et al., 2017). By averaging the cell displacement and velocity between consecutive frames, the mean cellular velocity and migrated distances was determined.

Immunofluorescence stainings and confocal microscopy Cells were fixed 4% paraformaldehyde, stained with antibodies against α -parvin, phospho-Myosin Light Chain 2 (Thr18/Ser19) and paxillin as well as labeled for Actin with Alexa Fluor 568 or 647-conjugated phalloidin. Fluorescence images were collected by laser scanning confocal microscopy (SP8X; Leica) with Leica Application Suite software (LAS X version 2.0.0.14332a). FAs were quantified with an intensity-based threshold area (10 pixels) and FA surface area was measured by Analyze particle tools in Fiji (Schindelin et al.,

2012). FA numbers were normalized by cell area, which was measured by manually tracing the cell boundary given by FA, phalloidin, and pMLC2 stainings.

3.3 ATP stabilizes ILK and focal adhesions

ATP structurally stabilizes the ILK pseudokinase domain

I set out to explore the effect of ATP on the equilibrium dynamics of the ILK pseudokinase using all-atom MD simulations with explicit water at the microsecond scale. I compared simulations of the wild type (WT) ILK in the holo state (with ATP; PDB-code: 3KMW) to the apo state (without ATP; PDB-code: 3KMU) and an ATP-binding deficient ILK (ILK(L207W); PDB-code: 6MIB). This ATP-deficient ILK contains the L207W mutation in the pseudokinase domain that was presented to sterically occlude ATP-binding to ILK without affecting the structural integrity of the protein (Vaynberg et al., 2018). To mimic the cellular conditions as closely as possible, I simulated each of the ILK pseudokinase domains mentioned above in complex with the obligate binding partner of ILK, the

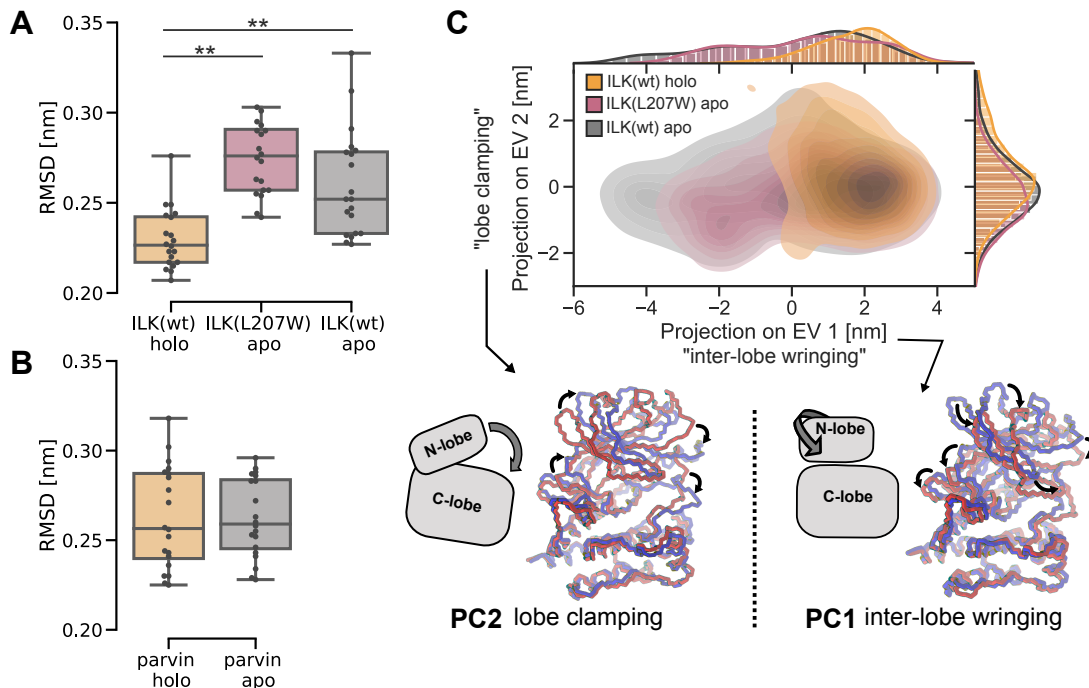


Fig. 3.5.: Destabilization of ILK pseudokinase without ATP. (A) Backbone RMSD of holo and apo ILK(WT) and apo ILK(L207W). $n=20$ trajectories, median of each trajectory is shown; ** $p = 0.001$, one-way ANOVA/ Tukey HSD. (B) Backbone RMSD of parvin from the holo or apo complex, calculated as in A. (C) PCA of holo and apo ILK(WT) and ILK(L207W); trajectories from equilibrium MD simulations are projected onto PC axes for the first and second PC of apo ILK(WT). Red and blue structures indicate the extreme conformations of apo ILK along PC1 and PC2 and are overlaid based on a least-squared fit to the C-lobe of the pseudokinase domain. Large-scale motions described by PC1 and PC2 are indicated by arrows and described by a schematic.

α -parvin CH2-domain. Due to the inherent instability of ILK alone, the crystal structures I used for the simulations already included the α -parvin CH2-domain bound to ILK.

The overall flexibility of the ILK(WT) pseudokinase domain, as quantified by the backbone RMSD relative to the respective starting structures, is significantly increased in the apo state compared to the holo state (Figure 3.5 A). Intriguingly and contrasting ILK, the RMSD of parvin is not influenced by the presence of ATP in the pseudokinase (Figure 3.5 B). Further it should be noted, that the starting structures of the holo and apo complex were found to be "essentially identical" to each other (K. Fukuda, Gupta, et al., 2009). Taken together, both illustrate that the increased RMSD of apo ILK(WT) is not reflective of differences in the starting structures of the holo and apo ILK:parvin complex. The ILK(L207W) mutant shows a similar destabilization than the holo ILK(WT) pseudokinase (Figure 3.5 A). Thus, ATP-binding decreases the internal kinase dynamics and therefore leads to an increased ILK stability.

I further characterized the effect of ATP on ILK dynamics using principle component analysis (PCA) to examine the differences in large-scale coordinated motions (Figure 3.5 C). Both pseudokinases without ATP, namely apo ILK(WT) and ILK(L207W), explore more of the available conformational space. This is especially pronounced along the most prominent motion (PC1), which describes an "inter-lobe wringing". Here, the N-lobe of the kinase fold twists on top of the C-lobe and thus turns around the nucleotide binding cleft. On the other hand, PC2 describes a "clamping" motion of both lobes. Hence, the higher internal dynamics of ILK lacking ATP manifests mainly in enhanced inter-lobe wringing of the pseudokinase domain which contributes to the increased internal flexibility of apo ILK.

Since the stability of ILK is required for proper FA and actin cytoskeleton architecture (Radovanac et al., 2013), I was interested whether focal adhesions also are generally affected by ATP-binding to ILK. The functional consequences of this requirement of ATP for the stabilization of ILK at the cellular level can however not be assessed by such small-scale, molecular simulations. Thus, for the next section I collaborated with Dr. Michele Nava and Prof. Dr. Sara Wickström (University of Helsinki, Finland) and describe the results of their cellular experiments aimed to analyze the cellular effects of ATP-binding on the ILK: α -parvin interaction.

ATP-binding to ILK stabilizes focal adhesions particularly on rigid substrates

Experiments and corresponding figures of this subsection were provided by Dr. Michele Nava and Prof. Dr. Sara Wickström (University of Helsinki). Text is adapted from our joint publication (I. M. Martin, Nava, et al., 2022).

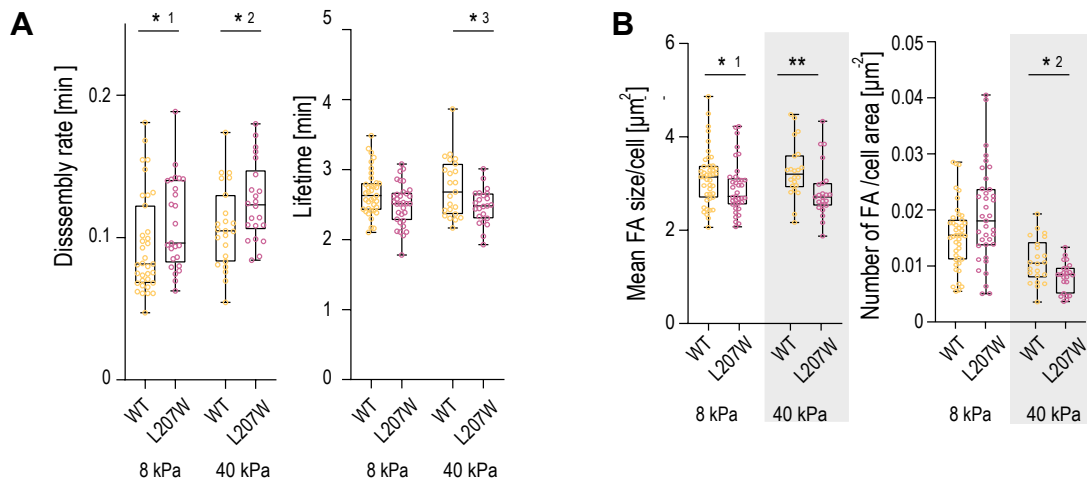


Fig. 3.6.: Loss of ILK:ATP binding destabilizes focal adhesions particularly on stiff substrates. Experiments and figure including legend were provided by collaborators Dr. Michele Nava and Prof. Dr. Sara Wickström, University of Helsinki. Results were published in I. M. Martin, Nava, et al., 2022. (A) Quantification of adhesion disassembly rate and lifetime in ILK(WT)-GFP and ILK(L207W)-GFP cells plated on 8 kPa and 40 kPa substrates ($n > 22$ cells/condition pooled across 4 independent experiments, $^{*1}p = 0.0469$, $^{*2}p = 0.0437$, $^{*3}p = 0.0479$, Mann-Whitney). (B) Quantification of mean FA size/cell and number of adhesion/cell area in ILK(WT) and ILK(L207W)-GFP cells cultured on 8 kPa and 40 kPa substrates from live imaging. FA area threshold set to 20 pixels. ($n > 22$ cells/condition pooled across 4 independent experiments, $^{*1}p = 0.0396$, $^{*2}p = 0.0258$, $^{**}p = 0.0022$, Mann-Whitney).

Dr. Michele Nava reconstituted ILK-deficient murine fibroblasts (Sakai et al., 2003) with either ILK(WT)-GFP or ILK(L207W)-GFP and performed co-immunoprecipitation assays. Similar to earlier studies (Vaynberg et al., 2018), subsequent western blot analyses showed that the L207W mutation does not introduce a substantial effect on steady-state α -parvin binding (Figure A.1 A). Consistently, ILK and parvin localization to FAs were not affected in ILK(L207W) cells compared to ILK(WT) cells in immunofluorescence analysis (Figure A.1 B).

With ILK and parvin still localized properly to FAs in L207W cells, we were interested in the effect of this mutation of the general stability of FAs, especially in conditions of low and high traction forces i.e. at low and high matrix stiffness. Time-lapse imaging of ILK(WT)-GFP and ILK(L207W)-GFP cells plated on polyacrylamide (PAA) gels with either low (8 kPa) or high (40 kPa) stiffness allowed to quantify the FA dynamics. Regardless of the substrate stiffness, the FA assembly rate is not significantly different in WT and L207W cells (Figure A.1 C). In contrast, the L207W mutant shows faster adhesion disassembly rates in combination with decreased FA lifetimes compared to WT (Figure 3.6 A). This effect is visible on both soft and stiff substrates but is more pronounced on rigid substrates. Consistently, analysis of FA morphology showed overall fewer FAs per cell area in L207W

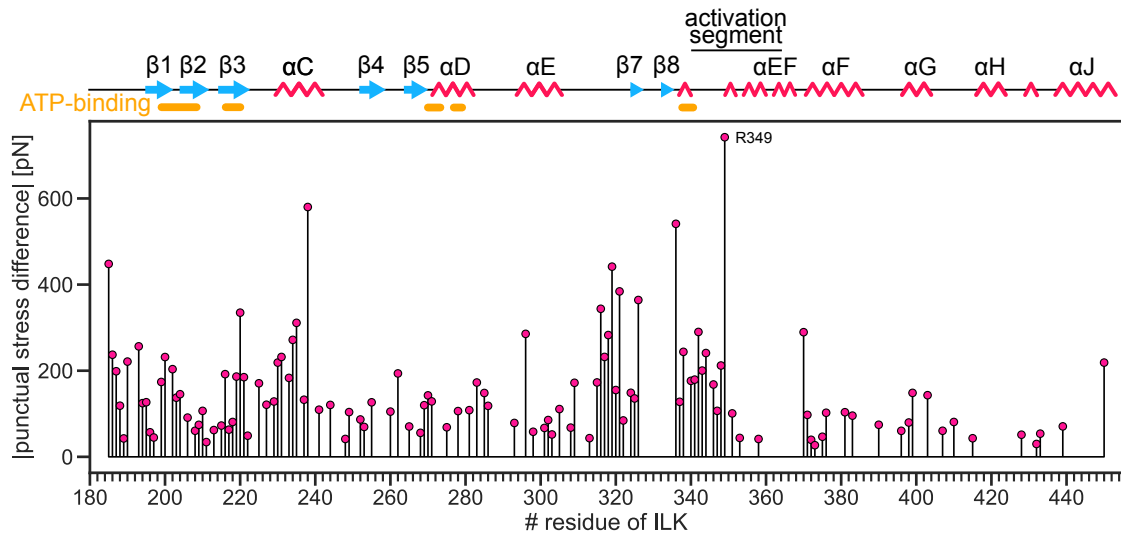


Fig. 3.7.: Absolute differences in punctual stress between holo and apo ILK (only statistically significant differences across 20 independent simulations are shown; $p < 0.05$, Mann-Whitney test). Secondary structure elements and ATP-binding patches are indicated.

cells compared to WT (Figure 3.6 B) as also reported previously (Vaynberg et al., 2018). Additionally, FA were of slightly smaller size in L207W cells (Figure 3.6 B), as also confirmed by paxillin staining (Figure A.1 D/E). As observed for the disassembly rate and lifetime, both the decreased FA number and FA size were more pronounced on stiff substrates. In conclusion, defects in ILK to bind ATP destabilize FAs, particularly on stiff substrates which entail high traction stresses, even though lack of ATP-binding does not substantially impair the ILK: α -parvin interaction.

3.4 ATP allosterically influences parvin-binding saltbridges

The ATP-dependent change in collective kinase dynamics and its effects on FA stability suggest that ATP not only influences residues in its immediate binding pocket, but would also exhibit long-range effects within the kinase-like domain. Thus, I investigated the specific residues that are explicitly altered by the presence of ATP on the molecular level. Using force distribution analysis (FDA) (Costescu and Gräter, 2013, subsection 2.3.4), I calculated the change in time-averaged punctual stresses on each residue upon binding of ATP to the pseudokinase. As predicted, ILK-residues both within the ATP-binding pocket and also interestingly in regions farther away from the pocket show notable differences in punctual stress which suggests ATP-dependent allostery (Figure 3.7). In contrast, only minor differences between the holo and apo state across a majority of ILK residues can

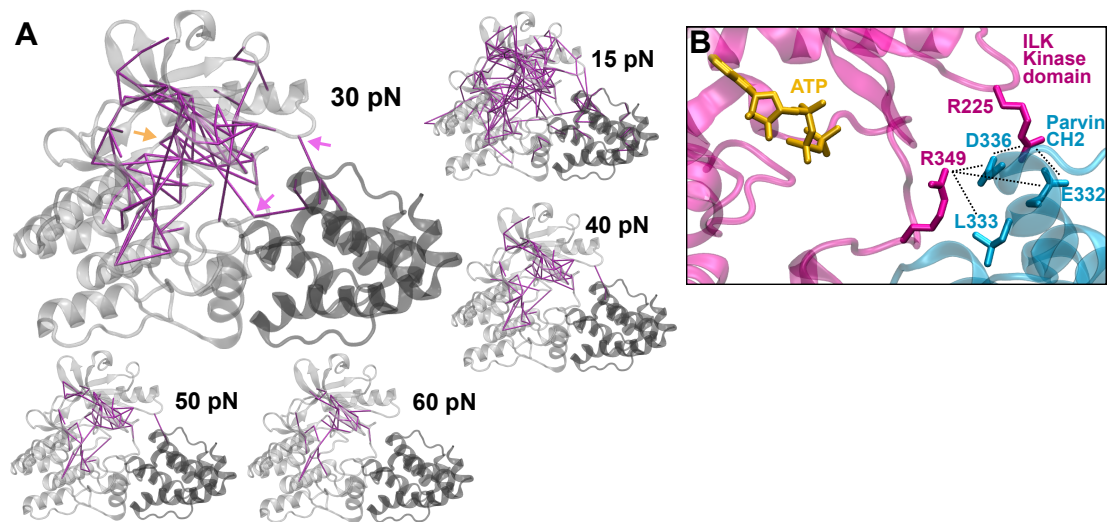


Fig. 3.8.: ATP allosterically influences parvin-binding saltbridges (A) Residue-based, pairwise forces compared between ILK holo and apo (purple lines) with different force thresholds. Approximate positions of the ATP-binding pocket (orange arrow) and saltbridge-forming arginines R225 and R349 (purple arrows) are shown. For all significantly changed pairwise forces see Table A.1. (B) Renders of selected ATP-influenced saltbridges and residue contacts between ILK and parvin as identified from FDA.

be detected calculating the RMSF (Figure A.2). This highlights the sensitivity of internal force calculations in revealing such long-distance allosteric effects.

Since determinations of altered punctual stresses do not allow to comprehend the allosteric pathways of ATP-dependent changes in internal force propagation, I further calculated the residue-based, pairwise forces from FDA. Here, those residues with altered pairwise forces to every other residue between the holo and the apo complex are influenced by the presence of ATP (Table A.1). The connected network of residue pairs exhibiting significant changes in pairwise forces larger than a given threshold visualizes the potential pathways to mitigate the ATP-induced allosteric effects (Figure 3.8 A). As already indicated by the punctual stresses, many residues composing the ATP-binding pocket adapt upon binding of ATP (Figure 3.8 A, orange arrow) and ATP also strongly affects residues outside of its binding pocket in the kinase N- and C-lobe.

Strikingly, the changes in force distribution patterns even extend into parvin, proposing that ATP has an allosteric effect on the obligatory binding partner of ILK. Two arginines at the ILK:parvin interface appear particularly important for this intermolecular allostery (Figure 3.8 A purple arrows, and B): R225 which is located on a loop of the kinase N-lobe and R349 which belongs to the activation segment known from conventional kinases. Structural inspection of these arginines revealed that they form previously unacknowledged saltbridges with E332 and D336 in parvin. R349 additionally interacts with L333 of parvin.

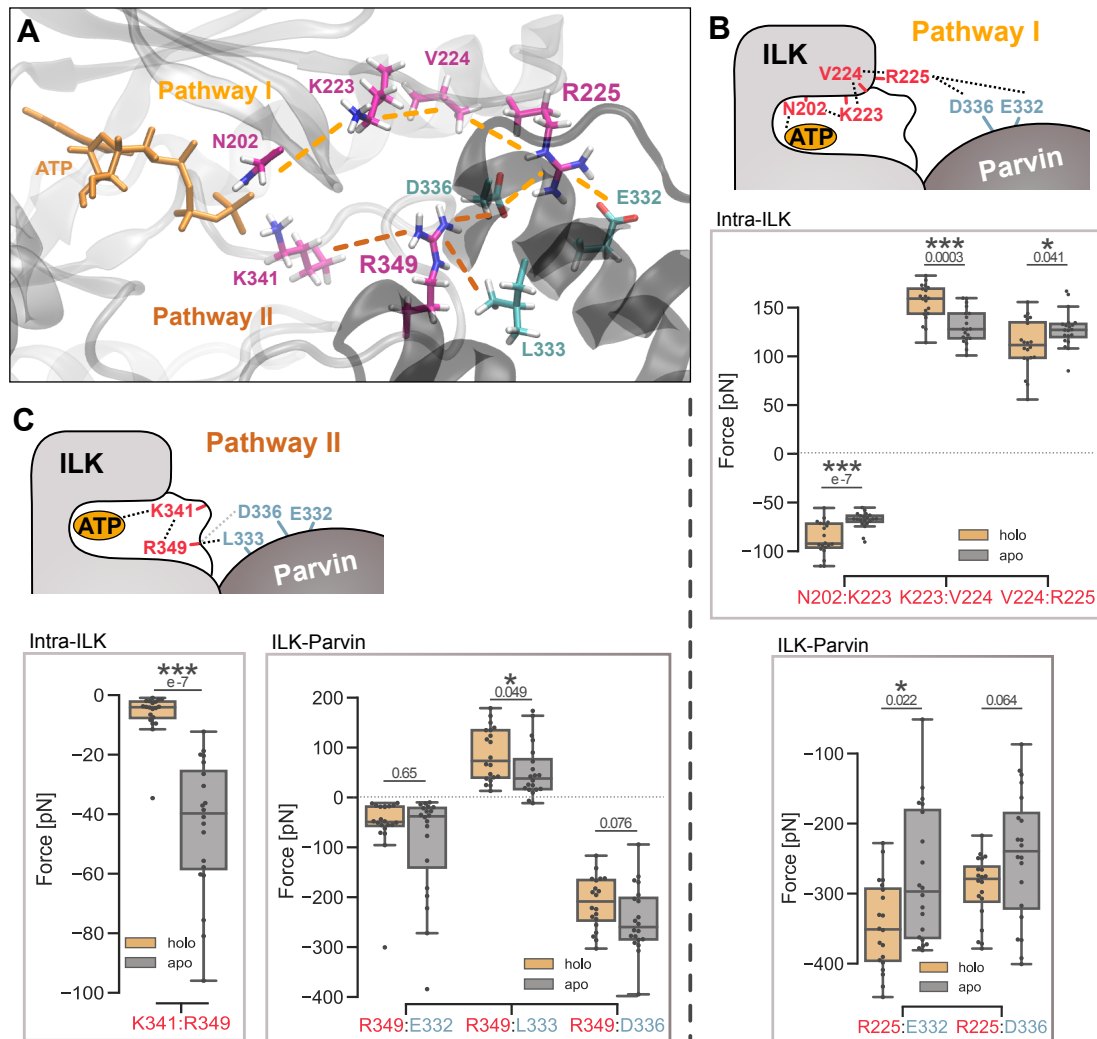


Fig. 3.9.: ATP-dependent pathways of internal force propagation between ILK and parvin. (A) Proposed force transduction pathways from ATP to saltbridge-forming arginines R225 and R349 and into α -parvin as determined by FDA. (B/C) Average pairwise forces between the indicated residue pairs as calculated from FDA for 20 individual runs compared between the apo and holo complex. Statistical significance determined by Mann-Whitney test. Positive and negative force values indicate repulsion and attraction, respectively. (B) Pathway I involving the saltbridge-forming residue R225. (C) Pathway II involving the saltbridge-forming residue R349.

The shortest pathway of significantly altered pairwise forces gives the predicted allosteric pathway from ATP towards the saltbridge-forming residues. The pathway of internal force changes from ATP to R225 encompasses a residue cascade involving N202, K223 and V224 (Figure 3.9 A and B). Further, FDA also hinted towards a secondary R225-dependent pathway involving K341 and S346 (Figure A.3). I observed R349 to be allosterically influenced by ATP over the ATP-coordinating residue K341 (Figure 3.9 A and C). Interestingly, K341 corresponds to a glycine from the crucial DFG motif of conventional kinases (K. Fukuda, Gupta, et al., 2009). Seemingly, since ILK is not catalytically active, a glycine of the DFG loop mutated to a residue that acquired a new function in the pseudokinase in mediating the ATP-dependent allosteric effect.

Influence of the saltbridges on the interaction with parvin

I further validated the importance of the two saltbridge-forming arginines for parvin binding by performing MD simulations of the holo ILK(WT) without parvin. In the absence of parvin, the two saltbridge-forming arginines R225 and R349 increase in flexibility (Figure 3.10 A). Previous investigations of the ILK:parvin binding interface primarily focused on the parvin-binding helix (α -G-helix) containing M402 and K403, which lead to a loss of ILK:parvin binding when mutated to alanine (K. Fukuda, Gupta, et al., 2009). In addition to R225 and R349, the α -G-helix also shows a higher flexibility in the MD simulations. This indicates that one of the main functions of R225 and R349 is to bind parvin.

By calculating the residue contact probability (i.e. percentage of total simulation time in which two residues are in contact) from MD simulations of the ILK:parvin complex, I could further assess the ability of the arginines to maintain saltbridges with parvin (Figure 3.10 B,C). The average occupancy for the R225-E332, R225-D336 and R349-D336 saltbridges of around 80 % in holo ILK corroborates their functional importance as parvin-binding residues. On the other hand, the average R349-L333 contact percentage of around 25 % implicating that this residue pair is of reduced importance for parvin binding.

The ATP-dependent ILK:parvin interaction as determined by FDA was further supported by my comparison of the contact probability of the studied interface residues between the ATP-bound state and the apo state. Interestingly, the absence of ATP significantly lowered the occupancy of the R225-E332 and of the R225-D336 saltbridges (Figure 3.10 B). This suggested an allosteric stabilization of the contacts between the ILK N-lobe and parvin upon ATP binding. Likewise, the contact probability of R349-L333 is also decreased in the absence of ATP. The two saltbridges involving R349 (R349-E332 and

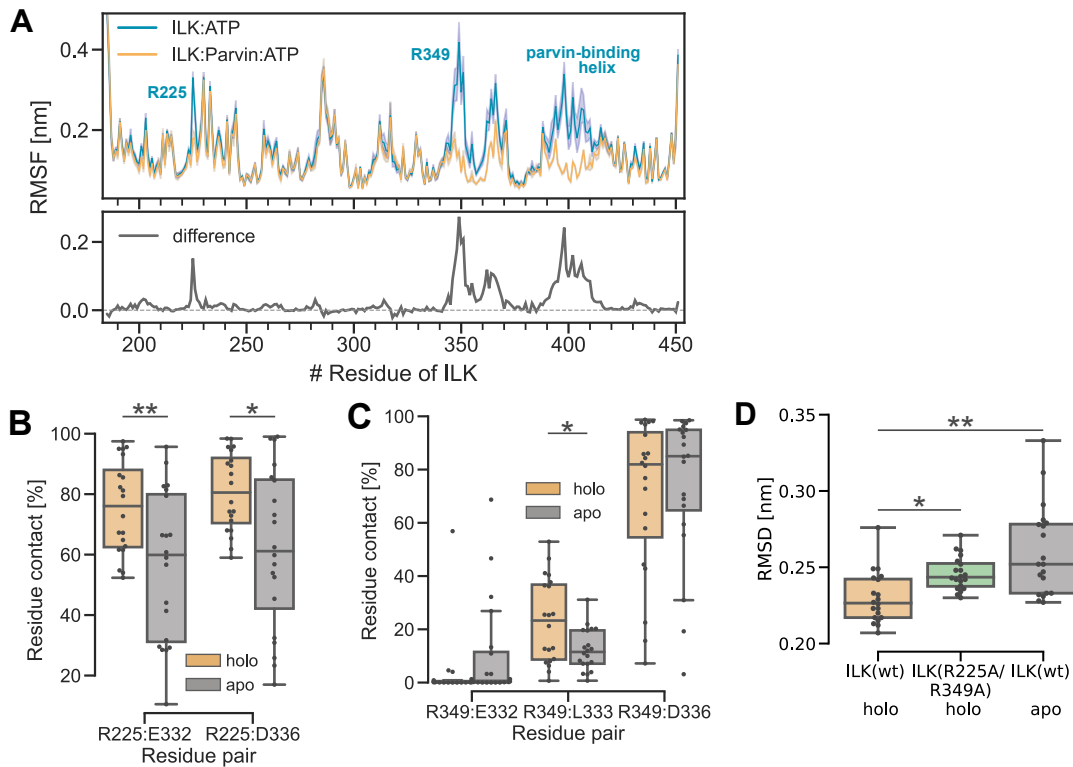


Fig. 3.10.: ATP alters contact probabilities of selected residues between ILK and parvin (A) RMSF of ILK in complex with parvin (orange) and without (cyan) computed for the backbone atoms as a function of residue number. Error bands denote the 95 % confidence interval. (B) Residue contact probability (threshold 0.35 nm) between ILK R225 and selected parvin residues depending on the presence of ATP (averaged from $n = 20$ independent trajectories). $**p = 0.0096$, $*p = 0.013$, Mann-Whitney). (C) Residue contact probability between ILK R349 and selected parvin residues as in B; $*p = 0.017$, Mann-Whitney. (D) Backbone RMSD of holo ILK(WT) and ILK(R225A/R349A). $n = 20$ trajectories, median of each trajectory is shown; $*p = 0.044$, $**p = 0.001$, one-way ANOVA/ Tukey HSD.).

R349-D336), however, did not significantly change their occupancy upon ATP removal (Figure 3.10 C). Thus, the lack of ATP appears to weaken the ILK:parvin interface while not fully abolishing the intra-molecular contacts. In conclusion, my equilibrium MD simulations provide evidence for the functional extension of the parvin binding interface towards the activation loop and N-lobe of ILK involving R349 and R225, respectively. Moreover, those interactions, which are allosterically influenced by ATP presumably, contribute to the stability of the ILK:parvin complex.

To examine the consequences of disruption of the ATP-dependent allosteric effect, I designed a double saltbridge mutant in which both saltbridge-forming arginines are mutated to alanine (R225A/R349A). Presumably, the exchange of the charged arginines to neutral alanines abolishes their abilities to form saltbridges and thus at least decreases

their interaction with the parvin residues. Interestingly, although I simulated this mutant still binding ATP, it displays an increased flexibility at an intermediate level between ILK(WT) holo and ILK(WT) apo (Figure 3.10 D). This provides a further hint towards a stabilizing ability of the two saltbridge-forming arginines on the ILK:parvin complex.

To verify that the saltbridges indeed confer parvin binding, I again collaborated with Dr. Michele Nava and Prof. Dr. Sara Wickström (University of Helsinki, Finland) for biochemical experiments. Furthermore, having established that the two saltbridge-forming residues are allosterically affected by ATP and show a tendency to affect ILK and ILK:parvin stability from MD simulation, I became interested in the cellular implications of saltbridge disruption. Motivated by my MD simulations suggesting that at least part of the effect of ATP is mediated by the salt bridges, it can be predicted that disruption of the saltbridges will have similar effects on focal adhesions as a whole as was observed for disruption of ATP. Thus, in the next section, I describe the results of cell-based experiments from my collaborators to test these two hypotheses and thereby determine the functional role of the saltbridge residues on the cellular level.

3.5 Saltbridge-coordinating residues stabilize α -parvin binding and focal adhesions

Experiments and corresponding figures of this subsection were provided by Dr. Michele Nava and Prof. Dr. Sara Wickström (University of Helsinki). Text is adapted from our joint publication (I. M. Martin, Nava, et al., 2022).

To determine the ability of the saltbridge residues to convey α -parvin binding, Dr. Michele Nava generated single R255A and R349A mutants as well as the R255A/R349A double saltbridge mutant and reconstituted ILK $-/-$ cells with these. Co-immunoprecipitation assays with α -parvin revealed that both R255A and R349A single mutants exhibit reduced parvin binding compared to ILK(WT). Strikingly, the R255A/R349A double mutant almost completely abolished parvin-binding (Figure 3.11 A). Furthermore, ILK(R255A/R349A) is still able to localize to FAs as shown by immunofluorescence analysis by Dr. Michele Nava. However, α -parvin fails to display correct FA localization and is instead present throughout the cytoplasm in dot-shaped patterns (Figure 3.11 B).

Since the saltbridges evidently mediate parvin binding we set out to understand how they affect FAs as a whole, especially considering varying degrees of traction forces. Qualitative analysis of FA dynamics by Dr. Michele Nava revealed that, in contrast to the ATP-binding mutant, the double-saltbridge mutant exhibits decreased FA assembly rates

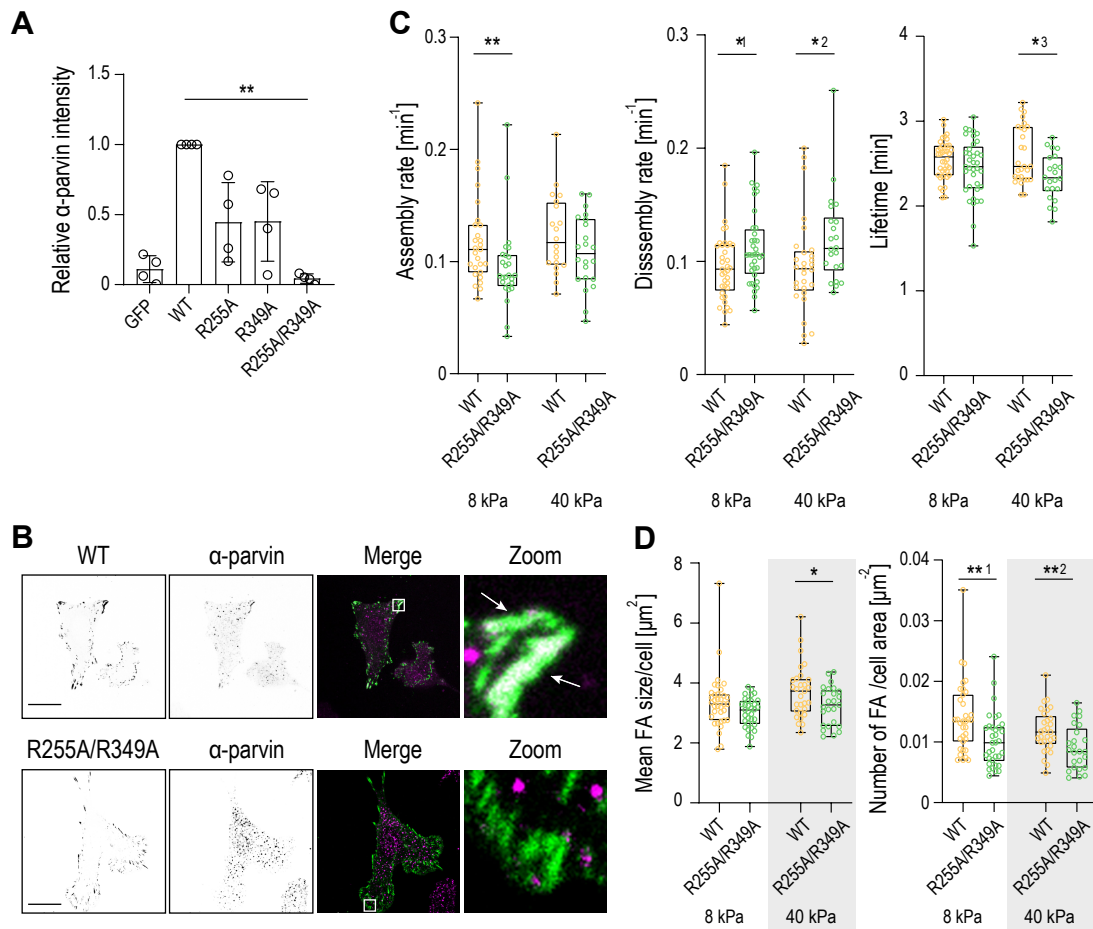


Fig. 3.11.: Point mutations in saltbridge-forming residues destabilize α -parvin binding and FAs. Figure and experiments were provided by the collaborators Dr. Michele Nava and Prof. Dr. Sara Wickström, University of Helsinki. Figure adapted from our joint publication (I. M. Martin, Nava, et al., 2022). (A) Quantification of α -parvin to GFP ratio from GFP pull-down experiments from ILK^{-/-} fibroblasts expressing GFP, ILK(WT)-GFP, ILK(R225A)-GFP, ILK(R349A)-GFP and ILK(R225A/R349A)-GFP mutants (mean \pm S.D., $n=4$ independent experiments, $**p=0.0035$, Friedman/Dunn). (B) Representative immunofluorescence images of α -parvin and ILK. α -parvin co-localizes at FAs in ILK(WT)-GFP cells (arrowheads); no obvious localization of α -parvin to adhesions in ILK(R225A/R349A)-GFP cells. Right panels: zoom of the area indicated by the white box. Scale bars $20\mu\text{m}$. (C) Quantification of FA assembly, disassembly and lifetime in ILK(WT)-GFP and ILK(R225A/R349A)-GFP cells on 8 kPa and 40 kPa substrates ($n > 20$ cells/condition pooled across 4 independent experiments, $*^1p=0.0394$, $*^2p=0.0210$, $*^3p=0.0113$, $**p=0.0084$, Mann-Whitney). (D) Quantification of the mean FA size and adhesion number in ILK(WT)-GFP and ILK(R225A/R349A)-GFP cells on 8 kPa and 40 kPa substrates. Area threshold set to 20 pixels. ($n > 25$ cells/condition pooled across 4 independent experiments, $*p=0.0454$, $**^1p=0.0016$, $**^2p=0.0054$, Mann-Whitney).

(Figure 3.11 C). Particularly evident on stiff substrates, ILK(R225A/R349A) additionally increases FA disassembly rates accompanied by decreased FA lifetimes, similar to the ATP-binding mutant. Consistently, FAs in ILK(R255A/R349A) cells are significantly smaller and present in overall lower numbers compared with WT cells (Figure 3.11 D). Decreased FA area was also confirmed by paxillin staining (Figure A.4). Again and similar to the ATP-binding mutant, the double saltbridge mutant generally exhibited a more pronounced phenotype on 40 kPa stiff gels.

In conclusion, the disruption of ATP-induced intra-molecular allostery eliminates α -parvin binding to ILK which, particularly on stiff substrates, leads to slower FA turnover.

3.6 ATP increases the mechanical stability of the ILK:parvin complex

Especially on stiff substrates, cells exhibit high traction forces and that is precisely where we observe a particular destabilization of FAs by disruption of ATP-binding or of the ATP-triggered allostery between ILK and parvin. This hints towards an implication of the ILK:parvin:ATP complex in force-dependent regulation of FAs. Therefore, it is extremely interesting to not only study the equilibrium behavior of ILK, but furthermore to ask how the ILK:parvin complex behaves under mechanical load and how ATP affects it in this condition. To this end, I set out to perform force-probe MD simulations of the ILK:parvin complex with regard to the influence of ATP.

Considering the IPP, since the mechanical stability of proteins and protein complexes is linkage-dependent (Carrion-Vazquez et al., 2003), the first question we need to ask is where the force acts on this complex. Mechanical force is transmitted to the IPP complex by both the ECM/integrins and the actomyosin network. Examining the overall composition of FAs (Figure 3.1), it becomes apparent that the most likely mediator of force from the cytoskeleton to the IPP is parvin, as it directly binds F-actin with its N-terminus.

For forces originating from the extracellular, two possible pathways for these forces to reach ILK within IPP can be identified: (A) originating from integrins, force could be transmitted to the ILK pseudokinase domain by kindlin-2, which binds both integrins and ILK (Montanez et al., 2008; Huet-Calderwood et al., 2014; Kadry et al., 2018), and (B) originating from receptor tyrosine kinases, force could be transmitted to the N-terminal ankyrin repeats of ILK via several adaptor proteins (Chiswell et al., 2008). However, without adequate and detailed characterization of the forces within focal adhesions,

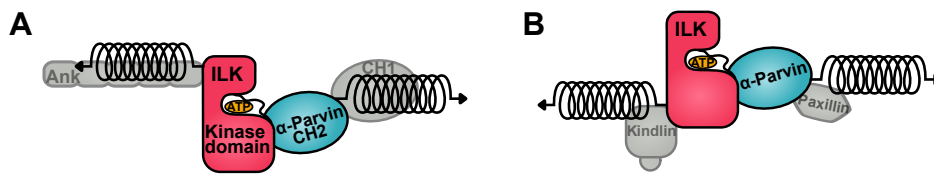


Fig. 3.12.: Pulling directions in force-probe MD of ILK:parvin. Stretching force along the ankyrin-actin axis (A) and the kindlin-actin axis (B) is applied to ILK and parvin in the form of virtual springs at indicated positions.

those two pathways can neither be differentiated nor prioritized. Therefore, as an initial exploratory investigation, I simulated the force propagation on the ILK:parvin complex from both conceivable directions separately, the results of which are presented in the following sections.

3.6.1 Force through the ankyrin-actin axis

To study the forces transmitted across the ankyrin-actin-axis, I chose a simple, first-order approximation for the pulling-patches. The ILK kinase domain is preceded in sequence by ankyrin repeats, however, a complete ILK crystal structure is not available to provide information on possible interdomain interactions. Thus, one can approximate that the force transmitted from the membrane propagates to the ILK kinase domain through its N-terminal residue. A similar approach can be taken considering the cytoskeletal side of the IPP force propagation pathway. α -parvin binds actin with its N-terminus over the recently discovered WASP-homology2 domain (Vaynberg et al., 2018) and again no complete parvin structure is available. Similarly, one can approximate that the force transmits through the N-terminus of the parvin CH2 domain. Therefore, I subjected the N-terminal residues of both ILK (H185) and parvin (A249) to harmonic pulling potentials moving in opposite directions with constant velocities of 1 m/s to 0.01 m/s and probed the effect of ATP removal on the mechanical stability of the ILK:parvin complex (Figure 3.12 A).

Given the subjected tension on the N-terminal residues of the two proteins, it is not unexpected that both termini begin to unfold (illustrated in Figure 3.13 A). Considering the separate unfolding distances of ILK and parvin (Figure 3.13 B and C), it becomes apparent that, irrespective of ATP, partial unfolding of parvin (up to ~ 8 nm) is followed by mutual further unfolding of ILK and parvin (up to ~ 9.5 nm for both proteins) in most trajectories. Interestingly, beyond that, almost all trajectories continue to further unfold parvin in the holo complex. In contrast, both parvin and ILK unfolding occurs with more equal rates in the apo complex. These data provide first hints towards a stabilization

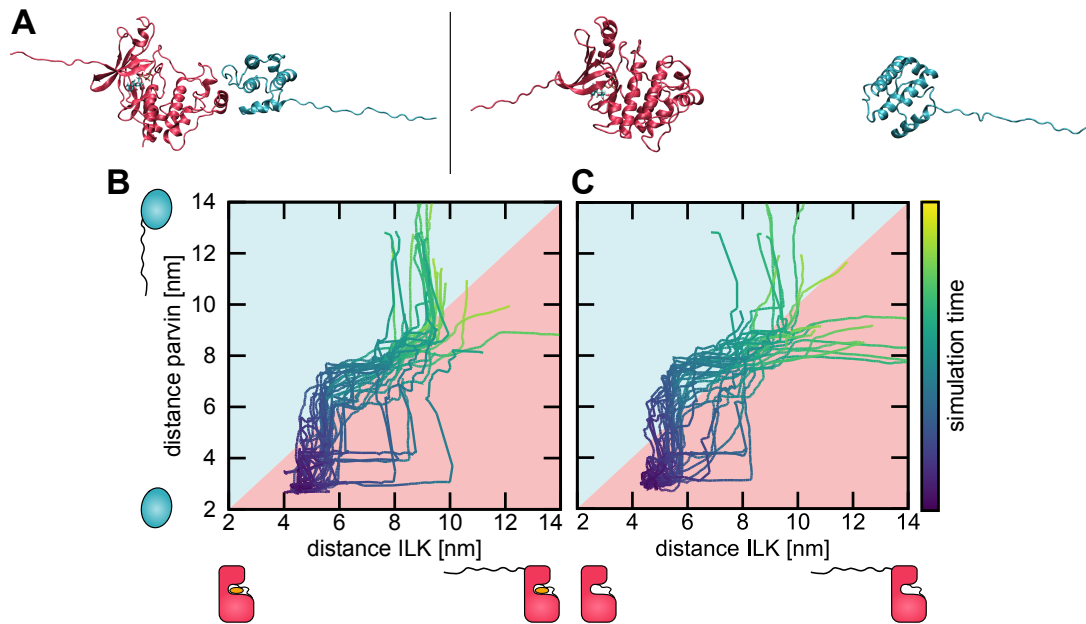


Fig. 3.13: Pulling on ILK:parvin via the anykrin-actin axis. (A) Snapshots of ILK (pink) with ATP in complex with parvin (blue) in force-probe MD simulations before and after complex dissociation. N-terminal unfolding of both proteins is occurring. (B) Individual extensions of ILK and parvin in simulations with ATP or (C) without ATP. 10 trajectories per velocity (1 m s^{-1} , 0.1 m s^{-1} and 0.01 m s^{-1}) totaling to $n = 30$ independent trajectories. Trajectories are smoothed with a rolling average. Simulation time is presented as fractions of the whole trajectory length.

of ILK through ATP-binding in conditions of mechanical stress. Owing to the observed N-terminal unfolding, the N-lobe of ILK, to which ATP is bound, appears to be better protected from unfolding during pulling. However, since integrins are regarded as the major players in cell-ECM signaling, a force transmission pathway involving integrins might be considered more physiological. Therefore, I further simulated mechanical force across the kindlin-actin axis, as described in the next section.

3.6.2 Force through the kindlin-actin axis

Besides the anykrin-actin axis, the IPP can be reasoned to experience force via the kindlin-actin axis (section 3.6). Here, parvin binds directly to actin, as described above, whereas the C-terminal part of the ILK kinase domain is connected to integrin via the adaptor protein kindlin-2. The pulling patches needed to describe the force along this axis cannot be approximated as straightforwardly as the ones used for the anykrin-actin axis. Thus, this subsection describes the determination of pulling-patches on ILK and parvin and presents the subsequent pulling simulations considering the kindlin-actin axis.

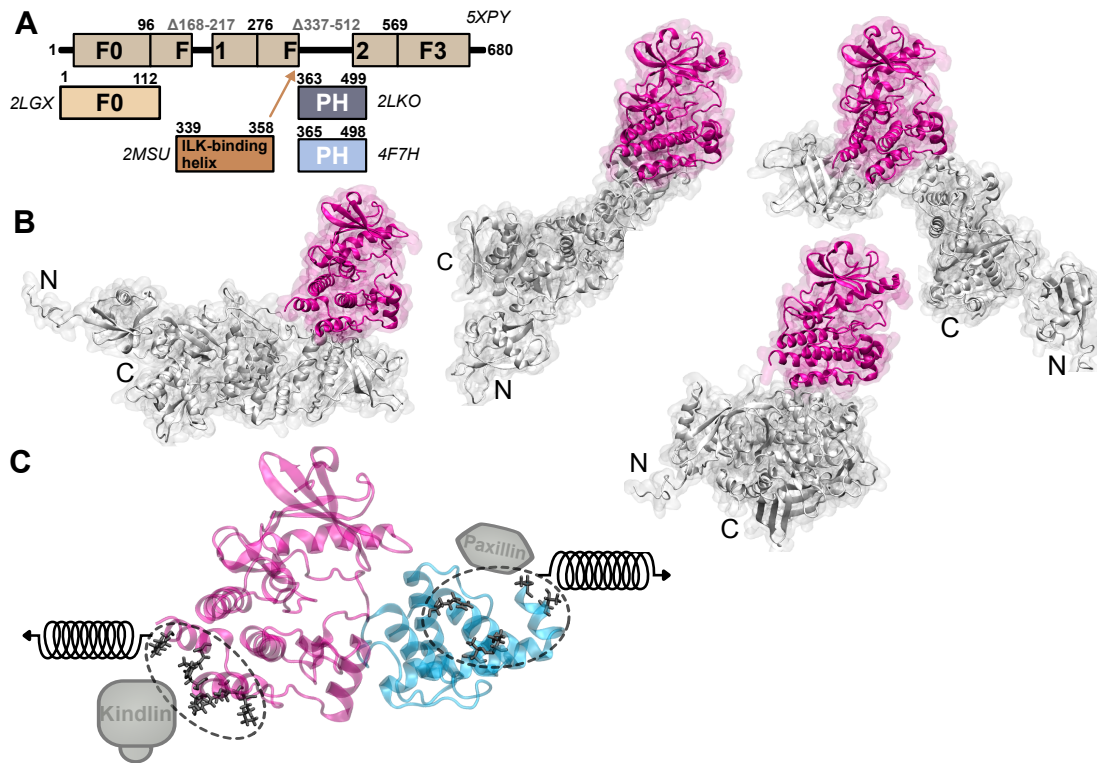


Fig. 3.14.: ILK:kindlin-2 docking to determine the ILK:kindlin pull group. (A) Schematic overview of available kindlin-2 partial crystal structures with associated PDB-codes. (B) 4 exemplary and diverse ILK:kindlin-2 docking poses from guided molecular docking (for more examples see Figure A.5). ILK in pink and kindlin-2 in light grey. N- and C-termini of kindlin-2 are labeled. (C) Contact residues (black sticks) between ILK (pink) and a kindlin-2 model (grey scheme) are defined as the ILK pulling patch. Contact residues (black sticks) between parvin (cyan) and paxillin-LD1 (grey) are defined as the parvin pulling patch.

Molecular docking of kindlin-2 to ILK

Within the kindlin-actin axis, the residue-patch within ILK that is most likely under force encompasses the binding site between ILK and kindlin-2. This is due to ILK itself not being able to bind integrins, but instead kindlin-2 associates both with ILK and integrins, as well as localizes to the membrane (Jianmin Liu et al., 2011; Yamamoto et al., 2016; Palmere et al., 2021). However, a crystal structure of the ILK:kindlin-2 complex is not available, yet the ILK residues K423 and I427 have been experimentally validated as interacting with kindlin-2 (Kadry et al., 2018). Since it is highly unlikely that kindlin would only encounter these two residues within ILK, a larger binding patch is expected. Consequently, the force from the ECM would propagate over this binding patch.

I used a combined homology modeling and guided molecular docking approach to predict a more extensive set of ILK:kindlin binding residues. There exists a nearly complete

kindlin-2 crystal structure in mouse and several single-domain structures, such as the free PH domain and interestingly, the ILK-binding helix (Figure 3.14 A). I modeled the full human kindlin-2 from this array of partial kindlin structures using homology modeling (subsubsection 3.2.1). These models differ primarily in the position and orientation of the PH domain (Figure A.5). I further used these kindlin-2 models to perform guided molecular docking of kindlin-2 to ILK using the experimentally validated binding residues within ILK as mandatory contact residues (Figure 3.14 B). Of note here is that the docked positions of kindlin:ILK do not appear to structurally interfere with kindlin's ability to bind the membrane (Yamamoto et al., 2016) which is a prerequisite for proper kindlin function. All docking positions include the experimentally confirmed binding residues, as required, and also comprise a number of recurrent binding residues as well as less frequently identified residues. From the heterogeneous ensemble of docking positions, I extracted those ILK residues that were reproducibly identified as interacting with kindlin-2 across all docking positions. While also interesting on their own, the ILK:kindlin-2 interacting residues proposed here can be considered the most likely force-bearing residues on the surface of the ILK kinase domain (Figure 3.14 C).

Considering the force propagation from the cytoskeleton, the force would most likely be transferred from actin to the N-terminal part of the CH2 domain, as is the case in the ankyrin-actin axis. However, in a scenario of two largely asymmetric pulling sites – a residue patch on ILK and one residue in parvin – simulation artifacts would result from a highly unequal force distribution. Thus, increasing the size of the parvin pulling patch alleviates the possibility of such artifacts. In addition, the N-terminus of parvin CH2 is in contact with the LD1 domain of paxillin (Lorenz et al., 2008; X. Wang et al., 2008). Paxillin further interacts with vinculin, which is another important focal adhesion protein that is likely under force (Dumbauld et al., 2013). In this way, paxillin is likely interfering with the inter-domain contacts within parvin and thus alters the force transmission pattern. Accordingly, the forces reaching the parvin CH2 domain would distribute over the residues that are encompassed by paxillin. For these combined reasons, I chose the CH2:paxillin binding residues as the pulling patch of parvin (Figure 3.14 C).

Force-probe MD of ILK:parvin

In force-probe MD simulations, I subjected the two pulling patches of force-bearing residues (Figure 3.14 C) to harmonic pulling potentials moving away from one another with constant pulling velocities of 1 m/s to 0.01 m/s. I compared the differences between the holo and apo state of the ILK:parvin complex and further related those results to the behavior of the double saltbridge mutant.

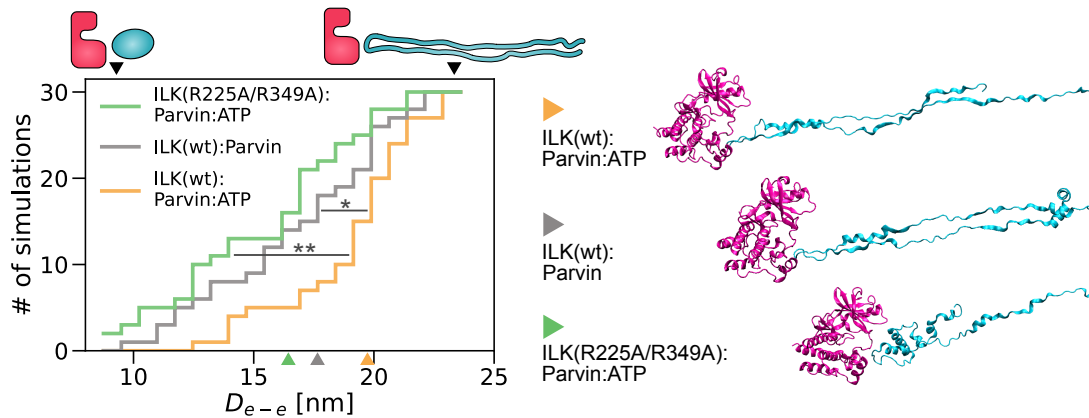


Fig. 3.15.: ATP stabilizes ILK:parvin under mechanical tension via the kindlin-paxillin-axis. Cumulative number of complex dissociation events as a function of distance between the pull-groups at dissociation (D_{e-e}), with a dissociation being defined by an interface area below 0.6 nm^2 . $n = 30$ independent trajectories, 10 per velocity (1 m s^{-1} , 0.1 m s^{-1} , 0.01 m s^{-1}), single trajectories of each velocity are shown in Figure A.6. ILK holo vs. ILK apo: * $p = 0.028$, ILK(WT) vs. ILK(R225A/R349A): ** $p = 0.001$, one-way ANOVA/Tukey HSD. Schemes and black arrowheads visualize the highest and lowest achieved D_{e-e} before dissociation. Colored arrowheads and corresponding snapshots indicate the median structure of each condition at the time of dissociation; snapshots of 15th and 85th percentile per condition are shown in Figure A.6.

In contrast to the ankyrin-actin axis, pulling along the kindlin-actin axis induced unfolding of predominantly parvin, as well as complex dissociation. The protein unfolding can be quantified by the distance between the pulling patches, D_{e-e} , whereas complex dissociation was measured by a decrease in interface area. I here defined a complex dissociation event to occur if the interface area drops below a low threshold (0.6 nm^2).

Across conditions and velocities, dissociation events could be observed with various stages of preceding protein unfolding. These ranged from dissociation events when only small portions of the proteins had straightened and unfolded ($D_{e-e} \sim 9 \text{ nm}$) to events in which parvin underwent massive unfolding ($D_{e-e} \sim 28 \text{ nm}$). Strikingly, upon depletion of ATP from the wildtype complex, the balance between dissociation and unfolding is shifted towards dissociation at lower extensions. In contrast, the ATP-bound complex only dissociates after more extensive parvin unfolding. The ATP-bound double-saltbridge mutant showed an indistinguishable behavior from the wildtype apo complex. Thus, a decrease in mechanical stability of the ILK:parvin interface relative to the stability of the individual proteins can be observed upon disruption of ATP-induced allostery and loss of ATP-binding.

As a common feature of both pulling axes, ATP appears to act as a stabilizing agent, both to stabilize ILK and the ILK:parvin interface. These data corroborate and build upon

my finding of ATP as an allosteric regulator of the ILK:parvin complex in equilibrium conditions (section 3.4). Further, the experimentally observed destabilization of FAs especially on stiff substrates i.e. in the presence of high traction forces (section 3.5), could be mechanistically explained by a weakened ILK:parvin interface. Therefore, it can be assumed that processes based on the generation of traction forces are affected by binding of ATP to ILK. Thus, I predicted that ILK mutants, which are defective in ATP-binding or ATP-based internal signaling would exhibit deficits in the establishment of traction forces and associated cellular processes. These predictions were again tested through cell-based experiments from Dr. Michele Nava and Prof. Dr. Sara Wickström (University of Helsinki) which are described in the next section.

3.7 ATP- and α -parvin-binding defective ILK impairs traction force generation and cell migration

Experiments and corresponding figures of this subsection were provided by Dr. Michele Nava and Prof. Dr. Sara Wickström (University of Helsinki). Text is adapted from our joint publication (I. M. Martin, Nava, et al., 2022).

Traction force microscopy (TFM) is perfectly suited to explore the influence of ATP within ILK on force-generating processes. Intriguingly, TFM performed by Dr. Michele Nava revealed that both loss of ATP (L207W mutant) and loss of the ATP-influenced saltbridges (R225A/R349A mutant) result in lower mean traction stresses compared to WT cells (Figure 3.16 A,B). Further, the reduced traction stresses are associated with impaired actomyosin contractility as both L207W and R225A/R349A mutants showed a substantial reduction in actin stress fibers and myosin II activity (Figure A.7).

The process of cell migration heavily relies on stable FAs and actomyosin contractility and which are both promoted by traction stresses (Ridley et al., 2003). Therefore, we predicted that ILK mutants which cause reduced traction forces also would impair cell migration. Indeed, analysis of migration trajectories of single cells by Dr. Michele Nava showed that ILK(R225A/R349A)-GFP cells exhibit a migration defect with migration rates smaller than ILK(WT)-GFP cells and comparable to ILK^{-/-} cells (Figure 3.16 C). Collectively, these experimental results show that destabilization of the ILK:parvin interface, either by loss of ATP or loss of ATP-influenced saltbridges, prevents proper build-up of traction forces and actomyosin contractility and thus impairs the migratory capacity of cells.

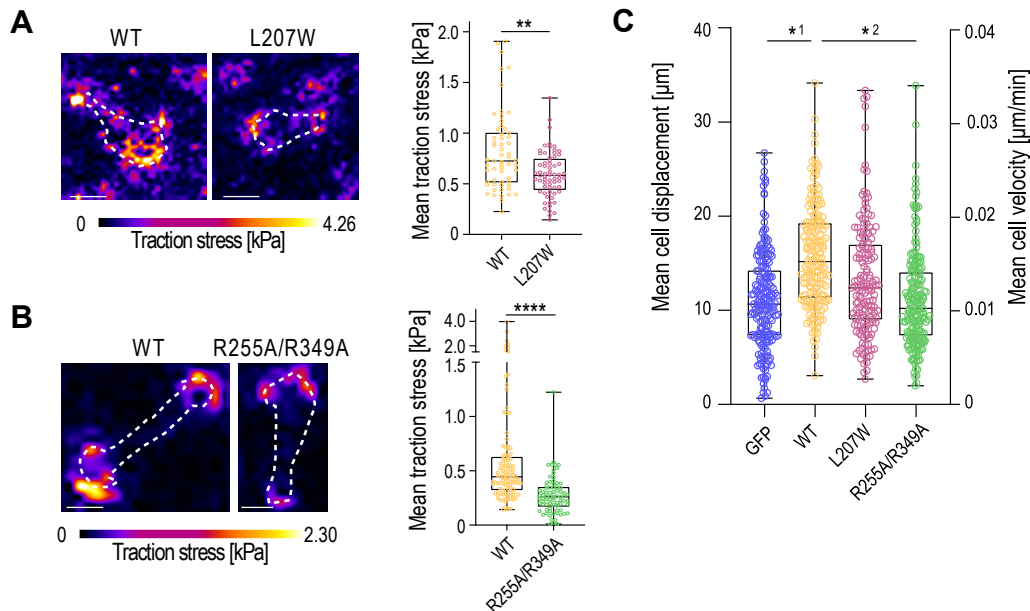


Fig. 3.16.: Impaired ATP- and α -parvin binding prevent traction force generation and leads to migration defect. Experiments and figure including legends were provided by collaborators Dr. Michele Nava and Prof. Dr. Sara Wickström, University of Helsinki. (A) Representative images and traction force heat maps (left) and quantification of mean traction stresses (right) of ILK(WT)-GFP and ILK(L207W)-GFP cells. $n > 59$ cells/condition pooled across 4 independent experiments, $**p = 0.0047$, Kolmogorov-Smirnov. Scale bars $20\ \mu\text{m}$. (B) Representative images and traction force heat maps (left) and quantification of mean traction stresses (right) of ILK(WT)-GFP and ILK(R255A/R349A)-GFP cells plated on $8\ \text{kPa}$ PAA gels. $n > 78$ cells/condition pooled across 4 independent experiments, $****p = 0.0001$, Kolmogorov-Smirnov. Scale bars $20\ \mu\text{m}$. (C) Quantitative analysis of average distance (μm , left Y-axis) and velocity ($\mu\text{m}/\text{min}$, right Y-axis) of ILK $^{-/-}$ GFP, ILK(WT)-GFP, ILK(L207W)-GFP and ILK(R255A/R349A)-GFP cells. ($n = 3$ independent experiments with > 35 cells/condition/experiment, $*^1p = 0.0114$, $*^2p = 0.0269$ Friedman/Dunn). Cell trajectories from 12 h acquisition.

3.8 Discussion

The data that I presented in this chapter show a combined computational and experimental approach to broaden the understanding of how the pseudokinase ILK integrates and transduces biochemical and mechanical signals. Particularly, I asked if and how ATP, which is interestingly still bound to the pseudokinase, plays a role in the molecular interactions of ILK and its function and especially in mechanotransduction.

Although pseudokinases are not capable of phosphoryl transfer, interestingly a large fraction of them nevertheless bind ATP with largely unknown functions. For some cases, specific functions have been assigned for ATP binding to pseudokinases. For example, in the case of the pseudokinase STRAD α , ATP-binding was shown to alter the conformation of the pseudokinase domain and to maintain it in a closed conformation to allow for efficient target binding and downstream signaling (Zeqiraj, Filippi, et al., 2009). Another example is the pseudokinase MLKL, where ATP-binding may serve to measure the propensity of the pseudokinase domain to undergo conformation switching (Mace and Murphy, 2021; Murphy, Czabotar, et al., 2013; Murphy, Lucet, et al., 2014).

For ILK on the other hand, initial evidence for ATP-function was provided by the observation that F-actin bundling is sensitized by ATP bound to ILK (Vaynberg et al., 2018). However, the exact molecular mechanism of ATP, particularly in the context of mechanical force, remained unclear. The data presented in this work point towards a multifaceted role for ATP in ILK function: ATP enhances the structural integrity of ILK, allosterically impacts the ILK:parvin interaction and increases the resistance of the IPP complex to dissociation upon force.

3.8.1 ILK stability and its binding partners

ILK likely co-evolved with α -parvin as an obligatory binding partner as seen from the fact that purified ILK forms highly insoluble aggregates in the absence of parvin (K. Fukuda, Gupta, et al., 2009). The inherent instability of ILK is further underlined by the requirement for the heat shock protein Hsp90 for a stable ILK:parvin interaction (Radovanac et al., 2013). Hsp90 is a molecular chaperone that interacts with client proteins to stabilize their structure and thus to ensure they acquire a functional active conformation (Schopf et al., 2017). This means that without the protection of its structural integrity by the chaperone Hsp90, ILK is subjected to proteasomal degradation (Radovanac et al., 2013). Inhibition of the Hsp90 chaperone further leads to removal of ILK from FAs which impairs force generation on the ECM as well as cell migration

(Radovanac et al., 2013). Combined, these findings signify that ILK is inherently unstable and requires protein interactions for stabilization.

Upon determination of the ILK crystal structure, ATP was found to only exhibit a negligible effect on the overall static ILK structure, in fact both the apo and holo structure were described as "essentially identical" (K. Fukuda, Gupta, et al., 2009). My simulation data reveals that ATP instead alters the dynamic properties of the ILK kinase domain. ATP influences the stability of ILK and the ILK:parvin complex which proposes ATP as a secondary binding partner, in addition to parvin, for structural integrity.

The ILK mutant deficient in ATP-binding, ILK(L207W), was originally described to sterically occlude ATP binding without affecting the structural integrity of the kinase domain (Vaynberg et al., 2018). Indeed, this mutant is still able to bind parvin (Vaynberg et al., 2018, subsection 3.3) which underlines its global structural integrity. However, on an atomistic level, my MD simulations show that the kinase-like domain of this mutant is more flexible compared to the wildtype holo complex and similar to the wildtype apo complex. Further, and analogous to apo ILK(WT), ILK(L207W) displays a more pronounced inter-lobe wringing motion. Although the structural integrity appears to be maintained on the global level, the loss of ATP results in considerable structural changes on the atomic level. Moreover, the cellular experiments from Dr. Michele Nava and Prof. Dr. Sara Wickström presented in this thesis, demonstrate that loss of ATP-binding to ILK leads to destabilization of FAs resulting in decreased FA numbers. Combined, these data suggest a more intriguing role of ATP for ILK function.

3.8.2 ATP-induced allostery

As the results discussed above point towards a more involved role for ATP in ILK function, I was interested in further investigating the detailed molecular effect of ATP. Here, my MD simulation data extended with FDA provide further evidence for two propagation pathways of internal forces triggered by ATP. Within those, I found ATP to allosterically influence previously unacknowledged saltbridge-forming residues (R225 and R349) that interact with parvin.

Regarding my examined pathway by which ATP affects the R225 and R349 saltbridge residues, it must be taken into account that the FDA method as used in this study is an end-point method, which means that it can only compute the differences in forces between two states, here ATP-bound and unbound. From those differences in interactions, one can deduce the shortest path of significantly altered interactions. However, this might be different from a sequential mechanistic pathway, which is not

possible to determine from FDA. Nevertheless, this method provides verifiable predictions of important residues within the force-propagation pathways. Importantly, collaboration with Prof. Dr. Sara Wickström and Dr. Michele Nava proved that R225 and R349 do indeed confer parvin binding. They cooperate in parvin binding with the previously analyzed residues M402/K403 in the C-lobe of ILK (K. Fukuda, Gupta, et al., 2009).

From the MD simulations, I could also determine that ATP reduces the saltbridge occupancy between both arginines and parvin residues, indicating that ATP inherently stabilizes the interaction between ILK and parvin. However, in contrast to the experimental data, parvin does not detach from ILK in the simulations upon mutation of the saltbridge residues. This is presumably at least partly due to an artifact of MD, as it tends to overstabilize proteins and thus also causes saltbridges to appear more stable than they actually are (Ahmed et al., 2018). In addition, the timescales considered in the simulations are seemingly too short to observe such a large-scale detachment event.

As expected, since the double-saltbridge mutant cannot bind parvin in experiments, it also fails to recruit parvin to FAs. Interestingly and in contrast to the previously studied parvin-binding M402A/K403A mutant (K. Fukuda, Gupta, et al., 2009), the double saltbridge mutant (R349A/R225A) itself still localizes correctly to FAs. In this way, the double saltbridge mutant phenotypically resembles the ILK mutant deficient in ATP-binding L207W. Similarly, ILK(L207W) contrasts another ATP-binding defective mutant (N200A/K341A) which fails to localize correctly to FAs (K. Fukuda, Gupta, et al., 2009). My FDA results imply that the reason for this mislocalization of the N200A/K341A mutant could be that K341 and ATP directly influence each other, which might greatly destabilize ILK. Very recently and also using MD simulations, three additional point mutations were identified to also alter the stability of the ILK:parvin complex which results in impaired kidney development in mice (Bulus et al., 2021). Those mutations were found to have an allosteric effect on parvin as well, which however has not yet been further characterized.

The combined computational and experimental data thus suggests a model that features two distinct parvin-binding modes within ILK: one ATP-dependent mode across the kinase N-lobe and activation segment which governs the two saltbridge-forming arginines and the previously established C-lobe pathway which seems independent of ATP. Intriguingly, it appears as though only the ATP-independent mode is required for localizing ILK into FAs, whereas ATP-dependent binding is required for adhesion stability.

3.8.3 ILK under mechanical stress

Beyond the equilibrium condition, where ATP stabilizes the pseudokinase, the presented data further shows a stabilizing effect of ATP on the ILK:parvin complex under mechanical force. The altered mechanical resistance I observed in the MD simulations at the molecular level is based on the assumption that forces within adhesions are transmitted to the IPP from F-actin as well as over two different axis from the ECM: the ankyrin-actin axis and the kindlin-actin axis. These force-transmission pathways were reflected in the choice of residue-patches for the force-probe MD.

Regarding the kindlin-actin axis, I used a combined molecular modeling and docking approach for the ILK:kindlin complex. In this way, I identified kindlin-binding residues within ILK, allowing robust simulation along the resulting pulling direction, at least according to the current limited knowledge. Thus, a more comprehensive view onto mechanotransduction across the kindlin-ILK axis can only be studied in simulation once an experimental ILK:kindlin structure is available. Given the critical role of the pulling direction on protein mechanical response (Carrion-Vazquez et al., 2003), the characterization of both force-transmission axes would also greatly profit from extended structural information of the full IPP complex and associated proteins. These would include inter-domain and protein interactions that could alter the direction of force transmission. First explorations in this direction stem from structural modeling of the IPP based on small-angle X-ray scattering (SAXS) data (Stiegler et al., 2013). However, a more detailed representation of the complete IPP complex using for example cryo-EM would be valuable.

The results of both force application routes point towards a role of ATP in mechanical stabilization of the ILK:parvin complex, although both axes manifest in different readouts from the simulation and appear to differently affect the ILK:parvin complex. Within simulations of force along the kindlin-actin axis, ATP shifts the distribution of complex dissociation to parvin unfolding while ILK remains folded. In contrast, in simulations of force through the ankyrin-actin axis, ATP shifts the balance from ILK unfolding to parvin unfolding. However, another intriguing question is whether the IPP actually receives forces via both axes and not just one, which is plausible since FAs are inherently complex structures. In this case, the observable role of ATP could shift again. However, setting up such a scenario of stress distributing through both axes in a way that is as close to reality as possible is inherently complex and requires further experimental studies of how force actually flows inside focal adhesions. Nevertheless, exploratory simulations could provide valuable hints towards experimentally testable predictions of various combined pulling scenarios. Additionally, such large-scale mechanotransduction investigations

could potentially also extend towards force propagation via the membrane as was done for FAK (Goñi et al., 2014; Zhou et al., 2015).

Beyond the sole effect of ATP, my simulations additionally showed indistinguishable mechanical instability of apo ILK and the double-saltbridge mutant, which is still capable to bind ATP. This leads to the hypothesis that the allosterically influenced saltbridges mediate, at least in part, the ILK:parvin stabilization by ATP which is observed under mechanical force. Assuming cellular force generation requires an intact ILK:parvin interface, the double-saltbridge mutant is thus predicted to resist generation of cellular forces due to its apparently weaker interface under mechanical load. Indeed, both the experimental disruption of ATP- and parvin-binding to ILK within the L207W and R225A/R349A mutant results in reduced force generation as well as cell migration. The joint computational and experimental results thus support the hypothesis that the stability of the ILK:parvin complex determines the resilience of FAs towards mechanical loads. One could even go so far as to propose ILK as a pseudo-mechanokinase, where ATP would convey a mechanosensory role.

Generally, it would be valuable to confirm the molecular-scale changes of the ILK:parvin complex in response to mechanical force using single-molecule force spectroscopy techniques such as AFM or optical tweezers (Nandi and Ainaravapu, 2021; Bustamante et al., 2020). This would narrow the current resolution gap between my simulations and the large-scale cellular effects. Traditionally, such comparison was tedious due to the vastly different loading rates used in simulation and experiment. With the recent advances in both high-speed AFM and acceleration of simulations, this time-scale gap is closing more and more, thus facilitating a direct comparison (Franz et al., 2020; Rico et al., 2019). The velocities I used for force-probe MD range between the highest velocity considered reliable, 1 m s^{-1} (Sheridan et al., 2019), and the lowest that was still computationally feasible for this project, 0.01 m s^{-1} . Within one condition, the overall results are similar across different velocities, indicating that the velocities are within an adequate range of pulling speeds. In this way, especially with respect to the lowest simulation speed, the possibility of direct verification with high-speed AFM is within reach (Rico et al., 2019).

3.8.4 Focal adhesion dynamics

Binding of parvin to ILK and thus assembly of the IPP complex likely occurs prior to the formation of cell-ECM adhesions (Y. Zhang et al., 2002). When quantifying FA assembly rates, the parvin-binding deficient mutant R225A/R349A leads to reduced assembly rates. This might point towards a function of ILK:parvin interaction in the formation of

focal adhesions, which is generally driven by the presence of the IPP. On the other hand, both R225A/R349A and L207W more severely perturb FA disassembly, indicating that both parvin and ATP bound to ILK regulate the disassembly of adhesions. Moreover, this influence on FA disassembly can be attributed to IPP stability under mechanical force, since the disassembly defects are more severe on stiff substrates where higher traction stresses are present.

The combined data on ILK:parvin stability and FA turnover hint towards a model where ATP acts as one adjusting factor to influence the amount of force build-up within FAs that is needed to disrupt the ILK:parvin interface. Ultimately, this termination of force signaling through disrupted IPP would lead to adhesion disassembly. In the context of cell migration, disassembly is required for efficient retraction of the cells rear-end (D. J. Webb et al., 2002; Cramer, 2013). In this way, the small molecule ATP would participate in the very large-scale process of cell migration.

3.8.5 Outlook on ILK as a pseudokinase

This work not only expands the knowledge of integrin-actin communication and the effect of ILK on FA dynamics, but also beyond that contributes to the understanding of pseudokinase evolution and function. In general, pseudokinases have proven to be useful models to study the non-catalytic properties of the kinase fold in isolation (Jacobsen and Murphy, 2017; Kung and Jura, 2016; Mace and Murphy, 2021). Many pseudokinases, including ILK, have in common that their non-catalytic functions exploit the nature of the kinase fold as a versatile hub for protein-protein interactions. Like ILK, whose functions rely on its substrate-recognition site that now constitutively binds parvin, other pseudokinases also show specifically divergent regions compared to active kinases that correlate with their mechanism of function (Mace and Murphy, 2021).

Conventional kinases are recognized as particularly druggable proteins because small-molecule inhibitors can effectively displace ATP, thereby blocking phosphoryl transfer. This is reflected by the fact that in 2021, over 60 therapeutic agents that target kinases were approved for clinical interventions by the U.S. Food and Drug Administration (Roskoski, 2021). Considering the current landscape of small molecules that can also modulate the non-catalytic functions of pseudokinases, it is not surprising that also pseudokinases are currently under investigation as therapeutic targets (Kung and Jura, 2019; Lucet and Murphy, 2018; Mace and Murphy, 2021; Byrne et al., 2017). ILK's dependence on the active site opens the possibility of modulating its scaffolding functions with small molecule antagonists that might displace ATP, similar to conventional kinases. With knowledge of the ATP-dependent allosteric pathway, one could now use

this molecular information to develop specific chemical probes that target ILK function without greatly disrupting focal adhesion signaling. In fact, efforts have already been made to design tripeptides that mimic an α -parvin segment for therapeutic purposes (Garcia-Marin et al., 2021). Further insights into ILK function thus might culminate in therapeutic implementations to specifically target ILK not as a biochemical kinase, but a non-catalytic mechanotransducer. Concluding, mechanotransducing (pseudo)kinases are uniquely suited to integrate mechanical signals into other signaling pathways, and more members of this intriguing class of proteins likely remain to be determined.

Case Study II: INCENP at the Kinetochores

This chapter first introduces kinetochores as force transduction hubs and describes the function of INCENP within kinetochores. Then it presents the results of MD simulations on two levels of resolution to determine the effect of phosphorylation on INCENP dimensions and conformational ensemble. My simulations on the atomic level are complemented by coarse-grain simulations by Dr. Camilo Aponte-Santamaría (Heidelberg Institute for Theoretical Studies (HITS), Heidelberg) which we mutually analyzed and interpreted. The joint results were published in the *Journal of Molecular Biology (JMB)* in January 2022 (I. M. Martin, Aponte-Santamaría, et al., 2022).

4.1 Background: Keeping genomic integrity

4.1.1 Cell division

Cell division is fundamental for life itself, enabling reproduction and organism growth. With the correct transfer of genetic material to their offspring, cells preserve the integrity of the organism's genome. Within the cell cycle, the genetic material of a cell is duplicated. In the final phase of the cell cycle, the mitotic phase, the replicated genetic content is evenly distributed into two identical daughter cells.

During mitosis, the DNA condenses into chromosomes which align in the center of the cell. There, the chromosomes are bi-oriented by microtubules (MTs) extending from the opposite cell poles, where the mitotic spindle is located. After the chromosomes are correctly aligned, their two identical sister chromatids are detached and pulled to each pole by shortening of the spindle MTs (Kapoor and Compton, 2002; Scholey et al., 2003). With subsequent cell division, each resulting daughter cell shares exactly the same genetic material.

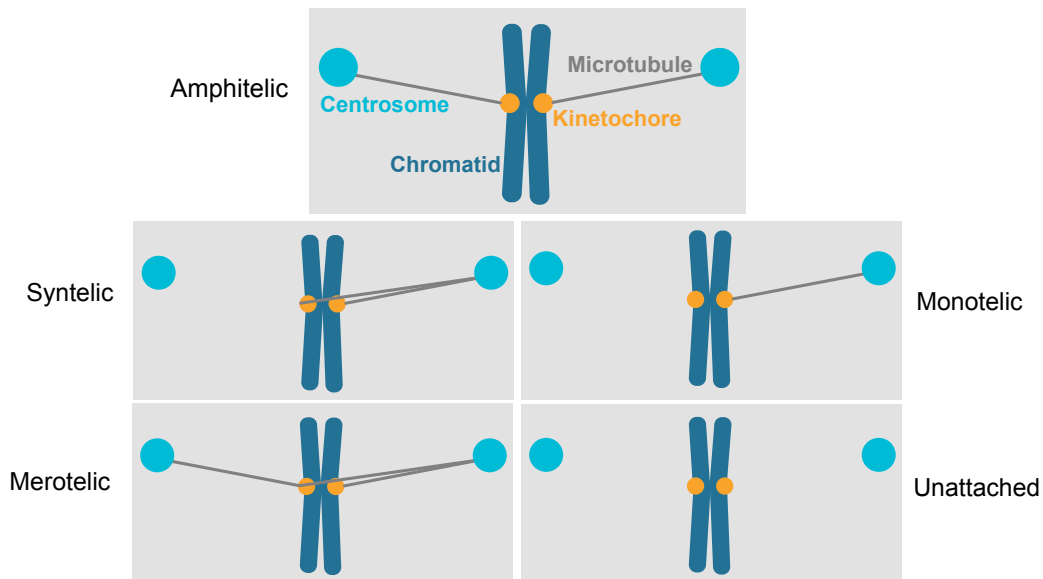


Fig. 4.1.: Correct and incorrect kinetochore-microtubule attachments. Proper bi-orientation of chromosomes is mediated by amphitelic kinetochore-microtubule attachment, in which each of the two sister kinetochores binds microtubules from opposite spindle poles. There are multiple types of incorrect attachment: In syntelic attachment, both sister kinetochores are attached to the same pole, whereas in merotelic attachment, one kinetochore is attached to both poles simultaneously. In addition, incomplete attachments e.g. completely unattached chromosomes or monotelic attachments, in which only one kinetochore is correctly attached, occur frequently. Both incorrect and incomplete attachments have to be resolved before completion of mitosis.

4.1.2 Kinetochore-microtubule attachments

The attachment of sister chromatides to the spindle MTs is established by large protein structures that assemble at the centromeric region of the chromatin, the kinetochores (KTs) (Santaguida and Musacchio, 2009; Cheeseman, 2014). To ensure correct distribution of chromosomes, both sister KT's have to attach to MTs from opposite poles, which is termed amphitelic attachment (Figure 4.1). These correct attachments, which provide chromosome bi-orientation, become stabilized (Nicklas and Koch, 1969; X. Li and Nicklas, 1995). However, chromosomes can also remain (partially) unattached or attached to the wrong spindle poles (Figure 4.1). Such erroneous attachments must eventually be destabilized and corrected before the onset of anaphase of mitosis, during which the chromosomes are pulled apart (Cimini, Moree, et al., 2003; Lampson, Renduchitala, et al., 2004; Nicklas and Koch, 1969).

Correct chromosome bi-orientation and thus segregation is ensured by a combination of the spindle-assembly checkpoint (SAC) and the error correction mechanism (Musacchio and Salmon, 2007; Nicklas and Ward, 1994; Lampson and Grishchuk, 2017). The

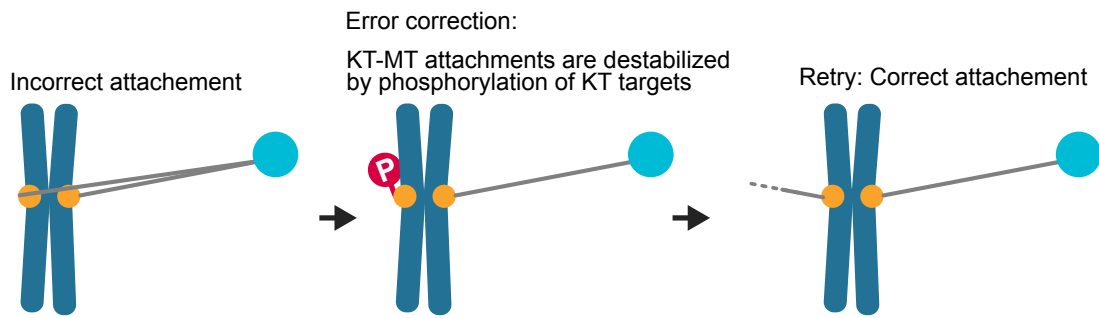


Fig. 4.2.: Mechanism to correct wrongly attached microtubules. Due to lack of tension, incorrectly attached kinetochores are destabilized by phosphorylation of outer kinetochore targets. Newly released kinetochores are provided with a new opportunity to reattach correctly.

SAC prevents mitotic exit on a global level until all chromosomes are properly attached while the error correction mechanism eliminates erroneous attachments to allow for proper attachment. The discrimination between correct and incorrect KT-MT connections depends on mechanical tension within the KT that is generated by successful attachment (Lampson and Cheeseman, 2011; Lampson and Grishchuk, 2017; Nezi and Musacchio, 2009). Apparent from the geometry of the mitotic spindle, amphitelic attachments produce the highest tension on both sister kinetochore, whereas incorrect attachments fail to generate sufficient tension. Missing tension triggers the error correction mechanism to promote attachment turnover by phosphorylation of kinetochore targets (Figure 4.2) (Nicklas, 1997; Lampson and Grishchuk, 2017).

4.1.3 INCENP: Scaffolding the chromosomal passenger complex

Essential to the tension-dependency of KT-MT attachment stability is the Chromosomal Passenger Complex (CPC) localized at the inner centromere (Carmena et al., 2012; Adams, Maiato, et al., 2001; Tanaka et al., 2002). Impaired CPC function leads to defective chromosome segregation due to stabilization of incorrect KT-MT binding and a malformed mitotic spindle (Carmena et al., 2012).

The inner centromere protein (INCENP) (Cooke et al., 1987) is the scaffold of the CPC that connects its chromosome localization module to its kinase module (Figure 4.3). The INCENP N-terminus, the CEN-box, forms a triple-helix bundle with survivin and borealin to anchor the CPC to the inner centromere (Ambrosini et al., 1997; Gassmann et al., 2004; Klein et al., 2006; Jeyaprakash et al., 2007). The C-terminus of INCENP contains the IN-box domain, that binds and allosterically activates the Ser/Thr kinase Aurora B

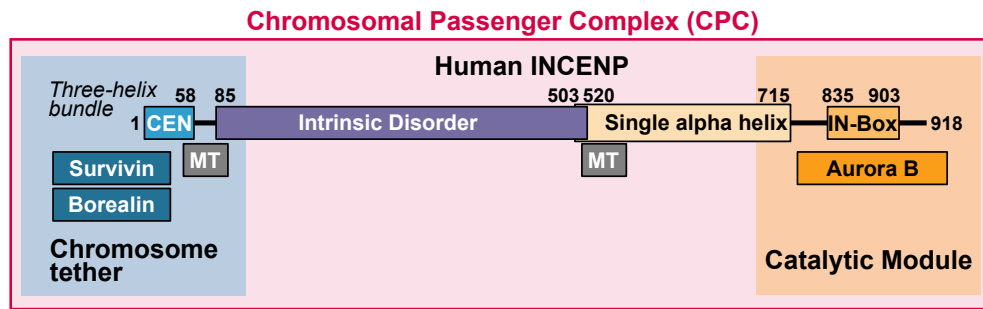


Fig. 4.3.: Architecture of the chromosomal passenger complex. INCENP is the scaffold of the CPC. It forms a three-helix bundle with borealin and survivin to tether the CPC to the chromosomes. Further, it binds and activates the kinase Aurora B, that destabilizes wrongly attached kinetochores. INCENP additionally contains a large unstructured domain, two microtubule binding sites and a single α -helix.

(Kimura et al., 1997; Adams, Wheatley, et al., 2000; Sessa et al., 2005; Honda et al., 2003), which is central to dissolve wrong KT-MT attachments.

Connecting the N- and C-terminal modules is the large middle domain of INCENP. It comprises a large unstructured domain of ~ 440 aminoacids (residue numbers ~ 80 -520) which is flanked on either end by a microtubule-binding site (Sally P. Wheatley et al., 2001; Samejima et al., 2015). Adjacent to the unstructured region is a single α -helix (SAH) between residues 503-715 (Samejima et al., 2015; Wheelock et al., 2017). In contrast to the well-defined roles of the INCENP N- and C-terminus, the function of its middle domains has not yet been fully elucidated. While there are theories about the importance of the SAH (described in subsection 4.1.4), the unstructured linker remains unexplored and its function has yet to be determined.

4.1.4 Mechanism of Aurora B action

Aurora B is the key kinase for regulating the stability of the KT-MT attachments (Cimini, Wan, et al., 2006). By phosphorylating outer kinetochore-associated targets like Ndc80/Hec1 it destabilizes incorrect KT-MT attachments in the absence of tension (DeLuca et al., 2011; Welburn et al., 2010; Yoo et al., 2018; Doodhi et al., 2021; G.-Y. Chen et al., 2021). Phosphorylated Aurora substrates generally display a lower MT binding affinity, thus triggering higher attachment turnover. The phosphorylation potential of Aurora B was found to be inversely proportional to tension within the KTs which led to the spatial separation model for correcting aberrant attachments (D. Liu et al., 2009; Krenn and Musacchio, 2015; Tanaka et al., 2002).

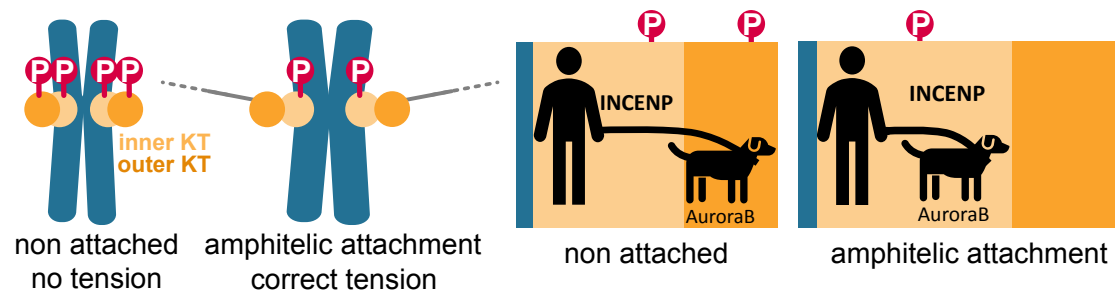


Fig. 4.4.: Dog-leash mechanism of Aurora B regulation. Correct chromosome bi-orientation generates kinetochore tension that separates the outer kinetochore from the centromere. The CPC scaffold INCENP may behave as a length-flexible dog-leash to determine the radius of Aurora B's action, thus regulating KT-MT attachment stability.

Herein, the phosphorylation of Aurora B targets is not controlled by regulation of intrinsic kinase activity but through a tension-dependent, physical separation between the kinase and its substrates. With improper attachment, the lack of tension allows Aurora B to reach the outer kinetochores targets to ultimately release wrongly attached microtubules. In contrast, symmetric tension created by correctly bi-oriented chromosomes moves the sister kinetochores away from the inner centromere. This spatially restricts the accessibility of the outer kinetochore targets from Aurora B, thus decreasing their phosphorylation level. In fact, the phosphorylation potential of Aurora B decreases sharply in the presence of sufficient intra-kinetochore stretch (D. Liu et al., 2009; Krenn and Musacchio, 2015; Welburn et al., 2010).

This mechanism allows to sense tension through the localization of Aurora B relative to outer KT substrates. It requires that Aurora B can extend into the outer kinetochore in the absence of tension, while the CPC itself remains tethered to the centromere. The CPC scaffold INCENP is a prime candidate to enable the spatial flexibility of Aurora B through its large middle domains. Summarized by the "dog-leash" model, it was proposed that the INCENP single α -helix domain could dynamically stretch upon physiological tension (Samejima et al., 2015). In this way, INCENP could act as a dog-leash for Aurora B, restricting or extending Aurora B's radius of action depending on its length (Santaguida and Musacchio, 2009; Samejima et al., 2015; Figure 4.4). The exact length INCENP requires and its fine-tuning through force or additional regulators is still under investigation.

4.1.5 Intrinsically disordered proteins

As predicted from its sequence content, INCENP is one example of a protein partially lacking a fixed tertiary structure, i.e. containing an intrinsically disordered region (IDR)

(Krenn and Musacchio, 2015; Oates et al., 2013). Such proteins which either comprise an IDR or are entirely disordered (intrinsically disordered proteins (IDPs)), are enriched at the kinetochore (Audett and Maresca, 2020).

According to the well-established structure-function paradigm, the function of a protein is tightly coupled to its three-dimensional structure which in turn results from the intrinsic properties of its amino acid sequence (Anfinsen, 1973). Nowadays, however, this requirement of a clearly defined structure for proper function is increasingly being contradicted. In recent decades, it has become apparent that over 40 % of the eukaryotic proteome consists of proteins with disordered regions (Babu, 2016; J. Chen et al., 2020; Bugge et al., 2020; Morris et al., 2021).

Instead of adopting a stable structure, IDPs exist in an ensemble of rapidly alternating conformations of almost equal energy (Fisher and Stultz, 2011). In contrast to the well-defined energy minimum observed for folded proteins, the energy landscape for an IDP is considerably flatter and does not exhibit a deep minimum. Still, the amino acid composition, such as the distribution of charges, determines the accessible states and ultimately dictates whether IDPs adopt predominantly extended or compact conformations (Mao et al., 2010; Das and Pappu, 2013; Müller-Späth et al., 2010; Das, Ruff, et al., 2015). The conformations of IDPs are therefore also particularly sensitive to post-translational modifications like phosphorylation (E. W. Martin, Holehouse, et al., 2016; Jin and Gräter, 2021; Rieloff and Skepö, 2021b). In addition, the environmental context around IDRs, such as flanking domains, influences the conformational ensemble (Bugge et al., 2020).

The function of IDPs depends on the entirety of its conformational ensemble, which cannot be described by traditional high-resolution structure determination methods. Instead, experiments that characterize ensembles like NMR, SAXS or MD simulations are necessary to fully capture the potential of IDPs (Chan-Yao-Chong et al., 2019; Fisher and Stultz, 2011).

4.1.6 Aim of this project

The IDR of INCENP has not yet been characterized but INCENP has been shown to contain numerous phosphorylation sites (Papini et al., 2019; Hornbeck et al., 2015). For example, the phosphorylated threonine and serines (892-894) that form the TSS-motif within the C-terminal IN-box domain activate Aurora B (Honda et al., 2003). Within the IDR, phosphorylation of Thr-59 and Thr-388 mediate recruitment of Plk1 to the kinetochore (Goto et al., 2006) and Ser91-P promotes the direct association of INCENP

with the kinesin-6 motor protein MKLP2 (Petsalaki and Zachos, 2021). However, apart from these few key examples, the function of INCENP's phosphorylation sites especially within the IDR remains largely unknown.

Due to its disordered nature and its multitude of phosphorylation sites, the IDR is also a prime target for dynamic extension in addition to the SAH. Therefore, it is conceivable that the IDR is involved as an additional player in the dog-leash mechanism for collective regulation of Aurora B phosphorylation potential. Altogether, one can propose that the regulatory ability of INCENP within the dog-leash model is directly related to its partially disordered nature. Thus, it is critical to characterize INCENP not just as a rigid scaffold but as a flexible IDP.

In this chapter, I explore the conformational ensemble of the INCENP IDR which is reflective of its average length using MD simulations. Further, I examined how varying degrees of phosphorylation affect the size of INCENP. Simulations of INCENP fragments on the all-atom level are complemented and expanded by simulations of the whole IDR on the coarse-grain (CG) level. The CG-level also allowed to investigate the effects of phosphorylation on the phase behavior of a condensate of INCENP IDRs, reminiscent of the dense environment of the centromere and kinetochore.

4.2 Simulation details

This section describes the detailed protocol of the simulations used for this chapter. I carried out and analyzed the all-atom simulations; the coarse-grained simulations were carried out by Dr. Camilo Aponte-Santamaría (HITS, Heidelberg). We jointly performed the analysis and the interpretation of the CG trajectories.

4.2.1 All-atom simulations

Structure generation

In collaboration with Lisa Schmidt, an intern student I supervised, I divided the sequence of the human INCENP disordered region into fragments of 75 residue length covering the entire IDR sequence (Figure 4.8 A, Table B.1). To generate starting structures for the all-atom MD simulations, I performed de novo structure prediction using the CABS-fold server (Blaszczyk et al., 2013) from which I chose quasi-linear structures without secondary structural elements. All fragments were capped with an ACE (acetyl group) and NME (N-methyl amide) at the N- and C-terminus, respectively using PyMOL (Schrödinger, LLC, 2015).

I simulated either native (n=10) or phosphorylated (n=9) fragments, and the comparison between the two conditions was performed only for fragments simulated in both states. Conversely, separate analysis i.e. the correlation between the charge and the size of the protein considered all simulated fragments. All detected phosphorylation sites on INCENP are summarized in the PhosphoSitePlus database (Hornbeck et al., 2015). I used the number of publications that detect a certain phosphorylation to set different phosphorylation levels (P-levels). In the all-atom simulations, I assumed all phosphorylation sites to be phosphorylated that display a P-level of 10. Accordingly, P-level 10 includes all phosphorylation sites that are evidenced by at least 10 publications. Phosphorylated residues were generated using the PyTMs plugin for PyMOL (Warnecke et al., 2014).

All-atom molecular dynamics simulations

Certain preliminary simulations and equilibrations were performed by Lisa Schmidt, all trajectories used for analysis were generated and evaluated by myself.

I performed all-atom (AA) MD simulations with GROMACS versions 2018.1, 2018.3 and 2020.4 (Abraham et al., 2015). Further, I used the Amber99sb*-ILDNP force-field (Best and Hummer, 2009; Aliev et al., 2014), phosphate parameters (Homeyer et al., 2006) and the TIP4P-D water model (Piana et al., 2015), that was developed for IDPs. I solvated the starting structures in the center of a dodecahedron box with (at least) 3 nm between the periodic images. During the whole simulation the minimal distance of the protein to each periodic image was kept above the cut-off distance of the long-range interactions. Sodium and chloride ions corresponding to a physiological concentration of 100 mM were added resulting in a system with overall zero charge.

The equilibration protocol was as follows: energy minimization using the steepest descent method, 500 ps in the NVT ensemble followed by 500 ps in the NPT ensemble, both with harmonic constraints on all protein atoms with a force constant of $1000 \text{ kJ mol}^{-1} \text{ nm}^{-1}$ to equilibrate water and ions. In the subsequent production runs in the NPT ensemble, only the bonds between hydrogens and protein heavy atoms were constrained using the LINCS algorithm (Hess, 2008) which allowed to use a timestep $\Delta t = 2 \text{ fs}$.

The simulation was kept at a constant temperature (T) of 300 K using the velocity rescaling thermostat (Bussi et al., 2007) with a coupling time of 0.1 ps. I chose two temperature coupling groups: (1) all protein atoms and phosphorylations and (2) all water and ions. The pressure was kept constant at 1 bar using the isotropic Parrinello-Rhman barostat (Parrinello and Rahman, 1981) with a coupling time of 2 ps and a compressibility of $4.5 \times 10^{-5} \text{ bar}^{-1}$. Using the Verlet scheme, the neighbors list was updated every 10 fs. I used a cutoff of 1.0 nm for all non-bonded interactions while treating long-range electrostatic interaction using PME (Darden et al., 1993) with a grid spacing of 0.16 nm with cubic interpolation.

To generate an initial conformations ensemble that is independent of the starting structures, the 75-residue fragments were simulated for 300 ns. I generated six new starting structures from these initial trajectories by extracting the coordinates every 50 ns. Consistently, six individual production trajectories were carried out with random velocities and own equilibration phases as described above. This procedure ensures adequate independence of the production trajectories from the initially generated, nearly linear structures. Additionally, this protocol broadens the conformational ensemble by diversifying the starting configurations. After inspection of the protein backbone RMSD, the first 20 ns of

each production trajectory were neglected as equilibration period. In this way, the total simulation time per fragment and phosphorylation condition is $1.7 \mu\text{s}$.

4.2.2 Coarse-grained simulations

These coarse-grained simulations were set up and run by Dr. Camilo Aponte-Santamaría, HITS, Heidelberg.

Coarse-grained model

Dr. Camilo Aponte-Santamaría carried out coarse-grain (CG) simulations of eleven 75-residue fragments, spanning the disordered region of human INCENP (Table B.1). Moreover, the entire predicted disordered region, ranging from residues 80 to 520 comprising a total of 441 aminoacids, could be simulated at the CG-level. The fragments and whole IDR were simulated either in their non-phosphorylated form or with different levels of phosphorylation. As described for the AA simulations, the phosphorylation levels were based on the number of literature detections according to the PhosphositePlus database (Hornbeck et al., 2015). Here, P-levels 1, 10, 20, 50 and 100 were considered, i.e. any residue mentioned as phosphorylated at least once in the literature was phosphorylated for P level 1. Accordingly, for a residue to be considered phosphorylated in P-level 100, it must have been detected in at least 100 studies.

As described in subsection 2.1.4, a chain of CG beads describes the peptide sequence, with one bead representing one amino acid. The harmonic springs connecting the beads had an elastic constant of 8368 kJ mol^{-1} and an equilibrium distance of 0.38 nm . The short range interaction potential between two beads was calculated according to the Ashbaugh-Hatch functional (Equation 2.10, Ashbaugh and Hatch, 2008). Therein, the strength of the interaction of the Lennard-Jones potential (ϵ , Equation 2.5) was set to $0.8368 \text{ kJ mol}^{-1}$. Parameters for the hydrophobicity (λ) and the size (σ) of standard amino acids were taken from Mammen Regy et al., 2021, whereas for their phosphorylated versions they were taken from Perdikari et al., 2021.

The electrostatic interaction between the beads was described according to the Debye-Hückel potential (Equation 2.11, Debye and Hückel, 1923). Therein, the dielectric constant of the solvent was $\epsilon_r = 80$ and the Debye-Hückel length was $\kappa = 0.974138 \text{ nm}$, which approximately represents 0.1 M ionic strength at 300 K . Charges for unphosphorylated and phosphorylated amino acids were taken from Mammen Regy et al., 2021 and Perdikari et al., 2021. Both, short-range and electrostatic interactions were truncated at a cutoff of 5 nm , i.e. $\sim 5\kappa$.

Replica exchange stochastic molecular dynamics simulations

The fragments were assumed to have an initial fully extended conformation. A cubic box with dimensions 56.24 nm × 56.24 nm × 56.24 nm for the 75-residue fragments and 334.4 nm × 334.4 nm × 334.4 nm for the whole 441-residue fragment was suitable to accommodate the completely linear fragments. Within the NVT ensemble, the size of the simulation box was kept constant. The CG beads were simulated with stochastic molecular dynamics using the leap-frog stochastic dynamics integrator in GROMACS version 2019 (Abraham et al., 2015) with a timestep $\Delta t = 10$ fs. The friction coefficient was computed as the mass of each aminoacid (Mammen Regy et al., 2021; Perdikari et al., 2021) divided by the relaxation time $\tau_t = 1$ ps (Dignon, W. Zheng, Kim, et al., 2018; Mammen Regy et al., 2021). Both short-range and electrostatic interactions were passed to GROMACS as user-defined, tabulated potentials.

To enhance the conformational sampling, Dr. Camilo Aponte-Santamaría used temperature replica-exchange simulations. For the 75-residue fragments, the reference temperatures were 157.26 K, 172.46 K, 189.13 K, 207.41 K, 227.46 K, 249.45 K, 273.56 K, 300.00 K, 329.00 K, 360.80 K, 395.67 K, 433.92 K, 475.86 K, 521.86 K, 572.30 K, and 627.62 K. For the whole 441-residue fragment, the reference temperatures were 154.76 K, 164.36 K, 174.55 K, 185.38 K, 196.87 K, 209.08 K, 222.05 K, 235.82 K, 250.45 K, 265.98 K, 282.48 K, 300.00 K, 318.61 K, 338.37 K, 359.35 K, 381.64 K, 405.31 K, 430.45 K, 457.15 K, 485.50 K, 515.61 K, 547.59 K, 581.55 K, and 617.62 K.

Accordingly, 16 replicas for the 75-residue fragments and 24 for the whole 441-residue IDR at the indicated temperatures ran in parallel, while swapping of coordinates between adjacent replicas was allowed every 1 ns. Each replica was simulated for a total of 2 μ s. The first 500 ns were excluded from the analysis as equilibration period.

Coarse-grained simulations of INCENP condensates

A condensate system of 100 whole IDR fragments in the above described coarse-grain model were simulated in three phosphorylation conditions: not phosphorylated, P-level 50 and P-level 10. The 100 initial conformations were extracted from the single-IDR simulations and subsequently placed in a cubic box with random positions and orientations. The box dimensions were 104.314 nm × 104.314 nm × 104.314 nm for non-phosphorylated, 115.095 nm × 115.095 nm × 115.095 nm for P-level 50 and 121.595 nm × 121.595 nm × 121.595 nm for P-level 10. Within 100000 integration steps ($\Delta t = 10$ fs) the box was shrunken to a target volume of $V = (4/3)\pi r^3 \times N$, where $r = 0.68/2$ nm the typical size of one coarse-grained bead, and $N=44100$ the total number of beads.

The systems starting configuration was defined when the pressure surpassed 1 bar. Using the Berendsen barostat (Berendsen et al., 1984) with a coupling time constant of 5 ps and reference compressibility $4 \times 10^{-5} \text{ bar}^{-1}$, the pressure was kept constant at 1 bar during the stochastic MD simulations as described above. The reference temperatures for the eleven independent simulations of each condition were 265.983 K, 282.48 K, 300 K, 318.607 K, 338.367 K, 359.354 K, 381.641 K, 405.312 K, 430.45 K, 457.147 K, and 485.501 K.

4.2.3 Analysis of simulations and predictions

This section describes the different methods both Dr. Camilo Aponte-Santamaría and I used for the joint analysis of simulation trajectories through GROMACS tools and Python 3+, shell and awk. VMD (visual molecular dynamics) (Humphrey et al., 1996) and PyMOL (Schrödinger, LLC, 2015) were used to visualize the protein structures. Time-averages and standard deviations are given for the results, otherwise the performed statistical analysis is mentioned in the corresponding figure.

Analysis of net charge and κ -value

I used the R-package 'Peptides' (Osorio et al., 2015) to determine the net charge of fragments and the whole IDR at $\text{pH} = 7$ with pKscale 'Lehninger'; one unprotonated phosphorylation contained a charge of -2 . For the coarse-grained fragments, net charge was determined by inspecting the GROMACS topology files. Using the python-package 'localCIDER' (Holehouse et al., 2017) I calculated the κ -value of the fragments.

Radius of gyration

As a measure of the conformational dynamics of the IDR and fragments therein, I calculated the radius of gyration R_g with GROMACS *gmx polystat* tool. For the 75-residue fragments, the R_g was either obtained from all-atom simulations or from the coarse-grained replica at 300 K. The R_g of the whole IDR was calculated at different temperatures.

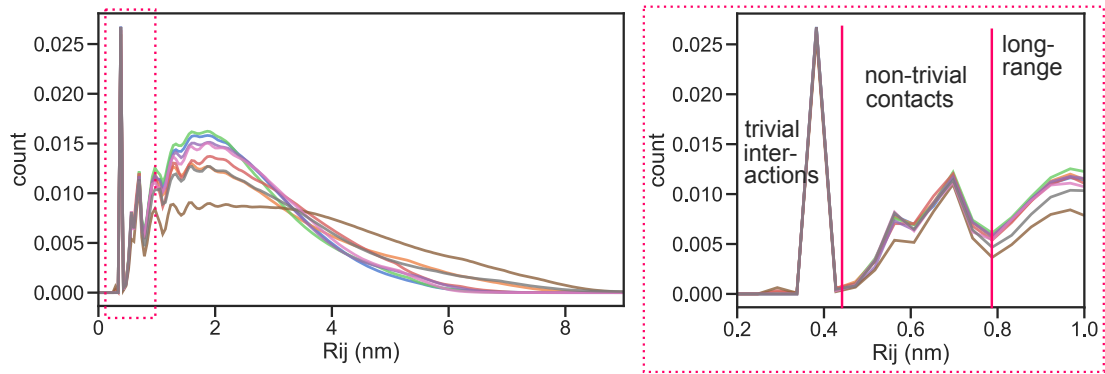


Fig. 4.5.: Visualization of non-trivial contacts. Frequency polygons of R_{ij} in AA simulations of different 75-residue fragments. Inset shows enlargement of the boxed region, red lines indicate the cutoff used to determine NTC (non-trivial contacts).

Inter-residue distances and non-trivial contacts (NTC)

Using all possible residue pairs (i, j) , I calculated the distribution of distances $(P(R_{i,j}))$ between coarse-grain beads for all simulation frames using the *gmx pairdist* tool. In the case of all-atom simulations, I calculated the distance matrix between each possible pair of $C\alpha$ - $C\alpha$ atoms. From these distributions, I computed the fraction of total simulation time two non-adjacent beads or residues are in contact and termed it non-trivial contacts (NTC). This fraction corresponds to the area corresponding to the second major peak of $P(R_{i,j})$ (Figure 4.5). Thus, for the CG simulations, NTC was calculated as the fraction of distances R_{ij} between $0.47 \text{ nm} \leq R_{ij} \leq 0.8 \text{ nm}$. For the AA case, NTC was calculated as the fraction of distances R_{ij} between $0.43 \text{ nm} \leq R_{ij} \leq 0.79 \text{ nm}$, as seen from their respective histograms.

Globule-to-coil transition temperature

The temperature at which an IDP converts from a globular to a coiled conformation is denoted as T_θ (Panagiotopoulos et al., 1998; Dignon, W. Zheng, Best, et al., 2018). At this temperature, the protein behaves like an ideal chain since the repulsive excluded volume interactions cancel the attractive interactions inside the protein (Flory, 1949). T_θ theoretically coincides with the critical temperature for liquid-liquid phase separation (LLPS) at the limit of infinite chain length. This relationship was shown to also be applicable to heteropolymeric, finite-length IDPs (Dignon, W. Zheng, Best, et al., 2018).

For single-chain simulations of IDPs, T_θ can be calculated by exploiting the relationship between R_g , the chain length (N) and the Flory scaling exponent (ν) (Flory, 1949;

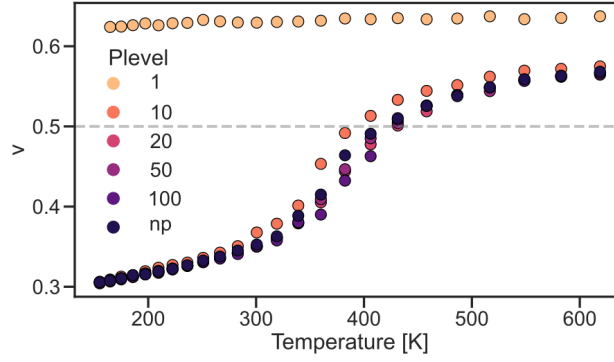


Fig. 4.6.: Scaling exponent of the whole IDR. Scaling exponent (v) of the whole INCENP IDR at different temperatures. Globule-to-coil transition temperature (T_θ) is determined at $v = 0.5$ (dashed line).

Dignon, W. Zheng, Best, et al., 2018): $R_g \propto N^v$. I estimated v (Figure 4.6) for different temperatures as described in (Dignon, W. Zheng, Best, et al., 2018) by fitting to

$$\langle r_{ij} \rangle = b |i - j|^v \quad (4.1)$$

where b is the Kuhn length determined for IDPs to be 0.55 nm, $\langle r_{ij} \rangle$ is the average distance between residues i and j and $|i - j|$ is the chain separation between the i -th and j -th residue. I further determined T_θ by interpolating the temperature at which $v = 0.5$ according to Dignon, W. Zheng, Best, et al., 2018.

Chain cohesiveness

This analysis was performed by Dr. Camilo Aponte-Santamaría.

Insights into the cohesiveness of the chains were gained by fitting the simulation data to the analytical equation of state (Sanchez and Lacombe, 1976; Sanchez and Lacombe, 1978) and solving it for T while taking T^* , \tilde{P} , and V^* as free fitting parameters:

$$\frac{\tilde{P}}{\tilde{T}} = - \left[\ln \left(1 - \frac{1}{\tilde{v}} \right) + \frac{1}{\tilde{v}} \right] - \frac{1}{\tilde{T}\tilde{v}^2} \quad (4.2)$$

where $\tilde{P} = P/P^*$, $\tilde{T} = T/T^*$, and $\tilde{v} = V/V^*$ are the pressure P , temperature T , and volume V reduced by the critical values P^* , T^* , and V^* , respectively. The parameter T^* is related to the overall interaction energy between chains and P^* evaluates the interaction energy of the chains per critical volume V^* .

Phosphorylation prediction

This analysis was performed by Marius Hedtfeld, Adel Iusupov and Andrea Musacchio at Max Planck Institute of Molecular Physiology, Dortmund.

Using the webservers NetPhos 3.1 (Blom et al., 1999) and MusiteDeep (D. Wang et al., 2020), prediction of generic phosphorylation sites was performed, where serine and threonine residues with a score greater than 0.5 were considered as phosphorylated

Additionally, kinase-specific phosphorylation for four different kinases was predicted. For CDK1, NetPhorest 2.1 (Horn et al., 2014) and Group-based Prediction System (GPS) 5.0 (C. Wang et al., 2020) with thresholds of 0.1 and 5.354, respectively, were used. MPS1 (threshold 19.314), PLK1 (threshold 12.239), and Aurora B (threshold 0.015) dependent phosphorylations were predicted using GPS. All kinases are located in the serine/threonine kinase tree of the GPS 5.0 server and were selected according to the following paths: CDK1: CMGC/CDK/CDC2; MPS1: Other/TTK; PLK1: Other/PLK/PLK1 and Aurora B: Other/Aur/AurB. The threshold for the GPS 5.0 is based on the theoretically maximal false positive rate of 6 %. Aurora B phosphosite predictions were further validated using Prediction of PK-specific phosphorylation site (PPSP; threshold 3.2) (Xue et al., 2006).

4.3 Charge distribution of INCENP IDR is altered by phosphorylation

To characterize the disordered segment of INCENP, I first further corroborated the assumed disordered nature of this region by combining several webservers that predict disorder (Figure B.1). Further, I set out to characterize the effect of phosphorylation on the INCENP IDR from sequence-based calculations. Given the lack of determination of a physiological phosphorylation pattern on INCENP, particularly in different phases of the cell cycle, I categorized the reported phosphorylation sites from the PhosphoSitePlus database (Hornbeck et al., 2015) into different phosphorylation levels (P-levels) (Figure 4.7 A; Table B.2). These P-levels are based on the number of studies, mostly high-throughput studies, in which a particular residue was detected to be phosphorylated. Following previous work (H. Li et al., 2017; Mattè et al., 2021), I assumed that a residue frequently detected in high-throughput studies is more likely to be a functional phosphorylation site across many cellular conditions and cell cycle phases. Accordingly, with the weakest P-level 100, I considered all phosphorylation sites that were detected at least 100 times, thus only leaving a few residues phosphorylated. Consequently, the most extreme P-level 1 includes every phosphorylation site mentioned in at least one study which produces a highly negatively charged IDR. Indeed, especially the higher P-levels are consistent with bioinformatic phosphorylation predictions based on the INCENP sequence by Adel Iusupov, Marius Hedtfeld and Andrea Mussachio (MPI of Molecular Physiology, Dortmund) (Table B.3). Generally, 35 out of 78 sites in P-level 1 were predicted to be phosphorylated by any of the kinases CDK1, PLK1, MPS1, or Aurora B. Further, 47 out of 78 P-sites were predicted to be unspecifically phosphorylated. Importantly, all sites considered with P-level 20 and above, including numerous sites below P-level 20, are predicted to be phosphorylated by both specific and nonspecific kinases based on consensus motifs (Figure B.2).

I calculated the charge distribution of the INCENP IDR for sliding windows matching the achievable fragment lengths from all-atom (AA) MD simulations. Additionally, I probed the change in charge distribution upon introducing phosphorylations corresponding to the P-levels define above (Figure 4.7 B). The unphosphorylated INCENP IDR shows four differentially charged regions: (1) the N-terminal region from residues 50 to 100, which also corresponds to a microtubule binding site, is highly positively charged, (2) the C-terminal region from residues 420 to 550 also carries a high positive charge, (3) from residues 300 to 420 the IDR is highly negatively charged and (4) the middle segment of IDR from residues 100 to 300 is mostly neutral. Upon phosphorylation, the charge distribution naturally shifts toward negative, since each phosphorylation in the

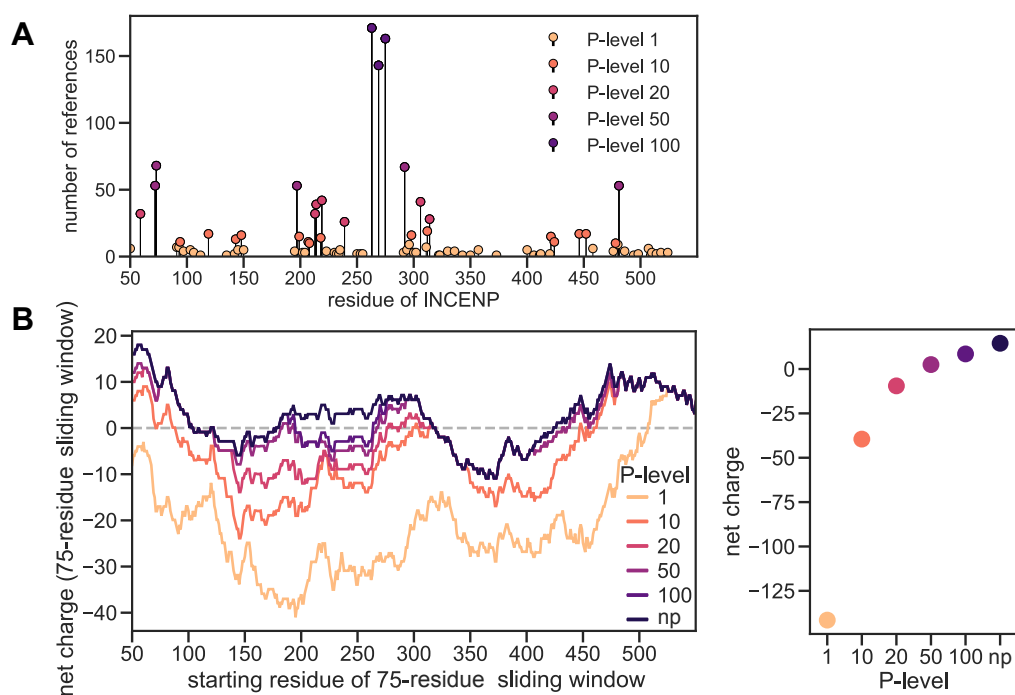


Fig. 4.7.: Sequence properties of INCENP (A) Phosphorylation sites within the INCENP IDR detected from low- and mostly high-throughput studies (Hornbeck et al., 2015). Colors represent the minimal P-level based on the number of studies detecting a phosphorylation site. (B) Charge distribution of the INCENP IDR along the aminoacid sequence using 75-residue sliding windows (left) or the whole disordered region (residues 80-520, right). The charge corresponds to the fragment starting with the indicated residue. Charge variations due to phosphorylations corresponds to the P-levels described in A (np: non-phosphorylated).

unprotonated state introduces two net negative charges. Herewith, phosphorylations across all P-levels most drastically affect the neutral middle region. While the global charge maxima for most P-levels remain at the N- and C-terminal regions, the charge minimum shifts from residues around 360 to residues around 150. The whole IDR displays its most neutral charge at P-level 50, while it is massively negatively charged at P-level 1 due to the introduction of a total of 78 phosphorylations. As evident from the fact that the dimensions of an IDP are greatly influenced by its net charge and charge distribution (Mao et al., 2010; Jin and Gräter, 2021; Rieloff and Skepö, 2021b; Bugge et al., 2020; Das and Pappu, 2013) it can be predicted that the phosphorylation-induced shifts in charge distribution will affect the IDR expansion both locally and globally. To accurately determine the size and explore its changes due to phosphorylation, I chose to perform MD simulations on the all-atom level, described in the next section.

4.4 Conformational ensemble of 75-residue fragments

Using all-atom (AA) MD simulations, I simulated fragments spanning the entire INCENP-IDR (Table B.1, Figure 4.8 A). The length of the fragments was set to 75 residues to balance computational feasibility with local information content on conformational dynamics. Their location was manually chosen by myself and Lisa Schmidt, an intern student I supervised, to provide overlap between fragments on the one hand and to include interesting features related to the net charge and phosphorylation pattern on the other hand. Also due to the computational limits of all-atom simulations, I could only investigate the fragments in the non-phosphorylated (np) form and in one phosphorylated condition. For this purpose, I chose P-level 10, where each residue is sufficiently demonstrated to be phosphorylated, but still allows each fragment to contain at least one phosphorylated residue.

I determined the collapse propensity of the fragments by calculating the radius of gyration (R_g). Across fragments and phosphorylation condition the R_g varies from 1.5 nm to 3 nm (Figure 4.8 B). For certain fragments like 121-195 and 453-527, phosphorylation

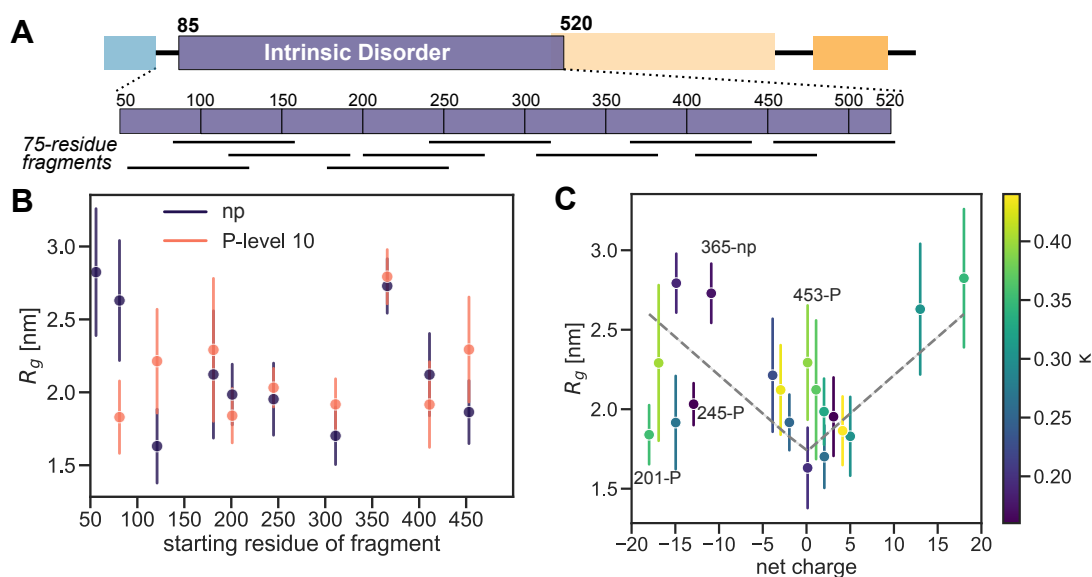


Fig. 4.8.: Properties of the INCENP IDR in all-atom MD simulations. (A) Scheme of INCENP with enlarged IDR. Dashes represent the 75-residue fragments simulated in all-atom MD simulations. *The fragments were selected jointly by myself and Lisa Schmidt.* (B) R_g of 75-residue fragments in non-phosphorylated (np; $n=10$) and a moderately-high phosphorylation state (P-level 10, $n=9$). (C) Correlation of R_g with the net charge of the fragments. Colors indicate the charge patterning parameter κ (Das and Pappu, 2013). Dashed line highlights the V-shaped dependency predicted in previous all-atom simulations of IDPs (Jin and Gräter, 2021), here adjusted to 75-residue fragments ($r_g = a + b|q|$, with $a = 1.73$ nm and $b = 0.048$ nm/e).

increases their R_g while for others like 81-155 phosphorylation leads to a decrease in R_g . Many fragments, however, do not dramatically change in R_g upon phosphorylation. Regarding the global fragment properties, highly charged fragments, either positive like 56-130 or negative like 365-440, generally show higher R_g than the more neutral ones (Figure 4.8 B). This observation is consistent with previous studies that demonstrated that sequences with higher net charge exhibit a higher R_g (Jin and Gräter, 2021; Perdikari et al., 2021; E. W. Martin, Holehouse, et al., 2016; Dignon, W. Zheng, Kim, et al., 2018). Thus, the collapse propensity depends on the net charge and follows a V-shape (Jin and Gräter, 2021). This observation is corroborated by the fact that my data on various fragments accommodates well around that prediction (Figure 4.8 B).

Interestingly, not all fragments follow the V-shape and show a lower or higher R_g than expected. Apart from the net charge, also the local charge patterning, described by the patterning parameter κ (Das and Pappu, 2013), can influence the extension of IDPs. Even with equal net charge, IDPs with well-mixed charges (low κ) display a more extended conformation while IDPs which exhibit local charge compensation (high κ) are generally more collapsed. However, the deviation from the V-shape in some fragments cannot be unambiguously explained by their κ . For example, although the fragments 365-440 and the phosphorylated version of 245-319 exhibit a comparable κ , their R_g is considerably different. Therefore, I suspected that additional internal contacts which cannot be fully described by the charge patterning influence the average size.

Therefore, I quantified the residue-residue contacts within one fragment and correlated them to changes in R_g . As a measure of intra-fragment contacts, I calculated the probability that two non-adjacent residues come into contact and termed it NTC (subsubsection 4.2.3). Across all fragments and phosphorylation conditions, R_g negatively correlates with the NTC (Figure 4.9 A), confirming that naturally more extended fragments display less intra-fragment contacts. To pinpoint the effect of phosphorylation on the internal contacts, I calculated the changes in R_g and NTC upon phosphorylation (Figure 4.9 B). Still, negative correlation between ΔR_g and ΔNTC is maintained and most fragments show no changes in either R_g or NTC upon phosphorylation. However, interestingly, for some cases phosphorylation either leads to an increase in R_g accompanied by a reduction in NTC (for example 121-195) or to a lowered R_g with increased contacts (for example 81-155).

However, the presented global NTC only measures the average contacts within a fragment. I was therefore interested in the contacts at the residue-level and their changes due to phosphorylation, as these may contribute to explaining the observed changes in R_g . I visualized those contact differences between the phosphorylation-altered residues as contact maps (Figure 4.10, Figure B.3). For the fragment 81-155, which upon phos-

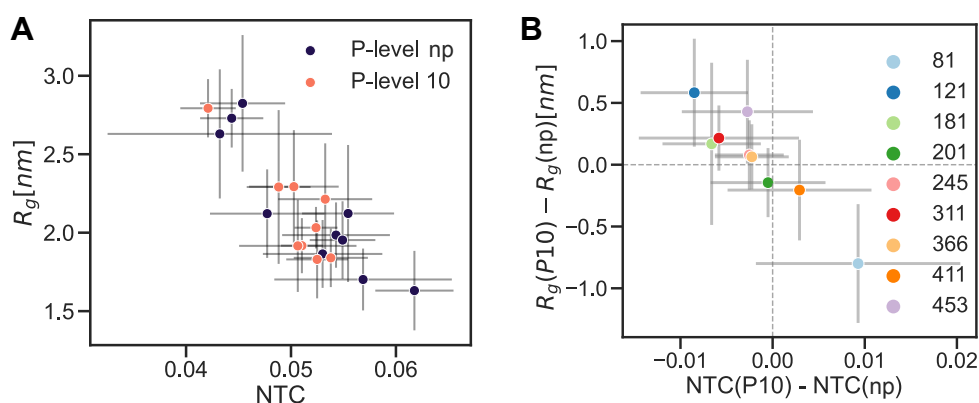


Fig. 4.9.: Contacts within the INCENP IDR fragments. (A) Correlation between non-trivial contacts (NTC) and R_g of INCENP IDR fragments in all-atom simulations. Average \pm standard deviation of six independent simulations; also for B. np: non-phosphorylated. (B) Difference in NTC between phosphorylated and non-phosphorylated states versus difference in R_g between phosphorylated and non-phosphorylated states. Color indicates the fragment's starting residue.

phorylation decreases in size and increases its internal contacts, I explored which specific contacts may lead to the compaction (Figure 4.10 A). I identified a small cluster of phosphorylation-induced contacts between residues 143-146, including the phosphoserine S143-P, and residues 114-115. This increased interaction manifests itself in the formation of a loop, that presumably compacts the fragment. For the fragment 201-275, which appears more compact in its phosphorylated state than its charge and moderate κ -value suggest (see Figure 4.8 C), I examined which contacts could be responsible for the apparent compaction. Residues 232-239, including the phosphothreonine T239-P, increases in contacts to residues 254-259, which again promotes loop formation (Figure 4.10 B). On the contrary, the phosphorylated fragment 453-527 is especially interesting since its R_g is higher than expected from its charge, displaying a decreased NTC and increased R_g upon phosphorylation. On the residue-level, this behaviour might be explained by many reduced contacts that appear to be rather a result of global conformational shifts introduced through phosphorylation (Figure 4.10 C).

In summary, my all-atom simulations identified the size of INCENP IDR fragments and the effect of phosphorylation on them on a local level. Their R_g 's generally follow a linear, V-shaped dependency on the net charge, with deviations due to the formation of non-adjacent residue-residue contacts upon phosphorylation. While the AA simulations provide an accurate description of IDRs, their computational cost dictated the use of only fragments of the whole \sim 440-residue IDR in one phosphorylation condition. These limitations can be overcome by reducing the resolution in the simulations. To accomplish this, I collaborated with Dr. Camilo Aponte-Santamaría (HITS, Heidelberg),

who adopted a previously proposed coarse-grain (CG) description of the fragments, whose establishment and validation is detailed in the next section.

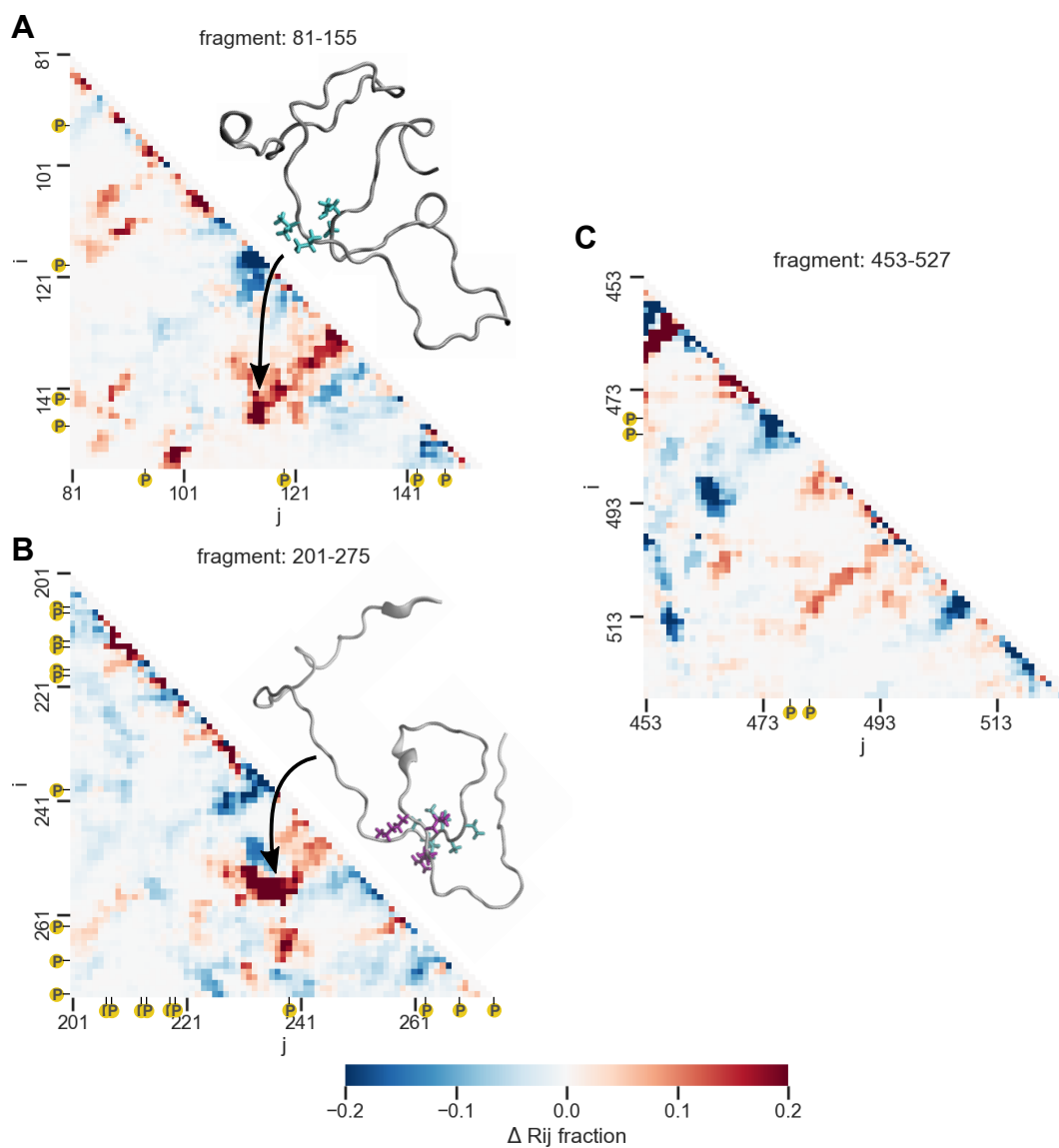


Fig. 4.10.: Intra-fragment contacts upon phosphorylation. (A-C) Differences in contact fractions for each residue pair i, j between phosphorylated and non-phosphorylated states for selected fragments (remaining fragments in Figure B.3). Blue and red depict reduced and increased contact probability in the phosphorylated state compared to non-phosphorylated. Cartoons highlight contacts that formed upon phosphorylation between the residues depicted as sticks, corresponding to the red patches in the contact maps. Position of phosphorylations indicated in yellow.

4.5 Establishment of a coarse-grain framework for INCENP

Simulations of this subsection were executed and analyzed by Dr. Camilo Aponte-Santamaría (HITS, Heidelberg). Text is adapted from our joint publication (I. M. Martin, Aponte-Santamaría, et al., 2022).

Within the coarse-grain description, that has already been proven suitable for IDPs, each amino acid is represented as one CG-bead that interact based on their HydroPathy Scale (Dignon, W. Zheng, Kim, et al., 2018; Mammen Regy et al., 2021) (subsection 4.2.2, subsection 2.1.4). The degree of correlation between radii of gyration recovered from GC and AA simulations is consistent with that obtained for such GC models compared to experiments (Figure 4.11 A, Dignon, W. Zheng, Kim, et al., 2018). In contrast to the AA simulations, the CG description allowed the investigation of more than one phosphorylation level. Therefore, Dr. Camilo Aponte-Santamaría simulated all fragments in the five different P-levels and found each fragment following a similar trend as observed from the AA simulations with P-level 10. Here, stronger phosphorylation i.e. P-level 1, generally leads to greater fragment expansion, while low phosphorylation i.e. P-level 100 or 50, can lead to fragment compaction, especially for the positively charged

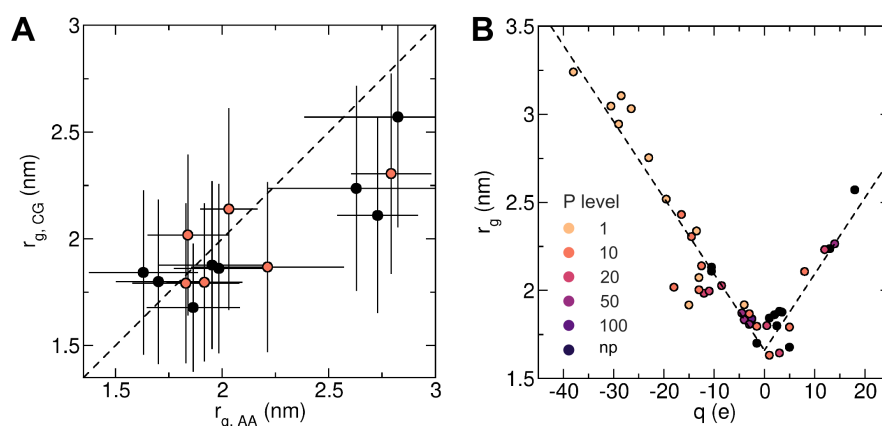


Fig. 4.11.: Coarse-grained description of INCENP intrinsically-disordered fragments. Simulations and content of the Figure provided by Dr. Camilo Aponte-Santamaría (HITS, Heidelberg). (A) R_g from CG simulations ($R_{g,CG}$) versus that from AA simulations ($R_{g,AA}$) for 75-residue fragments in non-phosphorylated (black) and phosphorylated (P-level 10, red) states. Average \pm standard deviation is shown. Correlation coefficient = 0.839. Dashed line indicates perfect correlation. (B) R_g as a function of the fragment's net charge. For clarity, only averages are shown. Dashed line depicts linear regression to the data, $r_g = a + b|q|$, with $a = 1.66$ nm and $b = 0.0433$ nm/e (correlation coefficient = 0.948) which is in good agreement with previous studies ($a = 1.73$ nm and $b = 0.048$ nm/e; Jin and Gräter, 2021). np: non-phosphorylated.

fragments (Figure B.4). However, and as also evident from the slope < 1 in Figure 4.11 A, the IDR ensemble in the CG model is slightly less responsive to phosphorylation than in the all-atom case.

Thus, Dr. Camilo Aponte-Santamaría next investigated whether the fragments in the CG description follow the same V-shaped, collapse propensity along the net charges. Indeed, across all fragments and all phosphorylation conditions, the R_g correlated well with the fragment's net charge (Figure 4.11 B). Again, this is in good agreement with the dependence previously found in all-atom simulations for other IDPs at a similar ionic strength (Jin and Gräter, 2021). As such, the simulations of the 75-residue fragments on the CG-level can replicate the probed behavior of the AA simulations reasonably well. The CG-framework therefore permits to explore the conformational dynamics of the whole disordered segment of INCENP in several phosphorylated states.

4.6 Phosphorylation-induced conformational dynamics of whole INCENP IDR

Simulations of this subsection were executed by Dr. Camilo Aponte-Santamaría (HITS, Heidelberg). If not stated otherwise, the analysis was carried out by myself.

From trajectories of the whole IDR (residues 80-520) in the above described CG-framework from Dr. Camilo Aponte-Santamaría, I determined the average R_g of the IDR at different phosphorylation levels and across different temperatures (Figure 4.12 A). Apart from the most extreme phosphorylation, all conditions lead to an S-shaped distribution of the R_g across temperatures, indicative of a critical conformational transition. The low to moderately phosphorylated states, P-levels 100, 50 and 20, cannot be distinguished from the non-phosphorylated state, whereas at P-level 10 and for temperatures above 300 K the R_g increases slightly compared to non-phosphorylated. In contrast, maximal phosphorylation (P-level 1) leads to a substantial increase in R_g which does not follow the S-shape. Naturally, the fraction of non-trivial contacts decreases with increasing temperature. In this way, the behavior of the NTC also hints towards a global transition behavior since the steepness of the NTC decrease flattens above 400 K for all phosphorylation conditions except the extreme phosphorylation. In resemblance of the R_g , the low to moderate phosphorylations are indistinguishable from the non-phosphorylated condition while P-level 10 behaves slightly differently. Especially at temperatures below 500 K, P-level 10 (i.e. phosphorylation of 27 sites) leads to a small decrease in contacts compared to non-phosphorylated. However, upon phosphorylation of 78 sites (P-level 1)

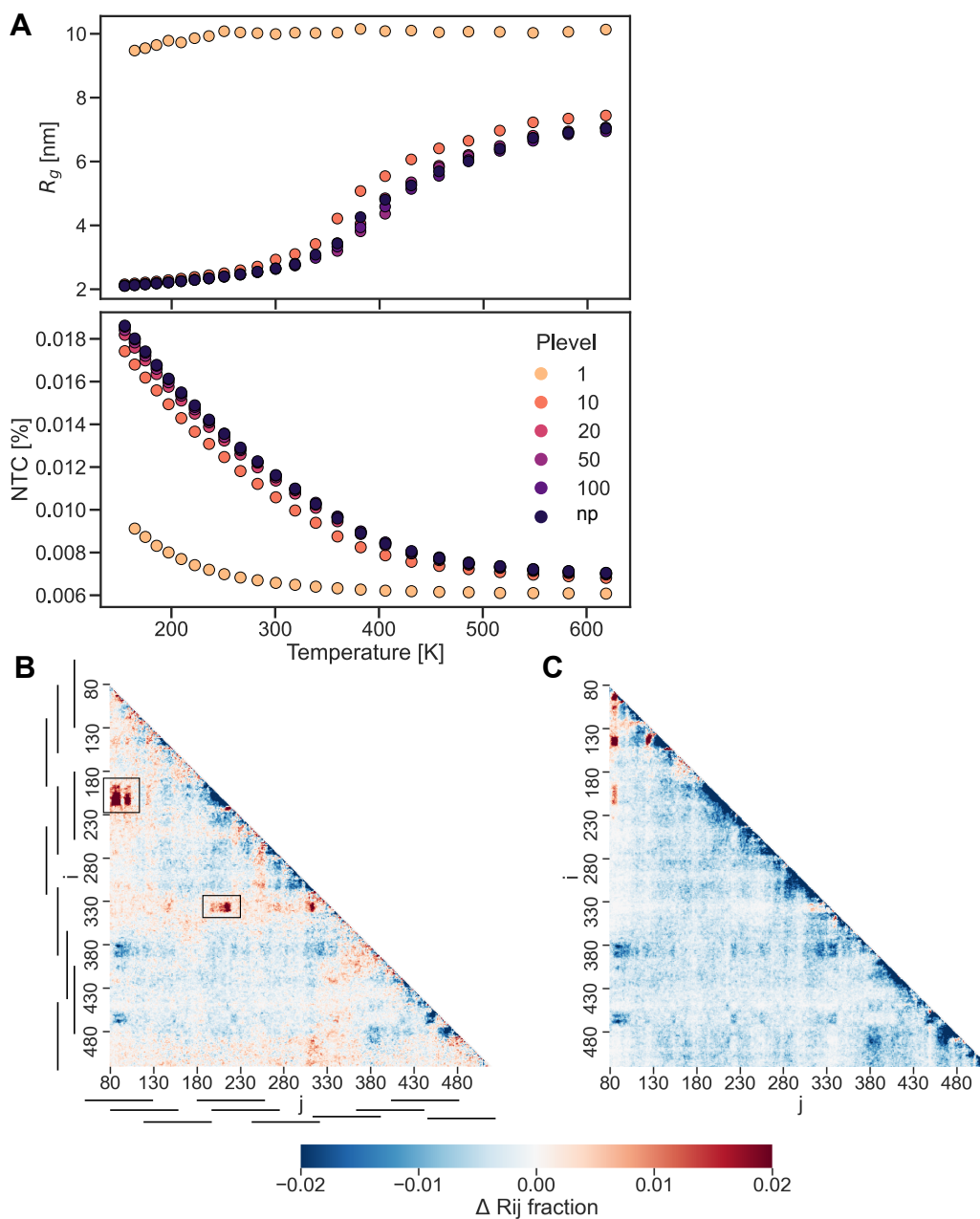


Fig. 4.12.: Phosphorylation influences the conformation of the whole INCENP IDR. (A) Temperature dependence of the mean R_g (top) and the fraction of non-trivial contacts (NTC) (bottom) of the whole 441-residue-long IDR at different P-levels; np: non-phosphorylated. (B/C) Difference in the fraction of contacts between phosphorylated and non-phosphorylated states for each residue pair i, j at 300 K. Red: increased contacts upon phosphorylation, blue: decreased contacts upon phosphorylation. (B) Phosphorylation at P-level 10. Black bars indicate the positions of the 75-residue fragments simulated at the AA-level. (C) Phosphorylation at P-level 1. (Contact maps for remaining P-levels are shown in Figure B.6.)

the IDR exhibits greatly reduced contacts compared to unphosphorylated across all temperatures.

Another advantage of investigating the entire IDR is that one can observe the long-range contacts at physiological temperature that extend beyond the 75-residue fragments i.e. would represent inter-fragment contacts. In general, the unphosphorylated IDR shows no internal secondary structure, as apparent from the missing stable residue-residue contacts within the contact maps (Figure B.5). This provides further evidence of the disordered nature of this segment. Upon phosphorylation at P-level 10, many transient intra-chain contacts are reduced compared to the non-phosphorylated case (Figure 4.12 B), reflecting the decrease in global NTC associated with the increase in R_g . In addition, the introduction of phosphorylated residues leads to selectively enhanced contacts. Within the whole IDR, these include the highly phosphorylated residue patch 205-220 which contacts residues 82-92, 97-102 and 330-346 (black boxes in Figure B.5 B). Such long-range contacts would correspond to interactions between the individually simulated, short fragments. In stark contrast, the drastically reduced contacts throughout the IDR upon extreme phosphorylation (P-level 1; Figure 4.12 C) are consistent with its enormous R_g and very low NTC.

Since the conformational dynamics of the single chains critically depend on temperature, I suggested that at this point the IDR transitions from a compact globular state to expanded coil states. This temperature at which the thermal fluctuations balance the intramolecular interactions and a sequence hence abruptly switches from compact to extended conformations is referred to as the globule-to-coil transition temperature, T_θ (Flory, 1949; Dignon, W. Zheng, Best, et al., 2018 ; subsection 4.2.3). Indeed, the T_θ I calculated for the IDR coincides with the inflection point of the R_g distribution over temperature and the temperature of regime change in NTC (Figure 4.13 A, compare to Figure 4.12 A; Table 4.1). Interestingly, introduction of phosphorylation affected T_θ in a

P-level	# P-sites	$T_\theta \pm s.d.$ [K]
1	78	NA
10	27	391(24)
20	12	432(24)
50	6	438(19)
100	3	436(28)
np	0	422(30)

Tab. 4.1.: Globule-to-coil transition temperature (T_θ) for the whole INCENP IDR calculated from CG simulations as described in (Dignon, W. Zheng, Best, et al., 2018, subsection 4.2.3). P-levels correspond to different numbers of phosphorylated residues (# P-sites). np: non-phosphorylated

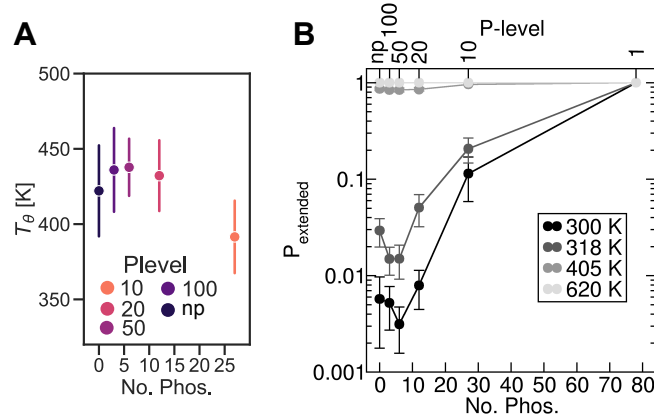


Fig. 4.13.: Globule-to-coil transition upon phosphorylation. (A) Temperature of globule-to-coil transition (T_θ) for different phosphorylation levels corresponding to different amounts of phosphorylated residues; np: non-phosphorylated. (Averages \pm s.d. from block averages.) (B) Probability to adopt an extended conformation, ($P_{\text{extended}} = P(R_g > \text{median})$) depending on the number of phosphorylated sites (No. Phos) which relates to each P-level. The median of R_g was obtained from the R_g probability distribution of all temperatures and P-levels as 3.29 nm (Figure B.7). The probability is shown for 4 temperatures, two near room temperature (300 K and 318 K), one at the transition temperature (405 K), and one well above the transition temperature (620 K). *The sub-panel B was provided by Dr. Camilo Aponte-Santamaría.*

non-monotonic manner. Upon phosphorylation of 27 residues (P-level 10), I observed the lowest T_θ . However, the highest T_θ is not obtained for the non-phosphorylated condition, but with low phosphorylation (six phosphorylation sites, P-level 50), which corresponds exactly to the most neutral fragment (Figure 4.7 B). Since the maximally phosphorylated and thus highly negatively charged IDR apparently does not collapse from the extended state, its transition temperature cannot be determined. I can therefore only provide an upper limit of 200 K for the globule-to-coil transition temperature of the fully phosphorylated IDR.

Given the effect of phosphorylation on the conformational dynamics of the IDR, I was intrigued by the minimal number of phosphorylation sites required to elicit the conformational transition. The distribution of R_g across all temperatures and P-levels shows a bimodal distribution, where the globular state ($R_g \sim 2$ nm) is separated from extended conformation ($R_g > 4$ nm) by the median R_g (3.29 nm; Figure B.7). Dr. Camilo Aponte-Santamaría used this criterion to calculate the probability that the IDR adopted an extended conformation (Figure 4.13 B). Here, the most neutral case i.e. P-level 50 exhibits the lowest probability of being extended, thus corroborating its highest globule-to-coil transition temperature. Interestingly, however, this analysis shows that even below the critical transition temperature, segments with moderate levels of phosphorylation exhibit a non-negligible probability to be found in the extended conformation. Accord-

ingly, at or near room temperature, 12 to 27 phosphorylation sites are sufficient to trigger extension with probabilities larger than 5%. Corroboratively, mildly phosphorylated sequences are consistently found in the extended state at temperatures above the transition temperature, whereas the maximally phosphorylated case is extended across all temperatures.

Knowing that even small amounts of phosphorylation enables the IDR to populate extended states, I visualized their explored conformational space in terms of R_g and NTC

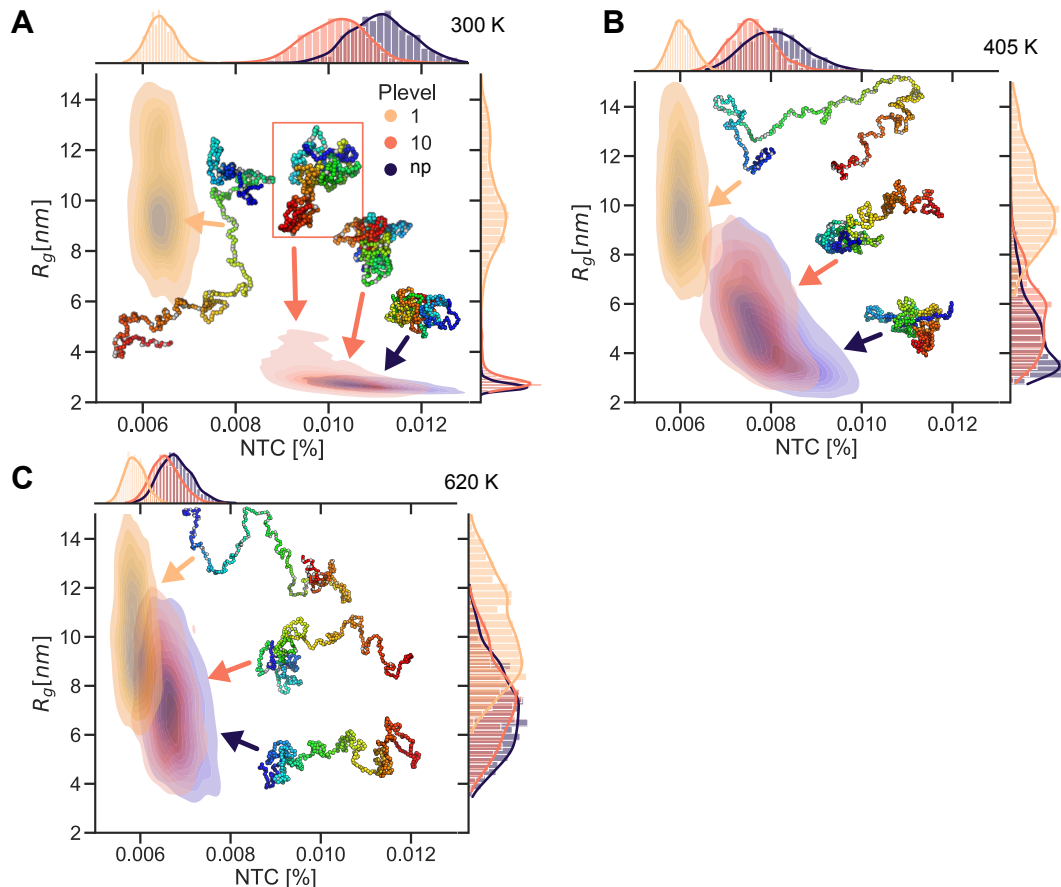


Fig. 4.14.: Conformational space of the whole INCENP IDR upon phosphorylation. (A-C) R_g as a function of NTC distributions at 300 K (A), around the globule-to-coil transition temperature 405 K (B) and at 620 K (C) for the non-phosphorylated fragment (blue), and for the phosphorylated fragment with P-levels 10 (red) and 1 (orange). Histograms of R_g and NTC are shown at the top and right side, respectively, of each panel. Structures of whole IDR at the indicated positions of the distributions are illustrated (each sphere represents one residue colored according to the sequence from N-terminus (blue) to C-terminus (red) and phosphorylation sites (grey)). Structures show the highest populated cluster of each distribution, while the additional structure of P-level 10 at 300 K depicts the behavior of the left distribution edge (red box); np: non-phosphorylated.

(Figure 4.14). At 300 K, the non-phosphorylated state, as well as the one containing 27 phosphorylated residues (P-level 10) display a horizontal distribution, in which the IDRs remain compact over a wide range of NTC. However, the phosphorylated ensemble additionally includes a moderately populated region of higher R_g and lowered contacts, where the IDR forms a bilobed structure, slightly increasing the average R_g (Figure 4.14 A, boxed region). This is in stark contrast to the vertical distribution observed for the maximally phosphorylated IDR, which contains 78 phosphorylated residues. Here, the extended states are characterized by an R_g from 6 nm to 14 nm over a relatively narrow range of low contacts, which is maintained across all temperatures. Conversely, the distributions of the non-phosphorylated and P-level 10 states show a drastic temperature dependency, which is manifested around T_θ (405 K) by an L-shaped distribution. Here, the fragments non-linearly transition into the regime of high R_g and low NTC. Meanwhile, the non- and moderately phosphorylated states have transitioned to extended coil structures at the highest temperature (620 K). Their approximately vertical distributions resemble the fully phosphorylated case, although still at lower R_g .

Finally, after examining the sequences purely on the level of R_g and contacts, I aimed to quantify the length of the segments in different conditions. Especially for very extended states, the R_g as a measure of compactness does not convey a meaningful length. Thus, I related the R_g to the fragment's end-to-end distance (d_{ee}) (Figure 4.15) and observed that at room temperature, the non- to moderately phosphorylated IDRs reach a maximum end-to-end distance of 10 nm. The maximally phosphorylated segment, on the other hand, can reach distances between 10 nm and 40 nm regardless of temperature. In the non- and moderately phosphorylated cases, the critical globule-to-coil transition becomes apparent as increasing temperature also allows for longer extensions.

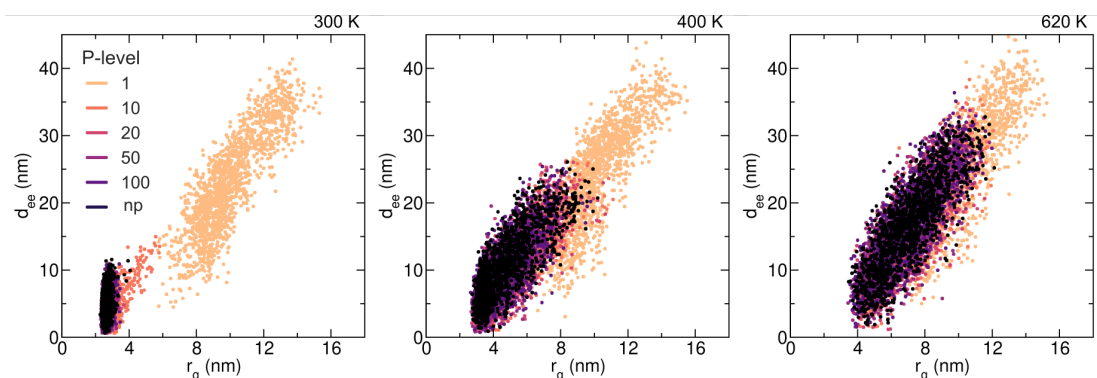


Fig. 4.15.: Correlation between radius of gyration and end-to-end distance. Correlation between R_g and end-to-end distance (d_{ee}) of the whole IDR at different phosphorylation levels (np: non-phosphorylated) for temperatures 300 K, 400 K and 620 K. This figure was generated by Dr. Camilo Aponte-Santamaría. Data was jointly analyzed.

In summary, the IDR of INCENP undergoes critical globule-to-coil transition and phosphorylation influences the transition behavior and temperature. Within, the highest tendency to stay collapsed on a global level is maintained for the most neutral segment i.e. with mild phosphorylation.

4.7 Cohesion of INCENP IDR condensates

Simulations of this subsection were executed and analyzed by Dr. Camilo Aponte-Santamaría (HITS, Heidelberg). Text is adapted from our joint publication (I. M. Martin, Aponte-Santamaría, et al., 2022).

So far, the simulations described above have only focused on single chains, yet the environment at the kinetochore is believed to be dense and crowded. Thus, INCENP would likely encounter multiple copies of itself, which would particularly influence its critical globule-to-coil transition associated with its phase separation properties (Dignon, W. Zheng, Best, et al., 2018). To explore the implications of multiple INCENP chains, I collaborated with Dr. Camilo Aponte-Santamaría, who simulated the packing properties of a condensate of 100 IDR segments. Across different phosphorylation conditions, the IDR condensates display volumes well above the closed packing condition

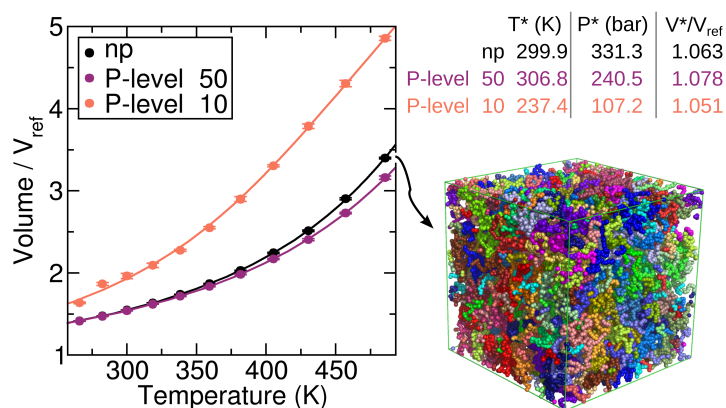


Fig. 4.16.: Coarse-grained simulations of a condensate of whole INCENP IDR chains. Simulations and content of the figure provided by Dr. Camilo Aponte-Santamaría (HITS, Heidelberg). Volume-temperature curves for systems containing 100 INCENP IDR chains with three phosphorylation conditions (np: non-phosphorylated; average \pm s.d.). $V_{\text{ref}} = (3\sqrt{2}/\pi)N(4/3)\pi r^3$, with $N = 44100$, the total number of beads, and $r = 0.6/2$ nm, the typical size of one coarse-grained bead. Lines denote a fit using equation of state (Equation 4.2) from the Sanchez-Lacombe model (Sanchez and Lacombe, 1976; Sanchez and Lacombe, 1978) with fitting parameters T^* , P/P^* , and V^* listed (top right). Bottom right: Simulation snapshot for the indicated data point with each chain in a different color.

(Figure 4.16). Interestingly, both mild and moderate phosphorylations modify the volume as a function of temperatures compared to the non-phosphorylated condition. Phosphorylation of 27 residues per chain (P-level 10) induces a strong volume increase which is expected for condensates containing high absolute net charge. The volume of a condensate phosphorylated to P-level 50 (six residues per chain) is even below the non-phosphorylated state. This behavior is to be expected from the nearly neutral net charge of these chains. Further, these results are in line with the single-chain globule-to-coil transition temperature T_{θ} , which displayed a maximum for P-level 50.

The cohesiveness of the chains can be examined by fitting to the analytical equation of state according to the Sanchez-Lacombe (Equation 4.2, subsection 4.2.3). The overall interaction energy between chains (T^*) is the highest for the most neutrally charged condensate i.e. at P-level 50, whereas both the non-phosphorylated and P-level 10 systems exhibit lower interchain cohesion, consistent with their higher charge. In contrast, the interaction energy of the chains per critical volume, described by P^* , is two orders of magnitude larger than the simulated pressure of 1 bar and is monotonically reduced by increasing phosphorylation. Overall and in agreement with the conformational dynamics for the single IDR in water, these data suggest that the cohesion of multiple IDR chains is modulated by phosphorylation with their added net charge.

4.8 Discussion

Since the the role of INCENP's disordered central domain, which contains many phosphorylation sites, is largely unknown, I here set out to characterize the effect of phosphorylation on the IDR. One theory concerning the function of INCENP is the "dog-leash"-model for control of Aurora B activity. Here, variation in the length of INCENP is important to allow Aurora B to be targeted to the right substrates at the correct place and time within the cell cycle (Samejima et al., 2015; Krenn and Musacchio, 2015). In this chapter, I explored possible prerequisites under which the INCENP IDR may function as a constraint of Aurora B accessibility to substrates within the framework of the dog-leash model. To this end, I determined the conformational ensemble of the INCENP IDR under different phosphorylation conditions using all-atom and coarse-grained MD simulations.

4.8.1 Multiscale MD simulation approach

By combining both levels of resolution, the here employed multiscale methodology can provide a detailed local description as well as a global picture of the IDR. My all-atom simulations of the short fragments provided both insights into the small-scale changes to the IDR upon phosphorylation and a data set to validate the coarse-grained methodology. Although fine-tuned by specific residue-residue contacts, the observed conformational change of the short fragments upon phosphorylation is mainly due to altered net-charges. In this way, my data is consistent with previous studies on other IDPs (Jin and Gräter, 2021; Perdikari et al., 2021; E. W. Martin, Holehouse, et al., 2016; Müller-Späth et al., 2010; Mao et al., 2010; Rieloff and Skepö, 2021a). This confirms that the concept of a linear charge-size relationship modifiable by post-translational modification also transfers to a broader range of disordered sequences.

Generally, these phosphorylation-induced changes of R_g were comparable between both levels of resolution considered in this chapter. This agreement was qualitatively similar to previous comparisons of the employed coarse-grained framework with experimentally determined data (Dignon, W. Zheng, Kim, et al., 2018). For the atomistic simulations, I used a water model specifically tailored to IDPs, TIP4P-D (Piana et al., 2015). Although this water model was designed to correctly capture the solvation of IDPs and therefore their propensity for hydrophobic collapse, it is also well-established that current force fields for proteins generally overestimate charge-charge interactions (Ahmed et al., 2018; Duboué-Dijon et al., 2020). Therefore, it is plausible that the all-atom simulations exaggerate the electrostatically induced conformation of the fragments. This might

partially explain the tendency of the all-atom simulations to show structures in the upper tail of the R_g distributions compared to the coarse-grained simulations.

On the other hand, due to the implicit nature of the solvent used for the coarse-grained simulation, the estimated temperatures are only approximations, which might also take a part in explaining the slight deviation in R_g between the two levels of resolution. This temperature uncertainty implies that the calculated globule-to-coil transition temperatures cannot be considered as absolute values and are not completely comparable to experiments (Dignon, W. Zheng, Kim, et al., 2018). However, relative comparisons between conditions of one simulation setup as I performed here are valid and useful. Additionally, the coarse-grain model, which was state-of-the-art at the time the simulations were prepared, has since been updated to better represent IDPs (Joseph et al., 2021; Tesei et al., 2021). With the latest generation of parameters, the models tend to predict less compact structures, and the properties related to phase separation are also predicted more accurately. Ongoing and further simulations of the INCENP IDR are now being performed with these improved parameters, allowing to more precisely capture its properties on the global scale.

4.8.2 Influence of phosphorylation on INCENP

Although many phosphorylation sites were detected within INCENP, to date there is no comprehensive characterization of its phosphorylation pattern in different stages of the cell cycle. In this chapter, I approached the classification of phosphorylation sites into phosphorylation levels by using the number of literature detections as a proxy for the functionality of a particular phosphorylation site. This is supported by previous studies that suggested and use such a relationship between the number of references and functionality (H. Li et al., 2017; Mattè et al., 2021). Nevertheless, the number of literature mentions does not unambiguously infer a function of that phosphorylation site. However, my goal with the phosphorylation levels was not to generate a scale from most to least functionally relevant. Rather, I aimed at a simple way to estimate the likelihood that a particular phosphorylation site would be phosphorylated in the relevant cell cycle phases. Therefore, I considered a site that is mentioned very frequently in high-throughput studies, which was over 170 times for some residues, to appear more likely to be phosphorylated under many cellular conditions. In addition, especially the higher P-levels are consistent with bioinformatic predictions of phosphorylation based on the sequence and kinase consensus motifs. Remarkably, all sites considered in P-level 20, 50 and 100 are predicted to be phosphorylated, either by a specific kinase or unspecifically. Moreover, many sites below P-level 20, which are considered in P-level 10 or even P-level 1, were also predicted to be phosphorylated. This analysis thus

supports the P-levels as a means of grading the IDR phosphorylation. I believe that while my selection of phosphorylated residues in each P-level does not have a purely functional basis, it still provides valuable biophysical and structural insights into the phosphorylation sensitivity of the conformational ensemble. For a complete picture of INCENP, a subsequent experimental determination of its phosphorylation sites during mitosis is vital.

At the global level, the effect of phosphorylation on IDR extension is mainly mediated by charge modulation. This manifests itself in a critical globule-to-coil transition whose temperature is non-monotonically influenced by the phosphorylation status. Below the transition temperature, the IDR adopts a multitude of compact conformations that differ greatly in their internal connectivity (NTC), while when T_θ is exceeded, it increases dramatically in size and displays a narrow range of NTC. Apart from temperature, phosphorylation also shifts the conformational population between these two regimes, demonstrating the regulatory capabilities that phosphorylation provides on INCENP. Although not as pronounced as for the fully phosphorylated IDR, even moderate levels of phosphorylation, comprising 12-27 phosphorylation sites, show a non-negligible probability to populate the extended regime and thus already drive swelling. I therefore propose the sites corresponding to P-level 10 with special focus to the ones also present within P-level 20 to serve as a starting point to experimentally validate the phosphorylation-mediated size dependency.

Combining coarse-grain with all-atom simulations, I was able to detect a further effect of phosphorylation, besides global changes. Specific local interactions driven by phosphorylation also lead to a compaction of the IDR due to loop formation. These include the increased interaction between the residue patch 205-220 with residues 82-92, 97-102 and 330-346 of the whole IDR. But also distinct interactions within the short fragments, which I determined on the all-atom level, increase. These comprise residues 143-146, including the phosphoserine S143-P, in contact with 114-115 as well as residues 232-239, including the phosphothreonine T239-P, in contact with residues 254-259. It will therefore be interesting to experimentally validate the size change of INCENP upon phosphorylation of these proposed phosphorylation sites, which potentially leads to compaction through loop formation.

Nevertheless, the effect of phosphorylation mostly stems from its added negative charge and associated charge shift in the IDR, rather than from individually phosphorylated positions. Therefore, I propose to test whether the phosphorylation-mediated size of INCENP depends crucially on the exact positions of the phosphates or rather on the total number of added negative charges at nonspecific locations. In general, the size of the full INCENP, its IDR and fragments can be determined experimentally by for example

SAXS or NMR measurements. Such experiments could first of all be used to validate the simulations and the applied coarse-grain model. On the other hand, they would provide data on the interaction between the INCENP IDR and its neighboring domains, which could not be included in the here presented analysis. Further, it will be crucial to identify the phosphorylation pattern of INCENP in different phases of the cell cycle, for example using mass spectrometry or conventional NMR. Also recently an extension to conventional NMR has been developed to unambiguously track phosphorylation on large IDPs (Lesovoy et al., 2021) which could be perfectly suited for INCENP.

4.8.3 Participation of the INCENP IDR in the dog-leash model

Having determined the conformational ensemble of the INCENP IDR in multiscale simulations, the question arises of how these sizes of INCENP relate to its function, more specifically within the dog-leash model of Aurora B regulation. Here, the length of INCENP determines the radius in which Aurora B can reach and therefore phosphorylate its outer kinetochore targets (Figure 4.17). This model was underpinned by previous work showing that the length of the INCENP SAH has an effect on the phosphorylation status of Aurora targets in the inner and outer kinetochore (Samejima et al., 2015).

To fully capture the dog-leash model, we require knowledge of the intra-kinetochore distance that Aurora B, while being tethered to the centromere, must travel to the outer KT targets. This intra-KT distance varies depending on the state of chromosome attachment, with bi-orientation stretching the outer kinetochore farther away from the inner kinetochore. Such extension of the intra-KT distance due to spindle tension, the intra-KT stretch, is observed in *Drosophila* cells in the range of 65 nm to 100 nm (Maresca and Salmon, 2009). In human cells, the intra-KT distance was initially estimated

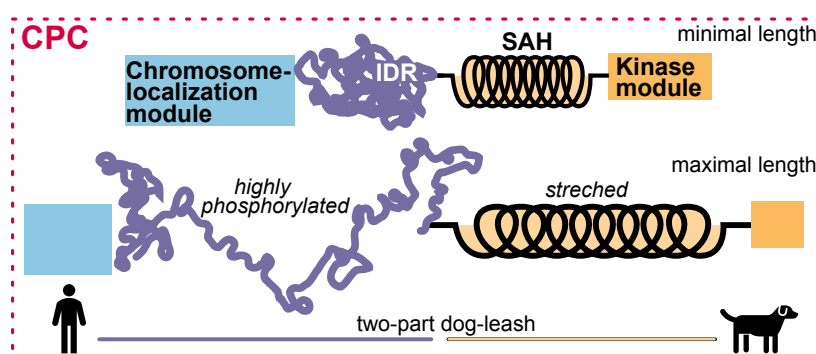


Fig. 4.17.: A possible combined dog-leash mechanism. The range of action of Aurora B, the kinase module of the CPC, is defined by the combined length of the INCENP middle domains (IDR and SAH) that can be imagined to act as a dog-leash for Aurora B.

to stretch from 20 nm to 60 nm (Suzuki, Badger, et al., 2014). However, the exact determination of the intra-KT distance in different conditions is not straightforward and also strongly depends on the exact geometry of the spindle (Suzuki, Long, et al., 2018). Therefore, no reliable values can yet be given for the distance that Aurora B has to cover, but for human cells it now appears roughly in the range of 40 nm to 60 nm (Suzuki, Badger, et al., 2014; Roscioli et al., 2020; C. A. Smith et al., 2016; Tauchman et al., 2015; Suzuki, Long, et al., 2018).

The previously identified SAH was proposed to be ~ 30 nm in length in the compact state based on its sequence. Under force, the SAH might be able to fully elongate up to ~ 80 nm, or if only the N-terminal part that binds the microtubules is stretched, it may reach a total length of ~ 50 nm (Samejima et al., 2015). These lengths need to be considered in combination with the mean extensions of the isolated IDR determined in this chapter. These are in the range of 10 nm to 40 nm for the heavily phosphorylated IDR and below 10 nm for the non- to moderately phosphorylated cases. The combined length of both INCENP middle domains is thus in the same order of magnitude as the approximate displacement Aurora B would require to reach its outer kinetochore targets. Depending on their mutual interaction, both domains could be considered as serial dog-leashes, that are regulated independently, or as one combined leash. The distinction between the two states will therefore benefit greatly from characterizing the interaction between the SAH and the IDR. Also, the interactions between the middle domains of INCENP and its N- and C-terminal domains are currently unclear, but will also dictate the overall length of INCENP. Therefore, a definitive answer to the question of INCENP length and its impact on the dog-leash model is not possible at the moment.

For the IDR itself, tight control of its phosphorylation status is required for the dog-leash model to be functional. Phosphoregulation is especially important in regimes close to the globule-to-coil transition, where small amounts of added phosphorylations lead to a sudden extension of INCENP. Additionally, we need to consider the interplay between the phosphorylation state of the IDR and the spindle forces. These forces could elongate the SAH, but could also stretch the IDR since it is framed by two MT-binding sites, which however has not yet been directly shown. Although much remains to be investigated to clarify whether and how precisely Aurora B is regulated by the dog-leash model, my data on the regulation of INCENP-IDR extension by phosphorylation presents the IDR as a plausible component of the dog-leash – as a length-tunable spacer between Aurora B and the chromosome localization module of the CPC.

4.8.4 Liquid-liquid phase separation

Another interesting possibility arises from the phosphorylation-induced single chain dynamic properties of the IDR, namely that INCENP may be prone for liquid-liquid phase separation (LLPS). Macromolecules undergoing LLPS condense into droplets which enhances the local concentration of biomolecules (Alberti et al., 2019; Banani et al., 2017; Walter and Brooks, 1995). Surrounding the condensed phase is the dilute phase, creating a membrane-independent compartmentalization. If energetically favorable, molecule-molecule interactions are preferred over molecule-water interactions. Such local concentration of biomolecules can enable biochemical reactions beyond the possibilities of the more mixed cytoplasm. With their intrinsically disordered regions, IDPs have emerged as key players within LLPS (Dignon, Best, et al., 2020; Shea et al., 2021; E. W. Martin and Holehouse, 2020; Darling et al., 2018), with differently composed sequences showing different recruitment tendencies into phase-separated protein condensates (Jo et al., 2022).

Phase separation has also been found to occur within the context of cell division (Jie Liu et al., 2020). For example, driven by its subunit borealin, the CPC was recently proposed to undergo LLPS (Trivedi, Palomba, et al., 2019; Trivedi and Stukenberg, 2020). Moreover, the interaction between Aurora B and the presumably partially disordered small kinetochore-associated protein (SKAP), which is important to guide end-on capture of the spindle microtubules, also depends on the formation of condensed heterogeneous droplets (M. Zhang et al., 2022). Thus, since INCENP is both intrinsically disordered and located in an environment prone for phase separation, it is tempting to consider its phase separation tendencies. My data on the phosphorylation-induced globule-to-coil transition indicate a possibility for phase separation since the temperature of globule-to-coil transition is related to the LLPS critical temperature (Panagiotopoulos et al., 1998; Dignon, W. Zheng, Best, et al., 2018). Further hints towards phase separation tendencies of INCENP come from the here presented multi-chain IDR simulations. The cohesiveness of IDR chains is sensitive to phosphorylation. Based on these observations, I speculate that the isolated IDR might have the propensity to undergo LLPS mediated by its phosphorylation status. However, whether these indications of a phase behavior of the INCENP IDR will solidify and whether they serve any biological function within faithful chromosome segregation remains to be shown. This would again primarily require a fundamental characterization of the phosphorylation pattern of INCENP and the inter-domain interactions within INCENP, as these two parameters largely influence whether phase separation might occur.

Partly owing to its apparent simplicity, phase separation is currently an explosively growing topic in biology. However, this simplicity might be deceiving, as opposing voices to

the phase separation boom argue. For example, many phase separation claims might not be adequately tested and therefore other explanations for the observed macromolecular concentration at intracellular compartments are overlooked (Musacchio, 2022). Therefore, a thorough investigation of phase separation of INCENP in particular and in biology in general is necessary.

4.8.5 Outlook on INCENP function

To summarize, in this chapter I systematically explored the phosphorylation-dependent conformational ensemble of the disordered INCENP region using multiscale MD simulations. I was able to show that, driven by extensive phosphorylation, the isolated IDR can transition from multiple globular to extended states. As already mentioned above, the next experiments will involve the determination of possible inter-domain interactions but even more immediately a detailed characterization of the INCENP phosphorylation pattern during the cell cycle.

Thinking beyond the static phosphorylation pattern I explored, the globule-to-coil transition might also be achieved by cooperative addition of phosphorylations, and simulations to test this hypothesis are currently underway. In this case, moderate levels of phosphorylation trigger slight expansion of the IDR, rendering additional phosphorylation sites more accessible. This would create a positive feedback loop for subsequent and rapid extension of the IDR. Dephosphorylation, on the other hand, would in the same way lead to abrupt collapse of INCENP, which can result in retraction of Aurora B from the outer KT. Generally, the transitional behavior of the IDR can be thought to act in tandem with the single α -helix domain (Samejima et al., 2015) to regulate Aurora B activity by influencing substrate accessibility.

However, the dog leash model is not the only activation mechanism for Aurora B hypothesized in the literature. There also exists the chromosomal gradient hypothesis, in which a gradient of Aurora B diffuses outwards from the centromere which is unable to reach the outer KT under amphitelic tension. Here, the length of INCENP would play only a minor role in Aurora B regulation, which is in contrast to previous findings (Samejima et al., 2015), where the length of the INCENP SAH is important for Aurora B function. In addition to these two variants of spatial separation of the kinase from its targets, another possibility is that Aurora B is directly regulated by mechanical forces. Again, an associated protein such as INCENP could act as a tensiometer, a spring-like protein, that deactivates Aurora B upon tension. Although INCENP is known to activate Aurora B with its C-terminus, no studies have shown that tension directly acts on the protein, except for the hypothesis that the SAH might be stretched under force.

Yet we are only at the beginning of correctly grasping the mechanisms behind the remarkable fidelity that nature has brought to the complex task of chromosome segregation that underlies every single cell in the human body.

Concluding Remarks and Future Perspectives

” *And following our will and wind we may just go
where no one's been
We'll ride the spiral to the end and may just go
where no one's been
Spiral out, keep going*

— **TOOL**
Lateralus (2001)

In recent years, mechanical forces have increasingly emerged as important players in cellular function and regulation in every aspect of life. This work aimed to expand our understanding of signaling mechanisms involved in converting mechanical force into biological signals. This mechanotransduction occurs predominantly in specialized cellular hubs to coordinate signaling pathways for both communication within the cell and communication with the cellular environment. Specifically, my dissertation focused on two proteins within different cellular mechanotransduction hubs, namely ILK at focal adhesions and INCENP at kinetochores. I investigated how these proteins play their role in signal transduction in an environment that converts mechanical forces into cellular output. Naturally, given the sheer number of different proteins and even more possible protein interactions involved in both focal adhesions and the kinetochore, my findings only represent a small piece of the vastly complex puzzle that is mechanical signaling.

5.1 Signal integration at mechanotransduction hubs

Although both proteins I studied play their role in mechanical signal transduction pathways, their mechanisms of action in mediating signals are quite different. The role of ILK in mechanotransduction might be rather direct. Since the force from the ECM on the cytoskeleton likely acts directly on the protein complex, it triggers protein unfolding and complex dissociation. As such, complex dissociation terminates the force connection between the ECM and the cytoskeleton and thus also mechanosignaling.

The balance between dissociation and unfolding is altered by the presence of ATP, with the complex containing ATP being more resistant to dissociation. Hence, my data on the ATP-influenced ILK:parvin dissociation pattern under force suggest a direct effect of ILK in the integration of mechanical stress. This is also confirmed by the cellular experiments showing that the complete ILK:parvin:ATP complex is required for traction force generation and subsequent cell migration.

On the other hand, INCENP can be currently considered to play an indirect role in mechanotransduction at kinetochores. Here, correct tension from the mitotic spindle microtubules pulls the outer KT away from the inner KT and chromosomes. Containing two MT-binding sites, INCENP might be directly affected by MT pulling force, but this has not yet been demonstrated. The theory I have been working within relies rather on indirect, force-induced spatial separation between proteins. In this dog-leash model, the action radius of the mitotic kinase Aurora B is defined by the length of the linker INCENP. INCENP, in turn, would be regulated to adapt to lengths required by different modes of microtubule tension. My data provide a mechanism for this length regulation of INCENP, and that is through the degree of its phosphorylation.

This illustrates how force plays quite different roles in biological signaling pathways and can have both direct and more indirect effects on proteins. Apart from these two possibilities in which proteins can participate in mechanotransduction, nature has come up with many other fascinating principles. FAK (focal adhesion kinase), for example, is a catalytically active tyrosine kinase that is also critical for integrin-based signaling within FAs. Its kinase activity was shown to be directly activated by tensile forces through freeing a key phosphorylation site from the autoinhibitory domain (Zhou et al., 2015; Bauer et al., 2019). A different view of such a force-induced presentation of protein domains is provided by the example of the von Willebrand factor, a blood plasma protein involved in blood clotting at injured blood vessels. Drag forces generated by the blood stream stretch and unfold the protein, which exposes protein binding domains for adaptor proteins (Butera et al., 2018; Fu et al., 2017; Schneider et al., 2007). This mechanopresentation of domains is regulated by switching of disulfide bonds (Butera et al., 2018). Another exciting mechanism of how mechanical force can be converted into a biochemical signal is the recent discovery that force-induced rupture of chemical bonds in the structural protein collagen leads to the formation of radicals (Zapp et al., 2020). These radicals may then diffuse into the collagen tissue and can propagate the now chemical signal.

These are just a few examples of how mechanical forces affect proteins, but there exist many more mechanisms spanning a wide range of biologically accessible time and length scales (Ricca et al., 2013; Martino et al., 2018). As an example, consider the drastic tissue movements in early embryonic development (Agarwal and Zaidel-Bar, 2021), where the

forces and responses to them occur on very different scales than the forces on individual proteins described in this thesis. Thus, my work contributes to the considerable breadth of mechanotransductive behavior.

5.2 The different roles of scaffold proteins

Although their mechanisms of action are different, ILK and INCENP have in common that they both function as scaffolding proteins. Cellular scaffolds serve as protein binding platforms that coordinate the physical assembly of functionally interacting signaling components required for a particular signaling pathway (Good et al., 2011; Mugabo and Lim, 2018). In this way scaffold proteins have evolved as organizers of information flow inside the cell (Good et al., 2011).

In my opinion, it is no surprise that mechanotransduction pathways also make use of scaffold proteins, and I would even argue that the very presence of mechanical force might necessitate the existence of scaffold proteins in their signaling pathways. This is because spatial organization is particularly important here, for instance to properly align proteins with the direction of force or to maintain appropriate spacing between proteins in the face of a constantly changing environment due to force. It may therefore be time to investigate other force transmission pathways as to whether the presence of scaffold proteins is of importance there as well.

Such a principle of assembling distinct subsets of signaling molecules at the right place and time to attain specificity of transduction pathways is also a feature of liquid-liquid phase separation (Musacchio, 2022; Ditlev et al., 2018). Both generate spatially organized signaling spheres inside the otherwise well-mixed cytoplasm. Therefore, it might be valuable to gain more knowledge about LLPS and the importance of the established concept of scaffold proteins therein, and then to further analyze the force transmission pathways in relation to LLPS and scaffold proteins as suggested above.

5.3 Life in the shadow of classic enzymes

In addition to expanding the palette of known signal transduction pathways at mechanotransduction hubs, my results also provide insights into signaling mechanisms of proteins that function beyond classical enzymatic catalysis. Both ILK and INCENP belong to protein classes that have only recently gained more attention, namely pseudokinases and IDPs, respectively. These families stood in the shadow of their well-studied conventional

counterparts, which are catalytic kinases for pseudokinases and the folded proteins for IDPs. It is crucial for us to advance our knowledge of how these protein classes mediate their various cellular functions if we are to fully understand the cell at the microscopic level.

As for pseudokinases, my results put forward the idea that this class of proteins is also proficient in acting as a player in mechanical signaling pathways. In addition to functioning as scaffolding proteins, which pseudokinases are known to be capable of, my data suggest that the ILK:parvin complex is able to directly transduce mechanical tension. In this way, ATP may have evolved from a phosphate donor to a mechanotransducing component, where it increases the mechanical stability and alters the mechanical behavior of the complex. Taken to its logical conclusion, the presence of ATP would tune the force threshold required for the ILK:parvin complex to relay the force signal, especially in proper focal adhesion disassembly and subsequent cell migration. In this way, not only do the pseudokinases acquire a new potential role, but also the presence of ATP within them is given more attention with respect to mediating functions beyond regular phosphate transfer. This knowledge could be used to construct pseudokinase modifiers based on mechanisms similar to conventional kinases (Kung and Jura, 2019).

With respect to IDPs, my data contribute to corroborate and further deepen our knowledge of how different degrees of phosphorylation alter the conformational ensemble of IDPs. This capacity for length adjustment of IDPs hence should be considered important for the accessibility-radius of bound proteins, which also represents another possible mechanism of regulating scaffold proteins. For INCENP in particular, my simulations examining its relationship between length and phosphorylation serve as a starting point for a targeted experimental characterization of its function in chromosome segregation. Another possibility, not yet investigated, is that INCENP is also directly influenced by force itself. In this regard, IDPs are currently also increasingly coming into the focus of mechanobiology. With their flexibility, they could obviously serve as a force buffer, but their disordered structure clearly does not provide much force resistance. Therefore, IDPs are generally interesting potential components of force transmission pathways worth exploring. Recent work in this direction has identified a force-regulated protein with an IDR, LIMD1, as important for focal adhesion assembly (Y. Wang et al., 2021). This scaffold protein condenses at FAs in a force-dependent manner and, intriguingly and analogous to INCENP, is also regulated by phosphorylation.

5.4 Future perspectives of molecular simulations

My aforementioned advances in various topics were only possible, at least in large part, through the use of molecular simulations. Their ability to reveal the underlying dynamics of protein function on time and length scales that are not, or only to a very limited extent, accessible with experiments makes them perfectly suited to answer the questions posed in my work. A key element of any simulation is to confirm that the properties accurately reflect the system under study. Hence, MD simulations continue to be improved and developed alongside experiments, and certain currently known shortcomings of simulations I have already discussed in the specific projects above. Still, it is definitely advantageous to couple simulation results with experiments, as such an approach maximizes the probability that the investigated properties are valid. This combination is exactly what takes my simulations of ILK to the next level. Although the time and length scales of simulations and cellular experiments are rather different, the ILK molecular properties I discovered with MD simulations can be related to cellular properties and large-scale effects through simulation-motivated mutations. Nevertheless, experimental validation of the pulling simulations, e.g. with AFM or optical tweezers, would add another layer of reproducibility and advancement to this project. For such single-molecule pulling experiments, the accessible range of loading rates for pulling is nowadays increasingly converging and even partially overlapping with those from simulations, not least due to improved computational efficiency (Franz et al., 2020).

Also owing to the increased computational power and effectiveness of MD software, including advances in coarse-graining schemes, that have all increased notably even during this thesis, it will soon be possible to simulate even larger systems that encompass more proteins in each system. For ILK, for example, this would include a more complete picture of the full ILK scaffold with more of its binding partners. In the case of INCENP, this would also allow exploration of the entirety of this protein. If the dog-leash model stands up to specific experimental validation, which is admittedly still lacking in this work, such large-scale simulations could also be used to actually tether Aurora B using INCENP and observe how far it can indeed reach.

Large-scale simulations in this regard would, of course, benefit from and require structure determination of the larger complexes. Here, too, technical progress in recent years has made it possible to obtain more and more structures at higher resolution that could previously not be retrieved by experiments. But also computationally, structure determination has advanced dramatically, not least with the release of AlphaFold, a computational prediction of protein structures with atomic accuracy that can compete with experimental structures (Jumper et al., 2021). For IDPs, though, these current machine

learning methods are not particularly well suited because the energy landscape of IDPs is rugged and multi-funneled, which underscores the importance of MD simulations to explore their conformational space (Ruff and Pappu, 2021; Strodel, 2021).

Furthermore, with the latest addition to the AlphaFold family, AlphaFold-Multimer, which has higher accuracy in predicting multimeric interfaces (Evans et al., 2021), we may be able to move towards simulating multiprotein systems such as focal adhesions or kinetochores in the future. Such high-level considerations of complete subcellular systems would truly advance biological science, as it would enable us to understand the complex interplay within these multiprotein complexes. To this end, we can also greatly benefit from the advances in super resolution microscopy, revealing the position and stoichiometry of proteins in certain compartments (Valli et al., 2021; Jing et al., 2021). Now that their resolutions touch the length scales of simulations, we could aim to physiologically set up the above mentioned ambitious large-scale simulations. This interplay between simulation and experiment, as well as interdisciplinary approaches, established an era in which large-scale MD simulations of whole cellular compartments, such as the photosynthetic chromatophore vesicle of purple bacteria, are now becoming possible (Singharoy et al., 2019; Wilson et al., 2021). I believe that these advances will eventually lead us into a world where one day we could begin to simulate whole cells in molecular detail; efforts to do so are already underway (Feig and Sugita, 2019; Maritan et al., 2022). My work thus provides a small puzzle piece that brings us closer to our common goal of fully understanding mechanotransduction and thereby grasping the complexity of a cell as a whole.

Bibliography

- Abraham, Mark James, Teemu Murtola, Roland Schulz, Szilárd Páll, Jeremy C. Smith, Berk Hess, and Erik Lindahl (2015). “GROMACS: High performance molecular simulations through multi-level parallelism from laptops to supercomputers”. In: *SoftwareX* 1-2, pp. 19–25. DOI: 10.1016/j.softx.2015.06.001.
- Adams, R. R., H. Maiato, W. C. Earnshaw, and M. Carmena (2001). “Essential roles of *Drosophila* inner centromere protein (INCENP) and aurora B in histone H3 phosphorylation, metaphase chromosome alignment, kinetochore disjunction, and chromosome segregation”. In: *The Journal of cell biology* 153.4, pp. 865–880. DOI: 10.1083/jcb.153.4.865.
- Adams, R. R., S. P. Wheatley, A. M. Gouldsworthy, S. E. Kandels-Lewis, M. Carmena, C. Smythe, D. L. Gerloff, et al. (2000). “INCENP binds the Aurora-related kinase AIRK2 and is required to target it to chromosomes, the central spindle and cleavage furrow”. In: *Current biology : CB* 10.17, pp. 1075–1078. DOI: 10.1016/s0960-9822(00)00673-4.
- Agarwal, Priti and Ronen Zaidel-Bar (2021). “Mechanosensing in embryogenesis”. In: *Current opinion in cell biology* 68, pp. 1–9. DOI: 10.1016/j.ceb.2020.08.007.
- Ahmed, Mustapha Carab, Elena Papaleo, and Kresten Lindorff-Larsen (2018). “How well do force fields capture the strength of salt bridges in proteins?” In: *PeerJ* 6, e4967. DOI: 10.7717/peerj.4967.
- Alberti, Simon, Amy Gladfelter, and Tanja Mittag (2019). “Considerations and Challenges in Studying Liquid-Liquid Phase Separation and Biomolecular Condensates”. In: *Cell* 176.3, pp. 419–434. DOI: 10.1016/j.cell.2018.12.035.
- Aliev, Abil E., Martin Kulke, Harmeet S. Khaneja, Vijay Chudasama, Tom D. Sheppard, and Rachel M. Lanigan (2014). “Motional timescale predictions by molecular dynamics simulations: case study using proline and hydroxyproline sidechain dynamics”. In: *Proteins* 82.2, pp. 195–215. DOI: 10.1002/prot.24350.
- Ambrosini, G., C. Adida, and D. C. Altieri (1997). “A novel anti-apoptosis gene, survivin, expressed in cancer and lymphoma”. In: *Nature medicine* 3.8, pp. 917–921. DOI: 10.1038/nm0897-917.
- Anfinsen, C. B. (1973). “Principles that govern the folding of protein chains”. In: *Science (New York, N.Y.)* 181.4096, pp. 223–230. DOI: 10.1126/science.181.4096.223.
- Angulo-Urarte, Ana, Tanne van der Wal, and Stephan Huvneers (2020). “Cell-cell junctions as sensors and transducers of mechanical forces”. In: *Biochimica et biophysica acta. Biomembranes* 1862.9, p. 183316. DOI: 10.1016/j.bbamem.2020.183316.
- Ashbaugh, Henry S. and Harold W. Hatch (2008). “Natively unfolded protein stability as a coil-to-globule transition in charge/hydrophathy space”. In: *Journal of the American Chemical Society* 130.29, pp. 9536–9542. DOI: 10.1021/ja802124e.

- Attwell, Sarah, Julia Mills, Armelle Troussard, Chuanyue Wu, and Shoukat Dedhar (2003). “Integration of cell attachment, cytoskeletal localization, and signaling by integrin-linked kinase (ILK), CH-ILKBP, and the tumor suppressor PTEN”. In: *Molecular biology of the cell* 14.12, pp. 4813–4825. DOI: 10.1091/mbc.e03-05-0308.
- Audett, Margaux R. and Thomas J. Maresca (2020). “The whole is greater than the sum of its parts: at the intersection of order, disorder, and kinetochore function”. In: *Essays in biochemistry* 64.2, pp. 349–358. DOI: 10.1042/EBC20190069.
- Babu, M. Madan (2016). “The contribution of intrinsically disordered regions to protein function, cellular complexity, and human disease”. In: *Biochemical Society transactions* 44.5, pp. 1185–1200. DOI: 10.1042/BST20160172.
- Banani, Salman F., Hyun O. Lee, Anthony A. Hyman, and Michael K. Rosen (2017). “Biomolecular condensates: organizers of cellular biochemistry”. In: *Nature reviews. Molecular cell biology* 18.5, pp. 285–298. DOI: 10.1038/nrm.2017.7.
- Bauer, Magnus Sebastian, Fabian Baumann, Csaba Daday, Pilar Redondo, Ellis Durner, Markus Andreas Jobst, Lukas Frederik Milles, et al. (2019). “Structural and mechanistic insights into mechanoactivation of focal adhesion kinase”. In: *Proceedings of the National Academy of Sciences of the United States of America* 116.14, pp. 6766–6774. DOI: 10.1073/pnas.1820567116.
- Berendsen, H. J. C., J. P. M. Postma, W. F. van Gunsteren, A. DiNola, and J. R. Haak (1984). “Molecular dynamics with coupling to an external bath”. In: *The Journal of Chemical Physics* 81.8, pp. 3684–3690. DOI: 10.1063/1.448118.
- Berginski, Matthew E. and Shawn M. Gomez (2013). “The Focal Adhesion Analysis Server: a web tool for analyzing focal adhesion dynamics”. In: *F1000Research* 2, p. 68. DOI: 10.12688/f1000research.2-68.v1.
- Best, Robert B. and Gerhard Hummer (2009). “Optimized molecular dynamics force fields applied to the helix-coil transition of polypeptides”. In: *The journal of physical chemistry. B* 113.26, pp. 9004–9015. DOI: 10.1021/jp901540t.
- Blaszczyk, Maciej, Michal Jamroz, Sebastian Kmiecik, and Andrzej Kolinski (2013). “CABS-fold: Server for the de novo and consensus-based prediction of protein structure”. In: *Nucleic acids research* 41.Web Server issue, W406–11. DOI: 10.1093/nar/gkt462.
- Blom, N., S. Gammeltoft, and S. Brunak (1999). “Sequence and structure-based prediction of eukaryotic protein phosphorylation sites”. In: *Journal of molecular biology* 294.5, pp. 1351–1362. DOI: 10.1006/jmbi.1999.3310.
- Boldon, Lauren, Fallon Laliberte, and Li Liu (2015). “Review of the fundamental theories behind small angle X-ray scattering, molecular dynamics simulations, and relevant integrated application”. In: *Nano reviews* 6, p. 25661. DOI: 10.3402/nano.v6.25661.
- Boudeau, Jérôme, Diego Miranda-Saavedra, Geoffrey J. Barton, and Dario R. Alessi (2006). “Emerging roles of pseudokinases”. In: *Trends in cell biology* 16.9, pp. 443–452. DOI: 10.1016/j.tcb.2006.07.003.
- Bugge, Katrine, Inna Brakti, Catarina B. Fernandes, Jesper E. Dreier, Jeppe E. Lundsgaard, Johan G. Olsen, Karen Skriver, et al. (2020). “Interactions by Disorder - A Matter of Context”. In: *Frontiers in molecular biosciences* 7, p. 110. DOI: 10.3389/fmolb.2020.00110.

- Bulus, Nada, Kyle L. Brown, Glenda Mernaugh, Anika Böttcher, Xinyu Dong, Charles R. Sanders, Ambra Pozzi, et al. (2021). “Disruption of the integrin-linked kinase (ILK) pseudokinase domain affects kidney development in mice”. In: *The Journal of biological chemistry* 296, p. 100361. DOI: 10.1016/j.jbc.2021.100361.
- Burridge, Keith (2017). “Focal adhesions: a personal perspective on a half century of progress”. In: *The FEBS journal* 284.20, pp. 3355–3361. DOI: 10.1111/febs.14195.
- Bussi, Giovanni, Davide Donadio, and Michele Parrinello (2007). “Canonical sampling through velocity rescaling”. In: *The Journal of Chemical Physics* 126.1, p. 014101. DOI: 10.1063/1.2408420.
- Bustamante, Carlos, Lisa Alexander, Kevin Maciuba, and Christian M. Kaiser (2020). “Single-Molecule Studies of Protein Folding with Optical Tweezers”. In: *Annual review of biochemistry* 89, pp. 443–470. DOI: 10.1146/annurev-biochem-013118-111442.
- Butera, Diego, Freda Passam, Lining Ju, Kristina M. Cook, Heng Woon, Camilo Aponte-Santamaría, Elizabeth Gardiner, et al. (2018). “Autoregulation of von Willebrand factor function by a disulfide bond switch”. In: *Science advances* 4.2, eaaq1477. DOI: 10.1126/sciadv.aaq1477.
- Byrne, Dominic P., Daniel M. Foulkes, and Patrick A. Eyers (2017). “Pseudokinases: update on their functions and evaluation as new drug targets”. In: *Future medicinal chemistry* 9.2, pp. 245–265. DOI: 10.4155/fmc-2016-0207.
- Calderwood, David A., Iain D. Campbell, and David R. Critchley (2013). “Talins and kindlins: partners in integrin-mediated adhesion”. In: *Nature reviews. Molecular cell biology* 14.8, pp. 503–517. DOI: 10.1038/nrm3624.
- Carmena, Mar, Michael Wheelock, Hironori Funabiki, and William C. Earnshaw (2012). “The chromosomal passenger complex (CPC): from easy rider to the godfather of mitosis”. In: *Nature reviews. Molecular cell biology* 13.12, pp. 789–803. DOI: 10.1038/nrm3474.
- Carrion-Vazquez, Mariano, Hongbin Li, Hui Lu, Piotr E. Marszalek, Andres F. Oberhauser, and Julio M. Fernandez (2003). “The mechanical stability of ubiquitin is linkage dependent”. In: *Nature structural biology* 10.9, pp. 738–743. DOI: 10.1038/nsb965.
- Chan-Yao-Chong, Maud, Dominique Durand, and Tâp Ha-Duong (2019). “Molecular Dynamics Simulations Combined with Nuclear Magnetic Resonance and/or Small-Angle X-ray Scattering Data for Characterizing Intrinsically Disordered Protein Conformational Ensembles”. In: *Journal of chemical information and modeling* 59.5, pp. 1743–1758. DOI: 10.1021/acs.jcim.8b00928.
- Cheeseman, Iain M. (2014). “The kinetochore”. In: *Cold Spring Harbor perspectives in biology* 6.7, a015826. DOI: 10.1101/cshperspect.a015826.
- Chen, Geng-Yuan, Fioranna Renda, Huaiying Zhang, Alper Gokden, Daniel Z. Wu, David M. Chenoweth, Alexey Khodjakov, et al. (2021). “Tension promotes kinetochore-microtubule release by Aurora B kinase”. In: *The Journal of cell biology* 220.6. DOI: 10.1083/jcb.202007030.
- Chen, Jianlin, Xiaorong Liu, and Jianhan Chen (2020). “Targeting Intrinsically Disordered Proteins through Dynamic Interactions”. In: *Biomolecules* 10.5. DOI: 10.3390/biom10050743.
- Chen, Yun, Sheena E. Radford, and David J. Brockwell (2015). “Force-induced remodelling of proteins and their complexes”. In: *Current opinion in structural biology* 30, pp. 89–99. DOI: 10.1016/j.sbi.2015.02.001.

- Chiswell, Brian P., Rong Zhang, James W. Murphy, Titus J. Boggon, and David A. Calderwood (2008). "The structural basis of integrin-linked kinase-PINCH interactions". In: *Proceedings of the National Academy of Sciences of the United States of America* 105.52, pp. 20677–20682. DOI: 10.1073/pnas.0811415106.
- Chu, Haiyan, Ingo Thievensen, Michael Sixt, Tim Lämmermann, Ari Waisman, Attila Braun, Angelika A. Noegel, et al. (2006). "gamma-Parvin is dispensable for hematopoiesis, leukocyte trafficking, and T-cell-dependent antibody response". In: *Molecular and cellular biology* 26.5, pp. 1817–1825. DOI: 10.1128/MCB.26.5.1817-1825.2006.
- Cimini, Daniela, Ben Moree, Julie C. Canman, and E. D. Salmon (2003). "Merotelic kinetochore orientation occurs frequently during early mitosis in mammalian tissue cells and error correction is achieved by two different mechanisms". In: *Journal of cell science* 116.Pt 20, pp. 4213–4225. DOI: 10.1242/jcs.00716.
- Cimini, Daniela, Xiaohu Wan, Christophe B. Hirel, and E. D. Salmon (2006). "Aurora kinase promotes turnover of kinetochore microtubules to reduce chromosome segregation errors". In: *Current biology : CB* 16.17, pp. 1711–1718. DOI: 10.1016/j.cub.2006.07.022.
- Cooke, C. A., M. M. Heck, and W. C. Earnshaw (1987). "The inner centromere protein (INCENP) antigens: movement from inner centromere to midbody during mitosis". In: *The Journal of cell biology* 105.5, pp. 2053–2067. DOI: 10.1083/jcb.105.5.2053.
- Costescu, Bogdan I. and Frauke Gräter (2013). "Time-resolved force distribution analysis". In: *BMC biophysics* 6.1, p. 5. DOI: 10.1186/2046-1682-6-5.
- Cramer, Louise P. (2013). "Mechanism of cell rear retraction in migrating cells". In: *Current opinion in cell biology* 25.5, pp. 591–599. DOI: 10.1016/j.ceb.2013.05.001.
- Darden, Tom, Darrin York, and Lee Pedersen (1993). "Particle mesh Ewald: An $N \times \log(N)$ method for Ewald sums in large systems". In: *The Journal of Chemical Physics* 98.12, pp. 10089–10092. DOI: 10.1063/1.464397.
- Darling, April L., Yun Liu, Christopher J. Oldfield, and Vladimir N. Uversky (2018). "Intrinsically Disordered Proteome of Human Membrane-Less Organelles". In: *Proteomics* 18.5-6, e1700193. DOI: 10.1002/pmic.201700193.
- Das, Rahul K. and Rohit V. Pappu (2013). "Conformations of intrinsically disordered proteins are influenced by linear sequence distributions of oppositely charged residues". In: *Proceedings of the National Academy of Sciences of the United States of America* 110.33, pp. 13392–13397. DOI: 10.1073/pnas.1304749110.
- Das, Rahul K., Kiersten M. Ruff, and Rohit V. Pappu (2015). "Relating sequence encoded information to form and function of intrinsically disordered proteins". In: *Current opinion in structural biology* 32, pp. 102–112. DOI: 10.1016/j.sbi.2015.03.008.
- Debye, Peter and Erich Hückel (1923). "Zur Theorie der Elektrolyte. I. Gefrierpunktserniedrigung und verwandte Erscheinungen". In: *Physikalische Zeitschrift* 24.185, p. 305.
- DeLuca, Keith F., Susanne M. A. Lens, and Jennifer G. DeLuca (2011). "Temporal changes in Hec1 phosphorylation control kinetochore-microtubule attachment stability during mitosis". In: *Journal of cell science* 124.Pt 4, pp. 622–634. DOI: 10.1242/jcs.072629.

- Dembo, M. and Y. I. Wang (1999). “Stresses at the cell-to-substrate interface during locomotion of fibroblasts”. In: *Biophysical journal* 76.4, pp. 2307–2316. DOI: 10.1016/S0006-3495(99)77386-8.
- Di Lullo, Gloria A., Shawn M. Sweeney, Jarmo Korkko, Leena Ala-Kokko, and James D. San Antonio (2002). “Mapping the ligand-binding sites and disease-associated mutations on the most abundant protein in the human, type I collagen”. In: *The Journal of biological chemistry* 277.6, pp. 4223–4231. DOI: 10.1074/jbc.M110709200.
- Di Tommaso, Paolo, Sebastien Moretti, Ioannis Xenarios, Miquel Orobitg, Alberto Montanyola, Jia-Ming Chang, Jean-François Taly, et al. (2011). “T-Coffee: a web server for the multiple sequence alignment of protein and RNA sequences using structural information and homology extension”. In: *Nucleic acids research* 39.Web Server issue, W13–7. DOI: 10.1093/nar/gkr245.
- Dignon, Gregory L., Robert B. Best, and Jeetain Mittal (2020). “Biomolecular Phase Separation: From Molecular Driving Forces to Macroscopic Properties”. In: *Annual review of physical chemistry* 71, pp. 53–75. DOI: 10.1146/annurev-physchem-071819-113553.
- Dignon, Gregory L., Wenwei Zheng, Robert B. Best, Young C. Kim, and Jeetain Mittal (2018). “Relation between single-molecule properties and phase behavior of intrinsically disordered proteins”. In: *Proceedings of the National Academy of Sciences of the United States of America* 115.40, pp. 9929–9934. DOI: 10.1073/pnas.1804177115.
- Dignon, Gregory L., Wenwei Zheng, Young C. Kim, Robert B. Best, and Jeetain Mittal (2018). “Sequence determinants of protein phase behavior from a coarse-grained model”. In: *PLoS computational biology* 14.1, e1005941. DOI: 10.1371/journal.pcbi.1005941.
- Ditlev, Jonathon A., Lindsay B. Case, and Michael K. Rosen (2018). “Who’s In and Who’s Out-Compositional Control of Biomolecular Condensates”. In: *Journal of molecular biology* 430.23, pp. 4666–4684. DOI: 10.1016/j.jmb.2018.08.003.
- Dominguez, Cyril, Rolf Boelens, and Alexandre M. J. J. Bonvin (2003). “HADDOCK: a protein-protein docking approach based on biochemical or biophysical information”. In: *Journal of the American Chemical Society* 125.7, pp. 1731–1737. DOI: 10.1021/ja026939x.
- Doodhi, Harinath, Taciana Kasciukovic, Lesley Clayton, and Tomoyuki U. Tanaka (2021). “Aurora B switches relative strength of kinetochore-microtubule attachment modes for error correction”. In: *The Journal of cell biology* 220.6. DOI: 10.1083/jcb.202011117.
- Duboué-Dijon, E., M. Javanainen, P. Delcroix, P. Jungwirth, and H. Martinez-Seara (2020). “A practical guide to biologically relevant molecular simulations with charge scaling for electronic polarization”. In: *The Journal of Chemical Physics* 153.5, p. 050901. DOI: 10.1063/5.0017775.
- Dumbauld, David W., Ted T. Lee, Ankur Singh, Jan Scrimgeour, Charles A. Gersbach, Evan A. Zamir, Jianping Fu, et al. (2013). “How vinculin regulates force transmission”. In: *Proceedings of the National Academy of Sciences of the United States of America* 110.24, pp. 9788–9793. DOI: 10.1073/pnas.1216209110.
- Eisenhaber, Frank, Philip Lijnzaad, Patrick Argos, Chris Sander, and Michael Scharf (1995). “The double cubic lattice method: Efficient approaches to numerical integration of surface area and volume and to dot surface contouring of molecular assemblies”. In: *Journal of Computational Chemistry* 16.3, pp. 273–284. DOI: 10.1002/jcc.540160303.

- Elosegui-Artola, Alberto, Xavier Trepas, and Pere Roca-Cusachs (2018). “Control of Mechanotransduction by Molecular Clutch Dynamics”. In: *Trends in cell biology* 28.5, pp. 356–367. DOI: 10.1016/j.tcb.2018.01.008.
- Essmann, Ulrich, Lalith Perera, Max L. Berkowitz, Tom Darden, Hsing Lee, and Lee G. Pedersen (1995). “A smooth particle mesh Ewald method”. In: *The Journal of Chemical Physics* 103.19, pp. 8577–8593. DOI: 10.1063/1.470117.
- Evans, Richard, Michael O’Neill, Alexander Pritzel, Natasha Antropova, Andrew Senior, Tim Green, Augustin Zidek, et al. (2021). “Protein complex prediction with AlphaFold-Multimer”. In: *bioRxiv*. DOI: 10.1101/2021.10.04.463034.
- Feig, Michael and Yuji Sugita (2019). “Whole-Cell Models and Simulations in Molecular Detail”. In: *Annual review of cell and developmental biology* 35, pp. 191–211. DOI: 10.1146/annurev-cellbio-100617-062542.
- Filipenko, Nolan R., Sarah Attwell, Calvin Roskelley, and Shoukat Dedhar (2005). “Integrin-linked kinase activity regulates Rac- and Cdc42-mediated actin cytoskeleton reorganization via alpha-PIX”. In: *Oncogene* 24.38, pp. 5837–5849. DOI: 10.1038/sj.onc.1208737.
- Fisher, Charles K. and Collin M. Stultz (2011). “Constructing ensembles for intrinsically disordered proteins”. In: *Current opinion in structural biology* 21.3, pp. 426–431. DOI: 10.1016/j.sbi.2011.04.001.
- Flory, Paul J. (1949). “The Configuration of Real Polymer Chains”. In: *The Journal of Chemical Physics* 17.3, pp. 303–310. DOI: 10.1063/1.1747243.
- Frantz, Christian, Kathleen M. Stewart, and Valerie M. Weaver (2010). “The extracellular matrix at a glance”. In: *Journal of cell science* 123.Pt 24, pp. 4195–4200. DOI: 10.1242/jcs.023820.
- Franz, Florian, Csaba Daday, and Frauke Gräter (2020). “Advances in molecular simulations of protein mechanical properties and function”. In: *Current opinion in structural biology* 61, pp. 132–138. DOI: 10.1016/j.sbi.2019.12.015.
- Friedl, Peter and Darren Gilmour (2009). “Collective cell migration in morphogenesis, regeneration and cancer”. In: *Nature reviews. Molecular cell biology* 10.7, pp. 445–457. DOI: 10.1038/nrm2720.
- Friedrich, Erik B., Emerson Liu, Sumita Sinha, Stuart Cook, David S. Milstone, Calum A. MacRae, Massimo Mariotti, et al. (2004). “Integrin-linked kinase regulates endothelial cell survival and vascular development”. In: *Molecular and cellular biology* 24.18, pp. 8134–8144. DOI: 10.1128/MCB.24.18.8134-8144.2004.
- Fu, Hongxia, Yan Jiang, Darren Yang, Friedrich Scheiflinger, Wesley P. Wong, and Timothy A. Springer (2017). “Flow-induced elongation of von Willebrand factor precedes tension-dependent activation”. In: *Nature communications* 8.1, p. 324. DOI: 10.1038/s41467-017-00230-2.
- Fukuda, Koichi, Kamila Bledzka, Jun Yang, H. Dhanuja Perera, Edward F. Plow, and Jun Qin (2014). “Molecular basis of kindlin-2 binding to integrin-linked kinase pseudokinase for regulating cell adhesion”. In: *The Journal of biological chemistry* 289.41, pp. 28363–28375. DOI: 10.1074/jbc.M114.596692.

- Fukuda, Koichi, Sudhiranjan Gupta, Ka Chen, Chuanyue Wu, and Jun Qin (2009). “The pseudoactive site of ILK is essential for its binding to alpha-Parvin and localization to focal adhesions”. In: *Molecular cell* 36.5, pp. 819–830. DOI: 10.1016/j.molcel.2009.11.028.
- Fukuda, Koichi, James D. R. Knight, Grzegorz Piszczek, Rashmi Kothary, and Jun Qin (2011). “Biochemical, proteomic, structural, and thermodynamic characterizations of integrin-linked kinase (ILK): cross-validation of the pseudokinase”. In: *The Journal of biological chemistry* 286.24, pp. 21886–21895. DOI: 10.1074/jbc.M111.240093.
- Fukuda, Tomohiko, Ka Chen, Xiaohua Shi, and Chuanyue Wu (2003). “PINCH-1 is an obligate partner of integrin-linked kinase (ILK) functioning in cell shape modulation, motility, and survival”. In: *The Journal of biological chemistry* 278.51, pp. 51324–51333. DOI: 10.1074/jbc.M309122200.
- Garcia-Marin, Javier, Mercedes Griera-Merino, Alejandra Matamoros-Recio, Sergio de Frutos, Manuel Rodríguez-Puyol, Ramón Alajarín, Juan J. Vaquero, et al. (2021). “Tripeptides as Integrin-Linked Kinase Modulating Agents Based on a Protein-Protein Interaction with alpha-Parvin”. In: *ACS medicinal chemistry letters* 12.11, pp. 1656–1662. DOI: 10.1021/acsmchemlett.1c00183.
- Gassmann, Reto, Ana Carvalho, Alexander J. Henzing, Sandrine Ruchaud, Damien F. Hudson, Reiko Honda, Erich A. Nigg, et al. (2004). “Borealin: a novel chromosomal passenger required for stability of the bipolar mitotic spindle”. In: *The Journal of cell biology* 166.2, pp. 179–191. DOI: 10.1083/jcb.200404001.
- Geiger, Benjamin and Kenneth M. Yamada (2011). “Molecular architecture and function of matrix adhesions”. In: *Cold Spring Harbor perspectives in biology* 3.5. DOI: 10.1101/cshperspect.a005033.
- Goktas, Melis, Chuanfu Luo, Ruby May A. Sullan, Ana E. Bergues-Pupo, Reinhard Lipowsky, Ana Vila Verde, and Kerstin G. Blank (2018). “Molecular mechanics of coiled coils loaded in the shear geometry”. In: *Chemical science* 9.20, pp. 4610–4621. DOI: 10.1039/c8sc01037d.
- Goñi, Guillermina M., Carolina Epifano, Jasminka Boskovic, Marta Camacho-Artacho, Jing Zhou, Agnieszka Bronowska, M. Teresa Martín, et al. (2014). “Phosphatidylinositol 4,5-bisphosphate triggers activation of focal adhesion kinase by inducing clustering and conformational changes”. In: *Proceedings of the National Academy of Sciences of the United States of America* 111.31, E3177–86. DOI: 10.1073/pnas.1317022111.
- González, M. A. (2011). “Force fields and molecular dynamics simulations”. In: *École thématique de la Société Française de la Neutronique* 12, pp. 169–200. DOI: 10.1051/sfn/201112009.
- Good, Matthew C., Jesse G. Zalatan, and Wendell A. Lim (2011). “Scaffold proteins: hubs for controlling the flow of cellular information”. In: *Science (New York, N.Y.)* 332.6030, pp. 680–686. DOI: 10.1126/science.1198701.
- Goto, Hidemasa, Tohru Kiyono, Yasuko Tomono, Aie Kawajiri, Takeshi Urano, Koichi Furukawa, Erich A. Nigg, et al. (2006). “Complex formation of Plk1 and INCENP required for metaphase-anaphase transition”. In: *Nature cell biology* 8.2, pp. 180–187. DOI: 10.1038/ncb1350.
- Goult, Benjamin T., Jie Yan, and Martin A. Schwartz (2018). “Talin as a mechanosensitive signaling hub”. In: *The Journal of cell biology* 217.11, pp. 3776–3784. DOI: 10.1083/jcb.201808061.

- Grubmüller, Helmut (2005). “Force probe molecular dynamics simulations”. In: *Methods in molecular biology (Clifton, N.J.)* 305, pp. 493–515.
- Hanks, S. K., A. M. Quinn, and T. Hunter (1988). “The protein kinase family: conserved features and deduced phylogeny of the catalytic domains”. In: *Science (New York, N.Y.)* 241.4861, pp. 42–52. DOI: 10.1126/science.3291115.
- Hannigan, G. E., C. Leung-Hagesteijn, L. Fitz-Gibbon, M. G. Coppelino, G. Radeva, J. Filmus, J. C. Bell, et al. (1996). “Regulation of cell adhesion and anchorage-dependent growth by a new beta 1-integrin-linked protein kinase”. In: *Nature* 379.6560, pp. 91–96. DOI: 10.1038/379091a0.
- Hannigan, G. E., P. C. McDonald, M. P. Walsh, and S. Dedhar (2011). “Integrin-linked kinase: not so ‘pseudo’ after all”. In: *Oncogene* 30.43, pp. 4375–4385. DOI: 10.1038/onc.2011.177.
- Hannigan, Gregory, Armelle A. Troussard, and Shoukat Dedhar (2005). “Integrin-linked kinase: a cancer therapeutic target unique among its ILK”. In: *Nature reviews. Cancer* 5.1, pp. 51–63. DOI: 10.1038/nrc1524.
- Hannigan, Gregory E., John G. Coles, and Shoukat Dedhar (2007). “Integrin-linked kinase at the heart of cardiac contractility, repair, and disease”. In: *Circulation research* 100.10, pp. 1408–1414. DOI: 10.1161/01.RES.0000265233.40455.62.
- Harburger, David S., Mohamed Bouaouina, and David A. Calderwood (2009). “Kindlin-1 and -2 directly bind the C-terminal region of beta integrin cytoplasmic tails and exert integrin-specific activation effects”. In: *The Journal of biological chemistry* 284.17, pp. 11485–11497. DOI: 10.1074/jbc.M809233200.
- Harvey, Stephen C., Robert K.-Z. Tan, and Thomas E. Cheatham (1998). “The flying ice cube: Velocity rescaling in molecular dynamics leads to violation of energy equipartition”. In: *Journal of Computational Chemistry* 19.7, pp. 726–740. DOI: 10.1002/(SICI)1096-987X(199805)19:7<726::AID-JCC4>3.0.CO;2-S.
- Hashimoto, Yutaka, Noriyuki Kinoshita, Todd M. Greco, Joel D. Federspiel, Pierre M. Jean Beltran, Naoto Ueno, and Ileana M. Cristea (2019). “Mechanical Force Induces Phosphorylation-Mediated Signaling that Underlies Tissue Response and Robustness in *Xenopus* Embryos”. In: *Cell systems* 8.3, 226–241.e7. DOI: 10.1016/j.cels.2019.01.006.
- Hess, Berk (2008). “P-LINCS: A Parallel Linear Constraint Solver for Molecular Simulation”. In: *Journal of chemical theory and computation* 4.1, pp. 116–122. DOI: 10.1021/ct700200b.
- Hoffman, Brenton D., Carsten Grashoff, and Martin A. Schwartz (2011). “Dynamic molecular processes mediate cellular mechanotransduction”. In: *Nature* 475.7356, pp. 316–323. DOI: 10.1038/nature10316.
- Holehouse, Alex S., Rahul K. Das, James N. Ahad, Mary O. G. Richardson, and Rohit V. Pappu (2017). “CIDER: Resources to Analyze Sequence-Ensemble Relationships of Intrinsically Disordered Proteins”. In: *Biophysical journal* 112.1, pp. 16–21. DOI: 10.1016/j.bpj.2016.11.3200.
- Hollingsworth, Scott A. and Ron O. Dror (2018). “Molecular Dynamics Simulation for All”. In: *Neuron* 99.6, pp. 1129–1143. DOI: 10.1016/j.neuron.2018.08.011.

- Homeyer, Nadine, Anselm H. C. Horn, Harald Lanig, and Heinrich Sticht (2006). “AMBER force-field parameters for phosphorylated amino acids in different protonation states: phosphoserine, phosphothreonine, phosphotyrosine, and phosphohistidine”. In: *Journal of molecular modeling* 12.3, pp. 281–289. DOI: 10.1007/s00894-005-0028-4.
- Honda, Reiko, Roman Körner, and Erich A. Nigg (2003). “Exploring the functional interactions between Aurora B, INCENP, and survivin in mitosis”. In: *Molecular biology of the cell* 14.8, pp. 3325–3341. DOI: 10.1091/mbc.e02-11-0769.
- Horn, Heiko, Erwin M. Schoof, Jinho Kim, Xavier Robin, Martin L. Miller, Francesca Diella, Anita Palma, et al. (2014). “KinomeXplorer: an integrated platform for kinome biology studies”. In: *Nature methods* 11.6, pp. 603–604. DOI: 10.1038/nmeth.2968.
- Hornbeck, Peter V., Bin Zhang, Beth Murray, Jon M. Kornhauser, Vaughan Latham, and Elzbieta Skrzypek (2015). “PhosphoSitePlus, 2014: mutations, PTMs and recalibrations”. In: *Nucleic acids research* 43.Database issue, pp. D512–20. DOI: 10.1093/nar/gku1267.
- Huet-Calderwood, Clotilde, Nina N. Brahme, Nikit Kumar, Amy L. Stiegler, Srikala Raghavan, Titus J. Boggon, and David A. Calderwood (2014). “Differences in binding to the ILK complex determines kindlin isoform adhesion localization and integrin activation”. In: *Journal of cell science* 127.Pt 19, pp. 4308–4321. DOI: 10.1242/jcs.155879.
- Humphrey, W., A. Dalke, and K. Schulten (1996). “VMD: visual molecular dynamics”. In: *Journal of molecular graphics* 14.1, pp. 33–8, 27–8. DOI: 10.1016/0263-7855(96)00018-5.
- Hur, Sung Sik, Ji Hoon Jeong, Myung Jin Ban, Jae Hong Park, Jeong Kyo Yoon, and Yongsung Hwang (2020). “Traction force microscopy for understanding cellular mechanotransduction”. In: *BMB reports* 53.2, pp. 74–81.
- Hynes, Richard O. (2002). “Integrins: bidirectional, allosteric signaling machines”. In: *Cell* 110.6, pp. 673–687. DOI: 10.1016/s0092-8674(02)00971-6.
- Ingber, Donald E. (2003). “Mechanobiology and diseases of mechanotransduction”. In: *Annals of medicine* 35.8, pp. 564–577. DOI: 10.1080/07853890310016333.
- Jaalouk, Diana E. and Jan Lammerding (2009). “Mechanotransduction gone awry”. In: *Nature reviews. Molecular cell biology* 10.1, pp. 63–73. DOI: 10.1038/nrm2597.
- Jacobsen, Annette V. and James M. Murphy (2017). “The secret life of kinases: insights into non-catalytic signalling functions from pseudokinases”. In: *Biochemical Society transactions* 45.3, pp. 665–681. DOI: 10.1042/BST20160331.
- Jagannathan, Bharat and Susan Marqusee (2013). “Protein folding and unfolding under force”. In: *Biopolymers* 99.11, pp. 860–869. DOI: 10.1002/bip.22321.
- Jahed, Zeinab, Zainab Haydari, Akshay Rathish, and Mohammad R. K. Mofrad (2019). “Kindlin Is Mechanosensitive: Force-Induced Conformational Switch Mediates Cross-Talk among Integrins”. In: *Biophysical journal* 116.6, pp. 1011–1024. DOI: 10.1016/j.bpj.2019.01.038.
- Jeyaprakash, A. Arockia, Ulf R. Klein, Doris Lindner, Judith Ebert, Erich A. Nigg, and Elena Conti (2007). “Structure of a Survivin-Borealin-INCENP core complex reveals how chromosomal passengers travel together”. In: *Cell* 131.2, pp. 271–285. DOI: 10.1016/j.cell.2007.07.045.

- Jin, Fan and Frauke Gräter (2021). “How multisite phosphorylation impacts the conformations of intrinsically disordered proteins”. In: *PLoS computational biology* 17.5, e1008939. DOI: 10.1371/journal.pcbi.1008939.
- Jing, Yingying, Chenshuang Zhang, Bin Yu, Danying Lin, and Junle Qu (2021). “Super-Resolution Microscopy: Shedding New Light on In Vivo Imaging”. In: *Frontiers in chemistry* 9, p. 746900. DOI: 10.3389/fchem.2021.746900.
- Jo, Yongsang, Jinyoung Jang, Daesun Song, Hyoin Park, and Yongwon Jung (2022). “Determinants for intrinsically disordered protein recruitment into phase-separated protein condensates”. In: *Chemical science* 13.2, pp. 522–530. DOI: 10.1039/d1sc05672g.
- Jorgensen, William L., Jayaraman Chandrasekhar, Jeffrey D. Madura, Roger W. Impey, and Michael L. Klein (1983). “Comparison of simple potential functions for simulating liquid water”. In: *The Journal of Chemical Physics* 79.2, pp. 926–935. DOI: 10.1063/1.445869.
- Joseph, Jerelle A., Aleks Reinhardt, Anne Aguirre, Pin Yu Chew, Kieran O. Russell, Jorge R. Espinosa, Adiran Garaizar, et al. (2021). “Physics-driven coarse-grained model for biomolecular phase separation with near-quantitative accuracy”. In: *Nature Computational Science* 1.11, pp. 732–743. DOI: 10.1038/s43588-021-00155-3.
- Jumper, John, Richard Evans, Alexander Pritzel, Tim Green, Michael Figurnov, Olaf Ronneberger, Kathryn Tunyasuvunakool, et al. (2021). “Highly accurate protein structure prediction with AlphaFold”. In: *Nature* 596.7873, pp. 583–589. DOI: 10.1073/pnas.2021785118.
- Kadry, Yasmin A., Clotilde Huet-Calderwood, Bertrand Simon, and David A. Calderwood (2018). “Kindlin-2 interacts with a highly conserved surface of ILK to regulate focal adhesion localization and cell spreading”. In: *Journal of cell science* 131.20. DOI: 10.1242/jcs.221184.
- Kanchanawong, Pakorn, Gleb Shtengel, Ana M. Pasapera, Ericka B. Ramko, Michael W. Davidson, Harald F. Hess, and Clare M. Waterman (2010). “Nanoscale architecture of integrin-based cell adhesions”. In: *Nature* 468.7323, pp. 580–584. DOI: 10.1038/nature09621.
- Kapcha, Lauren H. and Peter J. Rosky (2014). “A simple atomic-level hydrophobicity scale reveals protein interfacial structure”. In: *Journal of molecular biology* 426.2, pp. 484–498. DOI: 10.1016/j.jmb.2013.09.039.
- Kapoor, Tarun M. and Duane A. Compton (2002). “Searching for the middle ground: mechanisms of chromosome alignment during mitosis”. In: *The Journal of cell biology* 157.4, pp. 551–556. DOI: 10.1083/jcb.200202073.
- Karplus, M. and J. Kuriyan (2005). “Molecular dynamics and protein function”. In: *Proceedings of the National Academy of Sciences of the United States of America* 102.19, pp. 6679–6685. DOI: 10.1073/pnas.0408930102.
- Kechagia, Jenny Z., Johanna Ivaska, and Pere Roca-Cusachs (2019). “Integrins as biomechanical sensors of the microenvironment”. In: *Nature reviews. Molecular cell biology* 20.8, pp. 457–473. DOI: 10.1038/s41580-019-0134-2.
- Kemp, B. E. and R. B. Pearson (1990). “Protein kinase recognition sequence motifs”. In: *Trends in biochemical sciences* 15.9, pp. 342–346. DOI: 10.1016/0968-0004(90)90073-k.

- Kimura, M., S. Kotani, T. Hattori, N. Sumi, T. Yoshioka, K. Todokoro, and Y. Okano (1997). “Cell cycle-dependent expression and spindle pole localization of a novel human protein kinase, Aik, related to Aurora of *Drosophila* and yeast Ipl1”. In: *The Journal of biological chemistry* 272.21, pp. 13766–13771. DOI: 10.1074/jbc.272.21.13766.
- Klein, Ulf R., Erich A. Nigg, and Ulrike Gruneberg (2006). “Centromere targeting of the chromosomal passenger complex requires a ternary subcomplex of Borealin, Survivin, and the N-terminal domain of INCENP”. In: *Molecular biology of the cell* 17.6, pp. 2547–2558. DOI: 10.1091/mbc.e05-12-1133.
- Kohanoff, Jorge (2006). *Electronic Structure Calculations for Solids and Molecules*. Cambridge: Cambridge University Press. DOI: 10.1017/CB09780511755613.
- Kozakov, Dima, Ora Schueler-Furman, and Sandor Vajda (2008). “Discrimination of near-native structures in protein-protein docking by testing the stability of local minima”. In: *Proteins* 72.3, pp. 993–1004. DOI: 10.1002/prot.21997.
- Krenn, Veronica and Andrea Musacchio (2015). “The Aurora B Kinase in Chromosome Bi-Orientation and Spindle Checkpoint Signaling”. In: *Frontiers in oncology* 5, p. 225. DOI: 10.3389/fonc.2015.00225.
- Kung, Jennifer E. and Natalia Jura (2016). “Structural Basis for the Non-catalytic Functions of Protein Kinases”. In: *Structure (London, England : 1993)* 24.1, pp. 7–24. DOI: 10.1016/j.str.2015.10.020.
- (2019). “Prospects for pharmacological targeting of pseudokinases”. In: *Nature reviews. Drug discovery* 18.7, pp. 501–526. DOI: 10.1038/s41573-019-0018-3.
- Lampson, Michael A. and Iain M. Cheeseman (2011). “Sensing centromere tension: Aurora B and the regulation of kinetochore function”. In: *Trends in cell biology* 21.3, pp. 133–140. DOI: 10.1016/j.tcb.2010.10.007.
- Lampson, Michael A. and Ekaterina L. Grishchuk (2017). “Mechanisms to Avoid and Correct Erroneous Kinetochore-Microtubule Attachments”. In: *Biology* 6.1. DOI: 10.3390/biology6010001.
- Lampson, Michael A., Kishore Renduchitala, Alexey Khodjakov, and Tarun M. Kapoor (2004). “Correcting improper chromosome-spindle attachments during cell division”. In: *Nature cell biology* 6.3, pp. 232–237. DOI: 10.1038/ncb1102.
- Lange, Anika, Sara A. Wickström, Madis Jakobson, Roy Zent, Kirsi Sainio, and Reinhard Fässler (2009). “Integrin-linked kinase is an adaptor with essential functions during mouse development”. In: *Nature* 461.7266, pp. 1002–1006. DOI: 10.1038/nature08468.
- Latham, Andrew P. and Bin Zhang (2019). “Improving Coarse-Grained Protein Force Fields with Small-Angle X-ray Scattering Data”. In: *The journal of physical chemistry. B* 123.5, pp. 1026–1034. DOI: 10.1021/acs.jpcc.8b10336.
- Legate, Kyle R., Eloi Montañez, Oliver Kudlacek, and Reinhard Fässler (2006). “ILK, PINCH and parvin: the tIPP of integrin signalling”. In: *Nature reviews. Molecular cell biology* 7.1, pp. 20–31. DOI: 10.1038/nrm1789.
- Legate, Kyle R., Sara A. Wickström, and Reinhard Fässler (2009). “Genetic and cell biological analysis of integrin outside-in signaling”. In: *Genes & development* 23.4, pp. 397–418. DOI: 10.1101/gad.1758709.

- Lekka, Małgorzata, Kajangi Gnanachandran, Andrzej Kubiak, Tomasz Zieliński, and Joanna Zemła (2021). “Traction force microscopy - Measuring the forces exerted by cells”. In: *Micron (Oxford, England : 1993)* 150, p. 103138. DOI: 10.1016/j.micron.2021.103138.
- Lesovoy, Dmitry M., Panagiota S. Georgoulia, Tammo Diercks, Irena Matečko-Burmann, Björn M. Burmann, Eduard V. Bocharov, Wolfgang Bermel, et al. (2021). “Unambiguous tracking of protein phosphorylation by fast high-resolution FOSY NMR”. In: *Angewandte Chemie (International ed. in English)*. DOI: 10.1002/anie.202102758.
- Li, Huadong, Yi Deng, Kang Sun, Haibin Yang, Jie Liu, Meiling Wang, Zhang Zhang, et al. (2017). “Structural basis of kindlin-mediated integrin recognition and activation”. In: *Proceedings of the National Academy of Sciences of the United States of America* 114.35, pp. 9349–9354. DOI: 10.1073/pnas.1703064114.
- Li, X. and R. B. Nicklas (1995). “Mitotic forces control a cell-cycle checkpoint”. In: *Nature* 373.6515, pp. 630–632. DOI: 10.1038/373630a0.
- Lityagina, Olga and Gergana Dobрева (2021). “The LINC Between Mechanical Forces and Chromatin”. In: *Frontiers in physiology* 12, p. 710809. DOI: 10.3389/fphys.2021.710809.
- Liu, Dan, Gerben Vader, Martijn J. M. Vromans, Michael A. Lampson, and Susanne M. A. Lens (2009). “Sensing chromosome bi-orientation by spatial separation of aurora B kinase from kinetochore substrates”. In: *Science (New York, N.Y.)* 323.5919, pp. 1350–1353. DOI: 10.1126/science.1167000.
- Liu, Jianmin, Koichi Fukuda, Zhen Xu, Yan-Qing Ma, Jamila Hirbawi, Xian Mao, Chuanyue Wu, et al. (2011). “Structural basis of phosphoinositide binding to kindlin-2 protein pleckstrin homology domain in regulating integrin activation”. In: *The Journal of biological chemistry* 286.50, pp. 43334–43342. DOI: 10.1074/jbc.M111.295352.
- Liu, Jie, Zhongzhen Liu, Keng Chen, Wei Chen, Xiyuan Fang, Meng Li, Xuening Zhou, et al. (2020). “Kindlin-2 promotes rear focal adhesion disassembly and directional persistence in cell migration”. In: *Journal of cell science*. DOI: 10.1242/jcs.244616.
- Liu, Yan, Yun Zhu, Sheng Ye, and Rongguang Zhang (2012). “Crystal structure of kindlin-2 PH domain reveals a conformational transition for its membrane anchoring and regulation of integrin activation”. In: *Protein & cell* 3.6, pp. 434–440. DOI: 10.1007/s13238-012-2046-1.
- Livne, Ariel and Benjamin Geiger (2016). “The inner workings of stress fibers - from contractile machinery to focal adhesions and back”. In: *Journal of cell science* 129.7, pp. 1293–1304. DOI: 10.1242/jcs.180927.
- Lorenz, Sonja, Ioannis Vakonakis, Edward D. Lowe, Iain D. Campbell, Martin E. M. Noble, and Maria K. Hoellerer (2008). “Structural analysis of the interactions between paxillin LD motifs and alpha-parvin”. In: *Structure (London, England : 1993)* 16.10, pp. 1521–1531. DOI: 10.1016/j.str.2008.08.007.
- Lucet, Isabelle S. and James M. Murphy (2018). “CHAPTER 13. A Structural Perspective of the Pseudokinome: Defining the Targetable Space”. In: *Kinase Drug Discovery*. Ed. by Richard A. Ward and Frederick W. Goldberg. Drug Discovery. Cambridge: Royal Society of Chemistry, pp. 359–380. DOI: 10.1039/9781788013093-00359.

- Mace, Peter D. and James M. Murphy (2021). “There’s more to death than life: Noncatalytic functions in kinase and pseudokinase signaling”. In: *The Journal of biological chemistry* 296, p. 100705. DOI: 10.1016/j.jbc.2021.100705.
- Mackinnon, A. Craig, Hiroshi Qadota, Kenneth R. Norman, Donald G. Moerman, and Benjamin D. Williams (2002). “C. elegans PAT-4/ILK functions as an adaptor protein within integrin adhesion complexes”. In: *Current biology : CB* 12.10, pp. 787–797.
- Mammen Regy, Roshan, Wenwei Zheng, and Jeetain Mittal (2021). “Using a sequence-specific coarse-grained model for studying protein liquid-liquid phase separation”. In: *Methods in enzymology* 646, pp. 1–17. DOI: 10.1016/bs.mie.2020.07.009.
- Manning, G., D. B. Whyte, R. Martinez, T. Hunter, and S. Sudarsanam (2002). “The protein kinase complement of the human genome”. In: *Science (New York, N.Y.)* 298.5600, pp. 1912–1934. DOI: 10.1126/science.1075762.
- Mao, Albert H., Scott L. Crick, Andreas Vitalis, Caitlin L. Chicoine, and Rohit V. Pappu (2010). “Net charge per residue modulates conformational ensembles of intrinsically disordered proteins”. In: *Proceedings of the National Academy of Sciences of the United States of America* 107.18, pp. 8183–8188. DOI: 10.1073/pnas.0911107107.
- Maresca, Thomas J. and Edward D. Salmon (2009). “Intrakinetochore stretch is associated with changes in kinetochore phosphorylation and spindle assembly checkpoint activity”. In: *The Journal of cell biology* 184.3, pp. 373–381. DOI: 10.1083/jcb.200808130.
- Marion, Dominique (2013). “An introduction to biological NMR spectroscopy”. In: *Molecular & cellular proteomics : MCP* 12.11, pp. 3006–3025. DOI: 10.1074/mcp.0113.030239.
- Maritan, Martina, Ludovic Autin, Jonathan Karr, Markus W. Covert, Arthur J. Olson, and David S. Goodsell (2022). “Building Structural Models of a Whole Mycoplasma Cell”. In: *Journal of molecular biology* 434.2, p. 167351. DOI: 10.1016/j.jmb.2021.167351.
- Martin, Erik W. and Alex S. Holehouse (2020). “Intrinsically disordered protein regions and phase separation: sequence determinants of assembly or lack thereof”. In: *Emerging Topics in Life Sciences* 4.3, pp. 307–329.
- Martin, Erik W., Alex S. Holehouse, Christy R. Grace, Alex Hughes, Rohit V. Pappu, and Tanja Mittag (2016). “Sequence Determinants of the Conformational Properties of an Intrinsically Disordered Protein Prior to and upon Multisite Phosphorylation”. In: *Journal of the American Chemical Society* 138.47, pp. 15323–15335. DOI: 10.1021/jacs.6b10272.
- Martin, Isabel M., Camilo Aponte-Santamaría, Lisa Schmidt, Marius Hedtfeld, Adel Iusupov, Andrea Musacchio, and Frauke Gräter (2022). “Phosphorylation tunes elongation propensity and cohesiveness of INCENP’s intrinsically disordered region”. In: *Journal of molecular biology* 434.1, p. 167387. DOI: 10.1016/j.jmb.2021.167387.
- Martin, Isabel M., Michele M. Nava, Sara A. Wickström, and Frauke Gräter (2022). “ATP allosterically stabilizes integrin-linked kinase for efficient force generation”. In: *Proceedings of the National Academy of Sciences of the United States of America* 119.11, e2106098119. DOI: 10.1073/pnas.2106098119.

- Martino, Fabiana, Ana R. Perestrelo, Vladimír Vinarský, Stefania Pagliari, and Giancarlo Forte (2018). “Cellular Mechanotransduction: From Tension to Function”. In: *Frontiers in physiology* 9, p. 824. DOI: 10.3389/fphys.2018.00824.
- Mattè, Alessandro, Enrica Federti, Elena Tibaldi, Maria Luisa Di Paolo, Giovanni Bisello, Mariarita Bertoldi, Andrea Carpentieri, et al. (2021). “Tyrosine Phosphorylation Modulates Peroxiredoxin-2 Activity in Normal and Diseased Red Cells”. In: *Antioxidants (Basel, Switzerland)* 10.2. DOI: 10.3390/antiox10020206.
- Maydan, Mykola, Paul C. McDonald, Jasbinder Sanghera, Jun Yan, Charalampos Rallis, Sheena Pinchin, Gregory E. Hannigan, et al. (2010). “Integrin-linked kinase is a functional Mn²⁺-dependent protein kinase that regulates glycogen synthase kinase-3beta(GSK-3beta) phosphorylation”. In: *PLoS one* 5.8, e12356. DOI: 10.1371/journal.pone.0012356.
- Meagher, Kristin L., Luke T. Redman, and Heather A. Carlson (2003). “Development of polyphosphate parameters for use with the AMBER force field”. In: *Journal of computational chemistry* 24.9, pp. 1016–1025. DOI: 10.1002/jcc.10262.
- Miller, Cayla M., Young C. Kim, and Jeetain Mittal (2016). “Protein Composition Determines the Effect of Crowding on the Properties of Disordered Proteins”. In: *Biophysical journal* 111.1, pp. 28–37. DOI: 10.1016/j.bpj.2016.05.033.
- Möbitz, Henrik (2015). “The ABC of protein kinase conformations”. In: *Biochimica et biophysica acta* 1854.10 Pt B, pp. 1555–1566. DOI: 10.1016/j.bbapap.2015.03.009.
- Mofrad, M. R. Kaazempur, J. Golji, N. A. Abdul Rahim, and R. D. Kamm (2004). “Force-induced unfolding of the focal adhesion targeting domain and the influence of paxillin binding”. In: *Mechanics & chemistry of biosystems : MCB* 1.4, pp. 253–265.
- Montanez, Eloi, Siegfried Ussar, Martina Schifferer, Michael Bösl, Roy Zent, Markus Moser, and Reinhard Fässler (2008). “Kindlin-2 controls bidirectional signaling of integrins”. In: *Genes & development* 22.10, pp. 1325–1330. DOI: 10.1101/gad.469408.
- Morris, Owen Michael, James Hilary Torpey, and Rivka Leah Isaacson (2021). “Intrinsically disordered proteins: modes of binding with emphasis on disordered domains”. In: *Open biology* 11.10, p. 210222. DOI: 10.1098/rsob.210222.
- Mugabo, Yves and Gareth E. Lim (2018). “Scaffold Proteins: From Coordinating Signaling Pathways to Metabolic Regulation”. In: *Endocrinology* 159.11, pp. 3615–3630. DOI: 10.1210/en.2018-00705.
- Müller-Späth, Sonja, Andrea Soranno, Verena Hirschfeld, Hagen Hofmann, Stefan Rügger, Luc Reymond, Daniel Nettels, et al. (2010). “Charge interactions can dominate the dimensions of intrinsically disordered proteins”. In: *Proceedings of the National Academy of Sciences of the United States of America* 107.33, pp. 14609–14614. DOI: 10.1073/pnas.1001743107.
- Murphy, James M., Peter E. Czabotar, Joanne M. Hildebrand, Isabelle S. Lucet, Jian-Guo Zhang, Silvia Alvarez-Diaz, Rowena Lewis, et al. (2013). “The pseudokinase MLKL mediates necroptosis via a molecular switch mechanism”. In: *Immunity* 39.3, pp. 443–453. DOI: 10.1016/j.immuni.2013.06.018.

- Murphy, James M., Isabelle S. Lucet, Joanne M. Hildebrand, Maria C. Tanzer, Samuel N. Young, Pooja Sharma, Guillaume Lessene, et al. (2014). “Insights into the evolution of divergent nucleotide-binding mechanisms among pseudokinases revealed by crystal structures of human and mouse MLKL”. In: *The Biochemical journal* 457.3, pp. 369–377. DOI: 10.1042/BJ20131270.
- Musacchio, Andrea (2022). “On the role of phase separation in the biogenesis of membraneless compartments”. In: *The EMBO journal*, e109952. DOI: 10.15252/embj.2021109952.
- Musacchio, Andrea and Edward D. Salmon (2007). “The spindle-assembly checkpoint in space and time”. In: *Nature reviews. Molecular cell biology* 8.5, pp. 379–393. DOI: 10.1038/nrm2163.
- Nandi, Tathagata and Sri Rama Koti Ainavarapu (2021). “Applications of atomic force microscopy in modern biology”. In: *Emerging topics in life sciences* 5.1, pp. 103–111. DOI: 10.1042/ETLS20200255.
- Nezi, Luigi and Andrea Musacchio (2009). “Sister chromatid tension and the spindle assembly checkpoint”. In: *Current opinion in cell biology* 21.6, pp. 785–795. DOI: 10.1016/j.ceb.2009.09.007.
- Nicklas, R. B. (1997). “How cells get the right chromosomes”. In: *Science (New York, N.Y.)* 275.5300, pp. 632–637. DOI: 10.1126/science.275.5300.632.
- Nicklas, R. B. and C. A. Koch (1969). “Chromosome micromanipulation. 3. Spindle fiber tension and the reorientation of mal-oriented chromosomes”. In: *The Journal of cell biology* 43.1, pp. 40–50. DOI: 10.1083/jcb.43.1.40.
- Nicklas, R. B. and S. C. Ward (1994). “Elements of error correction in mitosis: microtubule capture, release, and tension”. In: *The Journal of cell biology* 126.5, pp. 1241–1253. DOI: 10.1083/jcb.126.5.1241.
- Nikolopoulos, S. N. and C. E. Turner (2001). “Integrin-linked kinase (ILK) binding to paxillin LD1 motif regulates ILK localization to focal adhesions”. In: *The Journal of biological chemistry* 276.26, pp. 23499–23505. DOI: 10.1074/jbc.M102163200.
- Nolen, Brad, Susan Taylor, and Gourisankar Ghosh (2004). “Regulation of protein kinases; controlling activity through activation segment conformation”. In: *Molecular cell* 15.5, pp. 661–675. DOI: 10.1016/j.molcel.2004.08.024.
- Oakes, Patrick W., Yvonne Beckham, Jonathan Stricker, and Margaret L. Gardel (2012). “Tension is required but not sufficient for focal adhesion maturation without a stress fiber template”. In: *The Journal of cell biology* 196.3, pp. 363–374. DOI: 10.1083/jcb.201107042.
- Oates, Matt E., Pedro Romero, Takashi Ishida, Mohamed Ghalwash, Marcin J. Mizianty, Bin Xue, Zsuzsanna Dosztányi, et al. (2013). “D²P²: database of disordered protein predictions”. In: *Nucleic acids research* 41.Database issue, pp. D508–16. DOI: 10.1093/nar/gks1226.
- Olmos, Gemma, Susana López-Ongil, and Maria Piedad Ruiz Torres (2017). “Integrin-linked kinase: A new actor in the ageing process?” In: *Experimental gerontology* 100, pp. 87–90. DOI: 10.1016/j.exger.2017.10.026.
- Olski, T. M., A. A. Noegel, and E. Korenbaum (2001). “Parvin, a 42 kDa focal adhesion protein, related to the alpha-actinin superfamily”. In: *Journal of cell science* 114.Pt 3, pp. 525–538.

- Osorio, Daniel, Paola Rondón-Villarreal, and Rodrigo Torres (2015). “Peptides: A Package for Data Mining of Antimicrobial Peptides”. In: *The R Journal* 7.1, p. 4. DOI: 10.32614/RJ-2015-001.
- Palmere, Robert D., David A. Case, and Andrew J. Nieuwkoop (2021). “Simulations of Kindlin-2 PIP Binding Domains Reveal Protonation-Dependent Membrane Binding Modes”. In: *Biophysical journal*. DOI: 10.1016/j.bpj.2021.11.021.
- Panagiotopoulos, Athanassios Z., Vicky Wong, and M. Antonio Floriano (1998). “Phase Equilibria of Lattice Polymers from Histogram Reweighting Monte Carlo Simulations”. In: *Macromolecules* 31.3, pp. 912–918. DOI: 10.1021/ma971108a.
- Papini, Diana, Xavier Fant, Hiromi Ogawa, Nathalie Desban, Kumiko Samejima, Omid Feizbakhsh, Bilge Askin, et al. (2019). “Cell cycle-independent furrowing triggered by phosphomimetic mutations of the INCENP STD motif requires Plk1”. In: *Journal of cell science* 132.21. DOI: 10.1242/jcs.234401..
- Parrinello, M. and A. Rahman (1981). “Polymorphic transitions in single crystals: A new molecular dynamics method”. In: *Journal of Applied Physics* 52.12, pp. 7182–7190. DOI: 10.1063/1.328693.
- Pelham, R. J. and Y. I. Wang (1997). “Cell locomotion and focal adhesions are regulated by substrate flexibility”. In: *Proceedings of the National Academy of Sciences of the United States of America* 94.25, pp. 13661–13665. DOI: 10.1073/pnas.94.25.13661.
- Perdikari, Theodora Myrto, Nina Jovic, Gregory L. Dignon, Young C. Kim, Nicolas L. Fawzi, and Jeetain Mittal (2021). “A predictive coarse-grained model for position-specific effects of post-translational modifications”. In: *Biophysical journal* 120.7, pp. 1187–1197. DOI: 10.1016/j.bpj.2021.01.034.
- Perera, H. Dhanuja, Yan-Qing Ma, Jun Yang, Jamila Hirbawi, Edward F. Plow, and Jun Qin (2011). “Membrane binding of the N-terminal ubiquitin-like domain of kindlin-2 is crucial for its regulation of integrin activation”. In: *Structure (London, England : 1993)* 19.11, pp. 1664–1671. DOI: 10.1016/j.str.2011.08.012.
- Persad, S., S. Attwell, V. Gray, N. Mawji, J. T. Deng, D. Leung, J. Yan, et al. (2001). “Regulation of protein kinase B/Akt-serine 473 phosphorylation by integrin-linked kinase: critical roles for kinase activity and amino acids arginine 211 and serine 343”. In: *The Journal of biological chemistry* 276.29, pp. 27462–27469. DOI: 10.1074/jbc.M102940200.
- Petsalaki, Eleni and George Zachos (2021). “An ATM-Chk2-INCENP pathway activates the abscission checkpoint”. In: *The Journal of cell biology* 220.2. DOI: 10.1083/jcb.202008029.
- Pettersen, Eric F., Thomas D. Goddard, Conrad C. Huang, Gregory S. Couch, Daniel M. Greenblatt, Elaine C. Meng, and Thomas E. Ferrin (2004). “UCSF Chimera—a visualization system for exploratory research and analysis”. In: *Journal of computational chemistry* 25.13, pp. 1605–1612. DOI: 10.1002/jcc.20084.
- Piana, Stefano, Alexander G. Donchev, Paul Robustelli, and David E. Shaw (2015). “Water dispersion interactions strongly influence simulated structural properties of disordered protein states”. In: *The journal of physical chemistry. B* 119.16, pp. 5113–5123. DOI: 10.1021/jp508971m.

- Qadota, Hiroshi, Donald G. Moerman, and Guy M. Benian (2012). “A molecular mechanism for the requirement of PAT-4 (integrin-linked kinase (ILK)) for the localization of UNC-112 (Kindlin) to integrin adhesion sites”. In: *The Journal of biological chemistry* 287.34, pp. 28537–28551. DOI: 10.1074/jbc.M112.354852.
- Qin, Ruifang, Heidrun Schmid, Christin Münzberg, Ulrike Maass, Denis Krndija, Guido Adler, Thomas Seufferlein, et al. (2015). “Phosphorylation and turnover of paxillin in focal contacts is controlled by force and defines the dynamic state of the adhesion site”. In: *Cytoskeleton (Hoboken, N.J.)* 72.2, pp. 101–112. DOI: 10.1002/cm.21209.
- Radom, Filip, Andreas Plückthun, and Emanuele Paci (2018). “Assessment of ab initio models of protein complexes by molecular dynamics”. In: *PLoS computational biology* 14.6, e1006182. DOI: 10.1371/journal.pcbi.1006182.
- Radovanac, Korana, Jessica Morgner, Jan-Niklas Schulz, Katrin Blumbach, Cam Patterson, Tamar Geiger, Matthias Mann, et al. (2013). “Stabilization of integrin-linked kinase by the Hsp90-CHIP axis impacts cellular force generation, migration and the fibrotic response”. In: *The EMBO journal* 32.10, pp. 1409–1424. DOI: 10.1038/emboj.2013.90.
- Rahikainen, Rolle, Tiina Öhman, Paula Turkki, Markku Varjosalo, and Vesa P. Hytönen (2019). “Talin-mediated force transmission and talin rod domain unfolding independently regulate adhesion signaling”. In: *Journal of cell science* 132.7. DOI: 10.1242/jcs.226514.
- Ribeiro, António J. M., Sayoni Das, Natalie Dawson, Rossana Zaru, Sandra Orchard, Janet M. Thornton, Christine Orengo, et al. (2019). “Emerging concepts in pseudoenzyme classification, evolution, and signaling”. In: *Science signaling* 12.594. DOI: 10.1126/scisignal.aat9797.
- Ricca, Benjamin L., Gautham Venugopalan, and Daniel A. Fletcher (2013). “To pull or be pulled: parsing the multiple modes of mechanotransduction”. In: *Current opinion in cell biology* 25.5, pp. 558–564. DOI: 10.1016/j.ceb.2013.06.002.
- Rico, Felix, Andreas Russek, Laura González, Helmut Grubmüller, and Simon Scheuring (2019). “Heterogeneous and rate-dependent streptavidin-biotin unbinding revealed by high-speed force spectroscopy and atomistic simulations”. In: *Proceedings of the National Academy of Sciences of the United States of America* 116.14, pp. 6594–6601. DOI: 10.1073/pnas.1816909116.
- Ridley, Anne J., Martin A. Schwartz, Keith Burridge, Richard A. Firtel, Mark H. Ginsberg, Gary Borisy, J. Thomas Parsons, et al. (2003). “Cell migration: integrating signals from front to back”. In: *Science (New York, N.Y.)* 302.5651, pp. 1704–1709. DOI: 10.1126/science.1092053.
- Rieloff, Ellen and Marie Skepö (2021a). “Molecular Dynamics Simulations of Phosphorylated Intrinsically Disordered Proteins: A Force Field Comparison”. In: *International journal of molecular sciences* 22.18. DOI: 10.3390/ijms221810174.
- (2021b). “The Effect of Multisite Phosphorylation on the Conformational Properties of Intrinsically Disordered Proteins”. In: *International journal of molecular sciences* 22.20. DOI: 10.3390/ijms222011058.
- Roca-Cusachs, Pere, Vito Conte, and Xavier Trepat (2017). “Quantifying forces in cell biology”. In: *Nature cell biology* 19.7, pp. 742–751. DOI: 10.1038/ncb3564.

- Roscioli, Emanuele, Tsvetelina E. Germanova, Christopher A. Smith, Peter A. Embacher, Muriel Erent, Amelia I. Thompson, Nigel J. Burroughs, et al. (2020). “Ensemble-Level Organization of Human Kinetochores and Evidence for Distinct Tension and Attachment Sensors”. In: *Cell reports* 31.4, p. 107535. DOI: 10.1016/j.celrep.2020.107535.
- Roskoski, Robert (2021). “Properties of FDA-approved small molecule protein kinase inhibitors: A 2021 update”. In: *Pharmacological research* 165, p. 105463. DOI: 10.1016/j.phrs.2021.105463.
- Ruff, Kiersten M. and Rohit V. Pappu (2021). “AlphaFold and Implications for Intrinsically Disordered Proteins”. In: *Journal of molecular biology* 433.20, p. 167208. DOI: 10.1016/j.jmb.2021.167208.
- Sakai, Takao, Shaohua Li, Denitsa Docheva, Carsten Grashoff, Keiko Sakai, Günter Kostka, Attila Braun, et al. (2003). “Integrin-linked kinase (ILK) is required for polarizing the epiblast, cell adhesion, and controlling actin accumulation”. In: *Genes & development* 17.7, pp. 926–940. DOI: 10.1101/gad.255603.
- Sally P. Wheatley, Stefanie E. Kandels-Lewis, Richard R. Adams, Alexandra M. Ainsztein, and William C. Earnshaw (2001). “INCENP binds directly to tubulin and requires dynamic microtubules to target to the cleavage furrow”. In: *Experimental cell research* 262.2, pp. 122–127. DOI: 10.1006/excr.2000.5088.
- Samejima, Kumiko, Melpomeni Platani, Marcin Wolny, Hiromi Ogawa, Giulia Vargiu, Peter J. Knight, Michelle Peckham, et al. (2015). “The Inner Centromere Protein (INCENP) Coil Is a Single alpha-Helix (SAH) Domain That Binds Directly to Microtubules and Is Important for Chromosome Passenger Complex (CPC) Localization and Function in Mitosis”. In: *The Journal of biological chemistry* 290.35, pp. 21460–21472. DOI: 10.1074/jbc.M115.645317.
- Sanchez, Isaac C. and Robert H. Lacombe (1976). “An elementary molecular theory of classical fluids. Pure fluids”. In: *The Journal of Physical Chemistry* 80.21, pp. 2352–2362. DOI: 10.1021/j100562a008.
- (1978). “Statistical Thermodynamics of Polymer Solutions”. In: *Macromolecules* 11.6, pp. 1145–1156. DOI: 10.1021/ma60066a017.
- Santaguida, Stefano and Andrea Musacchio (2009). “The life and miracles of kinetochores”. In: *The EMBO journal* 28.17, pp. 2511–2531. DOI: 10.1038/emboj.2009.173.
- Scheeff, Eric D., Jeyanthi Eswaran, Gabor Bunkoczi, Stefan Knapp, and Gerard Manning (2009). “Structure of the pseudokinase VRK3 reveals a degraded catalytic site, a highly conserved kinase fold, and a putative regulatory binding site”. In: *Structure (London, England : 1993)* 17.1, pp. 128–138. DOI: 10.1016/j.str.2008.10.018.
- Schiller, Herbert B., Caroline C. Friedel, Cyril Boulegue, and Reinhard Fässler (2011). “Quantitative proteomics of the integrin adhesome show a myosin II-dependent recruitment of LIM domain proteins”. In: *EMBO reports* 12.3, pp. 259–266. DOI: 10.1038/embor.2011.5.
- Schindelin, Johannes, Ignacio Arganda-Carreras, Erwin Frise, Verena Kaynig, Mark Longair, Tobias Pietzsch, Stephan Preibisch, et al. (2012). “Fiji: an open-source platform for biological-image analysis”. In: *Nature methods* 9.7, pp. 676–682. DOI: 10.1038/nmeth.2019.

- Schneider, S. W., S. Nuschele, A. Wixforth, C. Gorzelanny, A. Alexander-Katz, R. R. Netz, and M. F. Schneider (2007). “Shear-induced unfolding triggers adhesion of von Willebrand factor fibers”. In: *Proceedings of the National Academy of Sciences of the United States of America* 104.19, pp. 7899–7903. DOI: 10.1073/pnas.0608422104.
- Scholey, Jonathan M., Ingrid Brust-Mascher, and Alex Mogilner (2003). “Cell division”. In: *Nature* 422.6933, pp. 746–752. DOI: 10.1038/nature01599.
- Schopf, Florian H., Maximilian M. Biebl, and Johannes Buchner (2017). “The HSP90 chaperone machinery”. In: *Nature reviews. Molecular cell biology* 18.6, pp. 345–360. DOI: 10.1038/nrm.2017.20.
- Schrödinger, LLC (Nov. 2015). “The PyMOL Molecular Graphics System, Version 1.8”.
- Sepulveda, J. L. and C. Wu (2006). “The parvins”. In: *Cellular and molecular life sciences : CMLS* 63.1, pp. 25–35. DOI: 10.1007/s00018-005-5355-1.
- Sessa, Fabio, Marina Mapelli, Claudio Ciferri, Cataldo Tarricone, Liliana B. Areces, Thomas R. Schneider, P. Todd Stukenberg, et al. (2005). “Mechanism of Aurora B activation by INCENP and inhibition by hesperadin”. In: *Molecular cell* 18.3, pp. 379–391. DOI: 10.1016/j.molcel.2005.03.031.
- Shea, Joan-Emma, Robert B. Best, and Jeetain Mittal (2021). “Physics-based computational and theoretical approaches to intrinsically disordered proteins”. In: *Current opinion in structural biology* 67, pp. 219–225. DOI: 10.1016/j.sbi.2020.12.012.
- Sheridan, Steven, Frauke Gräter, and Csaba Daday (2019). “How Fast Is Too Fast in Force-Probe Molecular Dynamics Simulations?” In: *The journal of physical chemistry. B* 123.17, pp. 3658–3664. DOI: 10.1021/acs.jpcc.9b01251.
- Shi, Yigong (2014). “A glimpse of structural biology through X-ray crystallography”. In: *Cell* 159.5, pp. 995–1014. DOI: 10.1016/j.cell.2014.10.051.
- Singharoy, Abhishek, Christopher Maffeo, Karelia H. Delgado-Magnero, David J. K. Swainsbury, Melih Sener, Ulrich Kleinekathöfer, John W. Vant, et al. (2019). “Atoms to Phenotypes: Molecular Design Principles of Cellular Energy Metabolism”. In: *Cell* 179.5, 1098–1111.e23. DOI: 10.1016/j.cell.2019.10.021.
- Sittel, Florian, Abhinav Jain, and Gerhard Stock (2014). “Principal component analysis of molecular dynamics: on the use of Cartesian vs. internal coordinates”. In: *The Journal of Chemical Physics* 141.1, p. 014111. DOI: 10.1063/1.4885338.
- Smith, Chris A., Andrew D. McAinsh, and Nigel J. Burroughs (2016). “Human kinetochores are swivel joints that mediate microtubule attachments”. In: *eLife* 5, e16159. DOI: 10.7554/eLife.16159.
- Smith, Lucas R., Sangkyun Cho, and Dennis E. Discher (2018). “Stem Cell Differentiation is Regulated by Extracellular Matrix Mechanics”. In: *Physiology (Bethesda, Md.)* 33.1, pp. 16–25. DOI: 10.1152/physiol.00026.2017.
- Stacklies, Wolfram, Christian Seifert, and Frauke Graeter (2011). “Implementation of force distribution analysis for molecular dynamics simulations”. In: *BMC bioinformatics* 12, p. 101. DOI: 10.1186/1471-2105-12-101.

- Stanchi, Fabio, Carsten Grashoff, Carine Flore Nguemini Yonga, Dominique Grall, Reinhard Fässler, and Ellen van Obberghen-Schilling (2009). “Molecular dissection of the ILK-PINCH-parvin triad reveals a fundamental role for the ILK kinase domain in the late stages of focal-adhesion maturation”. In: *Journal of cell science* 122.Pt 11, pp. 1800–1811. DOI: 10.1242/jcs.044602.
- Stiegler, Amy L., Thomas D. Grant, Joseph R. Luft, David A. Calderwood, Edward H. Snell, and Titus J. Boggon (2013). “Purification and SAXS analysis of the integrin linked kinase, PINCH, parvin (IPP) heterotrimeric complex”. In: *PloS one* 8.1, e55591. DOI: 10.1371/journal.pone.0055591.
- Strodel, Birgit (2021). “Energy Landscapes of Protein Aggregation and Conformation Switching in Intrinsically Disordered Proteins”. In: *Journal of molecular biology* 433.20, p. 167182. DOI: 10.1016/j.jmb.2021.167182.
- Sugita, Yuji and Yuko Okamoto (1999). “Replica-exchange molecular dynamics method for protein folding”. In: *Chemical Physics Letters* 314.1-2, pp. 141–151. DOI: 10.1016/S0009-2614(99)01123-9.
- Suzuki, Aussie, Benjamin L. Badger, Xiaohu Wan, Jennifer G. DeLuca, and Edward D. Salmon (2014). “The architecture of CCAN proteins creates a structural integrity to resist spindle forces and achieve proper Intrakinetochore stretch”. In: *Developmental cell* 30.6, pp. 717–730. DOI: 10.1016/j.devcel.2014.08.003.
- Suzuki, Aussie, Sarah K. Long, and Edward D. Salmon (2018). “An optimized method for 3D fluorescence co-localization applied to human kinetochore protein architecture”. In: *eLife* 7, e32418. DOI: 10.7554/eLife.32418.
- Tanaka, Tomoyuki U., Najma Rachidi, Carsten Janke, Gislene Pereira, Marta Galova, Elmar Schiebel, Michael J. R. Stark, et al. (2002). “Evidence that the Ipl1-Sli15 (Aurora kinase-INCENP) complex promotes chromosome bi-orientation by altering kinetochore-spindle pole connections”. In: *Cell* 108.3, pp. 317–329. DOI: 10.1016/s0092-8674(02)00633-5.
- Tapia-Rojo, Rafael, Alvaro Alonso-Caballero, and Julio M. Fernandez (2020). “Direct observation of a coil-to-helix contraction triggered by vinculin binding to talin”. In: *Science advances* 6.21, eaaz4707. DOI: 10.1126/sciadv.aaz4707.
- Tauchman, Eric C., Frederick J. Boehm, and Jennifer G. DeLuca (2015). “Stable kinetochore-microtubule attachment is sufficient to silence the spindle assembly checkpoint in human cells”. In: *Nature communications* 6, p. 10036. DOI: 10.1038/ncomms10036.
- Tesei, Giulio, Thea K. Schulze, Ramon Crehuet, and Kresten Lindorff-Larsen (2021). “Accurate model of liquid-liquid phase behavior of intrinsically disordered proteins from optimization of single-chain properties”. In: *Proceedings of the National Academy of Sciences of the United States of America* 118.44. DOI: 10.1073/pnas.2111696118.
- Tinevez, Jean-Yves, Nick Perry, Johannes Schindelin, Genevieve M. Hoopes, Gregory D. Reynolds, Emmanuel Laplantine, Sebastian Y. Bednarek, et al. (2017). “TrackMate: An open and extensible platform for single-particle tracking”. In: *Methods (San Diego, Calif.)* 115, pp. 80–90. DOI: 10.1016/j.ymeth.2016.09.016.

- Tojkander, Sari, Gergana Gateva, and Pekka Lappalainen (2012). “Actin stress fibers—assembly, dynamics and biological roles”. In: *Journal of cell science* 125.Pt 8, pp. 1855–1864. DOI: 10.1242/jcs.098087.
- Treat, Xavier, Zaozao Chen, and Ken Jacobson (2012). “Cell migration”. In: *Comprehensive Physiology* 2.4, pp. 2369–2392. DOI: 10.1002/cphy.c110012.
- Trivedi, Prasad, Francesco Palomba, Ewa Niedzialkowska, Michelle A. Digman, Enrico Gratton, and P. Todd Stukenberg (2019). “The inner centromere is a biomolecular condensate scaffolded by the chromosomal passenger complex”. In: *Nature cell biology* 21.9, pp. 1127–1137. DOI: 10.1038/s41556-019-0376-4.
- Trivedi, Prasad and P. Todd Stukenberg (2020). “A Condensed View of the Chromosome Passenger Complex”. In: *Trends in cell biology*. DOI: 10.1016/j.tcb.2020.06.005.
- Tseng, Qingzong, Irene Wang, Eve Duchemin-Pelletier, Ammar Azioune, Nicolas Carpi, Jie Gao, Odile Filhol, et al. (2011). “A new micropatterning method of soft substrates reveals that different tumorigenic signals can promote or reduce cell contraction levels”. In: *Lab on a chip* 11.13, pp. 2231–2240. DOI: 10.1039/c01c00641f.
- Tu, Y., Y. Huang, Y. Zhang, Y. Hua, and C. Wu (2001). “A new focal adhesion protein that interacts with integrin-linked kinase and regulates cell adhesion and spreading”. In: *The Journal of cell biology* 153.3, pp. 585–598. DOI: 10.1083/jcb.153.3.585.
- Valli, Jessica, Adrian Garcia-Burgos, Liam M. Rooney, Beatriz Vale de Melo E Oliveira, Rory R. Duncan, and Colin Rickman (2021). “Seeing beyond the limit: A guide to choosing the right super-resolution microscopy technique”. In: *The Journal of biological chemistry* 297.1, p. 100791. DOI: 10.1016/j.jbc.2021.100791.
- van Zundert, G. C. P., J. P. G. L. M. Rodrigues, M. Trellet, C. Schmitz, P. L. Kastiris, E. Karaca, A. S. J. Melquiond, et al. (2016). “The HADDOCK2.2 Web Server: User-Friendly Integrative Modeling of Biomolecular Complexes”. In: *Journal of molecular biology* 428.4, pp. 720–725. DOI: 10.1016/j.jmb.2015.09.014.
- Vaynberg, Julia, Koichi Fukuda, Fan Lu, Katarzyna Bialkowska, Yinghua Chen, Edward F. Plow, and Jun Qin (2018). “Non-catalytic signaling by pseudokinase ILK for regulating cell adhesion”. In: *Nature communications* 9.1, p. 4465. DOI: 10.1038/s41467-018-06906-7.
- Velyvis, Algirdas, Julia Vaynberg, Yanwu Yang, Olga Vinogradova, Yongjun Zhang, Chuanyue Wu, and Jun Qin (2003). “Structural and functional insights into PINCH LIM4 domain-mediated integrin signaling”. In: *Nature structural biology* 10.7, pp. 558–564. DOI: 10.1038/nsb938.
- Verlet, Loup (1967). “Computer “Experiments” on Classical Fluids. I. Thermodynamical Properties of Lennard-Jones Molecules”. In: *Physical Review* 159.1, pp. 98–103. DOI: 10.1103/PhysRev.159.98.
- Vogel, Viola (2006). “Mechanotransduction involving multimodular proteins: converting force into biochemical signals”. In: *Annual review of biophysics and biomolecular structure* 35, pp. 459–488. DOI: 10.1146/annurev.biophys.35.040405.102013.
- Walter, H. and D. E. Brooks (1995). “Phase separation in cytoplasm, due to macromolecular crowding, is the basis for microcompartmentation”. In: *FEBS letters* 361.2-3, pp. 135–139. DOI: 10.1016/0014-5793(95)00159-7.

- Wang, Chenwei, Haodong Xu, Shaofeng Lin, Wankun Deng, Jiaqi Zhou, Ying Zhang, Ying Shi, et al. (2020). “GPS 5.0: An Update on the Prediction of Kinase-specific Phosphorylation Sites in Proteins”. In: *Genomics, proteomics & bioinformatics* 18.1, pp. 72–80. DOI: 10.1016/j.gpb.2020.01.001.
- Wang, Duolin, Dongpeng Liu, Jiakang Yuchi, Fei He, Yuexu Jiang, Siteng Cai, Jingyi Li, et al. (2020). “MusiteDeep: a deep-learning based webserver for protein post-translational modification site prediction and visualization”. In: *Nucleic acids research* 48.W1, W140–W146. DOI: 10.1093/nar/gkaa275.
- Wang, Xiaoxia, Koichi Fukuda, In-Ja Byeon, Algirdas Velyvis, Chuanyue Wu, Angela Gronenborn, and Jun Qin (2008). “The structure of alpha-parvin CH2-paxillin LD1 complex reveals a novel modular recognition for focal adhesion assembly”. In: *The Journal of biological chemistry* 283.30, pp. 21113–21119. DOI: 10.1074/jbc.M801270200.
- Wang, Yuan, Chunlei Zhang, Wenzhong Yang, ShiPeng Shao, Xinmin Xu, Yujie Sun, Pilog Li, et al. (2021). “LIMD1 phase separation contributes to cellular mechanics and durotaxis by regulating focal adhesion dynamics in response to force”. In: *Developmental cell* 56.9, 1313–1325.e7. DOI: 10.1016/j.devcel.2021.04.002.
- Warnecke, Andreas, Tatyana Sandalova, Adnane Achour, and Robert A. Harris (2014). “PyTMs: a useful PyMOL plugin for modeling common post-translational modifications”. In: *BMC bioinformatics* 15, p. 370. DOI: 10.1186/s12859-014-0370-6.
- Webb, Benjamin and Andrej Sali (2016). “Comparative Protein Structure Modeling Using MODELLER”. In: *Current protocols in bioinformatics* 54, pp. 5.6.1–5.6.37. DOI: 10.1002/cpbi.3.
- Webb, Donna J., J. Thomas Parsons, and Alan F. Horwitz (2002). “Adhesion assembly, disassembly and turnover in migrating cells – over and over and over again”. In: *Nature cell biology* 4.4, E97–100. DOI: 10.1038/ncb0402-e97.
- Welburn, Julie P. I., Mathijs Vleugel, Dan Liu, John R. Yates, Michael A. Lampson, Tatsuo Fukagawa, and Iain M. Cheeseman (2010). “Aurora B phosphorylates spatially distinct targets to differentially regulate the kinetochore-microtubule interface”. In: *Molecular cell* 38.3, pp. 383–392. DOI: 10.1016/j.molcel.2010.02.034.
- Wheelock, Michael S., David J. Wynne, Boo Shan Tseng, and Hironori Funabiki (2017). “Dual recognition of chromatin and microtubules by INCENP is important for mitotic progression”. In: *The Journal of cell biology* 216.4, pp. 925–941. DOI: 10.1083/jcb.201609061.
- Wickström, Sara A., Anika Lange, Eloi Montanez, and Reinhard Fässler (2010). “The ILK/PINCH/parvin complex: the kinase is dead, long live the pseudokinase!” In: *The EMBO journal* 29.2, pp. 281–291. DOI: 10.1038/emboj.2009.376.
- Wilson, Eric, John Vant, Jacob Layton, Ryan Boyd, Hyungro Lee, Matteo Turilli, Benjamín Hernández, et al. (2021). “Large-Scale Molecular Dynamics Simulations of Cellular Compartments”. In: *Methods in molecular biology (Clifton, N.J.)* 2302, pp. 335–356. DOI: 10.1007/978-1-0716-1394-8_18.
- Wu, Chuanyue (2004). “The PINCH-ILK-parvin complexes: assembly, functions and regulation”. In: *Biochimica et biophysica acta* 1692.2-3, pp. 55–62. DOI: 10.1016/j.bbamcr.2004.01.006.

- Xue, Yu, Ao Li, Lirong Wang, Huanqing Feng, and Xuebiao Yao (2006). “PPSP: prediction of PK-specific phosphorylation site with Bayesian decision theory”. In: *BMC bioinformatics* 7, p. 163. DOI: 10.1186/1471-2105-7-163.
- Yamaji, S., A. Suzuki, Y. Sugiyama, Y. Koide, M. Yoshida, H. Kanamori, H. Mohri, et al. (2001). “A novel integrin-linked kinase-binding protein, affixin, is involved in the early stage of cell-substrate interaction”. In: *The Journal of cell biology* 153.6, pp. 1251–1264. DOI: 10.1083/jcb.153.6.1251.
- Yamamoto, Eiji, Antreas C. Kalli, Kenji Yasuoka, and Mark S. P. Sansom (2016). “Interactions of Pleckstrin Homology Domains with Membranes: Adding Back the Bilayer via High-Throughput Molecular Dynamics”. In: *Structure (London, England : 1993)* 24.8, pp. 1421–1431. DOI: 10.1016/j.str.2016.06.002.
- Yang, Haibin, Leishu Lin, Kan Sun, Ting Zhang, Wan Chen, Lianghui Li, Yuchen Xie, et al. (2021). “Complex structures of Rsu1 and PINCH1 reveal a regulatory mechanism of the ILK/PINCH/Parvin complex for F-actin dynamics”. In: *eLife* 10, e64395. DOI: 10.7554/eLife.64395.
- Yoo, Tae Yeon, Jeong-Mo Choi, William Conway, Che-Hang Yu, Rohit V. Pappu, and Daniel J. Needleman (2018). “Measuring NDC80 binding reveals the molecular basis of tension-dependent kinetochore-microtubule attachments”. In: *eLife* 7, e36392. DOI: 10.7554/eLife.36392.
- Zapp, Christopher, Agnieszka Obarska-Kosinska, Benedikt Rennekamp, Markus Kurth, David M. Hudson, Davide Mercadante, Uladzimir Barayeu, et al. (2020). “Mechanoradicals in tensed tendon collagen as a source of oxidative stress”. In: *Nature communications* 11.1, p. 2315. DOI: 10.1074/jbc.M114.634915.
- Zeqiraj, Elton, Beatrice Maria Filippi, Simon Goldie, Iva Navratilova, Jérôme Boudeau, Maria Deak, Dario R. Alessi, et al. (2009). “ATP and MO25alpha regulate the conformational state of the STRADalpha pseudokinase and activation of the LKB1 tumour suppressor”. In: *PLoS biology* 7.6, e1000126. DOI: 10.1371/journal.pbio.1000126.
- Zeqiraj, Elton and Daan M. F. van Aalten (2010). “Pseudokinases-remnants of evolution or key allosteric regulators?” In: *Current opinion in structural biology* 20.6, pp. 772–781. DOI: 10.1016/j.sbi.2010.10.001.
- Zervas, C. G., S. L. Gregory, and N. H. Brown (2001). “Drosophila integrin-linked kinase is required at sites of integrin adhesion to link the cytoskeleton to the plasma membrane”. In: *The Journal of cell biology* 152.5, pp. 1007–1018. DOI: 10.1083/jcb.152.5.1007.
- Zhang, Manjuan, Fengrui Yang, Wenwen Wang, Najdat Zohbi, Xiwei Wang, Dongmei Wang, Xiaoxuan Zhuang, et al. (2022). “SKAP interacts with Aurora B to guide end-on capture of spindle microtubules via phase separation”. In: *Journal of molecular cell biology* 13.12, pp. 841–852. DOI: 10.1093/jmcb/mjab058.
- Zhang, Yongjun, Ka Chen, Yizeng Tu, Algirdas Velyvis, Yanwu Yang, Jun Qin, and Chuanyue Wu (2002). “Assembly of the PINCH-ILK-CH-ILKBP complex precedes and is essential for localization of each component to cell-matrix adhesion sites”. In: *Journal of cell science* 115.Pt 24, pp. 4777–4786. DOI: 10.1242/jcs.00166.

Zheng, Can-Can, Hui-Fang Hu, Pan Hong, Qi-Hua Zhang, Wen Wen Xu, Qing-Yu He, and Bin Li (2019). “Significance of integrin-linked kinase (ILK) in tumorigenesis and its potential implication as a biomarker and therapeutic target for human cancer”. In: *American journal of cancer research* 9.1, pp. 186–197.

Zhou, Jing, Camilo Aponte-Santamaría, Sebastian Sturm, Jakob Tómas Bullerjahn, Agnieszka Bronowska, and Frauke Gräter (2015). “Mechanism of Focal Adhesion Kinase Mechanosensing”. In: *PLoS computational biology* 11.11, e1004593. DOI: 10.1371/journal.pcbi.1004593.

Appendix for chapter 3: Integrin-linked kinase

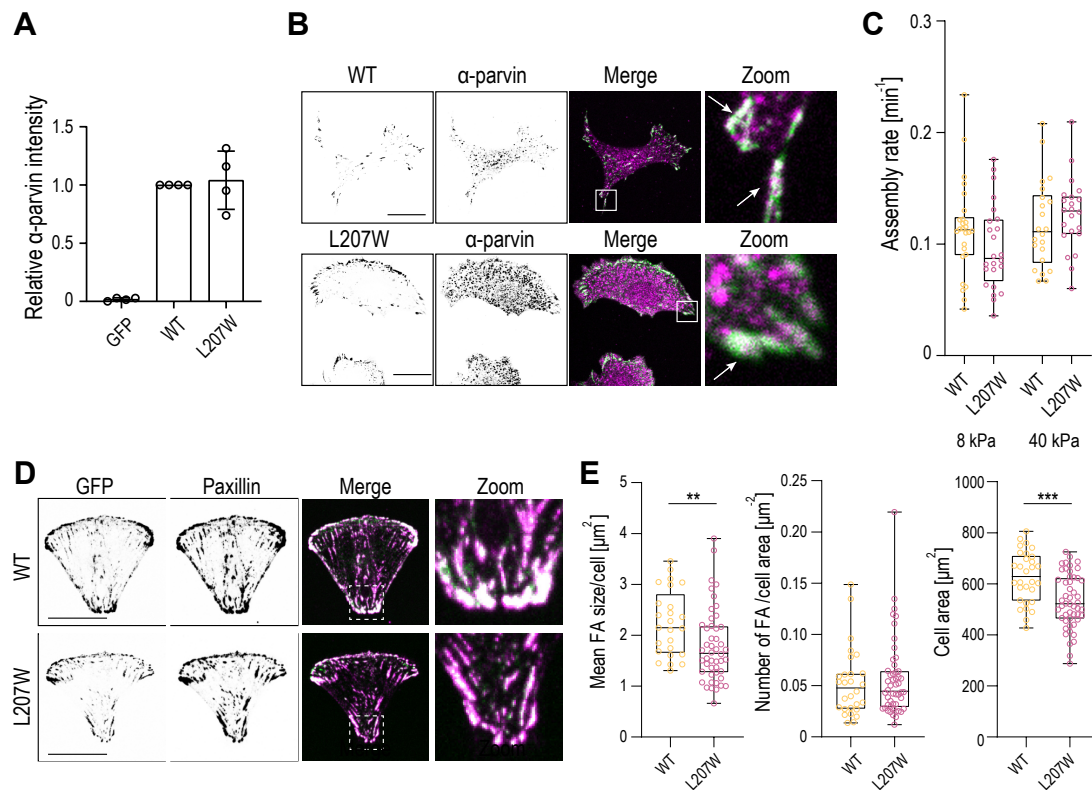


Fig. A.1.: Effect of disrupted ATP-binding to ILK. Experiments and figure including legend were provided by collaborators Dr. Michele Nava and Prof. Dr. Sara Wickström, University of Helsinki. (A) Quantification of α -parvin to GFP ratio from immunoprecipitation (mean \pm S.D., $n=4$ independent experiments). (B) Representative immunofluorescence images of α -parvin and GFP. α -parvin localizes at focal adhesions both in ILK(WT)-GFP and ILK(L207W)-GFP cells. Right panels show a zoom in of the area indicated by the white box. Arrows indicate colocalization of α -parvin (magenta) with ILK(WT)-GFP and ILK(L207W)-GFP (green). Scale bars $20\mu\text{m}$. (C) Quantification of FA assembly in ILK(WT)-GFP and ILK(L207W)-GFP cells plated on 8 kPa and 40 kPa substrates ($n > 22$ cells/condition pooled across 4 independent experiments). (D) Representative immunofluorescence images of ILK(WT)-GFP and ILK(L207W)-GFP cells stained with paxillin on crossbow micropatterned surfaces. Paxillin localizes at FAs in both conditions. Scale bars $20\mu\text{m}$. (E) Quantification of FA size and number as well as cell area. ($n > 25$ cells/condition pooled across 4 independent experiments. ** $p=0.0052$, *** $p=0.0004$, Mann-Whitney).

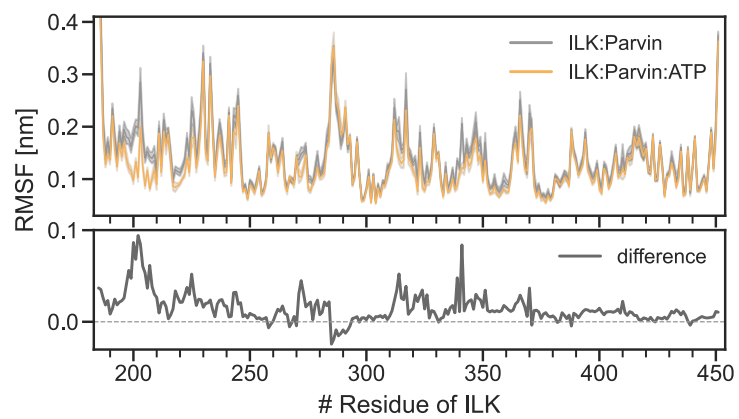


Fig. A.2.: Backbone root mean square fluctuation (RMSF) as a function of residue number for ILK holo (orange) and apo (grey). Error bands denote the 95 % confidence interval.

ID1	Protein	ID2	Protein	difference pairwise force [pN]	p-value
186	ILK	187	ILK	-16.38	0.031 517 102
190	ILK	192	ILK	-16.93	5.895 92 × 10 ⁻⁵
193	ILK	217	ILK	-18.16	0.001 014 099
193	ILK	219	ILK	18.75	1.104 47 × 10 ⁻⁵
194	ILK	195	ILK	-22.79	0.004 320 184
194	ILK	211	ILK	-43.21	0.000 509 073
195	ILK	208	ILK	-18.89	1.807 45 × 10 ⁻⁵
197	ILK	209	ILK	44.86	0.000 103 734
198	ILK	199	ILK	-36.32	1.104 47 × 10 ⁻⁵
198	ILK	200	ILK	-26.57	6.795 62 × 10 ⁻⁸
199	ILK	200	ILK	99.66	6.795 62 × 10 ⁻⁸
199	ILK	208	ILK	-21.41	6.795 62 × 10 ⁻⁸
199	ILK	271	ILK	22.23	3.705 12 × 10 ⁻⁵
199	ILK	323	ILK	33.04	6.795 62 × 10 ⁻⁸
200	ILK	201	ILK	128.52	6.795 62 × 10 ⁻⁸
200	ILK	202	ILK	124.32	6.795 62 × 10 ⁻⁸
200	ILK	206	ILK	16.73	0.000 247 061
200	ILK	207	ILK	-57.99	2.355 66 × 10 ⁻⁶
200	ILK	220	ILK	85.98	6.795 62 × 10 ⁻⁸
200	ILK	283	ILK	18.37	5.226 89 × 10 ⁻⁷
200	ILK	323	ILK	-20.14	0.001 782 376
201	ILK	202	ILK	24.72	0.002 341 273
201	ILK	205	ILK	34.27	7.898 03 × 10 ⁻⁸
201	ILK	206	ILK	53.72	9.172 77 × 10 ⁻⁸
201	ILK	223	ILK	-56.78	6.014 8 × 10 ⁻⁷
202	ILK	204	ILK	-56.31	0.000 509 073
202	ILK	205	ILK	-61.46	0.000 160 981
202	ILK	220	ILK	62.63	3.499 46 × 10 ⁻⁶
202	ILK	223	ILK	-18.74	0.000 115 901
202	ILK	323	ILK	16.67	1.657 08 × 10 ⁻⁷
202	ILK	351	ILK	-31.39	0.005 115 262
203	ILK	204	ILK	42.72	0.000 562 904
203	ILK	341	ILK	15.32	0.001 348 582
204	ILK	220	ILK	65.63	6.795 62 × 10 ⁻⁸
204	ILK	223	ILK	53.39	3.293 11 × 10 ⁻⁵
204	ILK	341	ILK	28.09	4.165 76 × 10 ⁻⁵
204	ILK	345	ILK	-23.17	0.022 269 911
205	ILK	206	ILK	-77.52	1.234 64 × 10 ⁻⁷
205	ILK	221	ILK	-32.38	0.000 160 981
206	ILK	207	ILK	-25.08	0.003 638 826
206	ILK	208	ILK	-24.74	1.575 67 × 10 ⁻⁶
206	ILK	220	ILK	124.52	9.172 77 × 10 ⁻⁸
206	ILK	221	ILK	-51.21	0.000 374 99
206	ILK	223	ILK	83.74	2.217 76 × 10 ⁻⁷
207	ILK	208	ILK	145.09	9.126 65 × 10 ⁻⁷
207	ILK	218	ILK	77.75	6.795 62 × 10 ⁻⁸
207	ILK	219	ILK	57.78	1.802 97 × 10 ⁻⁶
207	ILK	220	ILK	123.34	1.917 71 × 10 ⁻⁷
208	ILK	209	ILK	-35.12	0.002 798 602
208	ILK	218	ILK	35.85	2.924 86 × 10 ⁻⁵
208	ILK	219	ILK	-63.12	7.577 38 × 10 ⁻⁶
209	ILK	216	ILK	21.64	2.061 6 × 10 ⁻⁶
209	ILK	218	ILK	28.88	1.200 89 × 10 ⁻⁶
209	ILK	271	ILK	-50.35	7.898 03 × 10 ⁻⁸
210	ILK	217	ILK	-22.44	0.000 304 799
211	ILK	212	ILK	24.34	0.001 014 099
211	ILK	216	ILK	41.67	0.016 668 799
212	ILK	217	ILK	-23.13	0.000 144 383
216	ILK	217	ILK	56.04	3.705 12 × 10 ⁻⁵
216	ILK	270	ILK	-17.65	0.001 014 099
216	ILK	271	ILK	-58.23	6.795 62 × 10 ⁻⁸
217	ILK	218	ILK	170.17	6.795 62 × 10 ⁻⁸
217	ILK	219	ILK	-25.86	6.610 45 × 10 ⁻⁵
217	ILK	254	ILK	21.88	0.001 480 977
217	ILK	268	ILK	-35.18	2.061 6 × 10 ⁻⁶
217	ILK	270	ILK	20.75	2.562 95 × 10 ⁻⁷
217	ILK	271	ILK	-21.35	0.000 199 707
218	ILK	219	ILK	-40.88	0.019 292 38
218	ILK	268	ILK	62.09	9.126 65 × 10 ⁻⁷
218	ILK	269	ILK	-118.51	2.562 95 × 10 ⁻⁷
218	ILK	271	ILK	-18.88	0.013 320 516
219	ILK	220	ILK	-66.66	1.575 67 × 10 ⁻⁶
219	ILK	267	ILK	-33.75	0.000 920 913

ID1	Protein	ID2	Protein	difference pairwise force [pN]	p-value
219	ILK	268	ILK	47.33	0.002 341 273
220	ILK	221	ILK	-16.43	0.006 557 193
220	ILK	266	ILK	25.09	0.000 115 901
220	ILK	267	ILK	-33.81	0.019 292 38
220	ILK	338	ILK	-30.99	0.001 480 977
220	ILK	339	ILK	259.93	6.795 62 × 10 ⁻⁸
220	ILK	340	ILK	76.02	6.795 62 × 10 ⁻⁸
220	ILK	341	ILK	58.81	6.795 62 × 10 ⁻⁸
222	ILK	223	ILK	-31.91	0.001 227 183
222	ILK	224	ILK	-30.25	4.538 97 × 10 ⁻⁷
222	ILK	264	ILK	-36.15	3.0691 × 10 ⁻⁶
222	ILK	265	ILK	-22.72	0.031 517 102
222	ILK	342	ILK	-39.45	2.562 95 × 10 ⁻⁷
222	ILK	345	ILK	18.33	0.038 514 96
223	ILK	224	ILK	24.88	0.000 338 195
224	ILK	225	ILK	-16.27	0.041 123 594
225	ILK	227	ILK	27.78	0.031 517 102
225	ILK	332	Parvin	-71.31	0.022 269 911
226	ILK	335	Parvin	22.21	0.007 113 494
227	ILK	228	ILK	28.3	0.000 338 195
227	ILK	259	ILK	-23.45	0.036 048 327
229	ILK	233	ILK	23.12	0.041 123 594
232	ILK	259	ILK	46.86	0.000 247 061
234	ILK	235	ILK	-23.63	0.036 048 327
235	ILK	256	ILK	15.69	0.002 798 602
235	ILK	257	ILK	-17.18	0.036 048 327
235	ILK	266	ILK	33.04	0.000 247 061
235	ILK	267	ILK	-29.47	0.000 160 981
235	ILK	342	ILK	35.44	5.873 57 × 10 ⁻⁶
236	ILK	240	ILK	25.29	0.000 160 981
237	ILK	240	ILK	15.77	0.008 354 827
238	ILK	242	ILK	-25.11	0.002 139 261
239	ILK	256	ILK	37.45	3.705 12 × 10 ⁻⁵
239	ILK	267	ILK	-16.72	0.001 348 582
239	ILK	342	ILK	16.47	0.006 040 33
240	ILK	243	ILK	31.4	0.000 274 511
250	ILK	337	ILK	-22.47	0.022 269 911
251	ILK	269	ILK	-27.93	0.004 702 533
251	ILK	272	ILK	34.49	7.577 38 × 10 ⁻⁶
252	ILK	269	ILK	24.74	0.033 717 669
253	ILK	267	ILK	28.54	2.924 86 × 10 ⁻⁵
254	ILK	268	ILK	-86.48	0.000 920 913
255	ILK	267	ILK	24.3	0.000 199 707
256	ILK	267	ILK	-22.03	0.020 734 594
257	ILK	265	ILK	21.2	0.005 560 46
258	ILK	259	ILK	-32.62	0.000 920 913
258	ILK	262	ILK	-35.17	0.000 415 502
259	ILK	265	ILK	-18.15	0.004 320 184
262	ILK	264	ILK	-17.29	4.165 76 × 10 ⁻⁵
264	ILK	266	ILK	18.83	0.003 966 239
267	ILK	268	ILK	-43.51	0.000 460 073
267	ILK	338	ILK	-57.57	3.415 58 × 10 ⁻⁷
268	ILK	269	ILK	-34.37	0.011 432 829
269	ILK	270	ILK	-50.5	2.924 86 × 10 ⁻⁵
270	ILK	271	ILK	53.32	0.000 144 383
271	ILK	272	ILK	-34.58	0.009 045 397
272	ILK	275	ILK	-52.32	3.293 11 × 10 ⁻⁵
272	ILK	326	ILK	78.23	2.355 66 × 10 ⁻⁶
272	ILK	327	ILK	-38.48	5.165 78 × 10 ⁻⁶
272	ILK	328	ILK	-26.61	3.705 12 × 10 ⁻⁵
272	ILK	334	ILK	-23.08	0.000 338 195
273	ILK	274	ILK	73.03	0.000 247 061
273	ILK	275	ILK	-19.96	6.610 45 × 10 ⁻⁵
276	ILK	277	ILK	22.45	0.027 483 422
276	ILK	278	ILK	70.97	2.689 77 × 10 ⁻⁶
276	ILK	322	ILK	19.16	0.000 835 717
276	ILK	325	ILK	34.57	0.006 557 193
276	ILK	326	ILK	83.08	5.165 78 × 10 ⁻⁶
277	ILK	281	ILK	44.46	0.022 269 911
277	ILK	322	ILK	-24.4	0.025 639 272
277	ILK	325	ILK	-36.37	0.001 348 582
278	ILK	283	ILK	-32.07	0.000 460 073
278	ILK	323	ILK	-48.33	9.277 96 × 10 ⁻⁵

ID1	Protein	ID2	Protein	difference pairwise force [pN]	p-value
279	ILK	284	ILK	22.05	0.003 966 239
282	ILK	283	ILK	36.73	0.005 115 262
282	ILK	389	ILK	22.03	0.049 863 69
283	ILK	323	ILK	44.59	0.002 139 261
296	ILK	300	ILK	-38.04	0.023 903 146
296	ILK	451	ILK	27.75	0.003 638 826
298	ILK	301	ILK	20.67	0.033 717 669
300	ILK	304	ILK	-18.82	0.014 363 848
300	ILK	332	ILK	16.48	0.046 791 615
301	ILK	381	ILK	18.72	0.043 880 384
305	ILK	306	ILK	-17.13	0.007 711 805
307	ILK	310	ILK	16.37	0.043 880 384
307	ILK	311	ILK	-32.93	0.003 336 179
308	ILK	309	ILK	22.85	0.002 798 602
308	ILK	335	ILK	17.76	0.000 835 717
311	ILK	315	ILK	-19.88	0.023 903 146
312	ILK	317	ILK	15.55	0.022 207 185
315	ILK	340	ILK	16.19	0.031 517 102
317	ILK	340	ILK	23.39	0.009 786 487
317	ILK	366	ILK	26.95	0.001 782 376
317	ILK	374	ILK	54.25	0.036 048 327
318	ILK	324	ILK	-33.84	0.006 557 193
318	ILK	335	ILK	-41.81	0.000 509 073
318	ILK	340	ILK	21.33	0.025 639 272
318	ILK	341	ILK	27.66	0.011 432 829
319	ILK	324	ILK	37	0.000 686 822
319	ILK	339	ILK	-32.15	0.000 562 904
320	ILK	321	ILK	67.16	0.000 144 383
320	ILK	377	ILK	52.01	0.000 757 881
320	ILK	378	ILK	-29.61	0.003 056 629
321	ILK	323	ILK	60.47	0.001 115 947
321	ILK	325	ILK	-32.49	0.013 320 516
321	ILK	339	ILK	26.37	0.001 782 376
321	ILK	355	ILK	64.66	0.001 480 977
321	ILK	381	ILK	26.23	0.000 686 822
322	ILK	323	ILK	-48.68	0.019 292 38
322	ILK	324	ILK	-28.73	0.000 247 061
322	ILK	381	ILK	32.78	0.002 341 273
322	ILK	384	ILK	85	4.540 08 × 10 ⁻⁶
323	ILK	324	ILK	-54.77	0.001 115 947
323	ILK	326	ILK	52.39	2.562 95 × 10 ⁻⁷
323	ILK	339	ILK	63.3	0.000 415 502
323	ILK	355	ILK	-22.34	0.000 129 405
323	ILK	384	ILK	67.31	0.023 903 146
324	ILK	335	ILK	-16.84	0.007 711 805
324	ILK	336	ILK	62.02	0.049 863 69
325	ILK	326	ILK	-35.23	0.029 440 884
325	ILK	334	ILK	-21	0.007 113 494
326	ILK	327	ILK	49.2	0.003 638 826
326	ILK	333	ILK	28.94	0.001 625 258
326	ILK	334	ILK	30.84	0.031 517 102
326	ILK	336	ILK	19.12	0.041 123 594
326	ILK	339	ILK	-30.83	6.0148 × 10 ⁻⁷
328	ILK	332	ILK	-36.78	0.009 045 397
335	ILK	336	ILK	94.34	0.000 115 901
336	ILK	339	ILK	34.29	0.001 227 183
337	ILK	338	ILK	-54.5	0.003 336 179
337	ILK	339	ILK	79.45	0.000 144 383
338	ILK	339	ILK	55.18	0.001 782 376
338	ILK	340	ILK	-119.49	1.917 71 × 10 ⁻⁷
338	ILK	341	ILK	-33.41	6.795 62 × 10 ⁻⁸
339	ILK	341	ILK	-113.25	0.000 222 203
340	ILK	342	ILK	-41.42	2.0616 × 10 ⁻⁶
341	ILK	345	ILK	54.02	2.0616 × 10 ⁻⁶
341	ILK	346	ILK	40.31	6.795 62 × 10 ⁻⁸
341	ILK	349	ILK	37.75	1.917 71 × 10 ⁻⁷
341	ILK	351	ILK	-15.24	3.705 12 × 10 ⁻⁵
342	ILK	345	ILK	122.12	1.200 89 × 10 ⁻⁶
343	ILK	345	ILK	-42.76	5.895 92 × 10 ⁻⁵
345	ILK	346	ILK	63.7	0.000 222 203
348	ILK	349	ILK	-54.93	0.001 953 348
349	ILK	333	Parvin	32.97	0.049 863 69
355	ILK	356	ILK	26.1	0.036 048 327

ID1	Protein	ID2	Protein	difference pairwise force [pN]	p-value
355	ILK	377	ILK	59.59	1.59972×10^{-5}
355	ILK	384	ILK	48.48	0.03851496
359	ILK	360	ILK	-24.99	0.000509073
364	ILK	311	Parvin	-19.72	0.007711805
365	ILK	366	ILK	-16.05	0.003336179
366	ILK	370	ILK	21.95	0.016668799
370	ILK	373	ILK	20.31	0.020734594
370	ILK	374	ILK	-97.79	0.004702533
372	ILK	433	ILK	16.4	0.013320516
376	ILK	377	ILK	22.8	0.006557193
380	ILK	381	ILK	29.64	0.027483422
380	ILK	383	ILK	26.85	0.025639272
390	ILK	391	ILK	35.67	0.000103734
392	ILK	393	ILK	-19.31	0.031517102
397	ILK	398	ILK	-16.7	0.010581211
397	ILK	401	ILK	-15.1	0.002341273
399	ILK	403	ILK	33.51	0.001953348
400	ILK	401	ILK	32.92	0.003966239
400	ILK	404	ILK	-24.26	0.00604033
408	ILK	409	ILK	-16.62	0.015478602
432	ILK	436	ILK	-16.32	0.03851496
436	ILK	437	ILK	-17.5	0.033717669
450	ILK	451	ILK	-33.86	0.000415502
254	Parvin	362	Parvin	17.78	0.01929238
285	Parvin	287	Parvin	31.15	0.046791615
291	Parvin	352	Parvin	16.99	0.000103734
292	Parvin	294	Parvin	25.06	0.002139261
296	Parvin	300	Parvin	-17.37	0.015478602
299	Parvin	300	Parvin	40.85	0.001480977
308	Parvin	313	Parvin	19.37	0.005115262
309	Parvin	311	Parvin	34.06	0.004702533
310	Parvin	312	Parvin	-18.48	0.001625258
328	Parvin	332	Parvin	21.7	0.043880384
331	Parvin	334	Parvin	-15.69	0.001782376
331	Parvin	335	Parvin	31.26	0.006557193
332	Parvin	335	Parvin	-52.9	1.80745×10^{-5}
333	Parvin	335	Parvin	-21.47	0.013320516
333	Parvin	336	Parvin	-25.48	0.027483422
333	Parvin	337	Parvin	39.47	0.001953348
334	Parvin	335	Parvin	49.79	0.003056629
334	Parvin	336	Parvin	-16.11	0.007113494
334	Parvin	339	Parvin	23.5	0.027483422
336	Parvin	337	Parvin	-33.96	0.002798602
336	Parvin	338	Parvin	27.38	0.020734594
339	Parvin	340	Parvin	29.53	0.008354827
343	Parvin	344	Parvin	17.88	0.010581211
344	Parvin	345	Parvin	36.64	0.000686822
345	Parvin	346	Parvin	28.86	0.017938613
347	Parvin	348	Parvin	-19.89	0.020734594
347	Parvin	351	Parvin	21.97	0.009786487
348	Parvin	349	Parvin	31.93	0.000686822
350	Parvin	352	Parvin	27.12	0.007711805
354	Parvin	355	Parvin	21.76	0.04986369
356	Parvin	357	Parvin	15.97	0.036048327
357	Parvin	358	Parvin	23.12	0.046791615
359	Parvin	360	Parvin	23.94	0.009786487
364	Parvin	368	Parvin	55.99	0.001625258
367	Parvin	368	Parvin	21.08	0.041123594

Tab. A.1.: Significant differences in pairwise forces between the ILK:parvin holo and apo state calculated from FDA (n = 20 independent trajectories, p < 0.05, Mann-Whitney).

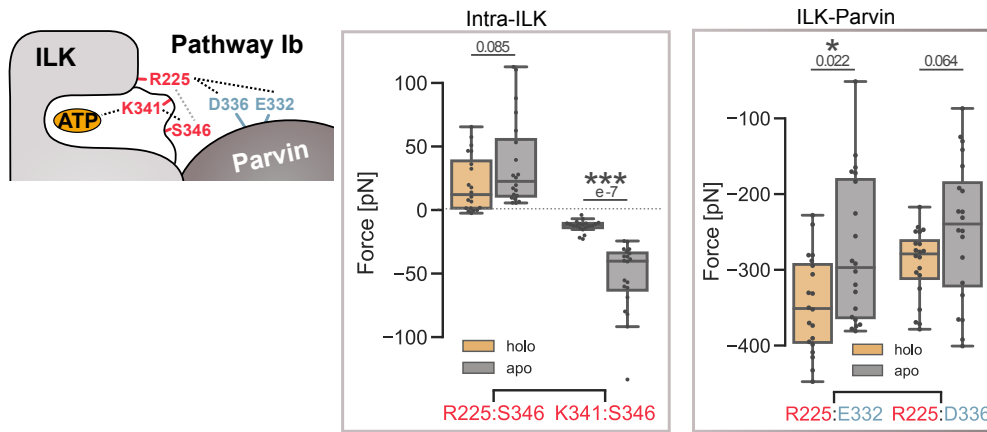


Fig. A.3.: Secondary ATP-dependent pathway of internal force propagation between ILK and parvin involving the saltbridge-forming residue R225. Average pairwise forces between the indicated residue pairs calculated from FDA for 20 individual runs compared between the ILK:parvin apo and holo complex. Statistical significance determined by Mann-Whitney test. Positive and negative values of force denote repulsion and attraction, respectively.

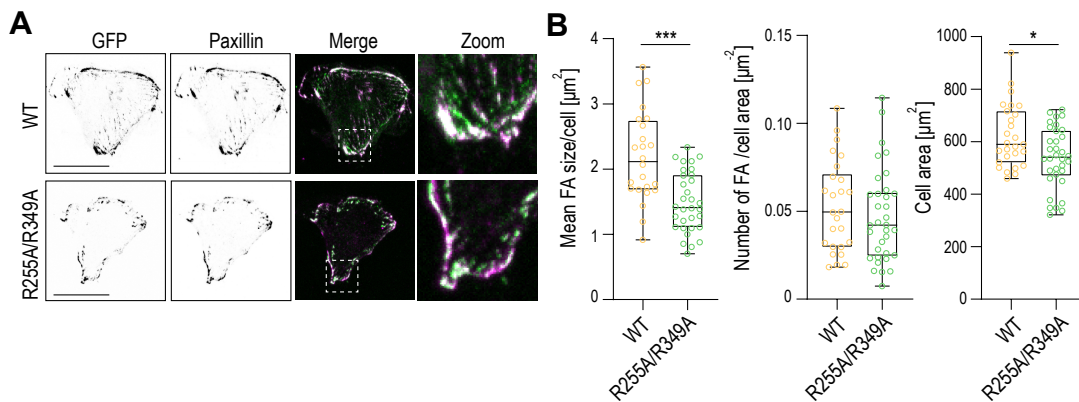


Fig. A.4.: Effect of disruption of parvin-binding saltbridges. Experiments and figure including legend were provided by the collaborators Dr. Michele Nava and Prof. Dr. Sara Wickström, University of Helsinki. (A) Representative immunofluorescence images of ILK(WT)-GFP and ILK(R255A/R349A)-GFP cells stained with paxillin on crossbow micropatterned surfaces. Paxillin localizes to focal adhesions both in ILK(WT)-GFP and ILK(R255A/R349A)-GFP cells (right panels). Scale bars 20 μm . (B) Quantification of FA size and number ($n > 24$ cells/condition pooled across 4 independent experiments). *** $p = 0.0001$, * $p = 0.0260$, Mann-Whitney).

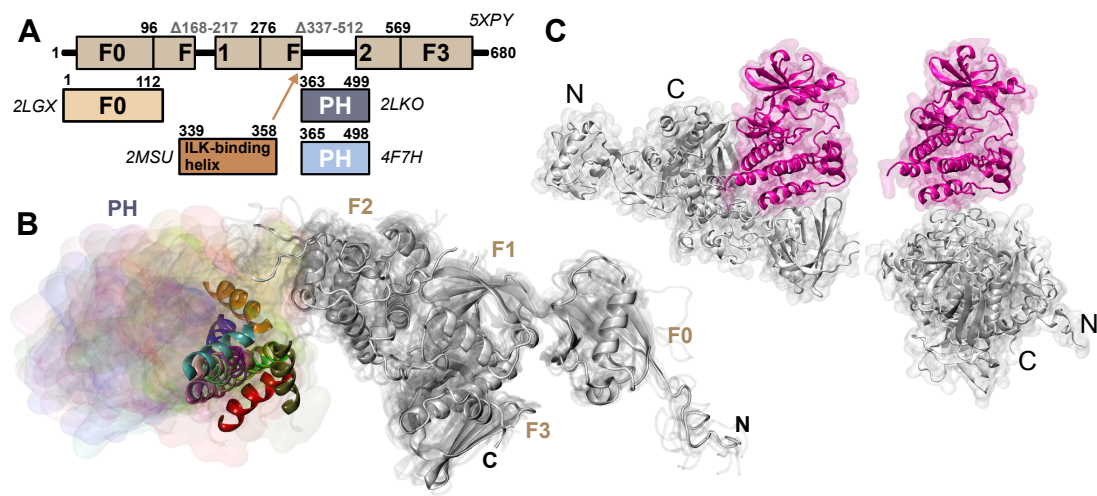


Fig. A.5.: Kindlin-2 modeling and ILK:kindlin-2 docking. (A) Schematic overview of available kindlin-2 partial crystal structures and associated PDB-codes. (B) Homology models of the full human kindlin-2. The placements of PH-domains are highlighted in surface representation and different colors. For visualization purposes one helix within the PH-domain is represented as cartoon. (C) Additional ILK:kindlin-2 docking poses from guided docking. ILK in pink and kindlin-2 in light grey. N- and C-terminus of kindlin-2 are labeled.

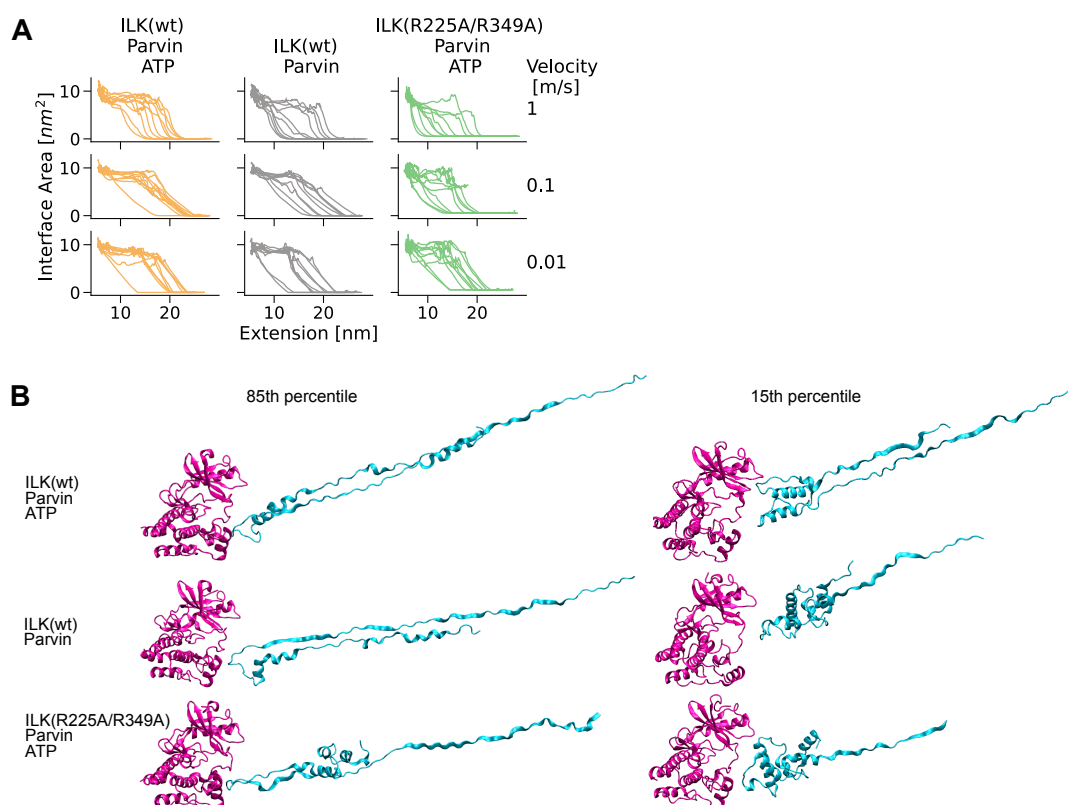


Fig. A.6.: ILK:parvin complex under mechanical tension along the kindlin-actin axis. (A) ILK:parvin interface area as a function of extension between the two force application patches for ILK(WT) holo and apo and ILK(R225A/R349A) at three different pulling velocities (1 m s^{-1} , 0.1 m s^{-1} , 0.01 m s^{-1}). Trajectories were smoothed with a rolling average. (B) Simulation snapshots at time of complex dissociation representing the 15th and 85th percentile of each distribution.

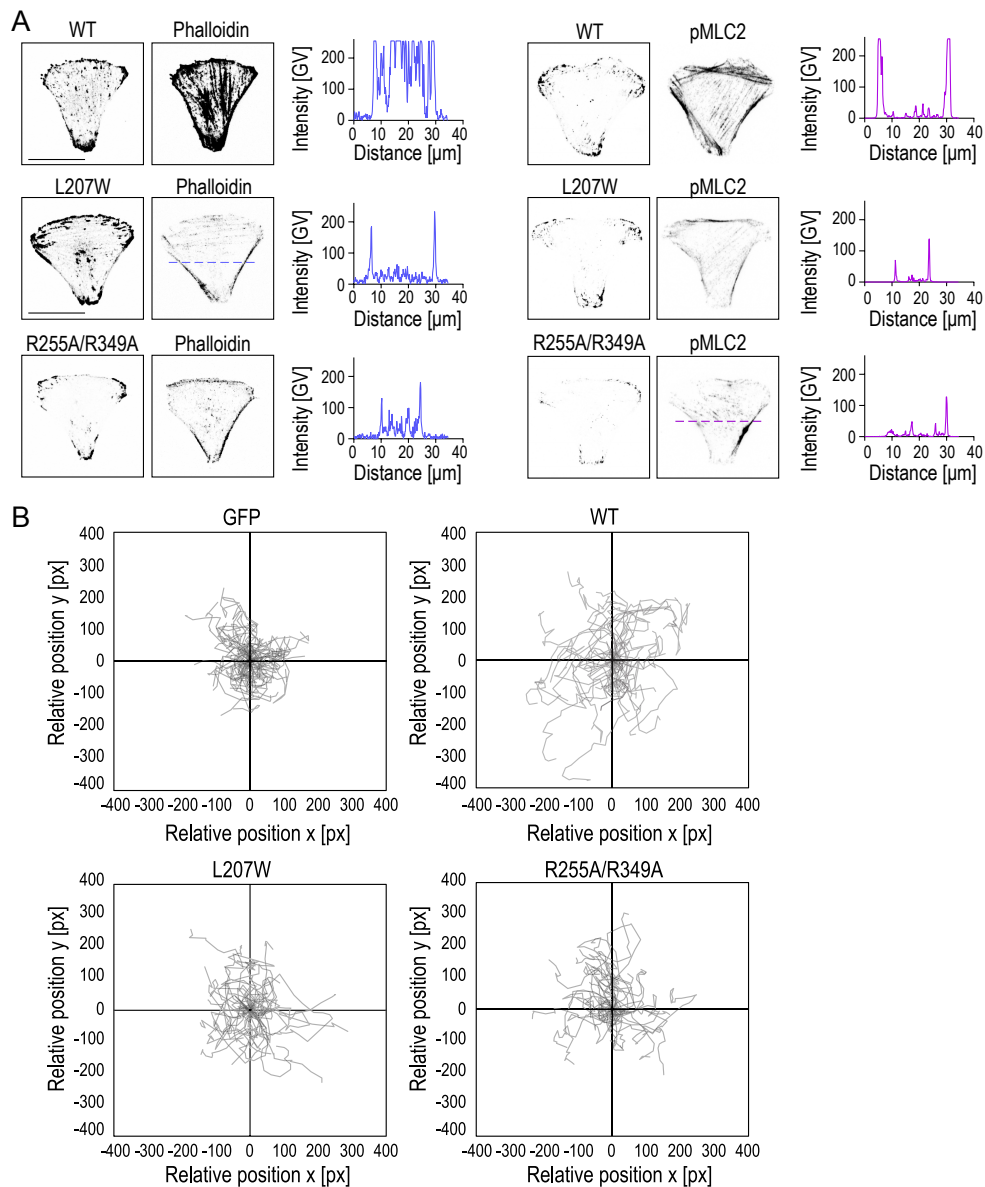


Fig. A.7.: Impaired ATP- and α -parvin binding impedes actomyosin contractility and cell migration. Experiments and figure including legend were provided by collaborators Dr. Michele Nava and Prof. Dr. Sara Wickström, University of Helsinki. (A) Representative images of ILK(WT)-GFP, ILK(L207W)-GFP and ILK(R255A/R349A)-GFP cells stained with phalloidin and pMLC2 on crossbow micropatterns. Corresponding quantification of fluorescence intensity of phalloidin (blue) and pMLC2 (magenta) using a line scan. GV = gray values. Scale bars $20\mu\text{m}$. (B) Representative cell trajectories of ILK^{-/-}-GFP, ILK(WT)-GFP, ILK(L207W)-GFP and ILK(R255A/R349A)-GFP during 12 h acquisition. $n > 30$ cell tracks/condition were set to a common origin (intersection of x and y axes).

Appendix for chapter 4: INCENP

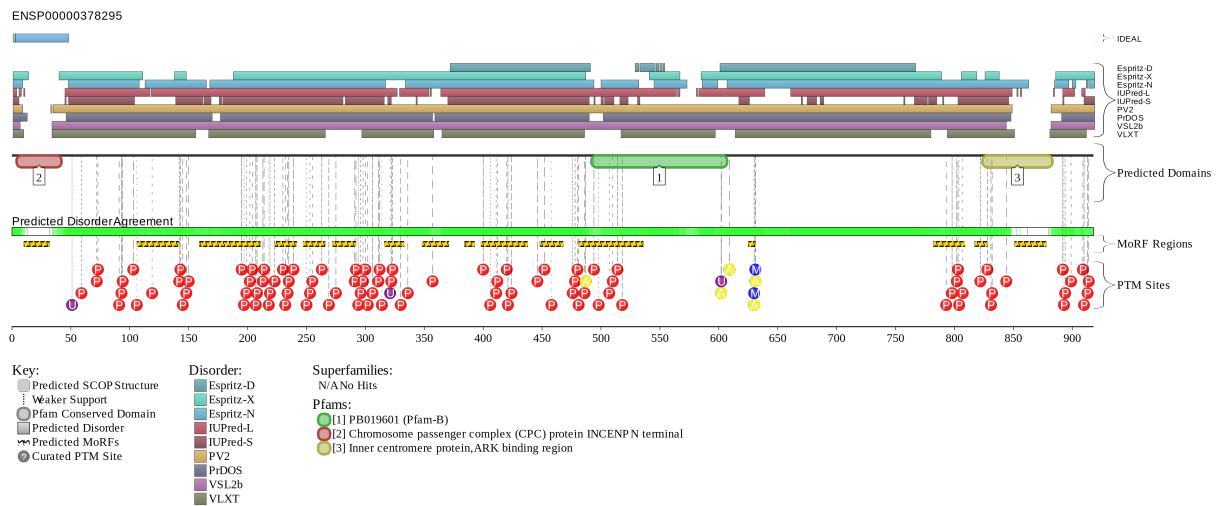


Fig. B.1.: Disorder prediction of INCENP from different disorder prediction servers, accumulated in the D²P² database of disordered protein predictions (Oates et al., 2013)

Range	Sequence
56-130 [‡]	MPKTPSQKNRRKKRRISYVQDENRDPIRRRLSRRKSRSSQ LSSRRLRSKDSVEKLATVVGENGSVLRRVTRAAAA
81-155	PIRRRLSRRKSRSSQLSSRRLRSKDSVEKLATVVGENGSV LRRVTRAAAAAAAATMALAAPSSPTPESPTMLTKK
121-195	LRRVTRAAAAAAAATMALAAPSSPTPESPTMLTKKPEDNH TQCQLVPVVEIGISERQNAEQHVTQLMSTEPLPRT
181-255*	QHVTQLMSTEPLPRTLSPASATAPTSQGIPTSDEESTP KKSKARILESITVSSLMATPQDPKGQGVGTGRSAS
201-275	ASATAPTSQGIPTSDEESTPKKSKARILESITVSSLMATP QDPKGQGVGTGRSASKLRIAQVSPGPRDSPAFPDS
211-285 [†]	IPTSDEESTPKKSKARILESITVSSLMATPQDPKGQGVGT GRSASKLRIAQVSPGPRDSPAFPDSPWRERVLAPI
245-319	GQGVGTGRSASKLRIAQVSPGPRDSPAFPDSPWRERVLAP ILPDNFSTPTGSRTDSQSVRHSPAPSSPSPQVLA
311-385	SSPSPQVLAQKYSLVAKQESVRRASRRLAKKTAEEPAAS GRIICHSYLERLLNVEVPQKVGSEQKEPPEEAEPV
325-399 [†]	VAKQESVRRASRRLAKKTAEEPAASGRIICHSYLERLLN VEVPQKVGSEQKEPPEEAEPVAAAPEVPENNGNN
366-440	EVPQKVGSEQKEPPEEAEPVAAAPEVPENNGNNSWPHND TEIANSTPNPKPAASSPETPSAGQQEAKTDQADGP
373-447 [†]	SEQKEPPEEAEPVAAAPEVPENNGNNSWPHNDTEIANST PNPKPAASSPETPSAGQQEAKTDQADGPREPPQSA
411-485*	STPNPKPAASSPETPSAGQQEAKTDQADGPREPPQSARRK RSYKQAVSELDEEQHLEDEELQPPRSKTPSSPCPA
453-527	YKQAVSELDEEQHLEDEELQPPRSKTPSSPCPASKVVRPL RTFLHTVQRNQMLMTPTSAPRSVMKSFIKRNTPLR

Tab. B.1.: Sequence of 75-residue fragments considered in the simulations. * Fragment only considered in all-atom simulations. † Fragment only considered in coarse-grained simulations. ‡ Fragment only simulated in the non-phosphorylated form in all-atom simulations.

type	residue	P-level				type	residue	P-level			
SER	91	1				THR	294	1			
SER	93	1				SER	296	1			
SER	94	1	10			THR	298	1	10		
SER	97	1				SER	300	1			
SER	103	1				SER	302	1			
SER	106	1				SER	306	1	10	20	
THR	112	1				SER	311	1			
SER	119	1	10			SER	312	1	10		
THR	135	1				SER	314	1	10	20	
SER	142	1				TYR	322	1			
SER	143	1	10			SER	323	1			
THR	145	1				SER	330	1			
SER	148	1	10			SER	336	1			
THR	150	1				THR	343	1			
THR	195	1				SER	350	1			
SER	197	1	10	20	50	SER	357	1			
THR	199	1	10			SER	373	1			
SER	202	1				SER	400	1			
THR	204	1				THR	406	1			
THR	207	1	10			SER	411	1			
SER	208	1	10			THR	412	1			
THR	213	1	10	20		SER	420	1			
SER	214	1	10	20		SER	421	1	10		
SER	218	1	10			THR	424	1	10		
THR	219	1	10	20		SER	446	1	10		
SER	223	1				SER	452	1	10		
SER	230	1				SER	458	1			
THR	232	1				SER	476	1			
SER	234	1				THR	478	1	10		
SER	235	1				SER	480	1			
THR	239	1	10	20		SER	481	1	10	20	50
THR	250	1				SER	486	1			
SER	253	1				THR	494	1			
SER	255	1				THR	498	1			
SER	263	1	10	20	50	100	THR	507	1		
SER	269	1	10	20	50	100	THR	509	1		
SER	275	1	10	20	50	100	SER	510	1		
SER	291	1				SER	514	1			
THR	292	1	10	20	50	SER	518	1			

Tab. B.2.: Phosphorylated residues of INCENP (taken from PhosphoSitePlus (Hornbeck et al., 2015) and their corresponding P-levels according to a threshold concerning the number of literature mentions.

residue	type	MusiteDeep	NetPhos 3.1.	NetPhorest	GPS	GPS	GPS	GPS	PPSP
		unsp.	unsp.	CDK1	CDK1	PLK1	MPS1	Aurora B	Aurora B
91	S	0.789	0.997		-0.545	7.961	14.282	0.078	6.43
93	S	0.595	0.749		1.931	9.79	12.886	0.01	
94	S	0.721	0.997		1.405	9.779	14.244	0.07	5.04
97	S	0.563	0.996	0.052	6.052	10.791	7.199	-0.008	
98	S	0.609	0.267	0.047	1.598	5.645	24.468	-0.002	
103	S	0.841	0.971		2.809	7.255	15.855	0.012	
106	S	0.836	0.984		4.03	9.366	16.077	0.012	
112	T	0.307	0.205		1.898	7.335	14.754	-0.006	
119	S	0.765	0.015	0.060	2.694	10.679	16.706	-0.003	
125	T	0.218	0.651		-0.514	8.191	17.266	0.076	6.9
135	T	0.181	0.046		-9.197	13.231	18.799	-0.0006	
142	S	0.618	0.078		0.624	8.957	11.437	0.004	
143	S	0.852	0.738	0.200	9.254	11.474	13.181	-0.006	
145	T	0.801	0.533	0.115	8.192	9.81	11.48	-0.004	
148	S	0.868	0.969	0.269	8.512	10.966	17.514	-0.003	
150	T	0.453	0.011		-8.715	9.414	21.638	-0.01	
153	T	0.15	0.965		1.633	8.142	16.68	-0.005	
161	T	0.085	0.034		-0.462	9.827	10.718	0.001	
174	S	0.071	0.345		-0.247	9.96	12.326	-0.003	
184	T	0.19	0.029		-1.496	9.484	18.932	-0.002	
188	S	0.419	0.761		1.337	9.535	15.957	-5 × 10 ⁻⁵	
189	T	0.274	0.017		-0.11	10.076	14.042	-0.005	
195	T	0.604	0.319		2.064	12.121	16.446	0.002	
197	S	0.844	0.955	0.164	8.785	8.309	10.679	0.009	
199	T	0.704	0.065	0.115	9.258	8.523	19.458	-0.005	
202	S	0.443	0.462		-0.605	7.973	20.303	-0.004	
204	T	0.324	0.026		-0.878	7.14	16.691	-0.005	
207	T	0.352	0.032		3.855	4.472	12.392	0.001	
208	S	0.556	0.402		1.775	6.28	13.987	-0.001	
213	T	0.548	0.925		1.563	10.161	19.738	-0.002	
214	S	0.769	0.991		1.061	7.396	22.746	-0.006	
218	S	0.511	0.791	0.064	2.769	9.741	12.781	-0.004	
219	T	0.843	0.993	0.349	11.135	9.653	14.1	-0.0009	
223	S	0.351	0.904		4.007	6.523	14.343	0.014	
230	S	0.488	0.066		1.033	11.075	15.71	0.000 07	
232	T	0.209	0.019		0.94	9.262	22.191	-0.007	
234	S	0.201	0.032		0.184	7.122	24.723	0.003	
235	S	0.461	0.583		1.176	11.968	17.255	-0.004	
239	T	0.806	0.37	0.244	8.387	6.743	12.933	-0.0001	
250	T	0.157	0.917		0.791	8.734	7.359	-0.006	
253	S	0.252	0.091		2.529	5.797	11.801	0.001	
255	S	0.237	0.976		3.241	7.707	15.585	0.001	
263	S	0.896	0.972	0.238	8.295	8.982	12.301	0.004	
269	S	0.894	0.993	0.189	8.659	10.887	14.224	0.069	3.76
275	S	0.897	0.973	0.321	12.397	15.046	7.126	-0.005	
291	S	0.655	0.016		0.344	9.958	6.468	0.0003	
292	T	0.86	0.594	0.173	8.453	8.977	12.025	-0.006	
294	T	0.505	0.225		2.731	5.463	10.342	0.001	
296	S	0.67	0.984		0.553	2.297	11.397	0.004	
298	T	0.245	0.02		0.993	9.707	9.772	0.003	
300	S	0.591	0.959		0.627	10.27	8.313	0.009	
302	S	0.743	0.992		2.817	12.107	13.166	-0.002	
306	S	0.897	0.997	0.224	8.143	10.454	14.638	0.069	4.4
311	S	0.715	0.053		1.517	7.63	13.221	-0.002	
312	S	0.89	0.986	0.189	8.161	8.534	8.933	-0.005	
314	S	0.884	0.548	0.195	9.492	9.852	12.525	-0.005	
323	S	0.353	0.004		0.171	11.366	7.504	0.016	5.37
330	S	0.547	0.317		3.182	11.012	8.342	-0.002	3.52
336	S	0.386	0.996		0.022	6.926	13.655	0.078	4.2
343	T	0.158	0.364		1.46	11.945	10.862	0.013	
350	S	0.145	0.661		0.399	6.472	12.759	0.002	
357	S	0.189	0.489		-0.967	8.922	9.832	0.002	
373	S	0.587	0.659	0.041	1.688	6.413	18.952	-0.004	
400	S	0.341	0.508		-10.958	10.824	14.219	-0.0007	
406	T	0.167	0.052		-0.111	11.488	16.653	-0.003	
411	S	0.167	0.943		1.271	8.329	13.127	0.003	
412	T	0.558	0.549	0.223	8.216	10.02	11.45	0.0003	
420	S	0.801	0.993		2.155	9.964	6.956	0.003	
421	S	0.889	0.993	0.145	8.11	10.315	14.141	0.0006	
424	T	0.879	0.571	0.202	7.183	10.033	13.73	-0.009	
426	S	0.67	0.74		-0.756	7.096	14.406	0.004	
434	T	0.19	0.031		0.361	8.785	22.989	0.006	

residue	type	MusiteDeep	NetPhos 3.1.	NetPhorest	GPS	GPS	GPS	GPS	PPSP
		unsp.	unsp.	CDK1	CDK1	PLK1	MPS1	Aurora B	Aurora B
446	S	0.753	0.992	0.239	4.213	9.92	10.329	-0.003	
452	S	0.819	0.997		-2.1	7.767	11.782	0.028	4.56
458	S	0.874	0.993		-0.046	10.955	14.388	0.002	
476	S	0.637	0.86		2.222	6.433	11.546	0.001	
478	T	0.857	0.94	0.256	7.697	10.591	20.968	0.002	
480	S	0.758	0.848		0.554	9.702	9.469	0.005	
481	S	0.876	0.992	0.278	9.725	9.394	13.177	-0.003	
486	S	0.279	0.062		0.931	7.242	12.691	0.0005	
494	T	0.099	0.053		2.125	8.589	12.607	0.006	
498	T	0.122	0.008		2.286	8.793	8.428	0.004	
507	T	0.783	0.512	0.157	8.639	9.815	17.62	-0.0003	
509	T	0.307	0.164		0.317	6.314	7.425	0.007	
510	S	0.668	0.42		2.74	8.03	15.291	-0.005	
514	S	0.422	0.987		2.346	9.215	8.656	-0.0008	
518	S	0.381	0.08	0.072	3.365	11.279	14.141	0.003	
524	T	0.809	0.826	0.290	11.453	9.927	15.254	0.072	3.45

Tab. B.3.: Prediction scores of phosphorylation sites in INCENP with different prediction tools: Musite Deep (D. Wang et al., 2020), NetPhos 3.1. (Blom et al., 1999); NetPhorest (Horn et al., 2014); GPS (C. Wang et al., 2020); PPSP (Xue et al., 2006). *Data generated by Marius Hedtfeld, Adel Iusupov and Andrea Mussachhio (MPI of Molecular Physiology, Dortmund).*

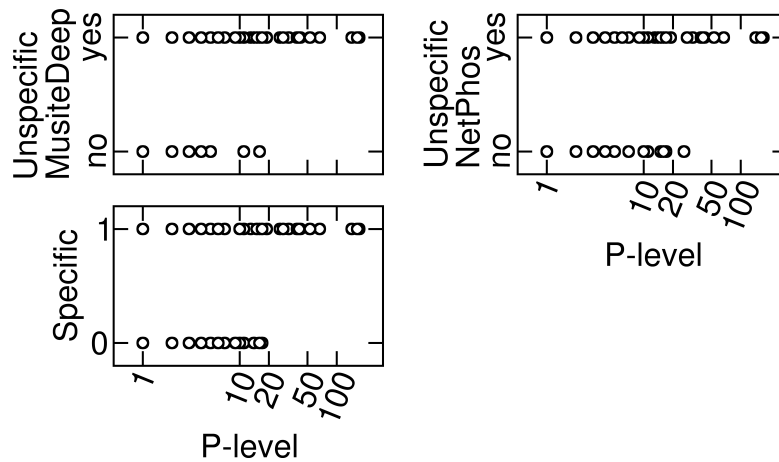


Fig. B.2.: Predictions of INCENP phosphorylation sites for unspecific (top) or specific kinases (bottom) according to different prediction tools (MusiteDeep (D. Wang et al., 2020); NetPhos 3.1. (Blom et al., 1999); NetPhorest (Horn et al., 2014); GPS (C. Wang et al., 2020); PPSP (Xue et al., 2006); see also Table B.3) in relation to the P-levels used in this work. Thresholds to determine a residue as phosphorylated are described in the methods. *This figure was generated by Dr. Camilo Aponte-Santamaría (HITS, Heidelberg) based on the data from Marius Hedtfeld, Adel Iusupov and Andrea Mussachhio (MPI of Molecular Physiology, Dortmund).*

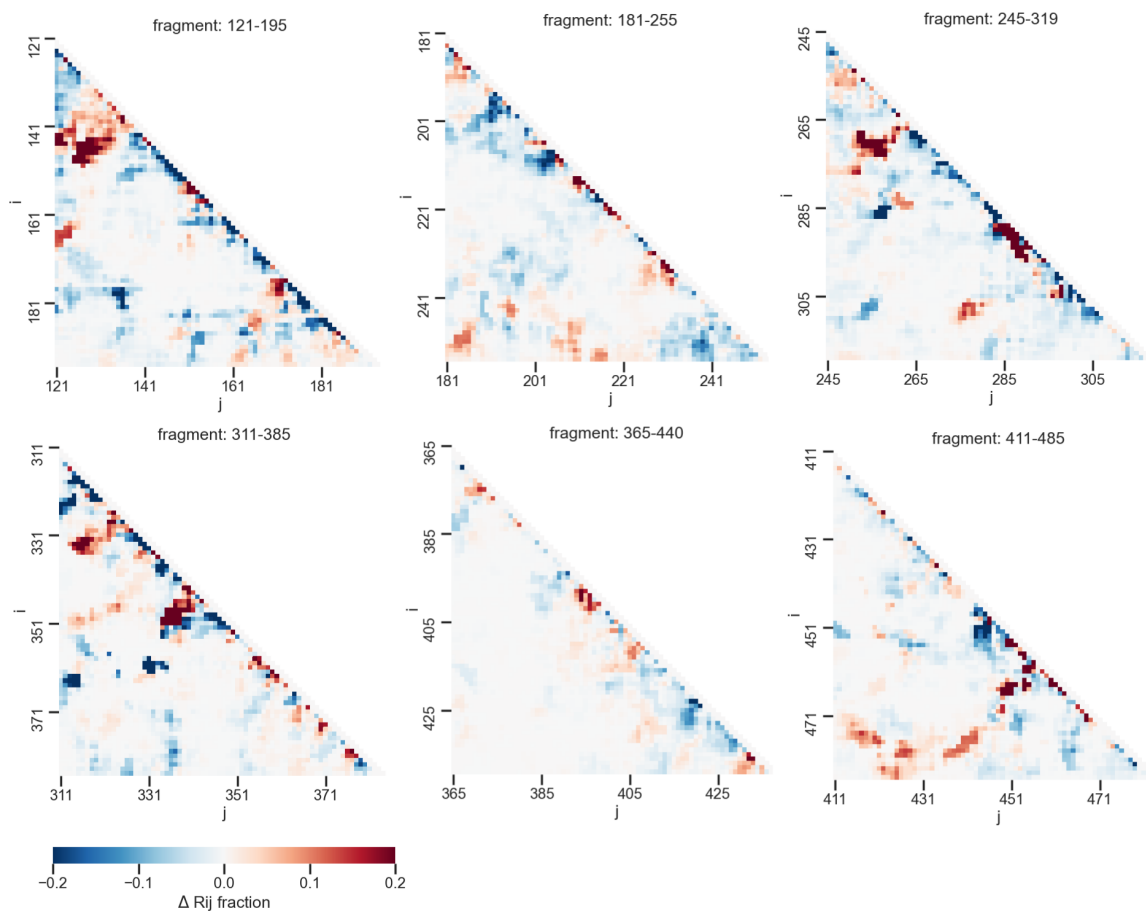


Fig. B.3.: Differences in residue-wise contact fractions between phosphorylated and non-phosphorylated states from all-atom simulations of 75-residue fragments not highlighted in the main text. Fractions range from reduced (blue) to increased (red) contact probability in the phosphorylated state.

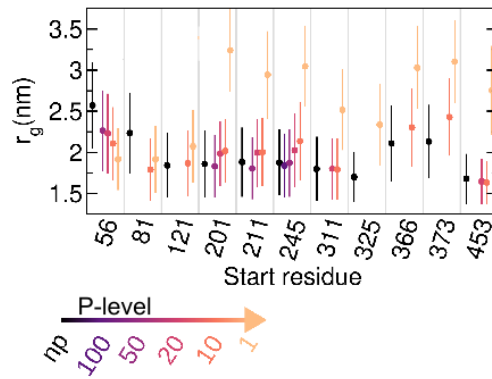


Fig. B.4.: R_g of 75-residue fragments in the coarse-grained simulations, where the starting residue of each fragment is indicated in the x -axis, separated by gray vertical lines. Different levels of phosphorylations were considered according to the P-level color-scale, np: non-phosphorylated. Average \pm standard deviation. *This data and figure was provided by Dr. Camilo Aponte-Santamaría.*

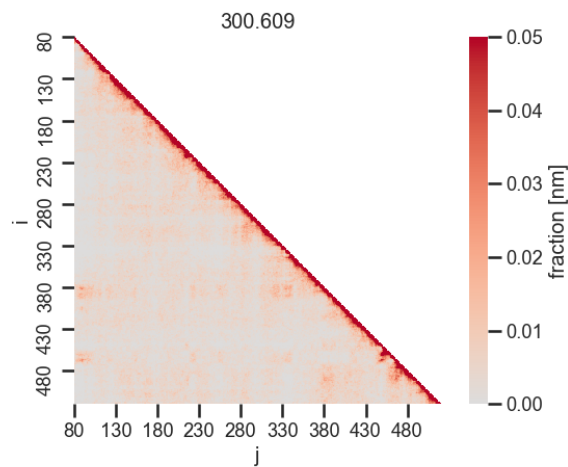


Fig. B.5.: Contact fraction at 300 K is depicted for each residue pair (i,j) of the whole non-phosphorylated IDR simulated by CG simulations.

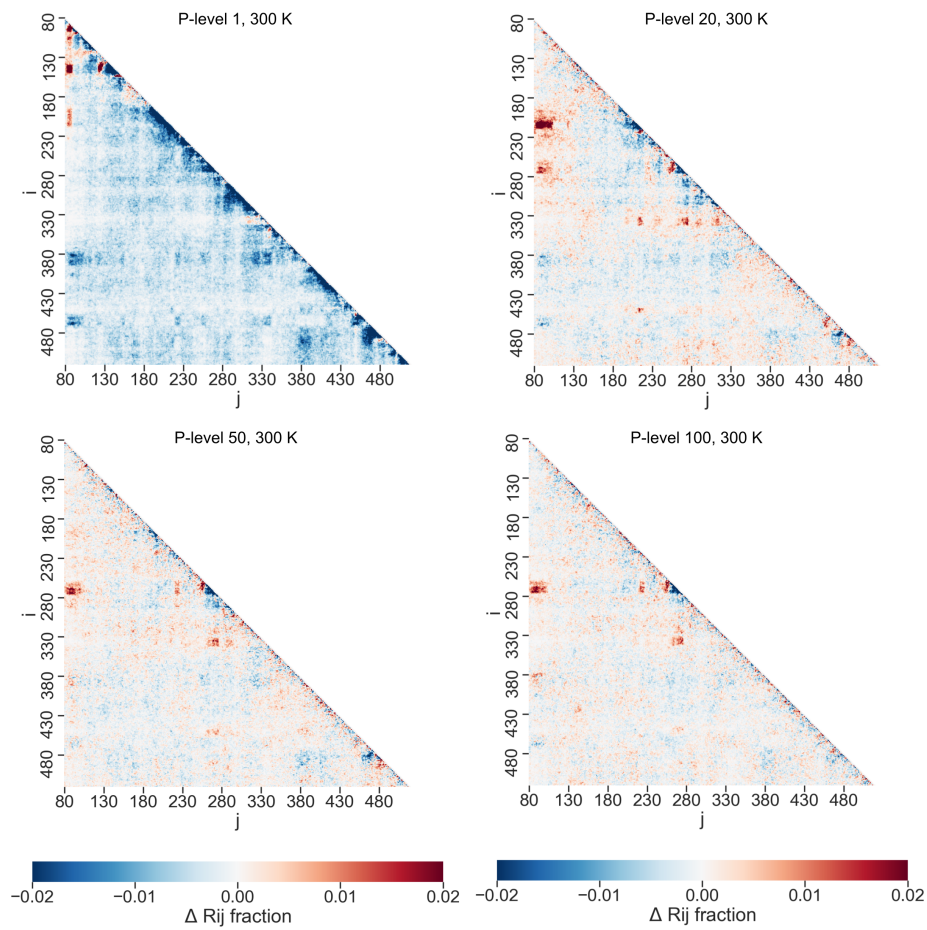


Fig. B.6.: Difference in the contact fraction between indicated phosphorylated states and non-phosphorylated states at 300 K is depicted for each residue pair (i,j) of the whole IDR simulated by CG simulations.

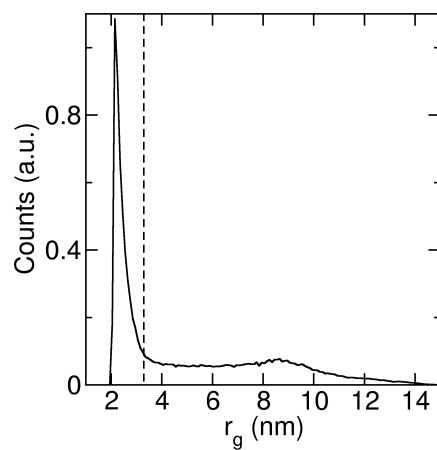


Fig. B.7.: Probability distribution of r_g for the entire 441-residue IDR considering all temperatures and P-levels. The vertical dashed line indicates the median r_g (3.29 nm). *This data and figure was provided by Dr. Camilo Aponte-Santamaría.*

